THEORETICAL STUDIES ON MOLECULAR INTERACTIONS UNDER NANOCONFINEMENT AND CATALYTIC PROPERTIES OF NANOCLUSTERS

By

MANOJ KUMAR TRIPATHY
CHEM01200804021

BHABHA ATOMIC RESEARCH CENTRE, MUMBAI

A thesis submitted to the

Board of Studies in Chemical Sciences

In partial fulfillment of requirements

for the Degree of

DOCTOR OF PHILOSOPHY

of

HOMI BHABHA NATIONAL INSTITUTE

August, 2015

Homi Bhabha National Institute

Recommendations of the Viva Voce Committee

As members of the Viva Voce Committee, we certify that we have read the dissertation prepared by **Manoj Kumar Tripathy** entitled **Theoretical studies on molecular interactions under nanoconfinement and catalytic properties of nanoclusters** and recommend that it may be accepted as fulfilling the thesis requirement for the award of Degree of Doctor of Philosophy.

Chairman - Dr. S. K. Ghosh	Sivaprasad Kumar Ghosh	**Date:** 9-5-2016
Guide / Convener - Dr. A. K. Samanta		**Date:** 09/05/2016
Co-guide - Dr. K. R. S. Chandrakumar	KRSChandrakumar	**Date:** 09/05/16
Examiner - Dr. Abhishek Kumar Singh	Abhishek Kumar Singh	**Date:** 9/5/2016
Member 1- Dr. T. K. Ghanty	Tapas Kumar Ghanty	**Date:** 09/05/16
Member 2- Dr. D. K. Maity		**Date:**

Final approval and acceptance of this thesis is contingent upon the candidate's submission of the final copies of the thesis to HBNI.

We hereby certify that we have read this thesis prepared under our direction and recommend that it may be accepted as fulfilling the thesis requirement.

Date: 09-05-2016

Place: Mumbai

KRSChandrakumar
Co-guide

Guide

STATEMENT BY AUTHOR

This dissertation has been submitted in partial fulfillment of requirements for an advanced degree at Homi Bhabha National Institute (HBNI) and is deposited in the Library to be made available to borrowers under rules of the HBNI.

Brief quotations from this dissertation are allowable without special permission, provided that accurate acknowledgement of source is made. Requests for permission for extended quotation from or reproduction of this manuscript in whole or in part may be granted by the Competent Authority of HBNI when in his or her judgment the proposed use of the material is in the interests of scholarship. In all other instances, however, permission must be obtained from the author.

Manoj Kumar Tripathy

DECLARATION

I, hereby declare that the investigation presented in the thesis has been carried out by me. The work is original and has not been submitted earlier as a whole or in part for a degree / diploma at this or any other Institution / University.

Manoj Kumar Tripathy

List of Publications arising from the thesis

Journals

a. Published

1. Theoretical investigations on Zundel cation present inside boron-nitride nanotubes: Effect of confinement and hydrogen bonding, **M. K. Tripathy**, N. K. Jena, A. K. Samanta, S. K. Ghosh, K. R. S. Chandrakumar, Chem. Phys., **2015,** 446, 127-133
2. Effect of confinement on the structure and energetics of Zundel cation present inside the hydrophobic carbon nanotubes: An *ab initio* study, **M. K. Tripathy**, N. K. Jena, A. K. Samanta, S. K. Ghosh, K. R. S. Chandrakumar, Theor. Chem. Acc., **2014,** 133, 1576 (1-12)
3. Protonated water under hydrophobic nanoconfinement: An *ab initio* study, **M. K. Tripathy**, K. R. S. Chandrakumar, and S. K. Ghosh, AIP Conf. Proc., **2013**, 1512, 168-169
4. Water molecule encapsulated in carbon nanotube model systems: Effect of confinement and curvature, N. K. Jena, **M. K. Tripathy**, A. K. Samanta, K. R. S. Chandrakumar, S. K. Ghosh, Theor. Chem. Acc., **2012,** 131, 1205 (1-12)
5. Solvation energy of multiply charged anions and dielectric constant for finite system : A microscopic theory based bottom-up and top-down approach, A. K. Pathak, **M. K. Tripathy**, A. Das, A. K. Samanta, Mol. Phys., **2013**, 111, 975 (1-8)

b. To be communicated

1. Effect of nanoconfinement on the charge-transfer complexes: A case study of Lewis acid-base complexes, **M. K. Tripathy**, Sagnik Dutta, Naresh K. Jena, K. R. S. Chandrakumar
2. Enhanced CO interaction ability of hydrogen doped gold nanoclusters: Hydrogen island effect; **M. K. Tripathy**, Sumalta Sonavane, K. R. S. Chandrakumar

Publication in Conferences

1. Theoretical study of water molecules trapped inside Carbon Nanotubes, **M. K. Tripathy**, K. R. S. Chandrakumar, S. K. Ghosh, International Symposium on Material Chemistry (ISMC), **2008**, 2, 407
2. Unraveling the factors affecting proton transfer energetics of Zundel cation nanoconfined in hydrophobic carbon nanotubes: an ab Initio Study, **M. K. Tripathy**, N. K. Jena, K. R. S. Chandrakumar, Current Trends in Theoretical Chemistry (CTTC), **2013**, 1, 153

Manoj Kumar Tripathy

Omm Maa Sarala, Jai Jagannath, Maa Tarini
JBB, JSM, JMM

Dedicated
To
My Family Members & Teachers

ACKNOWLEDGEMENTS

I owe my deepest gratitude and sincere thanks to my Ph. D supervisor Prof. Alok K. Samanta for his invaluable inspiration and guidance throughout my Ph. D tenure. He has been highly supportive and encouraging at all the times. His valuable suggestions and scientific discussions are highly simulating and encouraging throughout my research. My sincere thanks to Dr. K. R. S. Chandrakumar, the co-guide for the present thesis, who was with me at each and every step to solve the difficulties I faced throughout my work. Without his support and guidance, the thesis could not have been completed. I also thank Prof. S. K. Ghosh and other committee members, Dr. T. K. Ghanty and Dr. D. K. Maity for their valuable suggestions.

I would also like to acknowledge other members of TCS, Dr. K. Srinivasu, Dr. N. Choudhury, Dr, A. K. Pathak, Dr. M. K. Nayak, Dr. M. Sundararajan, Dr. Y. Sajeev, and B. Modak for sharing their knowledge and experiences with me. It is my pleasure to thank Shri R.C. Sharma, Dr. P. V Varde, Dr. R. S. Sharma and my other divisional colleagues for their support and encouragement for the work. The supercomputing facility of Bhabha Atomic Research Center is also gratefully acknowledged for providing the computational resources for my research work. The list of friends and seniors who helped me in many occasions during my work will be huge. I would like to mention a few of them namely, Naresh, Deepak, Siba, Raju, Shrinibas, M. Mohapatra for their help and wishes.

I wish to express my sincere gratitude to my parents, parents-in-laws, all other family members and all the well-wishers for their support and blessings on me. Finally I would like to thank my wife Jinu and my daughter Lineysha for their support and help.

……..Manoj

CONTENTS

SYNOPSIS

On the basis of length-scale, the material world can be broadly classified as macroscopic, mesoscopic, microscopic and finally a single atom or molecule. When a few atoms or molecules agglomerate to form assemblies of less than 100 nanometer in size (at least in one dimension), these new assemblies are categorized as nanomaterials. The main reason for this separate classification is due to their unique physical and chemical properties, which differ significantly from those of the atomic and the bulk materials. The surface induced effects (large surface to volume ratio) and the quantum size effects are recognized as the primary cause for these new properties. One of the simplest examples is the modification of electronic levels which become discrete in case of nanomaterials as compared to the bands in bulk.

The system under nanometer in size in a confined nanospace can also exhibit different properties which can significantly differ from their bulk counterpart primarily due to the quantum confinement effect. The significant effects on the chemical properties of these confined systems associated with nanoscale confinement have potential importance in a wide range of applications, e.g., catalysis, lubrication and separation science. However, our understanding of chemistry of these nanoconfined systems is still considered to be an elusive phenomenon and the corresponding mechanisms are also being uncovered. Such a molecular-level understanding can only be illuminated with the application of both experimental and theoretical studies. In order to theoretically investigate these exciting unravelled nanoconfined systems, one can use quantum chemical methods based electronic structure calculations. With the advancement of computing techniques, density functional theory (DFT) in particular has been a very helpful technique to handle hundreds of atom in a very accurate manner.

In the present thesis, the chemical properties of the nanomaterials have been investigated in isolated condition and under the confinement of various nanostructured media. In addition, we have also investigated the catalytic properties of nanomaterials through a few important reactions. The main objective is to investigate the modification in the chemical properties of system by changing the surrounding medium. We have mainly studied the change in structure, solvation, energetics, vibrational frequencies, chemical reactivity and catalytic activity using density functional based methods. The present thesis is composed of eight chapters and in what follows, we will briefly discuss the work presented in each chapter.

Chapter 1

This introductory chapter starts with a brief genesis of the nanomaterials, explaining how the properties of nanomaterials can be distinctly different from that of the bulk. Then the general aspect of confinement and its effect on the properties of the encapsulated system are discussed. When the length scale of the confinement medium approaches the atomic size, the properties of confined matter become distinctly different from the bulk and the gas phase behaviour. The geometric constraints offered by the confinement medium along with the diverse nature of interaction between the enclosed molecule and cavity lead to the change in the structure, bonding, chemical reactivity of the host system. Further, different type interactions and their importance in such nanoconfined environment are discussed. This chapter also describes the challenges that can be encountered in the detailed exploration of structure, property and reactivity of nanomaterials particularly in nanoconfinement by experimental and theoretical techniques. The importance of computational methods have been outlined which provides some of the most valuable information which experiments cannot

provide. Brief introduction of the computational methods and their importance have been provided. At the end, the scope of the thesis has been discussed in brief.

The first part of the work is focused on the exploration of chemical properties of the materials in a nanoconfined environment. In particular, the effect several confinement media such as carbon nanotubes (CNT), boron-nitride nanotubes (BNNT) and fullerenes on the molecular properties of water and acid-base complexes have been investigated. In addition, an analytical expression for the solvation energy for a finite system has been derived using microscopic theory-based bottom-up approach. This approach provides the information on solvation energies of anionic solutes in finite-size clusters, including the bulk ($N = \infty$), from the knowledge of the detachment energies for the system containing a few numbers of solvent molecules. In the last part of the work, the effect of nanostructured materials on the catalytic activity of different metal atoms especially, titanium, gold and vanadium on water splitting process to generate hydrogen and for the CO oxidation process has been investigated.

Chapter 2

In this chapter, the effect of confinement on the structure and properties of water clusters are presented. Water has been recognized as the matrix of life and plays a crucial role in many biological and chemical systems. In many of these systems, water is found to be confined in pores of diameter in the nanometer scale, for example, hydrophobic cavities of proteins. In these nanoconfined regimes, water molecules portray entirely different behaviour compared to the bulk water. In the present work, we have studied the structure, bonding and vibrational spectra of water clusters in carbon nanotubes (CNT) of diameter in the range of sub-nanometer. The effect of confinement has been systematically investigated by varying the

diameter of the CNT. One of the motivations of this study is the tremendous potential of CNT for various technologically important applications such as filtration devices, fuel cells etc. In addition, the hydrophobic similarity of CNT with biological channels can be exploited to get the primary behaviour of water in the complex biological systems.

From the stabilization energy values calculated by the dispersion corrected DFT method, it is confirmed that water can occupy the interior of a narrow nanotube such as CNT(4,4). In CNT(4,4) and CNT(5,5), one-dimensional water chains parallel to the CNT axis is formed whereas in CNT(6,6), zigzag structure is observed with radial O-O distance shorter than that of parallel to the CNT axis. More symmetric structures similar to gas phase structures are detected in larger diameter CNTs and the cluster gets stabilized close to the CNT wall. It has been observed that in highly confined medium like CNT(4,4), there is a reduction in the O-H bond length of water. An inverse relation between the electronic charge transfer (from CNT to water) and the CNT diameter is also established. It is found that the intra-molecular charge separation for each water molecule increases under confinement as compared to its gas phase counterpart. The highest tube-water interaction is achieved for a confinement length ~ 7Å. Under highly confined system, blue shift in the stretching frequency of O-H (non-hydrogen bonded) occurs due to the reduction in O-H bond length. In the case of CNT(6,6), a red shifting in stretching frequency of the hydrogen bond assisted O-H bond is observed due to the reduction in O–O separation distance and hence strengthening of the hydrogen bond. The important findings from this study is the degree of confinement (diameter and curvature of carbon nanotube) is extremely important in deciding the properties of confined water molecules.

Chapter-3

In this chapter, the spherical confinement effect due to the fullerene cages on the nature of acid-base complexes is presented. Owing to the unique cage structure and large polarizability, fullerenes are considered as one of the ideal hosts to study the structure-property relationship of the confined matter at nanoscale. Some recent studies show the modification in hydrogen bonding and vibrational spectra of the confined molecules in the fullerene cage. In addition, it has been observed that polar molecules are more stabilized over the nonpolar ones in fullerenes. Fullerenes also induce the formation of chemical bond in noble gas atoms. Inspired by these initial reports, we studied the chemical behaviour of both strong and weak acid-base pairs in carbon fullerenes. This chapter is divided in to two parts. In the first part, we have considered the NH_3-HCl pair as a prototype system and studied the effect of confinement and polarizability of fullerene cages on the behaviour of this acid-base pair by systematically varying the fullerene diameter (C_{36} to C_{180}) using density functional methods. In our important findings, it has been demonstrated that the diameter of fullerene is one of the crucial factor in deciding the chemical properties of the acid-base pair. In isolated case (gas phase) of the NH_3-HCl pair, the proton is associated with the acid and quite far away from the nitrogen of ammonia. In larger diameter fullerene such as C_{180}, only a slight increase (~ 5%) in chloride-proton distance (R_{Cl-H}) is observed and the acid is still in an undissociated form. As the diameter of fullerene decreases, the acid starts dissociating and a gradual reduction in the nitrogen-proton distance is observed. In C_{60} and other smaller diameter fullerenes, the proton is completely transferred from the acid to ammonia, and a symmetrical ammonium ion is formed.

In the second part, we have considered the Lewis acid-base complex (LABC) i.e., the ammonia-borane and its fluorine derivatives and tried to elucidate the effect of spherical confinement due to the fullerene bulky balls on the structure, bonding and energetics of LABC in a systematic way. In particular, we have considered two fullerene rings C_{60} and C_{80} as the nanoconfined medium and investigated their role on the charge transfer and binding energy of the LABC complex by gradually substituting the hydrogen atoms with fluorine. We have observed that the confinement effect along with the interaction of fullerene with the LABC, significantly modify the structure, interaction energy, chemical reactivity and charge transfer in LABC under the spherical cage of fullerene. The results obtained from our study can be utilized to control the effective charge transfer in the acid-base complex and to finely tune the interaction strength of the complex by using proper confinement medium.

Chapter-4

This chapter deals with the solvation of multiply charged anions in finite system. In this particular case, the solvent molecules are confined due to the presence of multiply charged anions. In a nanoconfined environment, the solvation of molecules and ions differ significantly from the bulk solvation due to the presence of restricted number solvent molecules. Therefore, the solvation energy values of an ion likely to differ in these two environments (N & ∞). In the present study, a microscopic theory-based bottom-up approach has been implemented to derive an analytical expression for the solvation energy for a finite (N) system, including the bulk. This bottom-up approach provides the information on solvation energies of anionic solutes in finite-size clusters, including the bulk ($N = \infty$), from the knowledge of the detachment energies for the system containing a few numbers of solvent molecules. However,

in case of dielectric constant, a microscopic theory-based top-down approach has been prescribed to derive an analytical expression for the static dielectric constant for the finite system. In this approach, the knowledge of the dielectric constant for the bulk provides a scheme to obtain the same quantity for a wide numbers of solvent molecules. As an illustrative example, the hydrated doubly charged anions, $SO_4^{-2}.NH_2O$ and $C_2O_4^{-2}.NH_2O$, have been considered, and the calculated bulk solvation energy for the $SO_4{-}2.NH_2O$ system is found to be in very good agreement (within 5%) with the available experimental result. However, the same quantity calculated based on the Born model is found to be largely deviating (32%) from the experimental result. The possible break down of Born theory is due to the fact that it has been derived based on the continuum theory wherein microscopic details are not included. However, if solute–solvent and solvent–solvent motions are strongly correlated, the continuum theory breaks down. The success of our theory is due to the inclusion of microscopic details through the system-dependent parameters. The theory therefore can be useful in deriving the solvation energy and dielectric constant of ions a precise and accurate manner.

Chapter-5

This chapter deals with the study of proton transfer energetics in water and ammonia under confinement. In many important physical, chemical and biological processes, PT occurs in a nanoconfined environment. Carbon and Boron-Nitride nanotubes have been used as model nanoconfinement media to study the proton transfer reactions and get detailed insights into the complex phenomena. In recent years, it has been shown that the proton mobility in the CNT channel exceeds by a factor of 40 as compared to that of bulk water using the sophisticated Molecular dynamics methods. Such fast proton hopping or diffusion process under

confinement has been explained by the alignment of water molecules inside the confinement media. Primarily, water molecules in the nanotube interior form a one-dimensional hydrogen bond network which causes the proton transfer mechanism to differ significantly from the bulk. To understand the molecular origin of the enhancement in proton transfer, we have studied the proton transfer energetics in CNT and BNNT using the protonated water dimer (Zundel cation) as a model system and employing dispersion corrected DFT method. The main objective of the study is to elucidate the effect of water-nanotube interaction and the diameter of nanotube (different degrees of confinement) on the structure and proton transfer energetics of Zundel cation (ZC). Our results reveal that the interaction of ZC with the nanotube largely depends on the diameter of the nanotube. The interaction energy of ZC with CNT is observed to be significantly higher (~40%) than that of BNNT. In larger diameter nanotubes, ZC is stabilized near the inner surface of the nanotube because of the formation of hydrogen bond between the ZC and the nanotube. It has also been shown that the effect of marginal change in degree of confinement on the energy barrier (12-45%) for the PT process is very remarkable. The vibrational frequencies of the ZC including the proton oscillation frequency (POF) have been calculated inside nanotubes. We have analyzed several important factors such as interaction energy, charge transfer and POF as a function of the degree of confinement. Among all the nanotubes considered in the present study, it has been concluded that the proton transfer may be facilitated in nanotubes with diameter in the range of 7 to 9 Å.

In the second part, proton transfer in the dissimilar system (ammonia and water) has investigated in CNTs of varying diameter. It has observed that the barrier for proton transfer is significantly high in highly confined situation and decreases sharply with the reduction in the

degree of confinement. It has also been observed that the PT towards water molecule can become energetically more feasible under confinement.

Chapter-6

This chapter deals with the effect of hydrogen doping in gold clusters for CO oxidation process. It is well known that CO can act like a poisoning agent specifically for the metal catalysts such as Pt and Pd. Hence, removal of CO is an extremely important requisite parameter for the effective function of these industrial catalysts. In normal practice, the smallest amount of CO present in air is oxidized using metal catalysts which however can only take place at very high temperature. In recent years, gold nanoclusters have been identified as the suitable catalyst for room temperature CO oxidation reaction. It has also been shown that the catalytic activity of gold cluster can be further improved by doping a hydrogen atom on the gold cluster. In the present study, we have systematically doped hydrogen atoms on gold clusters $\{(Au)_n$, n=1 to 6$\}$ and studied the structure and stability of each hydrogen doped clusters. For each gold cluster, we have considered various possible conformations and did the sequential hydrogen doping to the maximum extent possible. The important properties such as IP, EA and HOMO-LUMO gap have been thoroughly analysed for each of these clusters. In case of hydrogen doped clusters, it is observed that hydrogen atom withdraws electrons from the gold cluster and hence the gold atoms acquires high positive charge. Then the CO interaction has been studied with the pristine and hydrogen doped gold clusters. Interestingly, a substantial increase in the CO interaction energy (more than 20% in some cases) is observed when hydrogen atoms are doped with the gold clusters. One of the reasons for this remarkable enhancement in interaction energy is attributed to the charging of the gold cluster. Taking the

clue from this enhanced CO interaction, we have investigated the activation barrier for the CO oxidation leading to CO_2 process using some of the selected gold clusters for which the observed IE values are significantly higher than the pristine cluster. We also demonstrated that the CO oxidation can occur with these hydrogen doped gold clusters with a significantly lower barrier (100 %) in comparison to their pristine counterparts.

Chapter-7

Hydrogen is considered as the fuel of the next generation because of its ecofriendly advantages over other fuels. Production of hydrogen from the abundant water in a simple and economical way can certainly resolve the present energy crisis situation. Generation of hydrogen from water by electro-catalytic process is highly energy intensive. Other processes such thermal splitting is associated with large kinetic barrier and temperature requirement. Hence, the search for inexpensive and robust catalysts for water splitting is of considerable interest to the scientific community. Accordingly, in this chapter, we have made an attempt to investigate the effect of boron nitride nanotube on the catalytic activity of different metal atoms especially, titanium and vanadium for water dissociation reaction leading to the generation of hydrogen molecules.

Our results demonstrate that the adsorption of Ti or V atom on a BNNT surface depends on the surface curvature of the latter and among all the BNNTs considered in the study, highest adsorption energy (~ 1eV) is obtained in the case of BNNT(4,4). Then the interaction of water with the adsorbed Ti and V atom has been studied and the binding is found to be favourable in both cases with the corresponding binding energy value of -1.78 and -1.11 eV for Ti and V. The large binding energy values can be attributed to the significant

partial positive charge acquired by these adatoms. Further, we have investigated the water dissociation reaction with these BNNT decorated Ti and V atom. From our calculations, we have demonstrated that the dissociation of water to H and OH fragments is extremely facile with barrier height of 0.12 and 0.27 eV for Ti and V adsorbed structures respectively. We further studied the adsorption and dissociation of another water molecule on the final state (product) of the first water splitting reaction. It is observed that the second water molecule also interact strongly (binding energy > 1eV) with the product and the water dissociation proceed with very low energy barrier with the production of H_2 molecule. The barrier height for the water dissociation reaction estimated in the present study is lower than that of pure metal cluster and other supported nanostructured materials. Stabilization of the transition state structure by hydrogen bond involving O-H···N is the possible reason for the low barrier of this process. It is lucidly demonstrated through our study that the Ti-decorated BNNT system can be a potentially promising nanostructure for dissociation of water and generation of hydrogen.

Chapter-8

In this chapter, the conclusion and future directions that can be charted out from the present studies have been discussed. In particular, the outcomes of the present study and the possibility of extending the studies to chemically modified hosts in order to develop materials for specific application are briefly discussed.

List of figures

List of Tables

Chapter 1

Introduction
&
Theoretical background

1.1 Introduction to nanomaterials

The field of materials engineering is currently focused on developing advanced functional materials of tiny dimensions in the range of nanometer with enhanced performance for potential applications. This has generated a worldwide interest in investigating the growth and characterization of new nanomaterials for specific use [1-10]. In general, nanomaterials can be defined as the particles of organic or inorganic materials having sizes (at least one dimension) in the range of 1–100 nanometer [1-5]. A nanometer (nm) is one billionth of a meter, or 10^{-9} m. Nanomaterials are classified into nanostructured materials and nanophase/nanoparticle materials. The former refer to condensed materials that are made of grains with grain sizes in the nanometer range while the latter are usually the dispersive nanoparticles. Smaller nanoparticles containing 10^4 or less atoms are referred as nanoclusters.

The term nanomaterials may be a relatively new word, but these materials were in use from the Roman period. The Lycurgus Cup produced by the Romans in fourth century AD is one of the great work using colloidal nano gold and silver to achieve the color-shifting effect [11,12]. In the Middle Ages, colloidal gold was used for a diverse assortment of purposes including a s a colorant in stained glass windows and as a purported curative for a wide variety of diseases [13,14]. Probably the earliest scientific investigation into the synthesis of nanoparticle was by Michael Faraday, who in 1857 reported a method for preparing colloidal gold by electrochemical reduction of aqueous tetrachloroaurate ions, $AuCl_4^-$ [15]. This was followed by the great works of many eminent people such as Ostwald and Zsigmondy in the development of nanoparticles [16].

In addition, nature has many objects and processes that function on a micro to nanoscale. To mention, the flagella, a type of bacteria, is an example of a biological molecular machine. The

flagella motor is driven by the proton flow caused by the electrochemical potential differences across the membrane. The diameter of the bearing is about 20–30 nm, with an estimated clearance of about 1 nm [3,9,11,17-19].

The renewed interest in nanomaterials research started after the well-known lecture by Nobel laureate Richard. P. Feynman in 1959 at the California Institute of Technology where he stated, “There is a plenty of room at the bottom” and indicated the vast potential of materials having small dimensions [20]. Extrapolating from known physical laws, Feynman envisioned a technology using the ultimate toolbox of nature of building nanoobjects atom by atom or molecule by molecule. In subsequent years, numbers of technological applications were demonstrated for nanomaterials leading to development of an area referred as “nanoscience and nanotechnology” [3,4,21].

Nanoscience is the scientific study of objects on the nanometer regime and primarily focuses on finding governing laws of these tiny objects, deriving theoretical models to describe the behavior of those nanoscale materials and analyzing the properties of the whereas, nanotechnology uses the knowledge of nanoscience for practical applications starting from nanoscale electronics to nanomedicine [11,17,18,21-23]. This involves the synthesis and processing of nanomaterials, design and construction of novel tools for characterization of these materials and finally makes it useful for the particular application.

This field has been a rapidly developing area of the physical sciences in the past 20 years due to both the commercial potential and academic curiosity. The new aspects of nanoscience are the combination of our ability to see and manipulate the matter on nanoscale and our understanding of atomic scale interactions. Advances in the materials processing along with the precipitous rise in the sophisticated tools capable of characterizing materials with force,

displacement and spatial resolutions as small as picoNewtons (pN = 10^{-12} N), nanometer (nm = 10^{-9} m) and Angstrom (Å = 10^{-10} m), respectively, have provided unprecedented opportunities to probe the structure and mechanical response of materials on nanoscale [24]. Examples include scanning electron microscopy (SEM) and transmission electron microscopy (TEM) which use electron beam instead of light as the probe. In addition, major improvements in computer support have allowed the simulations of material structures and behavior with a degree of accuracy unimaginable as recently as a decade ago [6,25].

1.2 The fundamental importance of size: The nanoworld

The atomic theory of matter, formulated in the beginning of 19th century by John Dalton essentially tells that the smallest unit of matter which holds the physical significance of the matter is the atom. Atoms recombine among themselves and with the atoms of other species to create other molecules systems we come across in our everyday life. When a macroscopic object is cut into two, each of these two pieces in to two, and so on, the dimension of the material decreases from macroscopic to mesoscopic, mesoscopic to microscopic and then reaches to a few atoms (nanoclusters) and finally ends with a single atom (or molecule). Although the physical significance of the material does not alter throughout the above process, the fundamental properties of the pieces start to change once the size goes below roughly 100 nm. Although this observation was considered as strange behaviour of materials a few decades ago, it has now been reasonably explained through two effects, the quantum size effect and the surface area effect. [14,18-19, 26-30]. In a macroscopic metallic sphere of 2 cm diameter, less than 1 in 10 million atoms are on the surface layer. However, in a 10 nm diameter particle, 10% of its constituent atoms occupy the surface layer, and this proportion increases to 50% for a 2 nm particle. The

increase in the fraction of the total number of atoms on the surface to bulk leads to an immense surface area per unit volume of the material. Surface atoms are less coordinated as compared to the core atoms. Therefore increase in fraction on surface atoms greatly increases the surface energy. In addition, the finite size of the particle confines the spatial distribution of the electrons leading to the quantized energy level and thus exhibit quantum effects due to size [6-9,26,31-33].

Because of the large increase in the number of surface atoms with a small reduction in the material length, the fundamental properties become dependent on the size of the material. This regime (from 100 nm to single atom) where the fundamental properties depend on the size of the piece is known as "nanoworld" [1-5]. Several properties are modified with the reduction in size of the material. These include enhancement in strength, decrease in phase transition temperature, increase in diffusion coefficient, band gap, catalytic activity and magnetic permeability. As the size reduces, the particle become single domain and can display supermagnetism properties. Let us now discuss the band structure in material. In atoms or molecules, the electrons occupy

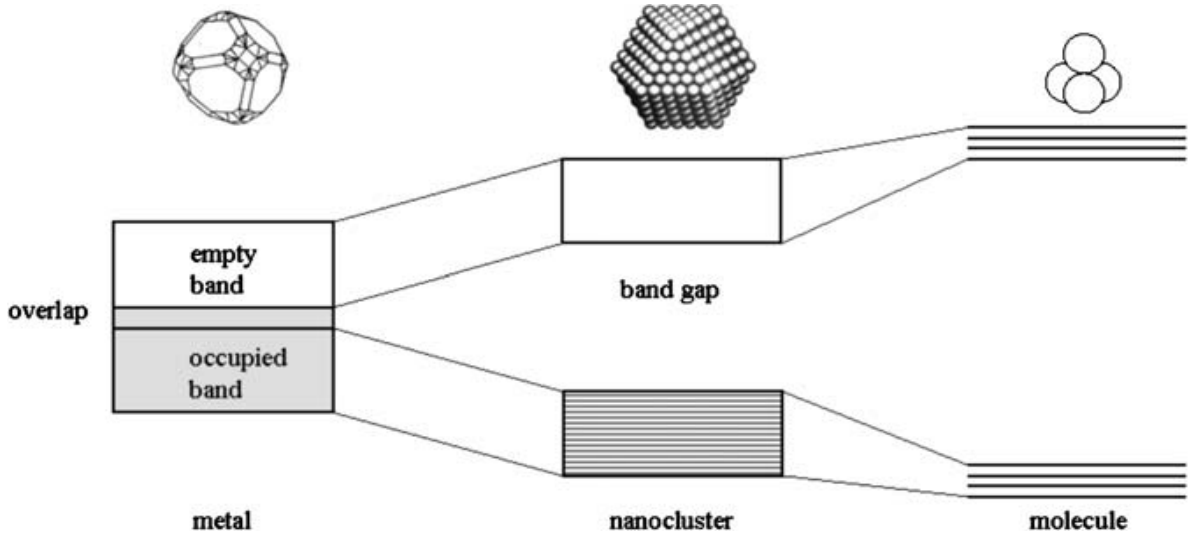

Figure 1.1: Variation in band structure of material with size [33].

discrete energy levels, whereas in a bulk metal the outermost electrons occupy energy bands, in which the energy, for all normal considerations, is a continuum. For nanoparticles smaller than 10 nm, the energy levels of the outermost electrons in the atoms start to display their discrete energies. In other words, the quantum nature of the particles starts to become apparent.

The chemical properties (reactivity) of nanomaterials are significantly different from bulk materials due to its high surface energy and surface area. The unique surface structure, electronic states and largely exposed surface area stimulate and promote chemical reactions. Thus, nanomaterials find great applications in the areas of catalysis and sensor devices [1,2,4,8-11]. This is demonstrated most dramatically by gold, which in the bulk is the archetypal inert material. This is one of the reasons why it is so highly valued since it does not corrode or tarnish and thus has a timeless quality. It would therefore seem that gold, would be useless as a catalyst to speed up chemical reactions, but this is not so for gold nanoparticles. When gold is in the form of nanoparticles with diameters less than about 5 nm, it becomes a powerful catalyst, especially for the oxidation of carbon monoxide (CO) more importantly at lower temperature [36-42]. In recent years, a number of research papers on the effectiveness of gold in catalyzing the above reaction have concluded that the dominant effect is that of the gold nanoparticle size, with the nature of the support playing a secondary role [43-57]. The impressive performance of gold nanoparticles towards CO oxidation on various supports as a function of their size has been shown in Figure 1.2. It is noteworthy that bulk gold is completely inert in macroscopic-sized pieces. Since catalysis can only occur at the surface layer of atoms, the dominant size effect is the proportion of gold atoms that are present at the surface. These low coordinated gold atoms react with carbon monoxide molecules preferentially during the reaction. The fraction of this

type of atom (highlighted in red in Fig. 1.2) is proportional to 1/*d*3, where *d* is the particle diameter and the black line in the Figure is a fit to the data using this law, demonstrating that the dominant size effect is indeed the corner atoms located at the surface.[21]

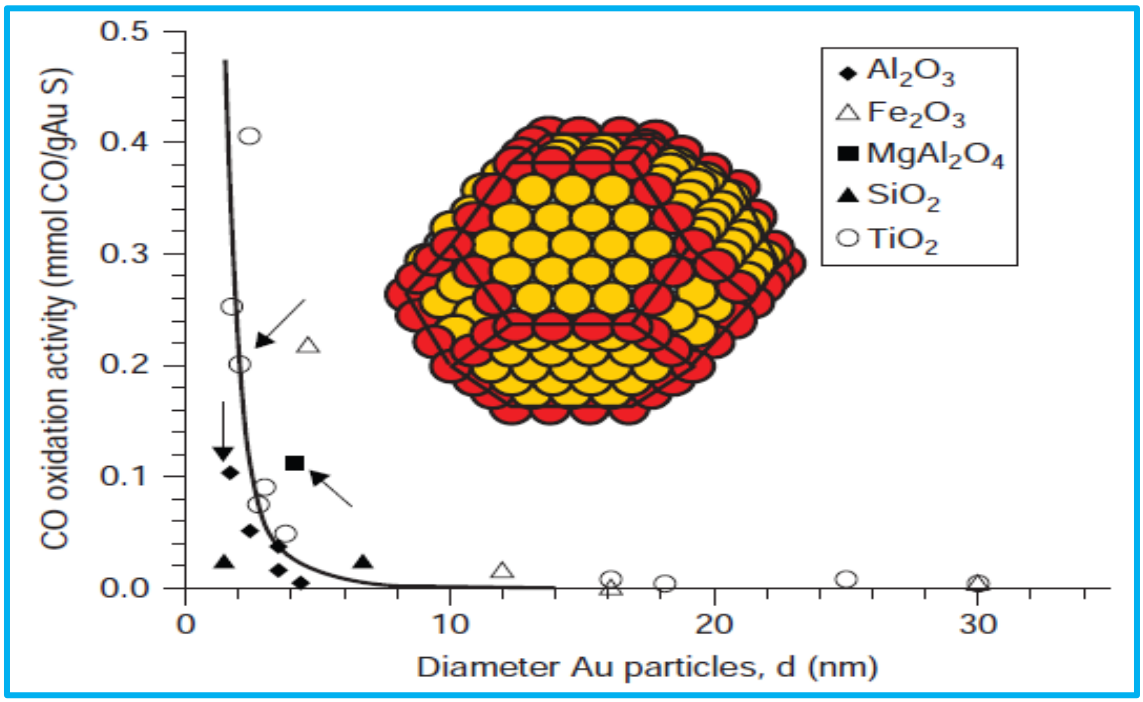

Figure 1.2: Reactivity of gold nanoparticles on various supports for carbon monoxide oxidation as a function of particle size. The black line is a fit using a 1/*d*3 law and is seen to broadly represent the variation indicating that the dominant effect of size. The low coordinated Au atoms are highlighted in red [21].

1.3 Classification of nanomaterials

Depending on the dimension in which the size effect on the resultant property becomes apparent, the nanomaterials can be classified as zero-dimensional (quantum dots) in which the movement of electrons is confined in all three dimensions, one-dimensional (quantum wires) in which the electrons can only move freely in the X-direction, two-dimensional (thin films) in which case the free electron can move in the X-Y plane, or three dimensional (nanostructured

material built of nanoparticles as building blocks) in which the free electron can move in the X, Y and Z directions.

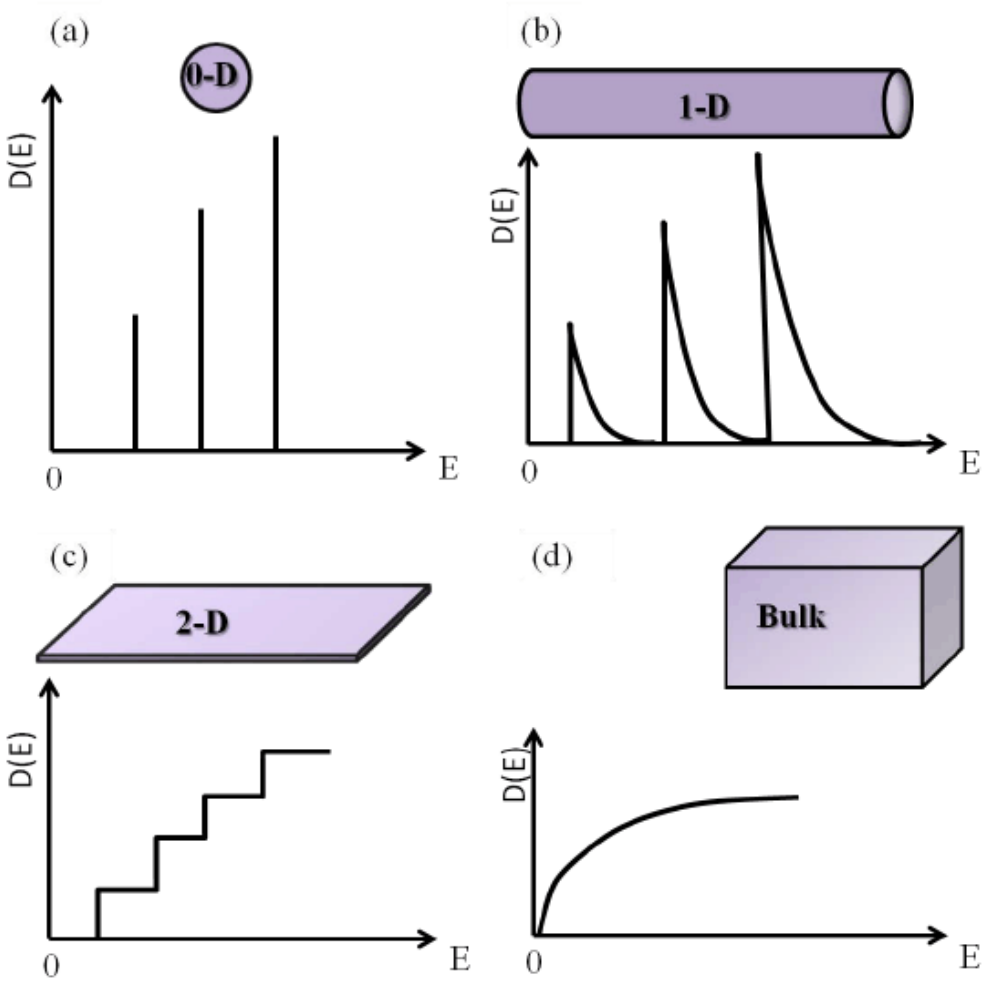

Figure 1.3: Variation of density of states with dimensionality of the nanomaterials.

Spherical nanoparticles, quantum dots, small gas phase clusters and fullerenes are the examples of zero-dimensional (0D) nanomaterials, whereas, carbon nanotubes or nanowires belong to the class of one-dimensional (1D) nanostructures. The nanofilms and graphene sheets are the examples of two-dimensional (2D) nanostructures.

There is wide variety of nanomaterials that has been identified till date and it is impossible to note all of them. However, a broad classification can be made on the basis of the structural configuration as metal based nanomaterials, carbon based nanomaterials, dendrimers and the composite nanomaterials (comprising more than one phase in it). In the present thesis, we have studied some of the basic chemical process such as proton and electron transfer under the confinement of fullerenes and nanotubes. Hence we will now discuss these two nanostructures in brief before going to the objective of the present work.

1.3.1 Fullerenes

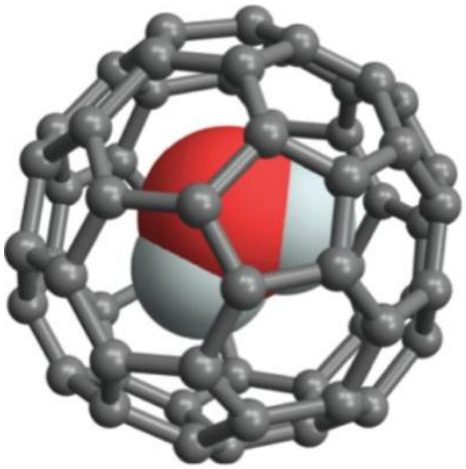

Figure 1.4: The endohedral complex of C_{60} fullerene containing water molecule**.**

Fullerenes are the third allotropic form of carbon and were discovered in 1985 after diamond and graphite [58,59]. Fullerenes comprises of hexagonal and pentagonal rings to get the closed cage structure. Each carbon atom in fullerene is sp^2 hybridized and bonded to three other carbon atoms of the ring. Among the several analogues of the fullerene family, C_{60} has been most thoroughly studied because it is produced abundantly in the carbon soot by the arc

discharge of graphite electrodes and has high symmetry (icosahedral (Ih) with all 60 carbons chemically equivalent). In addition, it is less toxic in nature and relatively inert under mild conditions (m.p. ~ 800K). The C_{60} fullerene has a closed shell electronic structure where 60 p-electrons are filled in 30 bonding molecular orbitals. The HOMO-LUMO gap is in the range of 1.5-2.0 eV. The highest occupied molecular orbital (HOMO) is fivefold degenerate and is completely filled. The lowest unoccupied molecular orbital (LUMO) is highly delocalized with threefold degeneracy. The low lying LUMO makes C_{60} a fairly good electron acceptor. On the other hand, the oxidation of C_{60} fullerene is difficult and only first three reversible oxidation states have been observed [60,61]. These properties make it an ideal host to study the structure-property relationship of the confined matter at nanoscale. In the endohedral complexes of fullerene, the hydrogen bonding and the relative stability of the confined molecule is strongly influenced by the fullerene cage. The fullerene cages also induce the formation of a genuine chemical bond in noble gas atoms [62]. In the present thesis, we have studied the chemical properties of acid-base complexes under the confinement of fullerene cages.

1.3.2 Nanotubes

Nanotubes constitute an exciting class of one-dimensional nanomaterials with remarkable physical properties and serve as nanoscale media to deliver fluids and molecular species of nanofluidic applications [1,5,8,18,27,62]. Carbon nanotubes (CNT) and several inorganic nanotubes have been synthesized and characterized over the years [63]. These include metal dichalcogenides (WS_2**,** MoS_2, $MoSe_2$), oxides (TiO_2, ZrO_2), nitrides (BN, GaN) and metallic nanotubes (Ni, Cu, Te)**,** BN, SiO2, TiO2, BCN, SiC, such as MoS_2, WS_2 and $MoSe_2$. Several possible applications for these nanotubes have been proposed but CNT has been recognized

widely as materials of importance because of its use in technological and biological applications [64-68].

A carbon nanotube can be simply described as a sheet of graphene coaxially rolled to create a cylindrical surface. Each CNT is characterized by a set of two integers (n, m) indicating the components of the chiral vector $C = na_1 + ma_2$ in terms of the 2D hexagonal Bravais lattice vectors of graphene, a_1 and a_2, as illustrated in Figure 1.5. When C involves only a_1 (corresponding to (n, 0)) the tube is called 'zigzag', and if C involves both a_1 and a_2 with n = m (corresponding to (n, n)) the tube is called 'armchair'. If (n – m) is divisible by 3, it may be metallic or else it may behave like semiconductor. In carbon nanotubes (CNTs), carbon has sp^2 hybridization as in graphite and the fourth electron is delocalized. But unlike the graphite structure, which is made up of a flat planar honeycomb, the structures of CNTs involve a high degree of curvature [69-72].

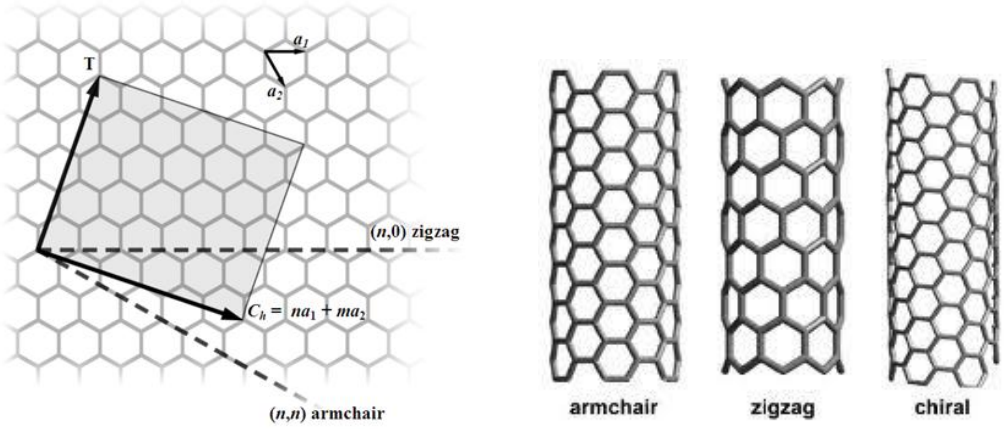

Figure 1.5: Different types of carbon nanotubes (CNTs) from the helicity vector C.

The excellent mechanical and electronic properties of carbon nanotubes are valuable for nanotechnology, electronics, optics and materials science [73]. In particular, owing to their extraordinary thermal conductivity (~ 2,000 W/m/K) and mechanical and electrical properties, carbon nanotubes find applications as additives to various structural materials. They are used water purification [74] and biomedical applications [75].

BNNTs are structural analogues of CNTs with alternative carbon atoms of CNT are substituted by boron and nitrogen atom [76, 77]. They posses wider band gap, greater thermal stability, more resistant to oxidation and enhanced hydrogen storage capability in comparison to the carbon structure counterpart. There are also reports which show the selective ion transport characteristics and superior water permeation properties of BNNTs as compared to the CNTs [78].

1.4 Effect of confinement on material properties at nanoscale

The chemistry within small pores of diameter in the nanometer scale is generally called ‘Chemistry under Nanoconefinement” and can be significantly different from the bulk chemistry [79-85]. In nanopores, the distance between atoms and molecules on the particles or in the holes is within a few nanometres, which allow them to interact with each other and with ions and molecules that approach the surface [79-80].

There are several processes in chemistry and biology which occurs in spatial confinements of nanometer regime. In this nanoconfined environment, material behavior can be severely affected primarily because of the geometric restrictions and the physical and chemical interactions with the confining material [81] Confinement also affects the reaction mechanism and change the rate of the reaction by several orders of magnitude and may lead to the

preferential formation of a particular isomer over other isomers [82]. Carbon or boron-nitrogen nanotubes, because of its unique morphology and thermal and mechanical stability, offer an excellent nanoconfinement medium to study structure-property relation at nanoscale [83] These studies have elucidated modification in structure, hydrogen bonding [84] and catalytic activity of the confined molecules [85]. Within the nanocavities of CNTs, metal or metal oxide nanoparticles exhibit different catalytic activities with respect to the same metals deposited on the CNT exterior walls. For instance, the reduction of Fe_2O_3 nanoparticles supported on the CNTs exteriors required a temperature higher than 1070 K, while those encapsulated in the CNT channels with an inner diameter of ~8 nm could be reduced at a much lower temperature (~900 K). The reduction become more facile and the temperature lowers to ~860K when the inner diameter of CNTs is reduced to ~2 nm [88]. In contrast, the oxidation of encapsulated metallic Fe nanoparticles can be retarded in comparison to that of the outside particles. For e.g., the Fischer−Tropsch reaction rate is found to be enhanced with such encapsulated Fe nanoparticles with respect to the outside Fe particles [89]. Similarly, the confinement of Rh particles in CNT leads to the increases in the catalytic activity of Rh for the conversion of CO and H_2 to ethanol [90]. These effects have recently been explained by the concept of "confinement energy" [91]. It is observed that the downshifting of d-band states of these metal particles happen inside CNT channels and consequently the adsorption of molecules such as CO, N_2, and O_2 is weakened. Thus, the confined space of CNTs provides essentially a unique microenvironment due to the electronic effects, which shifts the volcano curve of the catalytic activities toward the metals with higher binding energies. In another report, the enhanced visible-light activity of titania confined inside carbon nanotubes has been presented [92]. The primary reason for this has been attributed to the formation of Ti^{3+} or oxygen vacancies generated from the modified electronic

structure of TiO_2 via the confinement inside CNTs. In a very recent study, the encapsulated Pt clusters in CNT has shown to deliver a remarkably higher activity and stability than the clusters located on exterior wall of the CNT [93].

The primary effects which are responsible for the modification in the physical and chemical properties of a material in a confined nanospace are the quantum confinement effect and the diverse nature of interaction between the enclosed molecule and cavity [94]. However, our understanding of chemistry of these nanoconfined systems is still an elusive phenomenon and the corresponding mechanisms are still unexplored. Such a molecular-level understanding can only be illuminated with the application of both experimental and theoretical studies. In order to theoretically investigate these exciting nanoconfined systems, one can use quantum chemical methods based electronic structure calculations. With the advancement of computing techniques, density functional theory (DFT) in particular has been a very helpful technique to handle hundreds of atom in a very accurate manner.

1.5 Molecular interactions

Nanostructured assemblies are often spontaneously formed from simple molecular building blocks. Self-assembly is the process during which molecular fragments spontaneously organize themselves into nanomaterials [11,28,29]. The organization of these molecular building blocks is driven by a combination of thermodynamic factors, kinetic factors, and intermolecular interactions. Among the three, the last one plays the key role in the initiation of the self-assembly process. Therefore, we will discuss the intermolecular interactions in more details in this section.

Interactions between two or more molecules are called intermolecular interactions, while the interactions between the atoms within a molecule are called intramolecular interactions [95-

100]. The attractions between molecules are not nearly as strong as the intramolecular attractions that hold compounds together. They are, however, strong enough to control physical properties of the material such as boiling and melting points etc. Intermolecular interactions occur between all types of molecules or ions in all states of matter [95,97,99]. In general, the intramolecular interactions are of covalent origin whereas most of the forces which are involved in the intermolecular interactions are electrostatic in nature. They range from the strong, long distance electrical attractions and repulsions between ions to the relatively weak dispersion forces which have not yet been completely explained. The van der Waals interaction is the collective term used to describe attractive or repulsive forces, or non-covalent interactions, between molecules. Primarily it can be divided to six types as

- Ion-Ion Interaction
- Ion-Dipole Interaction
- Dipole-Dipole Interaction
- Dipole-Induced Dipole Interaction
- Dispersion Interaction
- Hydrogen Bonds

As these interactions are responsible for the formation of molecular aggregates at nanoscale, they are discussed in the following sections.

1.5.1 Ion-ion interactions

Ion-Ion Interactions are perhaps the most well-known intermolecular interactions and are among the strongest intermolecular interactions. Ion-ion interactions arise between two ionic (charged) species and the easiest way to understand this interaction is: like charges repel each other and opposite charges attract. These Coulombic forces operate over relatively long distances

in the gas phase. The force depends on the product of the charges (Z_1, Z_2) divided by the square of the distance of separation (d^2)

$$F = \frac{Z_1 Z_2}{4\pi\varepsilon_0 d^2} \qquad (1.1)$$

where, $\boldsymbol{\varepsilon}_0$ is the permittivity of free space (8.854×10^{-12} m^{-3} kg^{-1} s^4 A^2).

Due to this interaction, two oppositely charged particles come closer to each other and finally form an ion-pair, a new particle which has a positively charged area and a negatively charged area. There are fairly strong interactions between these ion pairs and free ions, so that these clusters tend to grow bigger in size, and eventually fall out of the gas phase as a liquid or solid.

1.5.2 Ion-dipole interactions

Polar molecules do not possess a permanent charge, but depending on the difference in the electronegativities of atoms bound in the molecule, certain regions of the molecule may have a partial positive or negative charge. In certain cases, this partial charge can lead to a permanent dipole. For example, a water molecule has a permanent dipole due to its bent geometry. When an ion comes closer to a molecule with a dipole, there is an electrostatic interaction between the dipole and the ionic species. The strength of this interaction depends on the dipole moment of the molecule, charge on the ion, distance between the ion and the center of the dipole moment and the angle of approach of the ion with the dipole axis.

1.5.3 Dipole-dipole interactions

Molecules with permanent dipoles can interact with each other through electrostatic means. The strength of this interaction is angle dependent similar to the Ion-Dipole interaction. The most attractive interaction may often be obtained when the two dipoles are anti-parallel to

each other with the positive region of one dipole adjacent to the negative region of the other. This anti-parallel orientation draws the molecules to come closer to each other and finally settle at a distance where the maximum attractive interaction energy is achieved.

In general, the charges on ions and the charge separation in polar molecules decide the strength of the interactions and therefore the order is; very strong in the case of ion-ion interactions, weaker in the case of ion-dipole interactions, and considerably weaker dipole-dipole interactions.

1.5.4 Dipole-induced dipole interaction

When an ion come closer to a non-polar molecule, the symmetric electronic cloud of the non-polar molecule feel the effect of the electric field produced by the ion. As a result, the electron cloud surrounding the non-polar molecule may become distorted. For example, when a cation approaches a non-polar molecule, the electron cloud of the non-polar molecule is pulled slightly toward the cation. The result of this distortion of the electron cloud is an effective charge separation in the non-polar molecule and is called an induced dipole. Polar molecules are also capable of inducing dipoles in non-polar molecules. The extent to which the electron cloud of a molecule becomes distorted in the presence of an ion or polar molecule is termed as polarizability. The presence of an induced dipole moment in a non-polar molecule means that there will be electrostatic interaction between the non-polar molecule and the ion or polar molecule that is inducing the dipole.

It can be noted that the interaction between an ion or a polar molecule and an induced dipole is always attractive. This is because the induced dipole created in a non-polar molecule by an ion or a polar molecule is oriented such a way that it is attracted toward the species inducing the dipole.

1.5.5 Dispersion interactions

In addition to the electrostatic forces discussed in the previous sections, there also exists a force between all molecules, regardless of charge or polarity. The origin of this force is the quantum mechanical correlation between the electrons in neighboring molecules. This force is called the dispersion or London force. Although a non-polar molecule has no permanent dipole moment, at any given moment the distribution of its electrons may be asymmetrical, resulting in an instantaneous or momentary dipole moment. This instantaneous dipole moment creates an electric field that perturbs the electrons of a neighboring molecule, producing in it an induced dipole moment and resulting in an attractive force between the two molecules. Electrical forces operate when the molecules are several molecular diameters apart, and become stronger as the molecules or ions approach each other. Dispersion forces are very weak until the molecules or ions are almost touching each other. Dispersion interaction varies as $1/r^6$ with distance and is always attractive between any two molecules. This force is the main source of attraction between two neutral, non-polar molecules and is inherently quantum mechanical in nature. Because of this interaction, boiling point of large non-polar molecules is higher than small polar molecules. Therefore, high level quantum mechanical calculation must be performed to calculate the dispersion force between two molecules.

Finite size of atoms does not allow two atoms to occupy the same point in space. According to the spherical model of atom, the repulsive force between two atoms starts rising as the distance between them become closer to the atomic radius. Ultimately, the overall interaction of two molecules is the sum of all the different types of interactions that we have discussed. The potential energy decreases as the distance between the molecules grows smaller, until the energy

reaches a minimum value. If the distance decreases beyond this, then the potential energy quickly increases due to the overlap repulsion term.

1.5.6 Hydrogen bonds

The hydrogen bond is an attractive interaction between a hydrogen atom from a molecule or a molecular fragment X–H in which X is more electronegative than H (such as N, O, or F) and an atom or a group of atoms in the same or a different molecule, in which there is evidence of bond formation [95,101,102]. The hydrogen bond is essentially electrostatic in origin and so is a subset of the dipole interactions already discussed. However, it is of particular importance and strength, and so has acquired a special classification. In such cases, the electron density surrounding the hydrogen atom is mostly drawn toward the more electronegative atom, leaving the hydrogen atom "exposed" with a strong partial positive charge through which it may form a strong dipole-dipole interaction with the electronegative element on an adjacent molecule. The reduced electron density around the hydrogen atom allows the neighboring molecule with which it is hydrogen bonded to come closer as compared to the non-hydrogen bonded ones. The magnitude of the attractive interaction energy is much greater in this case as the distance is comparatively shorter than other cases.

In addition to the molecular interactions discussed above, another effect which becomes significant in the case of large organic molecules in polar solvent such as water is hydrophobic effect. The characteristics of a large organic molecule are determined by its non-polar hydrocarbon portion in the molecule. When such molecules are placed in water, they spontaneously self-organize themselves into larger aggregates. This arrangement minimizes overall contact between the hydrocarbon part of the molecule and the water and also maximizes

the water-water intermolecular interactions. This is because the dipole-dipole interactions in water are stronger than the interactions between non-polar molecules. This leads to aggregation and results to the formation of dispersed nanoparticles within the aqueous solution.

1.6 Overview of theoretical methods

All the works presented in this thesis have been carried out by employing different quantum mechanical methods. Both wave function based methods and the density functional theory (DFT) based methods have been used. Within the framework of DFT, we have used several exchange-correlation energy functionals, such as the local density approximation (LDA), generalized gradient approximation (GGA) and Becke's three-parameter exchange functional and Lee-Yang-Parr correlation functional (B3LYP). The individual computational methods used will be discussed in respective chapters under the subsection computational details. The theoretical basis for all the methods used throughout the thesis is outlined here.

1.6.1 The Schrödinger equation

One of the major scientific breakthroughs of the 20th century is the development in the field of quantum mechanics. The Schrödinger equation,[103] introduced by the Austrian physicist Erwin Schrödinger can be considered as the heart of quantum mechanics [104-115]. Schrödinger equation is a partial differential equation, which describes the quantum state of a system and predicts how the states change with time. The time-independent Schrödinger equation for a system containing M nuclei with N electrons can be written as

$$\hat{H}\psi_i(r_1, r_2, r_3, ...r_N, R_1, R_2, R_3, ...R_M) = E_i\psi_i(r_1, r_2, r_3, ...r_N, R_1, R_2, R_3, ...R_M) \qquad (1.2)$$

where, $\hat{H}$ is the Hamiltonian operator and represents total energy of the system. ψ_i is the wave function which depends on both the electronic and nuclear coordinates and E_i is the eigenvalue of the i^{th} state of the system. The Hamiltonian operator for this system can be written it atomic units as

$$\hat{H} = -\frac{1}{2}\sum_{i=1}^{N}\nabla_i^2 - \frac{1}{2}\sum_{A=1}^{M}\frac{1}{M_A}\nabla_A^2 - \sum_{i=1}^{N}\sum_{A=1}^{M}\frac{Z_A}{r_{iA}} + \sum_{i=1}^{N}\sum_{j>i}^{N}\frac{1}{r_{ij}} + \sum_{A=1}^{M}\sum_{B>A}^{M}\frac{Z_A Z_B}{R_{AB}} \qquad (1.3)$$

Here, A and B run over the M nuclei whereas i and j run over the N electrons of the system. Z_A and M_A represent the charge and mass of the A^{th} nuclei in atomic units. The first two terms of the expression represent the kinetic energy of the electrons and nuclei respectively. The third term represents the attractive interaction between the nuclei and the electrons, whereas the last two terms represent the electron-electron and nucleus-nucleus repulsion energy respectively. Thus, the last three terms represent the potential energy part of the Hamiltonian.

Laplacian operator ∇_q^2 is defined as a sum of differential operators (in Cartesian coordinates)

$$\nabla_q^2 = \frac{\partial^2}{\partial x_q^2} + \frac{\partial^2}{\partial y_q^2} + \frac{\partial^2}{\partial z_q^2} \qquad (1.4)$$

Although the Schrödinger equation can be applied to any system, the solution becomes extremely difficult for larger systems. Therefore, certain approximations are imposed when solving the Schrödinger equation for a system containing large number of atoms and electrons. Only after these approximations are made, one can computationally solve the Schrödinger equation for many body systems. One such approximation is Born-Oppenheimer Approximation.

1.6.2 Born-Oppenheimer approximation

This approximation is based on the fact that the nuclei are much heavier as compared to the electrons. Because of the large difference in their mass, the nucleus can be considered as fixed for all purposes of electron movement. Which means the electrons can be approximated as if they are moving in the field of fixed nuclei. This approximation was proposed in 1927 by Max Born and J. Robert Oppenheimer [116]. Due to this approximation, the wave function can be spitted into the wave function of nuclear and electronic components.

$$\psi_{total}(r,R) = \psi_{electronic}(r;R) \times \psi_{nuclear}(R) \qquad (1.5)$$

Now, the electronic Hamiltonian for fixed nuclear coordinates can be written as

$$\hat{H}_{elec} = -\frac{1}{2}\sum_{i=1}^{N}\nabla_i^2 - \sum_{i=1}^{N}\sum_{A=1}^{M}\frac{Z_A}{r_{iA}} + \sum_{i=1}^{N}\sum_{j>i}^{N}\frac{1}{r_{ij}} = \hat{T}_{elec} + \hat{V}_{Ne} + \hat{V}_{ee} \qquad (1.6)$$

The three terms in the electronic Hamiltonian are kinetic energy of electron, potential energy due to electron-nucleus interaction and potential energy due to electron-electron interaction.

The electronic Schrödinger equation then solved to get the electronic energy component (E_{ele}).

$$\hat{H}_{elec}\psi_{elec} = E_{elec}\psi_{elec} \qquad (1.7)$$

However, it should be noted that the simple electronic energy E_{ele} represents only one component of the total energy of the system which is given by sum of electronic energy, nuclear repulsion energy and the nuclear kinetic energy, viz.

$$E_{tot} = E_{elec} + E_{nucl} \ . \qquad (1.8)$$

Then the total energy can be obtained by adding electronic energy with nuclear repulsion energy (a constant term) as

$$E_{tot} = E_{elec} + E_{nucl} \ . \qquad (1.9)$$

1.6.3 The Variational principle

In order to solve the Schrödinger equation for a molecule, first the Hamiltonian operator of the target system has to be set. This requires the knowledge of the total number of electrons in the system, and external potential V_{ext}. In the second step, we have to find the eigenfunction ψ_i and corresponding eigenvalue E_i of the Hamiltonian. Once the ψ_i is determined, all properties of interest can be obtained by applying the appropriate operators to the wave function. Unfortunately, no simple and straightforward method is available to solve the Schrödinger equation exactly for atomic and molecular systems.

The method which allows systematically approach the wave function of the ground state ψ_0, i.e., the state which has the lowest energy E_0 is known as the variational principle. According to the variational principle, the expectation value <*E*> of the Hamiltonian operator ($\hat{H}$) using any trial wave function (ψ_{trial}) is always greater than or equal to the true ground state energy (E_0) [104-107].

$E \geq E_0$ where,

$$<E> = \frac{\left\langle \psi_{trial} \mid \hat{H} \mid \psi_{trial} \right\rangle}{\left\langle \psi_{trial} \mid \psi_{trial} \right\rangle} \qquad (1.10)$$

The strategy for finding the ground state energy and wave function involves the minimization of the functional $E[\Psi]$ by searching through all acceptable N-electron wave functions.

1.6.4 The Hartree-Fock method

As discussed in the previous section, it is practically impossible to solve the electronic part of the Schrödinger equation of an N-electron system due electron-electron repulsion term. We need to define a suitable subset, which offers a physically reasonable approximation to the exact wave function and adopt some algebraic scheme to minimize and get the improved wavefunction.

According to Hartree, the many electron wavefunction can be represented by the product of one electron wavefunctions, known as the Hartree product.

$$\psi = \psi_1(r)\psi_2(r)\psi_3(r).....\psi_N(r) \qquad (1.11)$$

However, this product is not anti-symmetric and does not obey the Pauli Exclusion Principle. This electron exchange is incorporated by Fock and Slater by approximating the N-electron wavefunction as an anti-symmetrised product of N-one electron wave functions, the Slater determinant, given by

$$\psi_{HF}(\boldsymbol{r_1}, \boldsymbol{r_2}, ...\boldsymbol{r_N}) = \frac{1}{\sqrt{N!}} \begin{vmatrix} \phi_1(\boldsymbol{r_1}) & \phi_2(\boldsymbol{r_1}) & \cdots & \phi_N(\boldsymbol{r_1}) \\ \phi_1(\boldsymbol{r_2}) & \phi_2(\boldsymbol{r_2}) & & \phi_N(\boldsymbol{r_2}) \\ \vdots & \vdots & & \\ \phi_1(\boldsymbol{r_N}) & \phi_2(\boldsymbol{r_N}) & & \phi_N(\boldsymbol{r_N}) \end{vmatrix} \qquad (1.12)$$

Here, $1/\sqrt{N!}$ is the normalization factor and the one-electron wave functions are called spin-orbitals which are composed of both spatial orbitals and the spin functions. As it can be seen from the above equations, exchanging the coordinates of i^{th} and j^{th} particles is equivalent to interchanging i^{th} and j^{th} columns of the determinant. As the sign of the determinant changes on exchange of any two rows or columns of the matrix, exchange of any two particle coordinates changes the sign of the wavefunction making it antisymmetric.

Hartree developed the so called self-consistent field (SCF) procedure [117,118] which assumes that each electron moves in the field of the nuclei as well as the average (mean field) potential due to the other electrons. The one-electron Schrödinger equation corresponding to this average potential is then solved for each electrons of the system. Since the SCF potential depends on the wavefunction, the same has to be evaluated using the set of improved wave functions (orbitals) and the solution procedure is to be repeated using the new potential. This procedure is iteratively carried out and each time the new set of orbitals is compared to the same from the previous iteration till the values differ only insignificantly, leading to what is known as self-consistency and the computation is complete and the wavefunctions and energy values are said to be self-consistent [104, 107].

The energy evaluated by operating the Hamiltonian operator on the Slater determinant is called the Hartree-Fock energy (E_{HF}) and is given as

$$E_{HF} = \left\langle \psi_{HF} \mid \hat{H} \mid \psi_{HF} \right\rangle = \sum_{i=1}^{N} H_i + \frac{1}{2} \sum_{i,j=1}^{N} \left(J_{ij} - K_{ij} \right) \tag{1.13}$$

where,

$$H_i = \int \phi_i^*(r) \left\{ -\frac{1}{2}\nabla^2 - \sum_{A=1}^{M} \frac{Z_A}{r_{iA}} \right\} \phi_i(r) dr \tag{1.14}$$

$$J_{ij} = \iint \phi_i(\boldsymbol{r}_1) \phi_i^*(\boldsymbol{r}_1) \frac{1}{r_{12}} \phi_j^*(\boldsymbol{r}_2) \phi_j(\boldsymbol{r}_2) d\boldsymbol{r}_1 d\boldsymbol{r}_2 \tag{1.15}$$

$$K_{ij} = \iint \phi_i^*(\boldsymbol{r_1}) \phi_j(\boldsymbol{r_1}) \frac{1}{r_{12}} \phi_i(\boldsymbol{r_2}) \phi_j^*(\boldsymbol{r_2}) d\boldsymbol{r_1} d\boldsymbol{r_2} \tag{1.16}$$

J_{ij} is the coulomb integral and K_{ij} is the exchange integral. The later arises as a result of the anti-symmetric nature of the wavefunction.

Roothaan proposed a set of known basis functions to convert these differential equations to a set of algebraic equations which can be easily solved using the matrix procedure [119].

The unknown orbitals can be expressed as a linear combination of the known basis functions $\{\chi_\mu(\boldsymbol{r}) \mid \mu = 1, 2, 3, ...K\}$ as

$$\phi_i = \sum_{\mu=1}^{K} C_{\mu i}\chi_\mu \qquad (1.17)$$

The total energies calculated from the HF method are found to be associated with an error of 0.5-1.0%. Though it is not very high in terms of total energy, it is in the range of the chemical bond energies and hence it should be improved further. The improvement can be made by considering the electron correlation effect which is not properly accounted for in the HF method.

1.6.5. Electron correlation

The HF energy (E_{HF}) is always greater than the true ground state non-relativistic energy and the difference between the two is the correlation energy [104-107].

$$E_{corr} = E_0 - E_{HF} \qquad (1.18)$$

The instantaneous repulsion of electrons which is not included properly in the HF scheme is the main origin of this correlation energy. In order to take care of the electron correlation energy, several wavefunction based methods have been developed, viz. the Møller-Plesset perturbation, Configuration interaction, Coupled Cluster, etc. However, all these post Hartree-Fock methods are found to be highly expensive computationally and it may not be possible to deal with large systems of practical importance.

1.6.6. Density Functional Theory (DFT)

1.6.6.1 Electron density

Before we start the discussion about the density functional theory (DFT), let us introduce the concept of electron density at this point. The wave function Ψ introduced in the previous section may itself does not have any physical significance, but the square of the wave function is an observable quantity given as the probability function [120],

$$P = \left|\Psi\left(\vec{x}_1, \vec{x}_2, \ldots \vec{x}_N\right)\right|^2 d\vec{x}_1\, d\vec{x}_2 \ldots d\vec{x}_N\, 1 \qquad (1.19)$$

Which represents the probability that electrons 1, 2, …, N are found simultaneously in volume elements $d\vec{x}_1\, d\vec{x}_2 \ldots d\vec{x}_N$.

The normalization condition for the system of N electrons leads to the equation

$$\int\cdots\int \left|\Psi(\vec{x}_1, \vec{x}_2, \ldots, \vec{x}_N)\right|^2 d\vec{x}_1 d\vec{x}_2 \ldots d\vec{x}_N = 1 \qquad (1.20)$$

The single particle electron density $\rho(\vec{r})$ can be defined as

$$\rho(\vec{r}) = N\int\cdots\int\left|\Psi(\vec{x}_1, \vec{x}_2, \ldots, \vec{x}_N)\right|^2 ds_1 d\vec{x}_2 \ldots d\vec{x}_N \qquad (1.21)$$

$\rho(\vec{r})$ defines the probability of finding any of the N electrons within the volume element $d\vec{r}_1$ but with arbitrary spin while the other N-1 electrons have arbitrary positions and spin. Strictly speaking $\rho(\vec{r})$ is a probability density, but it is called as the electron density is common practice. We can easily write

$$\int \rho(\vec{r})\, d\vec{r} = N \qquad (1.22)$$

Unlike the wave function, the electron density depend only on three coordinates and is an observable which can be measured experimentally, e. g. by X-ray diffraction.

1.6.6.2 The Thomas-Fermi model

The main idea of DFT is to use the simple electron density $\rho(\boldsymbol{r})$ in place of the much complicated N-electron wavefunction and to extract information about the atomic or molecular systems. One of such earliest attempt was made by Thomas and Fermi in 1927 [121] The Thomas-Fermi model is a statistical model which assumes that the electrons are uniformly distributed over the six-dimensional phase space. The relation between the total kinetic energy and the electron density in this model is given as (atomic units are used)

$$T_{TF}[\rho] = C_F \int \rho^{5/3}(\boldsymbol{r}) d\boldsymbol{r}, \qquad (1.23)$$

$$C_F = \frac{3}{10}(3\pi^2)^{2/3} \qquad (1.24)$$

If this is combined with the classical expression for the nuclear-electron attractive potential and the electron-electron repulsive potential we have the famous Thomas-Fermi expression for the energy of an atom

$$E_{TF}[\rho(\boldsymbol{r})] = C_F \int \rho^{5/3}(\boldsymbol{r}) d\boldsymbol{r} - Z\int \frac{\rho(\boldsymbol{r})}{\boldsymbol{r}} d\boldsymbol{r} + \frac{1}{2}\iint \frac{\rho(\boldsymbol{r}_1)\rho(\boldsymbol{r}_2)}{|\boldsymbol{r}_1 - \boldsymbol{r}_2|} d\boldsymbol{r}_1 d\boldsymbol{r}_2 \qquad (1.25)$$

A large number of modifications have been proposed to improve the Thomas-Fermi model [122-125]. However, none of them could predict the bonding in molecules and hence not used for chemical applications. Thus we will not discuss these modifications here and straightway move to The Hohenberg-Kohn Theorem which is considered as the pillars on which all modern day density functional theories are established.

1.6.6.3 The Hohenberg-Kohn theorem

The Hohenberg-Kohn Theorem formulated in 1964 gave an important breakthrough in density functional theory [123]. The first theorem provides the proof that the electron density in fact uniquely determines all the properties of the system. The external potential $v(\boldsymbol{r})$ is a unique functional of $\rho(\vec{r})$. Since $v(\boldsymbol{r})$ fixes the Hamiltonian, the full many particle ground state is a unique functional of $\rho(\vec{r})$.

Thus, for an N-electron system, all the ground state properties can be determined from the total number of electron (N) and the external potential $v(\boldsymbol{r})$. For a non-degenerate ground state of an N-electron system, $\rho(\boldsymbol{r})$ determines the N as

$$\int \rho(\boldsymbol{r})d\boldsymbol{r} = N \tag{1.26}$$

and also determines the $v(\boldsymbol{r})$ and hence it can determine all the properties.

The total energy can be written as

$$E[\rho] = T[\rho] + V_{ne}[\rho] + V_{ee}[\rho] \tag{1.27}$$

$$= \int \rho(\boldsymbol{r})v(\boldsymbol{r})d\boldsymbol{r} + F_{HK}[\rho] \tag{1.28}$$

The Hohenberg-Kohn functional, F_{HK} contains the system independent terms (independent of N, R_A and Z_A)

$$F_{HK}[\rho] = T[\rho] + V_{ee}[\rho] \tag{1.29}$$

The second H-K theorem states that $F_{HK}[\rho]$, the functional that delivers the ground state energy of the system, delivers the lowest energy if and only if the input density is the true ground state density, ρ_0. This theorem reestablishes the variational principle and states that for a positive trial

density $\rho(\boldsymbol{r})$ satisfying the condition $\int \rho(\boldsymbol{r})d\boldsymbol{r} = N$, the energy functional $E[\rho]$ is an upper bound to the true ground state energy.

$$E[\rho] \geq E_0$$

1.6.6.4 The Kohn-Sham method

In 1965, Kohn and Sham invented an indirect way of calculating the kinetic energy thereby making the DFT method as an efficient tool for carrying out rigorous calculations.[123] The idea was "if we are not able to accurately determine the kinetic energy through an explicit functional, we should be a bit less ambitious and concentrate on computing as much as we can of the true kinetic energy exactly. We then have to deal with the remainder in an approximate manner". Hence, they suggested to use the same expression and to obtain the kinetic energy of the non-interacting reference system with the same density as the real, interacting one

$$T_s[\rho] = \left\langle \psi_{KS} \left| \sum_{i=1}^{N} \left(-\frac{1}{2}\nabla_i^2 \right) \right| \psi_{KS} \right\rangle . \tag{1.30}$$

The exact ground state wavefunction for such a non-interacting system will be the Slater determinant of the one electron wavefunctions

$$\psi_{KS}(\boldsymbol{r_1}, \boldsymbol{r_2}, ...\boldsymbol{r_N}) = \frac{1}{\sqrt{N!}} \begin{vmatrix} \phi_1(\boldsymbol{r_1}) & \phi_2(\boldsymbol{r_1}) & \dots & \phi_N(\boldsymbol{r_1}) \\ \phi_1(\boldsymbol{r_2}) & \phi_2(\boldsymbol{r_2}) & & \phi_N(\boldsymbol{r_2}) \\ \vdots & \vdots & & \\ \phi_1(\boldsymbol{r_N}) & \phi_2(\boldsymbol{r_N}) & & \phi_N(\boldsymbol{r_N}) \end{vmatrix} \tag{1.31}$$

The non-interacting kinetic energy is not equal to the true kinetic energy of the interacting system, even if the systems share the same density. Kohn and Sham accounted for that by

introducing the the unknown Exchange-Correlation functional $E_{XC}[\rho]$. The overall energy functional can be written as

$$E[\rho] = \int \rho(\mathbf{r})v(\mathbf{r})d\mathbf{r} + T_s[\rho] + J[\rho] + E_{XC}[\rho] \quad (1.32)$$

where

$$E_{XC}[\rho] = T[\rho] - T_s[\rho] + V_{ee}[\rho] - J[\rho] \quad (1.33)$$

The residual part of the true kinetic energy, T_C, which is not covered by T_S, is simply added to the non-classical electrostatic contributions. In other words, the exchange-correlation energy E_{XC} is the functional which contains everything that is unknown, a kind of junkyard where everything is stowed away which we do not know how to handle exactly. Let us also underline that in spite of its name, E_{XC} contains not only the non-classical effects of self-interaction correction, exchange and correlation, which are contributions to the potential energy of the system, but also a portion belonging to the kinetic energy. The exchange correlation energy does not have any exact form and hence has to be approximated. In fact the main challenging aspect of DFT is to find a good approximation to the exchange-correlation energy functional $E_{XC}[\rho]$. There are various approximations to calculate $E_{XC}[\rho]$, such as Local Density Approximation (LDA), Local Spin density Approximation (LSDA), Generalised Gradient Approximation (GGA) and many other hybrid functionals like B3LYP, HSE, M06 etc. We will discuss LDA and GGA briefly here.

1.6.6.5 Local density approximation (LDA)

Local Density Approximation is the simplest approximation to the $E_{XC}[\rho]$ using the uniform electron gas formula, viz. [122]

$$E_{xc}^{LDA}[\rho] = \int \rho(\boldsymbol{r})\varepsilon_{xc}(\rho)d\boldsymbol{r} \qquad (1.34)$$

where, $\varepsilon_{xc}(\rho)$ is the exchange-correlation energy per electron in a homogeneous electron gas with density ρ . The functional $\varepsilon_{xc}(\rho)$ can be separated into exchange and correlation contributions as $\varepsilon_{xc}(\rho) = \varepsilon_x(\rho) + \varepsilon_c(\rho)$, so that the exchange part can be obtained from the Dirac exchange-energy functional as

$$\varepsilon_x(\rho) = -\frac{3}{4}\left(\frac{3}{\pi}\rho(\boldsymbol{r})\right)^{1/3}. \qquad (1.35)$$

The correlation part $\varepsilon_c(\rho)$ is unknown and for homogeneous electron gas it has been simulated through the quantum Monte Carlo approach.

1.6.6.6 Generalized gradient approximation (GGA)

Though the LDA approximation is successful for many systems where the electron density varies slowly, it fails for highly inhomogeneous systems.[120, 123-125] One way to improve the LDA method is by considering that the exchange-correlation energy depends not only on the density $\rho(\boldsymbol{r})$ but also on its gradient $\nabla\rho(\mathbf{r})$ and the typical GGA functional can be written as

$$E_{xc}^{GGA}[\rho] = \int \rho(\mathbf{r})\varepsilon_{xc}(\rho, \nabla\rho)d\mathbf{r} \qquad (1.36)$$

A large number of GGA functionals have been developed to handle the $E_{XC}[\rho]$ more exactly and some of the widely used GGA functionals are Perdew, Burke and Enzerhof (PBE), Perdew and Wang (PW91), Becke (B88) etc. In addition to these pure DFT functionals, large numbers

of hybrid DFT functionals are developed by incorporating the exact HF exchange into the $E_{XC}[\rho]$ like B3LYP, PBE0, Heyd-Scuseria-Ernzerhof (HSE) etc. As a next step to the GGA methods and hybrid methods, the meta-GGA functionals are developed in recent years where in addition to density and gradient the Laplacian (second derivative of electron density) is also incorporated, as is done in TPSS and the Minnesota Functionals.

In what follows, some of the common exchange energy, functional, and potential terms used in DFT are described, [123d]. Herein, ρα and ρβ are the α, β spin densities. The gradients of the density enter through

$$\sigma = \nabla\rho.\nabla\rho, \quad \hat{\sigma} = \nabla\rho.\nabla\hat{\rho}, \quad \hat{\hat{\sigma}} = \nabla\hat{\rho}.\nabla\hat{\rho}, \; \upsilon = \nabla^2\rho, \; \hat{\upsilon} = \nabla^2\hat{\rho}$$

The Vosko-Wilk-Nusair Correlation Energy Functional

$$E_C^{\mathrm{VWN}}[\rho_\alpha, \rho_\beta] = \int \mathrm{d}r\rho\varepsilon_C^{\mathrm{VWN}}(\rho_\alpha, \rho_\beta)$$

$$\varepsilon_C^{\mathrm{VWN}}(\rho_\alpha, \rho_\beta) = \varepsilon_i(\rho_\alpha, \rho_\beta) + \Delta\varepsilon_c(r_s, \zeta)$$

$$\varepsilon_i(\rho_\alpha, \rho_\beta) = A_i\left[\ln\frac{x^2}{X(x)} + \frac{2b}{Q}\tan^{-1}\left(\frac{Q}{2x+b}\right) - \frac{bx_0}{X(x_0)}\left(\ln\frac{(x-x_0)^2}{X(x)} + \frac{2(b+2x_0)}{Q}\tan^{-1}\left(\frac{Q}{2x+b}\right)\right)\right]$$

$$x = r_s^{1/2}; \; Q = \left(4c_i - b_i^2\right)^{1/2}; \; X(x) = x^2 + b_i x + c_i : (i = I, II);$$

$$\Delta\varepsilon_c(r_s, \zeta) = \varepsilon_{III}(\rho_\alpha, \rho_\beta)\left[\frac{f(\zeta)}{f''(0)}\right]\left[1 + \beta_i(r_s)\zeta^4\right]$$

$$\beta_i(r_s) = \left[\frac{f''(0)}{\varepsilon_{III}(\rho_\alpha, \rho_\beta)}\right]\Delta\varepsilon(r_s, 1) - 1$$

$$\Delta\varepsilon(r_s, 1) = \varepsilon_I(\rho_\alpha, \rho_\beta) - \varepsilon_{II}(\rho_\alpha, \rho_\beta)$$

Constants for the Vosko-Wilk-Nusair parametrization

Parameter	I	II	III
A_i	0.0621841	0.0310907	-0.033774
b_i	3.72744	7.06042	1.131071
c_i	12.9352	18.0578	13.0045
x_{0i}	-0.10498	-0.32500	-0.0047584

The Becke Exchange Energy Functional and the Potential

$$E_X^{\mathrm{BEC}} = \left[\rho_\alpha, \rho_\beta\right] = E_X^{\mathrm{LSD}}\left[\rho_\alpha, \rho_\beta\right] - \sum_\sigma^{\alpha,\beta} \int \mathrm{d}r \rho_\sigma \varepsilon_x^{NL}$$

$$= E_X^{\mathrm{LSD}}\left[\rho_\alpha, \rho_\beta\right] - \sum_\sigma \int \mathrm{d}r \rho_\sigma^{4/3} \frac{bX_\sigma^2}{1 + 6bX_\sigma \sinh^{-1} X_\sigma};$$

$$X_\sigma = \frac{\left|\nabla \rho_\sigma\right|}{\rho_\sigma^{4/3}}; b = 0.0042;$$

$$\upsilon_{X\sigma}^{BEC} = \upsilon_{X\sigma}^{LSD} + \frac{\partial\left(\varepsilon_X^{NL}\rho\right)}{\partial\rho_\sigma} - \sum_i \frac{\partial}{\partial x_i} \frac{\partial\left(\varepsilon_X^{NL}\rho\right)}{\partial\rho_\sigma, x_i};$$

$$\upsilon_{X\sigma}^{NL} = -bF\rho_\sigma^{-4/3} \frac{4}{3} \rho_\sigma^{5/3} X_\sigma^2 - \nabla^2 \rho_\sigma \left(1 + F\left(1 - \frac{6bX_\sigma^2}{\sqrt{1 + X_\sigma^2}}\right)\right)$$

$$+ 6bF\nabla\rho_\sigma.\nabla X_\sigma \left\{\left(1 + 2F\right)\sinh^{-1} X_\sigma\right)\}$$

$$+ \frac{X_\sigma}{\sqrt{1 + X_\sigma^2}} \left[\frac{1}{1 + X_\sigma^2} + 2F\left[2 - \frac{6bX_\sigma^2}{\sqrt{1 + X_\sigma^2}}\right]\right]$$

$$F = \frac{1}{1 + 6bX_\sigma \sinh^{-1} X_\sigma}$$

The Lee, Yang, and Parr Correlation Energy Functional and the Potential

$$E_C^{\mathrm{LYP}}\left[\rho_\alpha,\rho_\beta\right]=-a\int dr\,\frac{\gamma(r)}{1+d\rho^{-1/3}}\Big\{\rho+2b\rho^{-5/3}\Big[2^{2/3}C_F\rho_\beta^{8/3}$$

$$-pt_w+\frac{1}{9}\left(\rho_a t_w^a+\rho_\beta t_w^\beta\right)+\frac{1}{18}\left(\rho_\alpha\nabla^2\rho_\alpha\right)\Big]\exp\left(-c\rho^{-1/3}\right)\Big\}$$

$$\gamma(r)=2\left(1-\frac{\rho_\alpha^2(r)+\rho_\beta^2(r)}{\rho^2(r)}\right)$$

$$t_w(r)=\frac{1}{8}\frac{\left|\nabla\rho(r)\right|^2}{\rho(r)}-\frac{1}{8}\nabla^2\rho$$

$$CF=\frac{3}{10}\left(3\pi^2\right)^{2/3};\ a=0.04918;\ b=0.132;\ c=0.2533;\ d=0.349$$

$$\upsilon_{c\sigma}^{\mathrm{LYP}}=-a\left(F_2'\rho+F_2\right)-2^{5/3}abC_F\left[G_2'\left(\rho_\alpha^{8/3}+\rho_\beta^{8/3}\right)+\frac{8}{3}G_2\rho_\beta^{8/3}\right]$$

$$-\frac{ab}{4}\left[\rho\nabla^2G_2+4\nabla G_2\nabla\rho+4G_2\nabla^2\rho+G_2'\left(\rho\nabla^2\rho-\left|\nabla\rho\right|^2\right)\right]$$

$$-\frac{ab}{36}\left[3\rho_\alpha\nabla^2G_2+4\nabla\rho_\alpha\nabla G_2+4G_2\nabla^2\rho_\alpha+3G_2'\left(\rho_\alpha\nabla^2\rho_\alpha+\rho_\beta\nabla^2\rho_\beta\right)\right]$$

$$+G_2'\left(\left|\nabla\rho_\alpha\right|^2+\left|\nabla\rho_\beta\right|^2\right)$$

$$F_2=\frac{\gamma(r)}{1+d\rho^{-1/3}};\ G_2=F_2(\rho)\rho^{-5/3}\exp\left(-c\rho^{-1/3}\right)$$

$$F_2'=\frac{\partial F_2}{\partial\rho_\sigma};\ G_2'=\frac{\partial G_2}{\partial\rho_\sigma}$$

The Perdew 86 Correlation Energy Functional and the Potential

$$E_C^{\mathrm{P86}}\left[\rho_\alpha,\rho_\beta\right]=E_C^{\mathrm{LSD}}\left[\rho_\alpha,\rho_\beta\right]-\int \mathrm{d}r d^{-1}\exp\left(-\Phi\right)\mathrm{C}\left(\rho\right)\frac{\left|\nabla\rho\right|^2}{\rho^{4/3}}$$

$$\Phi=1.745\,f\left[\frac{C\left(\infty\right)}{C\left(\rho\right)}\right]\frac{\left|\nabla\rho\right|}{\rho^{7/6}}$$

$$C\left(\rho\right)=0.001667+\frac{0.002568+\alpha r_s+\beta r_s^2}{1+rs+\delta r_s^2+10^4\,\beta r_s^3}$$

$$d=2^{1/3}\left[\left(\frac{1+g}{2}\right)^{5/3}+\left(\frac{1-g}{2}\right)^{5/3}\right]^{1/2}$$

$$\alpha=0.023266;\ \beta=7.389\times10^{-6};\ \gamma=8.723;\ \delta=0.472;\ \widetilde{f=0}.11$$

$$\upsilon_{c\alpha}^{\mathrm{P86}}=\upsilon_{c\sigma}^{LSD}-d^{-1}\exp\left(-\Phi\right)C\left(\rho\right)\rho^{-1/3}$$
$$\times\left[\frac{\left(2-\Phi\right)\nabla^2\rho}{\rho}-\left(\frac{4}{3}-\frac{11\Phi}{3}+\frac{7\Phi^2}{6}\right)\frac{\left|\nabla\rho\right|^2}{\rho^2}+\frac{\Phi\left(\Phi-3\right)\nabla\rho\cdot\nabla\left|\nabla\rho\right|}{\rho\nabla\rho}\right.$$
$$\left.-\frac{5\rho^{1/3}n^{2/3}-\sigma}{6d^2\rho^4}\left[2^{2/3}\left(1-\Phi\right)\rho-\sigma\left|\nabla\rho\right|^2-2^{2/3}\left(2-\Phi\right)\rho\nabla\rho-\sigma\nabla\rho\right]\right]$$
$$+\ d-1\exp\left(-\Phi\right)\frac{\left|\nabla\rho\right|^2}{\rho^{4/3}}\left(\Phi^2-\Phi-1\right)\frac{\mathrm{d}C}{\mathrm{d}\rho}$$

1.7 Scope of the Thesis

The physical and chemical properties of the material in nanoscale length differ significantly from those of the atomic and the bulk materials. The primary reasons for these modifications are attributed to the surface induced effects (large surface to volume ratio) and the quantum size effects. On the other hand, physical and chemical properties of a material can also be significantly modified from the bulk primarily in a confined nanospace. In this particular case, the diverse nature of interaction between the enclosed molecule and the confinement medium also play a crucial role in addition to the quantum confinement effect. The significant effects on the chemistry of these confined systems associated with nanoscale confinement have potential importance in a wide range of applications, e.g., catalysis, lubrication and separation science. However, our understanding of chemistry of these nanoconfined systems is still an elusive phenomenon and the corresponding mechanisms are also being uncovered.

In the present thesis, the chemical properties of nanomaterials have been investigated in isolated condition and under the confinement of various nanostructured media. In addition, we have also investigated the catalytic properties of nanomaterials for a few important chemical reactions. The main objective is to investigate the modification in the chemical properties of system by changing the surrounding medium. We have primarily studied the change in structure, solvation, energetics, vibrational frequencies, chemical reactivity and catalytic activity using density functional based methods. All the works contributed towards the thesis are discussed from chapter 2 to chapter 7. The last chapter (chapter 8) presents an overview of the possible future directions contingent upon the results of the present thesis. In the following section, a brief summary of different chapters is discussed.

In chapter-2, the effect of confinement on the structure and properties of water clusters are presented. Water has been recognized as the matrix of life and plays a crucial role in many biological and chemical systems. In many of these systems, water is found to be confined in pores of diameter in the nanometer scale, for example, hydrophobic cavities of proteins. We have investigated the structure, bonding and vibrational spectra of water clusters in carbon nanotubes (CNT) of diameter in the range of sub-nanometer. The effect of confinement has been systematically investigated by varying the diameter of the nanotube. From the stabilization energy values calculated by the dispersion corrected DFT method, it is confirmed that water can occupy the interior of narrow nanotube such as CNT(4,4). In CNT(4,4) and CNT(5,5) 1-dimensional water chains parallel to the CNT axis is formed whereas in CNT(6,6), zigzag structure is observed with radial O-O distance shorter than that of parallel to the CNT axis. More symmetric structures similar to gas phase structures are detected in larger diameter CNTs and the cluster gets stabilized close to the CNT wall. It has been observed that in highly confined medium like CNT(4,4), there is a reduction in the O-H bond length of water. An inverse relation between the electronic charge transfer (from CNT to water) and the CNT diameter is also established. It is found that the intra-molecular charge separation for each water molecule increases under confinement as compared its gas phase counterpart. Under highly confined system, blue shift in the stretching frequency of O-H (non-hydrogen bonded) occurs due to the reduction in O-H bond length. In the case of CNT(6,6), a red shifting in stretching frequency of the hydrogen bond assisted O-H is observed due to the reduction in O—O separation distance and hence strengthening of the hydrogen bond. The important findings from this study is the degree of confinement (diameter and curvature of carbon nanotube) is extremely important in deciding the properties of confined water molecules.

In chapter-3, the spherical confinement effect due to the fullerene cages on the nature of acid-base complexes is presented. This chapter is divided in to two parts. In the first part, we have considered the NH_3-HCl pair as a prototype system and studied the effect of confinement and polarizability of fullerene cages on the behaviour of this acid-base pair by systematically varying the fullerene diameter (C_{36} to C_{180}) using density functional methods. In our important findings, it has been demonstrated that the diameter of fullerene is one of the crucial factor in deciding the chemical properties of the acid-base pair. In isolated case (gas phase) of the NH_3-HCl pair, the proton is associated with the acid and quite far away from the nitrogen of ammonia. In larger diameter fullerene such as C_{180}, only a slight increase (~ 5%) in chloride-proton distance (R_{Cl-H}) is observed and the acid is still in the undissociated form. As the diameter of fullerene decreases, the acid starts dissociating and a gradual reduction in the nitrogen-proton distance is observed. In C_{60} and other smaller diameter fullerenes, the proton is completely transferred from the acid to ammonia, and a symmetrical ammonium ion is formed.

In the second part, we have considered the Lewis acid-base complex (LABC) i.e., the ammonia-borane as well as its fluorine derivatives and tried to elucidate the effect of spherical confinement due to the fullerene buckyballs on the structure, bonding and energetics of LABC in a systematic way. In particular, we have considered two fullerene rings C_{60} and C_{80} as the nanoconfined medium and investigated their role on the charge transfer and binding energy of the LABC complex by gradually substituting the hydrogen atoms with fluorine. We have observed that the confinement effect along with the interaction of fullerene with the LABC, significantly modify the structure, interaction energy, chemical reactivity and charge transfer in LABC under the spherical cage of fullerene.

Chapter-4 deals with the solvation of multiply charged anions in finite system under the confined medium of bulk solvent system. In a nanoconfined environment, the solvation of molecules and ions differ significantly from the bulk solvation due to the presence of restricted number solvent molecules. Therefore, the solvation energy values of an ion likely to differ in these two environments (N & ∞). In the present study, a microscopic theory-based bottom-up approach has been implemented to derive an analytical expression for the solvation energy for a finite (N) system, including the bulk. This bottom-up approach provides the information on solvation energies of anionic solutes in finite-size clusters, including the bulk ($N = \infty$), from the knowledge of the detachment energies for the system containing a few numbers of solvent molecules. However, in case of dielectric constant, a microscopic theory-based top-down approach has been prescribed to derive an analytical expression for the static dielectric constant for the finite system. In this approach, the knowledge of the dielectric constant for the bulk provides a scheme to obtain the same quantity for a wide numbers of solvent molecules. As an illustrative example, the theory has tested for sulphate and oxalate ion and found to be in very good agreement (within 5%) with the available experimental result.

Chapter-5 deals with the study of proton transfer (PT) energetics in water and ammonia under confinement. In many important physical, chemical and biological processes, PT occurs in a nanoconfined environment. Carbon and Boron nitride nanotubes have been used as model nanoconfinement media to study the proton transfer reactions and get detailed insights into this complex phenomenon. Experimentally it has been shown that the PT rate is enhanced in multiple orders under nanoconfinement. In order to understand the molecular origin of the enhancement in proton transfer, we have investigated the proton transfer energetics in CNT and BNNT using

the protonated water dimer (Zundel cation) as a model system and employing dispersion corrected DFT method. The main objective of the study is to elucidate the effect of water-nanotube interaction and the diameter of nanotube (different degrees of confinement) on the structure and proton transfer energetics of Zundel cation (ZC). Our results reveal that the interaction of ZC with the nanotube is observed to be largely depends on the diameter of the nanotube. The interaction energy of ZC with CNT is observed to be significantly higher (~40%) than that of BNNT. In larger diameter nanotubes, ZC is stabilized near the inner surface of the nanotube because of the formation of hydrogen bond between the ZC and the nanotube. It has also been shown that the effect of marginal change in degree of confinement on the energy barrier (12-45%) for the PT process is very remarkable. We have analyzed several important factors such as interaction energy, charge transfer and POF as a function of the degree of confinement. Among all the nanotubes considered in the present study, it has been concluded that the proton transfer may be facilitated in nanotubes with diameter in the range of 7 to 9 Å.

Chapter-6 deals with the effect of hydrogen doping in gold clusters for CO oxidation process. It is well known that CO can act like a poisoning agent specifically for the metal catalysts such as Pt and Pd. In the present study, we have systematically doped hydrogen atoms on gold clusters (Au_n, n=1 to 6) and investigated the structure and stability of each hydrogen doped clusters towards CO oxidation process. For each gold cluster, we have considered various possible conformations and did the sequential hydrogen doping to the maximum extent possible. The important properties such as IP, EA and HOMO-LUMO gap have been thoroughly analysed for each of these clusters. In case of hydrogen doped clusters, it is observed that hydrogen atom withdraws electrons from the gold cluster and hence the gold atoms acquire high positive charge. Then the CO interaction has been studied with the pristine and hydrogen doped gold clusters.

Interestingly, a substantial increase in the CO interaction energy (more than 20% in some cases) is observed when many hydrogen atoms are doped with the gold clusters. One of the reasons for this remarkable enhancement in interaction energy is attributed to the charging of the gold cluster. We have also investigated the activation barrier for the CO oxidation leading to CO_2 process using some of the selected gold clusters for which the observed IE values are significantly higher than the pristine cluster. We also demonstrated that the CO oxidation can occur with these hydrogen doped gold clusters with a significantly lower barrier (100 %) in comparison to their pristine counterparts.

Chapter-7 deals with the generation of hydrogen from water through a catalytic process. In particular we have made an attempt to investigate the effect of boron nitride nanotube on the catalytic activity of different metal atoms especially, titanium and vanadium for water dissociation reaction leading to the generation of hydrogen molecules. From our calculations, we have demonstrated that the dissociation of water to H and OH fragments is extremely facile with barrier height of 0.12 and 0.27 eV for Ti and V adsorbed structure respectively. We further studied the adsorption and dissociation of another water molecule on the final state (product) of the first water splitting reaction. It is observed that the second water molecule also interact strongly (binding energy > 1eV) with the product and the water dissociation proceed with very low energy barrier with the production of H_2 molecule. The barrier height for the water dissociation reaction estimated in the present study is lower than that of pure metal cluster and other supported nanostructured materials. Stabilization of the transition state structure by hydrogen bond involving O-H⋯N is the possible reason for the low barrier of this process. It is lucidly demonstrated through our study that the Ti-decorated BNNT system can be a potentially promising nanostructure for dissociation of water and generation of hydrogen.

Chapter 2

Effect of nanoconfinement on the structure and properties of water clusters

2.1 Water in nanoconfinement

Water has been recognized as the matrix of life. It plays an invaluable role in governing the structure, stability, and function of biomolecules such as proteins and enzymes [126-130]. It has been established that the long-range transfer of ions and metabolites along the biosurfaces is possible only because of the presence of the spanning network of water. Water molecules are also found in rocks, zeolites and many other inorganic materials. In many of these systems, water molecules are present in the small pores of dimension in nanoscale. The influence of these confined water molecules on the thermodynamics of the equilibrium process occurring in these systems is very significant.

Water molecules in the bulk phase are bonded to each other through hydrogen bonds. Each water molecule accepts two hydrogen bonds and donates two hydrogen bonds to other water molecules. Thus, each molecule is tetrahedrally coordinated to four other water molecules and water is considered as a highly structured liquid. The hydrogen bond network of water is extended in space in three dimensions. Therefore, the properties of water confined in nanometer-scale pores are expected to differ significantly from the bulk as the hydrogen-bond network is truncated in these confining geometries. The loss of hydrogen-bond energy should render the transfer of a single water molecule into a nonpolar environment energetically unfavorable [131]. However, experimental evidence for water penetrating into weakly polar cavities in the protein interior has been obtained in recent years [127-131].

The exact behavior of water in these confined nanocavities remain as a challenge to scientific community because of the difficulties in performing experiment in nanoscale and the limitation of computational facility to treat such large systems accurately. Thus, in the last decade, large numbers of studies have been performed on water in various kinds of model

nanopores to develop the understanding of water behavior in the real systems. Among these model studies, water in carbon nanotubes (CNTs) [132] has been thoroughly investigated primarily because of two reasons. The hydrophobic interior of CNT resembles with the biomolecules [133] and the tremendous potential of CNT for technological applications. The applications involving CNT-water system include hydroelectric power converters [134, 135], desalination of seawater [136] and drug delivery [137]. The excellent thermal stability (stable up to 700^0 C in air), mechanical robustness (with tensile strength higher than that of steel) and unique electronic properties of CNT make it an excellent model system to study the structure property relationship of molecules under nanoconfinement, the water molecules in particular. Nevertheless many groups also investigated the behavior of water inside parallel graphene sheets [138-141], in boron nitride nanotubes [142, 143], zeolites [144], and many other porous structures.

The initial molecular dynamics (MD) report of Hummer and co-workers [145] indicated that water molecules can occupy the hydrophobic interior of CNT(6,6) which opened the door for the upsurge research in this particular topic. Their prediction of water occupying CNT has been confirmed through neutron diffraction [146], NMR [147], X-ray diffraction [148, 149] and IR spectroscopic [150] studies.

A large number of experimental and theoretical studies have been performed on water in CNTs. The important findings from these studies have been discussed in a recent review article [151]. Water molecules undergo molecular ordering to form stacked-ring structure with a linear chain at the center of the nanotube [150]**.**There is a reduction in the number of hydrogen bonds for each water molecule inside the nanotube [152]. But the weak interaction between water and CNT, and the tight hydrogen-bonding network leads to a pulse-like transport of water molecules

in these CNTs [145, 153-158] which exceeds expectations from macroscopic hydrodynamics by several orders of magnitude. This high fluid velocity results from an almost frictionless interface at the carbon-nanotube wall [159]. In addition, phase transition [160, 161] viscosity modification [162] and wetting-drying transition [145] have also been observed in these studies.

In spite of such large number of studies on water under carbon nanotubes, the molecular level understanding is still lacking. Since most of studies performed earlier are based on molecular dynamic simulation, *ab initio* study of water in CNT can bring more details of this particular system. A recent DFT based study of water clusters in CNT(6,6) by Wang et al. [163] predicted weak coupling between the molecular orbitals of the encapsulated water molecules and the delocalized π electrons of carbon nanotube. Therefore, water in CNT cannot be considered as a case of simple geometrical confinement. In another very recent study, it has been shown that water-nanotube interaction influence water flow through CNT [164]. Although a recent study by Rojas and co-workers [165] has shed some light in this direction, there is no first principle study dealing with water molecules in various nanotubes. As *ab initio* investigations can bring out molecular details of the system, an organized first principle study in this regard can give more insight to this particular problem. In this chapter, we have presented the results obtained from the systematic study performed on water in CNT by DFT method. The main objective of the present study is to find out how the properties of water molecules vary as the degree of confinement changes. In particular, we have studied the structure, bonding and vibrational spectra of water clusters in carbon nanotubes (CNT) of diameter in the range of sub-nanometer. The effect of confinement on the properties of water cluster has been systematically investigated by varying the diameter of the CNT.

2.2 Computational details

The equilibrium structure of the water clusters {$(H2O)_n$, n=1 to 4} are initially obtained in gas phase. Then these optimized water clusters are placed inside the CNTs and the complexes comprising of water clusters and CNTs have been optimized to get the minimum energy structure of the CNT-Water complexes. The structure of the CNT framework is in general observed to be least affected during the course of optimization. The terminal atoms of the CNTs are saturated with dangling hydrogen atoms to minimize the end effects. At the same time, the electronegativity of hydrogen atom is comparable with that of carbon and it does not affect the electron delocalization inside the carbon ring. To investigate the effect of confinement on the properties of water molecules, several CNTs have been considered and the degree of confinement has been systematically varied. It can be mentioned that the smaller is the nanotube diameter, the higher is the degree of confinement and vice versa. We have considered the armchair CNTs from CNT(4,4) to CNT(8,8) with the corresponding diameter of 5.7 to 11.2 Å.

All the calculations have been performed by employing density functional theory with B3LYP exchange-correlation hybrid functional as implemented in TURBOMOLE program [166]. The reliability of DFT calculations in describing the water clusters and other hydrogen-bonded systems has been already tested with respect to other schemes such as MP2 and CCSD, in earlier studies [167]. The correlation-consistent triple-zeta basis set augmented with diffuse basis functions (augCC-pvTZ) is used for water molecules, whereas for the nanotube framework, simple contracted Gaussian basis sets (SVP or split valence with polarization) are used. Since in these types of systems, dispersion interaction plays an important role, dispersion correction has been incorporated in all the calculations [168]. The infra-red vibrational modes of the confined water molecules have been calculated by freezing the coordinates of the CNT framework and

following the NumForce module of the TURBOMOLE program. A scaling factor of 0.97 has been used for the vibrational frequencies as recommended by Merrick and co-workers [169]. To get the electronic population on individual atoms, natural bond orbital (NBO) population analysis procedure has been adopted here.

2.3 Structure and properties of gas phase water clusters

Before going to the effect of confinement, let us have a small discussion on the structure and properties of water cluster in gas phase. As a representative case, herein we have considered water clusters consisting one to four water molecules $\{(H2O)_n$, n=1 to 4$\}$. The optimized structures of these water clusters are presented in Figure 2.1. It can be seen from this figure that water molecules (n < 5) form 2-dimensional cluster. The geometrical parameters of these optimized water clusters are presented in Table 2.1. The geometrical parameters and the interaction energy (IE) of the water cluster obtained in the present study using B3LYP/augCC-pvTZ method are quite close to the results available from experiment and other theoretical methods such as MP2 and CCSD [170]. For example, the interaction energy value in the case of water trimer in the present study is (-16.56 kcal/mol) in good agreement with MP2/ aug-cc-pVTZ value of -16.29 kcal/mol. Similarly, the O-H bond length of water monomer obtained in the present study is 0.962 Å and the available results from MP2 method [171] is 0.959 Å. Thus the B3LYP functional in combination with a good basis set can describe the water cluster with reasonable accuracy and validates the choice of our method for the current study. As the number of water molecules increases in a cluster, the number if hydrogen bond increases and therefore the increase in interaction energy value is quite sharp with the increase in water molecules in the cluster.

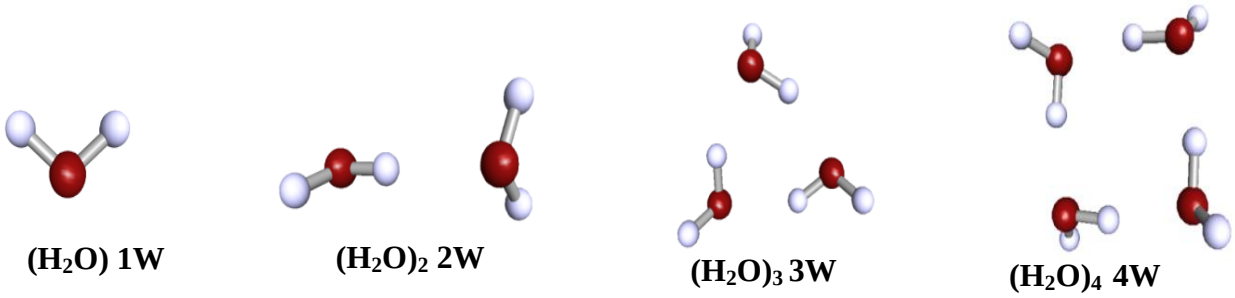

Figure 2.1: Structure of water clusters {$(H2O)_n$, n=1 to 4}predicted from DFT/B3LYP method

Table 2.1: Geometrical parameters and interaction energy of water clusters {$(H2O)_n$, n=1 to 4}in gas phase.

System	$R_{(O-H)}$ (Å)		$\Theta_{(H-O-H)}$	Hydrogen Bond Parameters			IE
				$\Theta_{(O\cdot H\cdot O)}$	$\delta_{(O\cdot\cdot O)}$	$\delta_{(H\cdot\cdot O)}$	kcal/mol
1W	0.962	0.962	105.09	--	--	--	--
2W	0.961 0.963	0.961 0.963	105.38 105.50	171.42	2.912	1.949	-5.26
3W	0.961 0.961 0.961	0.976 0.976 0.976	106.13 106.43 106.30	151.60 149.18 151.54	2.795 2.802 2.796	1.897 1.920 1.899	-16.56
4W	0.961 0.961 0.961 0.961	0.984 0.984 0.984 0.984	106.16 106.24 106.17 106.18	167.62 167.69 167.64 167.66	2.735 2.735 2.735 2.736	1.766 1.766 1.766 1.766	-29.45

Let us discuss the vibrational frequency of the water clusters in the present case. It is important to mention here that in bulk water each water molecule is tetrahedrally coordinated, simultaneously donating and accepting two hydrogen atoms. The hydrogen bonded network is extended throughout the bulk water. However, the arrangement of water clusters of finite size is disrupted and different types of OH groups are observed (bulk-like, free OH groups etc.). Whether a particular OH group is involved in the hydrogen bonding or not, can be easily identified by means of vibrational spectroscopy. In general, there are four major types of OH stretching modes present in water cluster. These modes originate from the OH groups that belong to the following water species: free OH groups dangling from the surface (3690-3720 cm^{-1}), double H-atom donor-single O-atom acceptor (3450-3550 cm^{-1}), water molecules in a distorted tetragonal coordination (3400-3450 cm^{-1}), and single donor-double acceptor (3050-3200 cm^{-1}) [172-175]. The values given parentheses correspond to the spectral region in which these modes are observed. Thus, the position of the OH stretching mode highly depends on the involvement of the OH group in the hydrogen-bond network. As mentioned earlier, the calculated vibrational frequencies are scaled by a factor of 0.97 according to the report of Merrick and co-workers [169] and the scaled frequency values are presented in Table 2.2. It can be seen from this table that as the number of water molecules in the cluster increases the stretching frequency of water molecule decreases. This is because of the strong hydrogen bonds in the larger clusters. This is also supported by the reduction in H—O distance from 1.95 Å to 1.77 Å on going from $(H_2O)_2$ to $(H_2O)_4$. The vibrational frequencies obtained in the present study are reasonably close to the results from other high level correlated calculations [176]. In these water clusters, one OH is involved in the hydrogen bond formation whereas the other just dangles away from the cluster.

Accordingly, the stretching mode which is dominated by the dangling OH bond appears at a higher frequency as compared to the other stretching modes.

Table 2.2: Vibrational modes of water clusters {$(H2O)_n$, n=1 to 4} in gas phase.

Vibrational Frequency (cm^{-1})	1W	2W	3W	4W
Bending	1587	1576 1595	1586 1587 1611	1591 1602 1604 1632
Symmetric Stretching	3696	3560 3675	3415 3478 3492	3219 3321 3322 3358
Asymmetric Stretching	3756	3727 3775	3737 3746 3755	3728 3744 3745 3749

2.4 Structure and properties of water molecules under the confinement of CNTs

In this section, the interaction of water molecule with single walled carbon nanotubes, the modification in structure of water molecules due to confinement and the charge transfer from CNT to water molecule are discussed. The optimized structures of water molecules in CNTs (CNT-Water complex) are presented in Figure 2.2.

It can be seen from Figure 2.2 that the water molecules form a linear chain parallel to the nanotube axis in CNT(4,4) and CNT(5,5) irrespective of the number of water molecules present in the cluster. This is obviously due to the steric hindrance offered by these two CNTs because of their small diameter. On the contrary, in CNT(7,7) and CNT(8,8), cyclic water clusters are

formed in the case of three and four water molecules. The geometrical parameters of water clusters in these two wider nanotubes are very much similar to that of gas phase clusters.

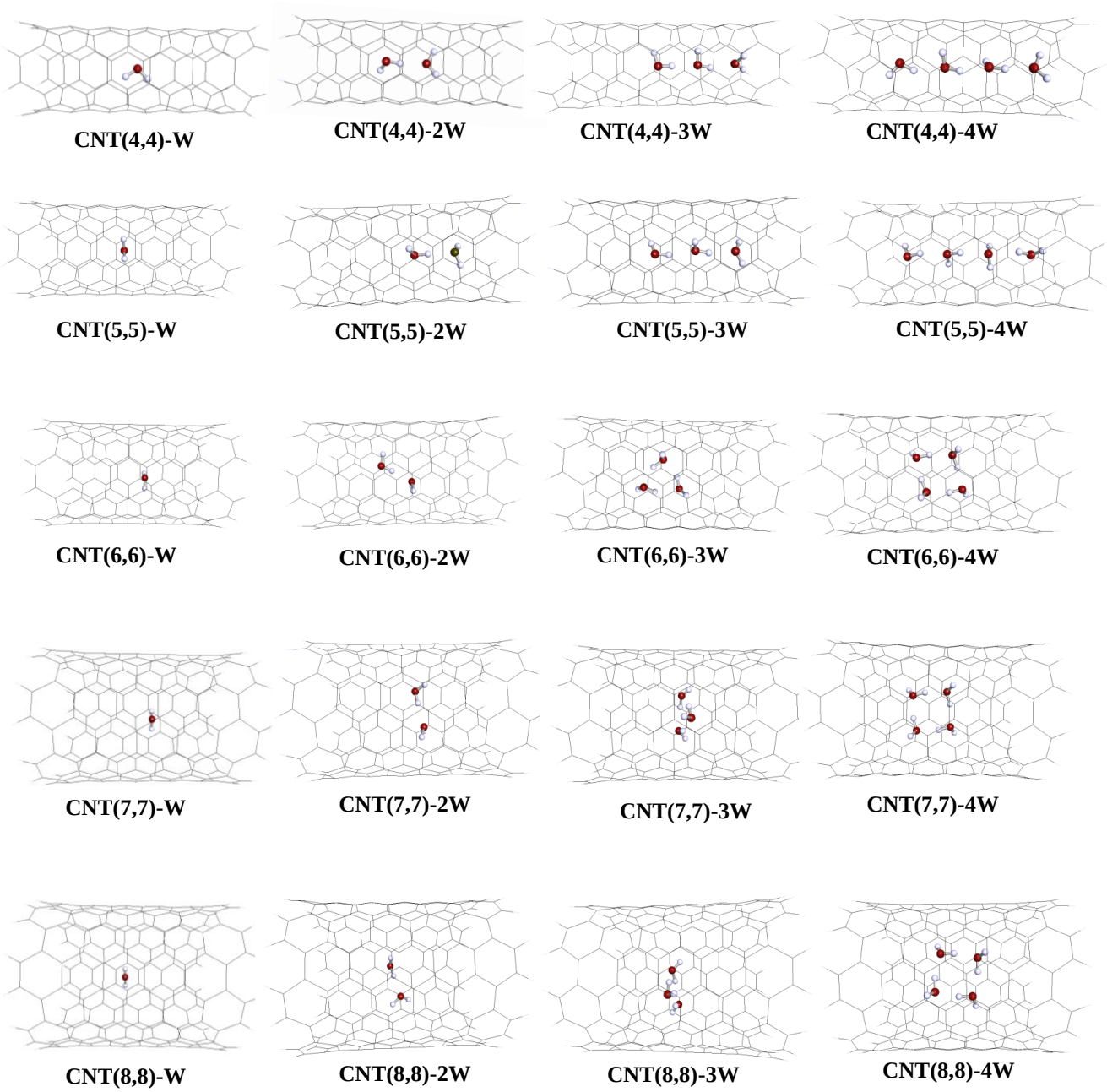

Figure 2.2: Optimized structures of CNT-Water complex.

However, in case of CNT(6,6), zigzag type of arrangement is observed. That means, the structures formed in this particular nanotube is neither perfectly linear nor perfectly circular in nature. For example, in CNT(6,6)-4W, the oxygen atom of one water molecule is not exactly on the top of the other water molecule, but shifts slightly away in the axial direction. This introduces asymmetry in the structure of water cluster and two different O-O distances are observed. The radial O-O distance is slightly shorter in comparison to the axial O-O distance. The exact values of axial and radial O-O distance in the case of three water molecules in CNT(6,6) are 2.87 and 2.68 Å respectively. From the preceding discussion it can be said that the structure of water cluster in CNT largely depends on the diameter of the CNT.

We have also analyzed the distance of nearest neighbor carbon atom from each atom of the water cluster. Interestingly, we observed that the hydrogen atoms are relatively closer to the carbon atom of CNT in comparison to the oxygen atom. This can be attributed to the hydrogen bonding between the H atom of water cluster and the π-cloud of CNT [163, 177, 178]. Due to this particular mode of interaction, water clusters get optimized close to the CNT surface and not at the centre of the nanotube. To get a clear picture of it the radial view of the optimized geometries of CNT(8,8)-4W is presented in Figure 2.3.

Table 2.3: Geometrical parameters of water clusters under the confinement of CNTs.

System	$R_{(O-H)}$ (Å)		$\Theta_{(H-O-H)}$	$\Theta_{(O\cdot H\cdot O)}$	$\delta_{(O\cdot\cdot O)}$	$\delta_{(H\cdot\cdot O)}$
CNT(4,4)-1W	0.956	0.957	105.39	--	--	--
CNT(4,4)-2W	0.951 0.955	0.969 0.955	106.03 105.49	171.03	2.795	1.834
CNT(4,4)-3W	0.951 0.952 0.957	0.965 0.968 0.957	105.99 103.44 104.95	174.96 158.64	2.828 2.787	1.865 1.863
CNT(4,4)-4W	0.954 0.953 0.954 0.957	0.962 0.966 0.969 0.957	106.58 103.69 103.71 105.23	149.35 156.86 166.20	2.853 2.784 2.780	1.983 1.834
CNT(5,5)-1W	0.962	0.962	104.65	--	--	--
CNT(5,5)-2W	0.961 0.964	0.972 0.964	104.84 105.35	176.39	2.869	1.898
CNT(5,5)-3W	0.961 0.962 0.963	0.970 0.973 0.964	104.79 103.80 105.51	160.64 164.08	2.825 2.816	1.892 1.867
CNT(5,5)-4W	0.961 0.962 0.962 0.964	0.969 0.969 0.974 0.964	105.11 103.91 104.77 105.33	158.48 146.97 171.20	2.807 2.766 2.819	1.883 1.902 1.853
CNT(6,6)-1W	0.963	0.963	104.44	--	--	--
CNT(6,6)-2W	0.961 0.964	0.971 0.964	105.13 104.68	175.96	2.884	1.914
CNT(6,6)-3W	0.961 0.961 0.961	0.978 0.974 0.979	105.74 106.00 106.48	153.25 148.38 152.30	2.679 2.868 2.679	1.769 1.999 1.773
CNT(6,6)-4W	0.961 0.961 0.960 0.961	0.987 0.987 0.986 0.987	104.76 106.59 104.67 106.41	167.52 166.17 167.34 166.40	2.586 2.699 2.587 2.701	1.613 1.731 1.615 1.732
CNT(7,7)-1W	0.963	0.963	104.24	--	--	--
CNT(7,7)-2W	0.961 0.963	0.971 0.963	105.35 104.99	172.06	2.886	1.922
CNT(7,7)-3W	0.961 0.961 0.961	0.976 0.976 0.976	106.41 106.39 106.10	149.77 150.64 151.55	2.786 2.793 2.787	1.899 1.901 1.890
CNT(7,7)-4W	0.961 0.962 0.961 0.962	0.984 0.983 0.984 0.983	106.97 105.86 106.80 105.98	166.67 168.00 166.80 167.72	2.742 2.749 2.738 2.746	1.775 1.780 1.771 1.778
CNT(8,8)-1W	0.963	0.963	104.20	--	--	--
CNT(8,8)-2W	0.961 0.964	0.972 0.963	105.49 104.19	174.18	2.869	1.900
CNT(8,8)-3W	0.961 0.962 0.962	0.976 0.975 0.974	106.59 106.33 106.66	151.79 149.59 147.94	2.796 2.803 2.823	1.900 1.918 1.950
CNT(8,8)-4W	0.961 0.962 0.961 0.961	0.985 0.982 0.985 0.982	106.39 106.10 106.42 106.26	168.66 165.73 168.28 165.70	2.730 2.741 2.727 2.743	1.757 1.779 1.755 1.780

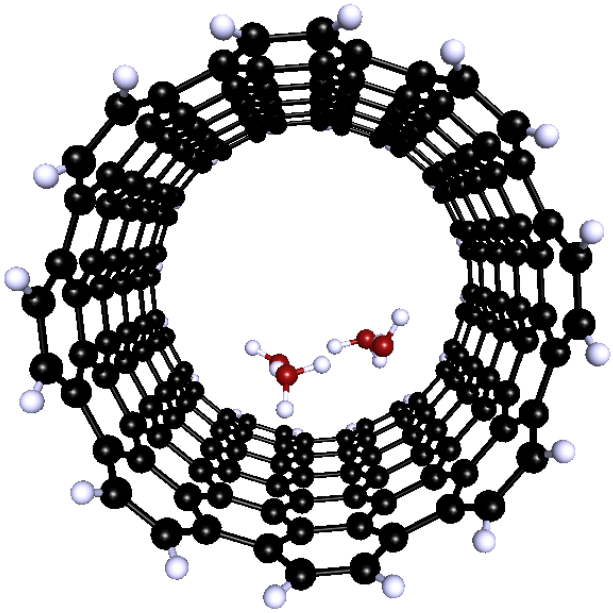

Figure 2.3: Radial view of the optimized geometry of CNT(8,8)-4W complex.

Let us now discuss the interaction of the water molecules with CNT. The interaction energy of water and CNT has been calculated using relation 2.1.

$$IE = E_{(CNT-W)} - [E_{(CNT)} + E_{(W)}] \qquad (2.1)$$

where, $E_{(CNT-W)}$, $E_{(CNT)}$, and $E_{(W)}$ are the energy values of CNT-water complex, bare CNT and the water cluster respectively.

We observed negative interaction energy for single and double water clusters for all the CNTs. For 3W and 4W, negative interaction energy values are obtained in case of all the CNTs, except CNT(4,4). This indicates CNT(4,4) cannot accommodate more than two water molecules. The plot of interaction energy as a function of confinement length (diameter of CNT) is given in figure 2.4. It is interesting note from this figure that the interaction energy does not monotonically increase with CNT diameter but for an intermediate diameter CNT. This clearly

indicates that in addition to the CNT diameter, the effective interaction of the water cluster with CNT also plays an important role in the stabilization of water clusters inside CNT.

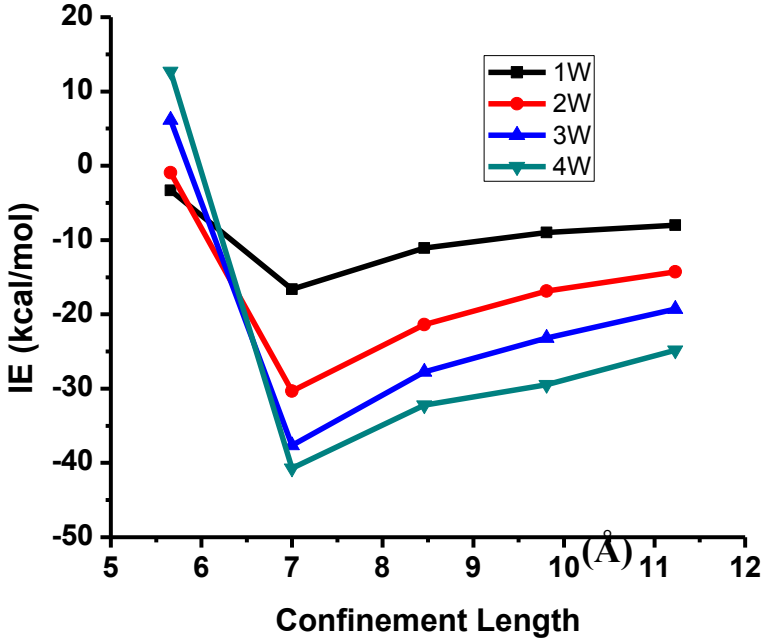

Figure 2.4: Interaction energy of water molecules and CNT as function of CNT diameter.

Let us now discuss the electronic properties of the water clusters under the confinement of CNTs. The population analysis has been done following the NBO method. In general, it is observed that the intra-molecular charge separation for each water molecule increases under the confinement of CNT as compared to the water molecule in gas phase. For example, the charge on oxygen and hydrogen atom of a water molecule increases from its gas value of -0.93, 0.46 to -1.55 and 0.67 a.u. inside CNT(4,4). This indicates there is a substantial amount of charge transfer occurs between CNT and the water cluster. When the charge on oxygen and hydrogen atom of water molecule is added, it is observed that electrons are transferred from CNT to the water cluster. A plot of the electronic charge transfer as a function of confinement length (diameter of CNT) is presented in Figure 2.5.

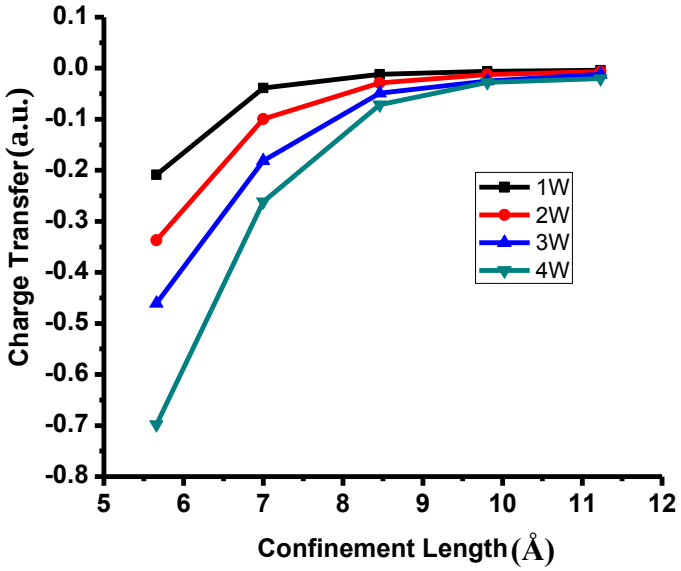

Figure 2.5: Electronic charge transfer as a function of confinement length (diameter of CNT)

It can be seen from the above figure that the charge transfer in the case of CNT(4,4) is substantially higher compared to all other CNTs. As the diameter of CNT increases, the amount of charge transfer from CNT to the water cluster gradually decreases. This electronic exchange is also expected to contribute significantly to the net interaction energy.

Let us now discuss the vibrational frequency of the water molecules under the confinement of CNTs. As mentioned earlier, vibrational spectroscopy is a great tool to identify the water structures in in a confined environment [179]. For example, Byl et al. [150] observed two different stretching modes corresponding to inter and intra ring water molecules in CNT(10,10). In the present study, the system is quite large and comprises of more than 200 atoms in some cases. Therefore, the vibrational frequencies of the water clusters have been calculated by following the NumForce module of the Turbomole program. After the geometry optimization is done, the CNT coordinates are fixed while computing the vibrational modes in the NumForce module. These results are presented in Table 2.4. In highly confined situation like

CNT(4,4), a significant blue shifting in the stretching frequency mode is observed. For instance, the two stretching frequency values for a single water molecule in CNT(4,4) are 3734 and 3823 cm^{-1} which is significantly higher in comparison to their corresponding gas phase value of 3696 and 3756 cm^{-1}. The primary reason for this blue shifting is the reduction on the O-H bond length in CNT(4,4). As the diameter of the CNT increases the amount of blue shifting sharply reduces and in CNT(5,5) and other higher CNTs, the stretching frequency values are quite close to the gas phase values. Since there is a transition from linear to cyclic cluster with the increase in tube diameter, the hydrogen bonded stretching modes are drastically affected due to confinement. Therefore, the stretching frequency values corresponding to these hydrogen bonded modes are significantly blue shifted in CNT(4,4) and CNT(5,5) where linear chain of water is formed (irrespective of the number of water molecules in the cluster).

Table 2.4: Vibrational modes of water molecules under the confinement of CNTs. The first row inside each column represents the bending modes whereas the second row corresponds to the stretching modes. All the frequency values are in cm^{-1}.

Conf. Medium	**1W**	**2W**	**3W**	**4W**
CNT(4,4)	1576 3734, 3823	1542, 1592 3546, 3734, 3780, 3833	1572, 1588, 1645 3552, 3611, 3711, 3770, 3811, 3848	1563, 1572, 1614, 1640 3525, 3594, 3649, 3713, 3767, 3770, 3789, 3817
CNT(5,5)	1574 3676, 3760	1573, 1623 3520, 3655, 3735, 3743	1568, 1600, 1620 3496, 3556, 3657, 3710, 3737, 3744	1569, 1595, 1605, 1633 3475, 3551, 3582, 3652, 3717, 3728, 3729, 3748
CNT(6,6)	1574 3666, 3750	1577, 1601 3536, 3657, 3733, 3748	1582, 1599, 1612 3348, 3419, 3495, 3716, 3728, 3737	1590, 1595, 1623, 1645 3116, 3222, 3261, 3310, 3723, 3726, 3728, 3732
CNT(7,7)	1578 3667, 3752	1577, 1602 3548, 3665, 3743, 3745	1582, 1586, 1605 3414, 3477, 3477, 3725, 3729, 3734	1584, 1595, 1602, 1626 3241, 3317, 3338, 3371, 3724, 3725, 3732, 3734
CNT(8,8)	1582 3669, 3753	1586, 1607 3517, 3668, 3745, 3751	1576, 1583, 1605 3435, 3490, 3510, 3732, 3735, 3749	1583, 1597, 1605, 1632 3231, 3296, 3352, 3374, 3723, 3727, 3743, 3743

More importantly, H---O and O---O distances increase from their original gas phase value due to the linear chain formation (see Table 2.2 and 2.3). This causes the reduction in hydrogen bond strength between water molecules and blue shifting in hydrogen bonded stretching modes. In wider nanotubes, CNT(7,7) and CNT(8,8) no significant change in the stretching modes of water molecule is observed. But we observed very interesting results for the case of CNT(6,6). The stretching modes in this particular case are significantly red shifted in comparison to the gas phase cluster. A thorough analysis of the modes reveals that the red shifted modes are associated with those hydrogen bonds where the oxygen atom of the donor is relatively closer to the oxygen atom of the acceptor water molecule. While discussing the structural parameters of water clusters in nanotube, we have highlighted that the oxygen atoms which are not present in the axial direction come closer to each other in CNT(6,6). As a result, the H---O and O---O distance become shorter in comparison to the axial O--O distance. Therefore, it can be concluded from these results that the hydrogen bond strength between water molecules is strongest in CNT(6,6). Our result also indirectly support the burst transmission of water molecules in CNT(6,6) reported in the earlier studies [145]. Strong hydrogen bonding between water molecules is recognized as the main reason for this particular phenomenon.

2.5 Summary of the work

From the stabilization energy values calculated by the dispersion corrected DFT method, it is confirmed that water can occupy the interior of narrow nanotube such as CNT(4,4). As the number water molecule increases, the interaction energy attains a positive value for CNT(4,4). In CNT(4,4) and CNT(5,5), 1-dimensional water chains parallel to the CNT axis is formed whereas in CNT(6,6), zigzag structure is observed with radial O-O distance shorter than that of axial O-O distance parallel to the CNT axis. Relatively more symmetric structures similar to the gas phase structures are predicted in larger diameter CNTs. It is also observed that the water cluster gets stabilized close to the CNT wall due to H-π interaction between the water molecule and the pi-cloud of CNT. In a highly confined medium like CNT(4,4), a significant reduction in the O-H bond length of water molecule compared to the gas phase geometry is observed. An inverse relation between the electronic charge transfer (from CNT to water) and the CNT diameter is also established. It is found that the intra-molecular charge separation for each water molecule increases under confinement as compared its gas phase counterpart. Irrespective of the number of water molecules, the highest tube-water interaction energy is achieved for CNT(5,5) with the diameter value of ~ 7Å. Under highly confined system, blue shift in the stretching modes of water molecule occurs due to the reduction in O-H bond length. In the case of CNT(6,6), a red shifting in stretching frequency of the hydrogen bond assisted O-H is observed due to the reduction in O-O separation distance and hence strengthening of the hydrogen bond. Our results also supports some of the earlier findings such as burst transmission in CNT(6,6). The important findings from this study can be summarized as the degree of confinement (diameter and curvature of CNT) is the key in deciding the properties of confined water molecules.

Chapter 3

Effect of nanoconfinement on acid-base complexes

3.1 Introduction

The chemical properties of an acid or base can be significantly modified by the surrounding medium in a confined nanospace due to the geometric constraints and the interaction of the enclosed molecule with the cavity [180-187]. For example, the hardness of the system increases and the system get less polarizable in a spherical cavity with the decrease in confinement volume[185]. Energy spectra [181] and electronic shells in atoms [188, 189] are also modified in a spatially confined environment. Owing to the unique cage structure and large polarizability, fullerenes are considered as one of the ideal hosts to study the structure-property relationship of the confined matter at nanoscale [190-193]. Recent studies on the endohedral complexes of fullerene show the modification in hydrogen bonding [194,195] and enhanced stability [196,197] of the confined molecule in the fullerene cage. Theoretical studies have also predicted NMR chemical shift [198], and more pronounced stability for the polar molecules over nonpolar ones in fullerenes [180, 199]. More interestingly, the fullerene cage also induces the formation of a genuine chemical bond in noble gas atoms [182, 200, 201]. There is another report which describes the catalytic role of C_{60} cage in facilitating the proton transfer in the complex $H_3N\cdots HCl$ to form the ion pair $NH4^+Cl^-$ [202].

From the above discussion, one would expect the chemical behaviour of acid-base complexes in nanoconfined environment to be different from its gas phase. However, to the best of our knowledge, a systematic report on this topic is not available in the literature. Therefore, in the present study, the main objective is to investigate the chemical behavior of acid-base complexes under the nanoconfinement of fullerene cage to rationalize the role played by the fullerene cage in a more generalized way. In particular, we have considered the “ammonia-hydrochloric acid” and “ammonia-borane” pairs as two representative cases and tried to elucidate

the effect of fullerene bucky ball on the structure and energetics of these complexes in a systematic way. We have considered several fullerene rings as the nanoconfinement medium. In our important findings, it has been demonstrated that the diameter of fullerene is one of the crucial factor in deciding the chemical properties of the acid-base pair.

This chapter is divided in to two parts. In the first part, we have considered the NH_3-HCl pair as a prototype system and studied the effect of confinement and polarizability of fullerene cages on the behaviour of this acid-base pair by systematically varying the fullerene diameter (C_{36} to C_{180}) using density functional methods. In the second part, we have considered the Lewis acid-base complex (LABC) i.e., the ammonia-borane as well as its fluorine derivatives and tried to elucidate the effect of spherical confinement due to the fullerene bucky balls on the structure, bonding and energetics of LABC in a systematic way.

3.2 Computational details

Initially, fully optimized geometries of acid-base (AB) complexes are obtained in gas phase (isolated case). Thereafter, the complexes comprising of AB and fullerene have been optimized to get the minimum energy structure of the endohedral complexes ($AB@C_n$). All the calculations have been performed by employing density functional theory methods as implemented in the TURBOMOLE program [166]. We have used two types of exchange-correlation functional namely, TPSSH (meta-GGA) and B3LYP (hybrid) in our calculations. The triple-zeta basis set (def2-TZVP) is used for acid-base complexes, whereas for the fullerene framework, simple contracted basis sets (SVP or split valence with polarization) are used to reduce the computational time. Dispersion correction has been incorporated in all the calculations [168]. The reliability of TPSSH method in describing the acid-base system has

already been tested in earlier studies [203]. The amount of charge transfer take place from the base to the acid in the complex has been estimated through natural bond orbital (NBO) analysis.

3.3 Results and discussion

3.3.1 Structure and energetics of NH_3-HCl in fullerenes

The optimized structure of NH_3-HCl complex in gas phase is presented in Figure 3.1(a). The H-Cl bond distance is 1.36 Å and the hydrogen atom is at 1.65 Å from the nitrogen atom of ammonia. Thus it can be inferred that NH_3 and HCl do not react to form the ion pair $NH4^+Cl^-$ in gas phase.

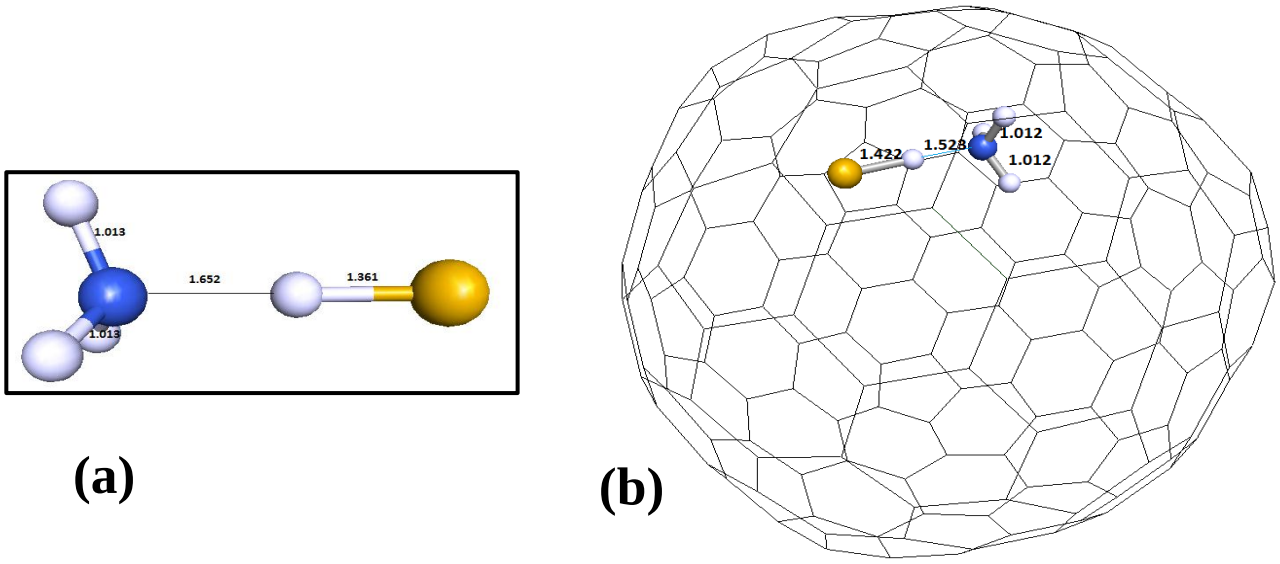

Figure 3.1: Structure of NH_3-HCl complex (a) in gas phase and (b) under the confinement of C_{180}.

In Figure 3.1 (b), the geometry of the NH_3-HCl complex in fullerene C_{180} is shown. It is observed that in C_{180}, the Cl-H distance is 1.42 Å and hence, the acid can be considered as undissociated. All the structural parameters of the complex are presented in Table 3.1.

Table 3.1: Geometrical parameters of NH_3-HCl complex in gas phase (isolated case) and in fullerenens. Bond distance values are in Angstrom and bond angles are in degree.

Conf. Medium	$\mathbf{R_{(Cl\text{-}H1)}}$	$\mathbf{R_{(Cl\text{-}H2)}}$	$\mathbf{R_{(Cl\text{-}H3)}}$	$\mathbf{R_{(Cl\text{-}H4)}}$	$\mathbf{R_{(Cl\text{-}N)}}$	$\mathbf{R_{(N\text{-}H1)}}$	$\mathbf{R_{(N\text{-}H2)}}$	$\mathbf{R_{(N\text{-}H3)}}$	$\mathbf{R_{(N\text{-}H4)}}$	$\mathbf{\Theta_{(Cl\text{-}H\text{-}N)}}$
Isolated	**1.361**	3.484	3.485	3.485	3.013	**1.652**	1.013	1.013	1.013	**179.9**
$\mathbf{C_{180}}$	**1.422**	3.410	3.423	3.455	2.944	**1.523**	1.012	1.012	1.014	**177.2**
$\mathbf{C_{96}}$	**1.737**	3.231	3.434	3.440	2.882	**1.153**	1.019	1.020	1.020	**171.2**
$\mathbf{C_{80}}$	**1.575**	3.155	3.162	3.157	2.692	**1.117**	1.012	1.012	1.011	**179.6**
$\mathbf{C_{70}}$	**1.672**	2.761	2.768	3.436	2.584	**1.088**	1.011	1.011	1.002	**138.0**
$\mathbf{C_{60}}$	**2.075**	2.083	2.072	3.239	2.260	**1.009**	1.009	1.010	0.979	**87.2**
$\mathbf{C_{50}}$	**2.071**	2.071	2.020	3.128	2.124	**1.008**	1.008	1.007	1.004	**81.7**
$\mathbf{C_{36}}$	**2.157**	2.157	2.159	3.213	2.223	**0.988**	0.988	0.988	0.989	**80.7**

Let us now discuss the effect of smaller diameter fullerenes on the nature of bonding in NH_3-HCl complex. From Table 3.1, it can be observed that there is a drastic change in the structural parameters of NH_3-HCl complex as the diameter of the fullerene is reduced. For instance, the distance between the proton and nitrogen atom of ammonia is observed to be decreasing as the diameter of fullerene decreases. More importantly, it is interesting to note that the proton-nitrogen distance in C_{60} and other smaller fullerenes, become equal to the other three N-H distance of ammonia. This indicates that the HCl molecule becomes fully dissociated in these smaller fullerenes and a symmetrical ammonium ion is formed. The optimized structures of all the "NH_3-HCl—fullerene" complexes are presented in Figure 3.2. We however, did not observe a linear decrease in the Cl-H distance with the diameter of fullerenes. This may be due to the non-spherical structure of these fullerenes which enforces the structure to deviate from linearity, particularly in the case of C_{96} and C_{70} (Figure 3.2).

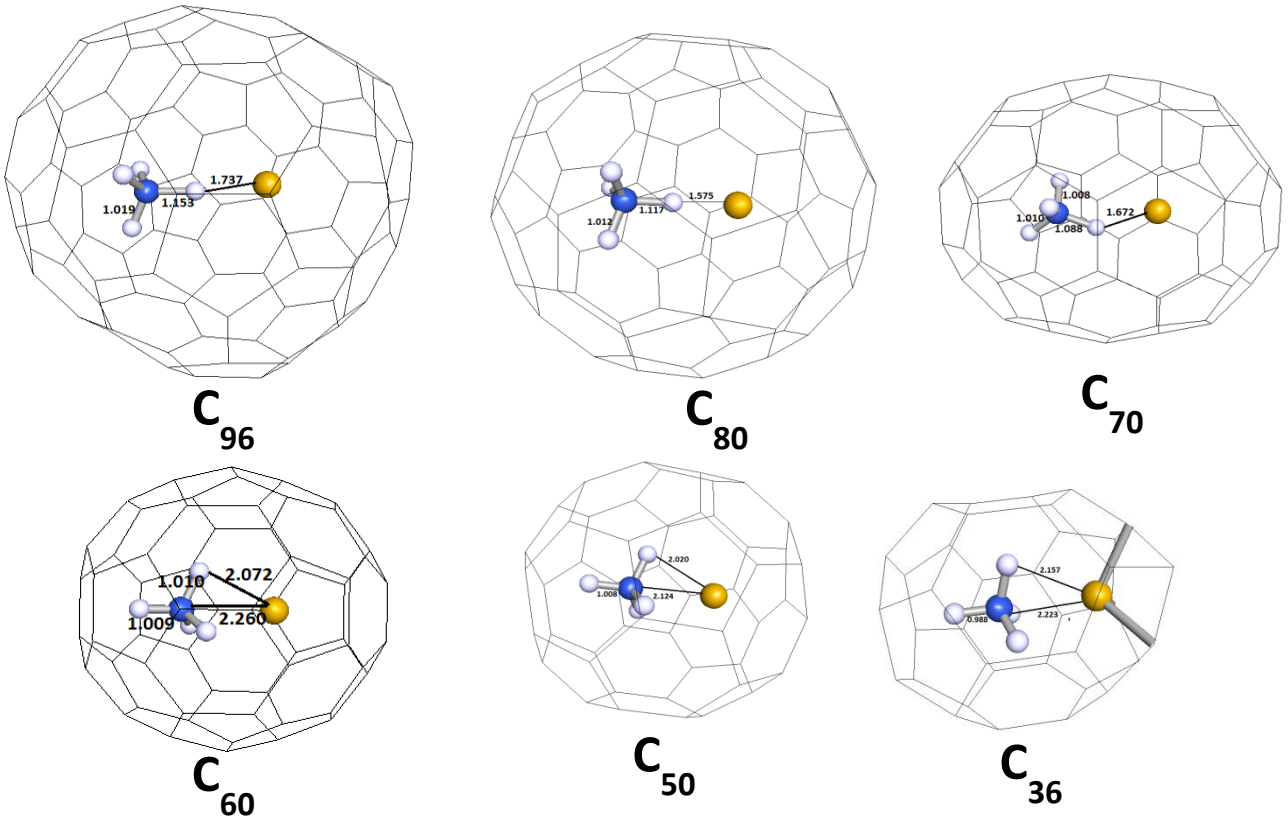

Figure 3.2: Optimized structures of all (NH_3-HCl)—fullerene complexes.

To get a clear picture on the effect of confinement, we have plotted the Cl-H-N angle as function of fullerene diameter. This is presented in Figure 3.3. Since the structure is changing from linear to nonlinear (in terms of Cl—H—N angle), a nonlinear decrease in the Cl-H distance.

From the above results it can be mentioned that the diameter of fullerene is one of the crucial parameters for the proton transfer in the NH_3-HCl complex. In order to understand the role of fullerenes and their diameter for the above complex, we have done the charge analysis based on the NBO scheme. The natural charge on each atom of the NH_3-HCl complex is listed in Table 3.2. In general, it is observed that the charge on Cl atom gradually increases with decrease in diameter up to C_{60}. This indicates that the Cl atom exists as an anion in these

confined situations. However, further reduction in diameter has reverse effect on the charge state of Cl atom. This is due to the transfer of electrons to fullerene ring as the whole NH_4-Cl complex acquires high positive charge (See last two rows of the last column). Thus, the fullerene cage acts as an electron rich centre to tune the charge state of the NH_3-HCl complex and promote the proton transfer process.

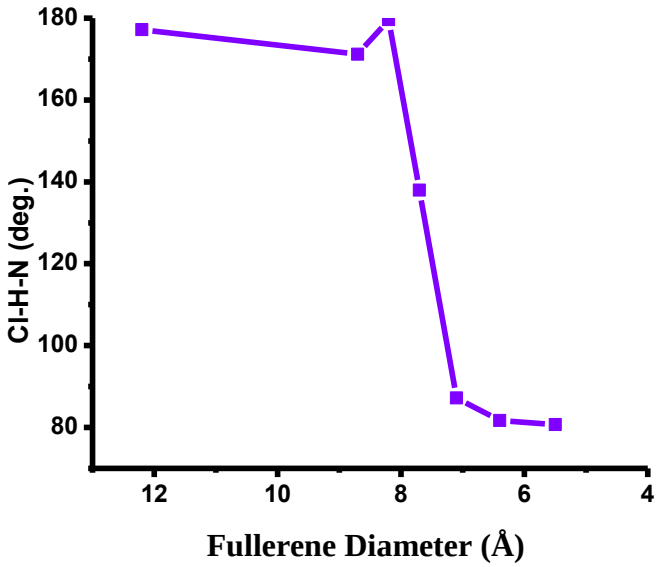

Figure 3.3: Variation in Cl-H-N angle as function of fullerene diameter.

Table 3.2: Natural charge on each atom of the NH_3-HCl complex by NBO analysis.

Confinement Medium	$q_{(Cl)}$	$q_{(H1)}$	$q_{(N)}$	$q_{(H2)}$	$q_{(H3)}$	$q_{(H4)}$	$q_{(NH4)}$	$q_{(NH4-Cl)}$
Isolated	-0.41	0.29	-1.02	0.38	0.38	0.38	0.41	0.0
C180	-0.49	0.31	-0.99	0.38	0.39	0.39	0.48	-0.01
C96	-0.76	0.42	-0.91	0.42	0.42	0.42	0.77	0.01
C80	-0.74	0.37	-0.92	0.42	0.42	0.42	0.71	-0.03
C70	-0.80	0.41	-1.00	0.46	0.44	0.44	0.75	-0.05
C60	-0.89	0.50	-1.17	0.50	0.52	0.50	0.83	-0.06
C50	-0.10	0.62	-1.63	0.61	0.62	0.64	0.87	0.77
C36	1.24	0.72	-2.18	0.72	0.74	0.72	0.71	1.95

3.3.2 Lewis acid-base complexes under the confinement of fullerenes

Lewis acid-base complexes (LABCs) are the group of electron donor-acceptor compounds in which the electron pair of the connecting dative bond is provided by one of the bonding species [204]. The simplest example is the amine-borane system (NH_3-BH_3 and its derivatives), in which the electron transfer takes place from the lone pair on nitrogen (Lewis base) to the vacant orbital of boron (Lewis acid). In terms of resonance theory, NH_3-BH_3 can be described by two diabatic states; one neutral state and one ionic charge-transferred state [205, 206]. The bond strength of LABC lies between the strong covalent bond and weak van der Waal bond, and it is related to the magnitude of charge transfer from the donor to the acceptor [207, 208]. Due to its high gravimetric hydrogen density, there is a lot of interest in the NH_3-BH_3 system in exploring the feasibility of using it as a hydrogen storage system for mobile applications [209-212]. Moreover, this simplest Lewis acid-base complex has been used as a model system in several studies to understand the nature of bonding and other chemical properties in this group of compounds [205, 213-215]. Similarly to the NH_3-HCl case, fully optimized geometries of Lewis acid (BH_XF_{3-X}), Lewis base (NH_YF_{3-Y}) and the Lewis acid-base complexes [$BH_3F_{(3-X)}$–$NH_3F_{(3-Y)}$] are obtained in gas phase (isolated case). Then, the complexes comprising of LABC and fullerene (C_{80} and C_{60}) have been optimized to get the minimum energy structure of the endohedral complexes (LABC@C_n).

3.3.2.1 Structure and energetics of isolated LABC

As mentioned previously, we have considered a series of LABC in the present study. Therefore let us discuss the isolated geometries first. The geometrical parameters and interaction energy values of isolated LABC are summarized in Table 3.3 and 3.4. The agreement between

our results and the results available from the earlier experiments and theoretical studies (employing other methods like MP2) is quite satisfactory [216-218].

Table 3.3: Optimized bond lengths (in Å) and net charge transfer in Lewis acid base complexes in gas phase. The first line in each column corresponds to the results from TPSSH/TZVP method and the second line represents results from B3LYP/TZVP method. In the third line, results from experiments and other theoretical studies (wherever available) are presented.

LABC	$R_{(B-H)}$	$R_{(B-F)}$	$R_{(N-H)}$	$R_{(N-F)}$	$R_{(B-N)}$	q
BH_3	1.19 1.20 1.19[a]					
BH_2F	1.19 1.19 1.19[a]	1.33 1.34 1.33[a]				
BHF_2	1.19 1.19 1.19[a]	1.32 1.33 1.33[a]				
BF_3		1.32 1.32 1.32[a]				
NH_3			1.02 1.02 1.02[a]			
NH_2F			1.02 1.03 1.02[a]	1.43 1.44 1.43[a]		
NHF_2			1.03 1.03 1.03[a]	1.41 1.42 1.41[a]		
NF_3				1.38 1.39 1.38[a]		
BH_3-NH_3 (1)	1.21 1.22 1.21[a]		1.02 1.02 1.02[a]		1.66 1.66 1.66[a]	0.38 0.38 0.32[a], 0.31[b]
BH_3-NH_2F (2)	1.21 1.21 1.21[a]		1.02 1.02 1.02[a]	1.43 1.45 1.42[a]	1.59 1.60 1.61[a]	0.32 0.32 0.31[a], 0.27[b]
BH_3-NHF_2 (3)	1.21 1.21 1.20[a]		1.03 1.02 1.03[a]	1.41 1.41 1.39[a]	1.59 1.59 1.60[a]	0.28 0.29 0.28[a], 0.23[b]
BH_3-NF_3 (4)	1.20 1.20 1.20[a]			1.37 1.38 1.37[a]	1.63 1.63 1.63[a]	0.26 0.26 0.24[a], 0.18[b]

BH_2F-NH_3 (5)	1.21 1.21 1.21[a]	1.40 1.42	1.02 1.02 1.02[a]		1.68 1.68 1.68[a]	0.36 0.35 0.29[a], 0.28[b]
BH_2F-NH_2F (6)	1.22 1.22 1.21[a]	1.39 1.40 1.42[a]	1.02 1.03 1.03[a]	1.42 1.44 1.42[a]	1.63 1.63 1.68[a]	0.30 0.30 0.27[a], 0.25[b]
BH_2F-NHF_2 (7)	1.21 1.21	1.37 1.38	1.03 1.03	1.39 1.40	1.67 1.67	0.27 0.27 0.20[b]
BH_2F-NF_3 (8)	1.20 1.19	1.34 1.34		1.37 1.38	2.28 2.39	0.11 0.04 0.02[b]
BHF_2-NH_3 (9)	1.21 1.21 1.21[a]	1.39 1.40 1.39[a]	1.02 1.02 1.02[a]		1.69 1.69 1.69[a]	0.34 0.34 0.27[a], 0.27[b]
BHF_2-NH_2F (10)	1.22 1.22	1.37 1.38	1.02 1.02	1.41 1.42	1.70 1.70	0.30 0.30 0.23[b]
BHF_2-NHF_2 (11)	1.20 1.20	1.35 1.36	1.03 1.03	1.38 1.39	1.92 1.88	0.22 0.06 0.16[b]
BHF_2-NF_3 (12)	1.19 1.19	1.32 1.33		1.38 1.39	2.91 2.79	0.02 0.01 0.01[b]
BF_3-NH_3 (13)		1.37 1.38 1.38[a]	1.02 1.02 1.02[a]		1.69 1.68 1.68[a]	0.33 0.33 0.26[a], 0.26[b]
BF_3-NH_2F (14)		1.37 1.38	1.02 1.02	1.40 1.41	1.72 1.72	0.30 0.30 0.22[b]
BF_3-NHF_2 (15)		1.35 1.36	1.03 1.03	1.38 1.39	1.90 1.87	0.22 0.09 0.14[b]
BF_3-NF_3 (16)		1.32 1.33 1.33[a]		1.38 1.39 1.38[a]	2.71 2.60 2.58[a]	0.02 0.02 0.01[a], 0.01[b]

[a] ref [208], [b]ref [217]

For example, in the present study, the N-B bond length ($R_{(N-B)}$) for the complex BH_3-NH_3 has been estimated as 1.660 Å and 1.656 Å respectively by TPSSH and B3LYP method. These values are quite close to the MP2 result [217] of 1.664 Å and the experimentally determined value of 1.6576 Å [218]. Similarly, the estimated interaction energy values of the complex BH_3-

NH_3 by these two methods are -34.5 and -30.9 kcal/mol whereas, the experimental [204] and MP2 results [217] are -31.1 and -34.4 kcal/mol respectively. From these results, it can be inferred that the both TPSSH and B3LYP functional with dispersion correction are able to describe the parameters of LABC in a fairly accurate manner.

Table 3.4: Interaction energy (IE) of Lewis acid-base complex in gas phase. The numbers corresponding to the LABC are indicated in 3.3.

LABC No.	IE (kcal.mol^{-1})	
	TPSSH/TZVP	B3LYP/TZVP
1	-34.5	-30.9
2	-33.2	-29.8
3	-25.9	-22.9
4	-14.2	-11.6
5	-24.6	-21.5
6	-21.1	-18.1
7	-11.2	-8.6
8	-1.8	-1.5
9	-20.3	-17.4
10	-13.1	-10.3
11	-4.3	-3.6
12	-1.3	-1.3
13	-24.0	-21.4
14	-16.0	-13.5
15	-6.2	-4.8
16	-1.7	-1.9

The other important aspect of LABC is the electron transfer from the Lewis base to acid as it has a direct correlation with the interaction energy of the LABC [197, 219]. The charge transfer values obtained through natural bond orbital (NBO) analysis are presented in the last column of Table 3.3. There is a gradual decrease in the amount of charge transfer as the hydrogen atoms in the LABC are substituted by the fluorine atom. Substitution of electronegative fluorine atom to nitrogen diminishes the ability of nitrogen to donate electrons to boron. On the other hand, fluorine atom substitution in place of boron increases the back

donation from the former to the empty p orbital of boron and hence reduces the ability of boron to accept the electron from nitrogen. Therefore, the maximum charge transfer (0.38 a.u.) occurs in the case of BH_3-NH_3 and nearly zero charge transfer in the case of BF_3-NF_3. The charge transfer values obtained in the present study is slightly higher compared to the MP2 result [217, 219]. Nevertheless, the trend remains unaltered and the highest and lowest interaction energy values are observed for BH_3-NH_3 and BF_3-NF_3 respectively in agreement with the net charge transfer.

3.3.2.2 LABC under the confinement of fullerene cages

The optimized geometry of the isolated LABC is placed inside the fullerene cages (C_{60} and C_{80}) and the endohedral complex of LABC and fullerene is fully optimized without any symmetry constraint to get the equilibrium structure. The stabilization energy value of all the LABC in C_{60} is positive. Therefore, we will mainly focus our discussion on the C_{80} fullerene. In addition, both Lewis acid and base are separately optimized inside C_{80} cage to get the minimum energy structures. The optimized geometries of all the fullerene-LABC complexes are presented in Figure 3.4. In general, the structure of C_{80} is least affected during the course of optimization. For Lewis bases (NH_3F_{3-Y}), both the $R_{(N-H)}$ and $R_{(N-F)}$ remain unchanged under the confinement of C_{80}. Similarly, there is not an appreciable change in $R_{(B-H)}$ and $R_{(B-F)}$ of Lewis acids (BH_3F_{3-X}) in C_{80}. From these results, it can be inferred that the Lewis acid and bases are structurally least affected inside the C_{80} cage. Hence, the effect imposed by C_{80} on Lewis acid (or base) is primarily arises from the electronic interaction between the confined species and the C_{80} cage.

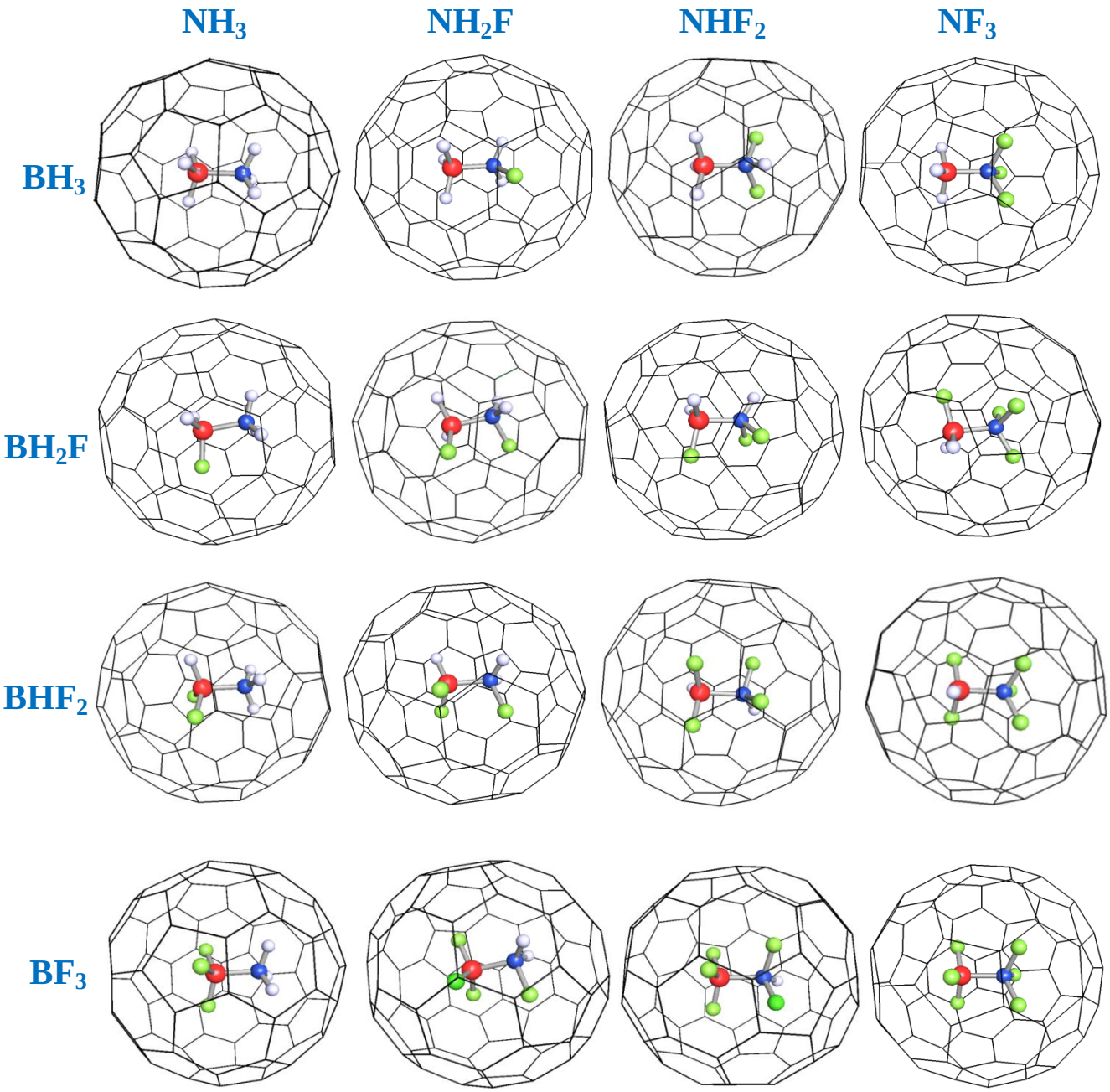

Figure 3.4: Optimized geometries of Fullerene-LABC complexes.

The stabilization (SE) energy of Lewis acid (or base) in C_{80} has been calculated using relation (3.1).

$$SE = [E_{(LA@C80)} - E_{LA} - E_{C80}] \quad (3.1)$$

Where, E_{LA}, E_{C80} and $E_{(LA@C80)}$ denotes the energy of Lewis acid (or base), C_{80} cage and the endohedral complex of acid (or base) in C_{80} respectively.

The SE values presented in Table 3.5 indicate that all the Lewis acid and bases considered in the present study can be encapsulated in C_{80} in an energetically favorable manner. The SE for $NH_3@C_{80}$ is -16.4 kcal/mol, which is slightly higher than the earlier reported value of NH_3 in C_{60} (i.e. -14.6 kcal/mol) [220]. This may be due to the large size and high polarizability of the C_{80} cage which can accommodate NH_3 more efficiently than the C_{60} cage. A recent study has shown that the encapsulated molecule gets stabilized inside C_{80} due to the transfer of large number of electrons from the guest molecule to the C_{80} [221]. It is worth noting that the C_{60} cage can encapsulate only a single molecule of NH_3 [220, 222] or a dimer of HF [194]. The stabilization energy initially increases with fluorine substitution and then falls sharply in the case of NF_3. Similarly, the SE value for the complex $BH_3@C_{80}$ is -18.04 kcal/mol which increases to -18.8 kcal/mol upon the substitution of one hydrogen atom by a fluorine atom. However, further fluorine substitution has negative effect on the stabilization energy. This can be related to ability of boron to accept electron, which decreases as the back donation from fluorine to boron becomes significant.

To quantify the contribution of structural deformation to stabilization energy, the structural deformation energy (SDE) has been calculated as the difference in energy of the isolated optimized structure of Lewis acid (or base) and the energy of the optimized geometry

inside the C_{80} cage. The later has been estimated by performing a single point energy calculation on the confined optimized structure of acid/base after taking it out of the C_{80} cage. The SDE values presented in the last column of Table 3.5 indicate that its contribution is insignificant and the main contribution to SE is from the electronic interaction.

Table 3.5: Stabilization energy (SE) and Structural Deformation Energy (SDE) values of Lewis acid/base in C_{80}.

Molecule	SE ($kcal.mol^{-1}$)	Structural Deformation Energy ($kcal.mol^{-1}$)
BH_3	-18.04 -17.32	0.00 0.00
BH_2F	-18.80 -18.80	0.00 0.01
BHF_2	-18.46 -19.00	0.03 0.05
BF_3	-17.13 -18.29	0.06 0.08
NH_3	-16.41 -16.38	0.01 0.00
NH_2F	-18.85 -19.48	0.01 0.01
NHF_2	-19.16 -19.66	0.02 0.01
NF_3	-16.14 -17.16	0.04 0.03

Let us now discuss the geometrical parameters of optimized Lewis acid-base complexes under the confinement of C_{80}. To get a clear picture, the variation in bond length of LABC in isolated case and in C_{80} is presented in Figure 3.5. It is observed that the $R_{(B-H)}$ of LABC in C_{80} is shorter than its original value in the isolated geometry. Within a series (say from 1 to 4 or 5 to 8), we did not find any specific trend in $R_{(B-H)}$ of the isolated LABC with the increase in number of fluorine atoms on nitrogen whereas, in C_{80}, a continuous decrease in $R_{(B-H)}$ is observed. On the

other hand, both in isolated state and in C_{80}, $R_{(B-F)}$ decreases with the increase in number of fluorine atoms on nitrogen. It is interesting to note that, there is a significant elongation in $R_{(B-F)}$ in C_{80} from the unconfined value (particularly in the first two series of LABC). On the contrary, $R_{(N-H)}$ of LABC increases with the increase in number of fluorine atoms on nitrogen in both cases. Moreover, the $R_{(N-H)}$ value in C_{80} is either equal to or greater than that of the isolated geometry. In both cases, $R_{(N-F)}$ decreases with increase in fluorine atoms on nitrogen but the decrease is quite sharp in the 3rd and 4th series of LABC in C_{80}. In addition, $R_{(N-F)}$ in C_{80} is always shorter than its corresponding value in the isolated geometry.

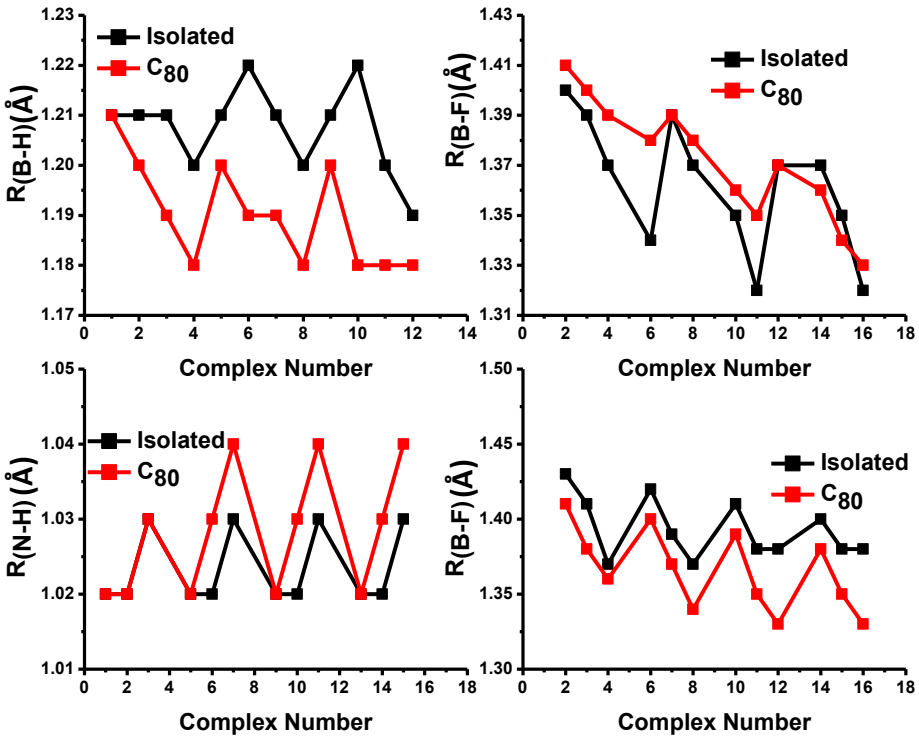

Figure 3.5: Variation in bond length of LABC in isolated case and in C_{80}.

It is difficult to obtain the exact value of interaction energy of Lewis acid and base in C_{80} (i.e. IE_{C80}) in a direct way. Therefore, it has been estimated using the approximate relation (3.2) and the same has presented in Table 3.6.

$$IE_{C80} = E_{(LABC@C80)} - E_{(LA@C80)} - E_{(LB)} \quad (3.2)$$

where, $E_{(LABC@C80)}$ and $E_{(LA@C80)}$ are the energy of Lewis acid-base complex and Lewis acid in C_{80} respectively, and E_{LB} is the energy of Lewis base.

A significant increase (~50%) has been observed in the interaction energy of BH_3-NH_3 in C_{80} as compared to its isolated value. The difference between the two energy values decreases as the number of fluorine atoms on nitrogen increases. For the LABC comprising of NHF_2 and NF_3, the IE in C_{80} is less than that of the isolated case. One of the reasons for the gradual reduction in IE in C_{80} is the insertion of bulky fluorine atom. As the number of fluorine atom increases in a Lewis acid-base complex, the acid and base in C_{80} are pushed closer to each other due to the effect of confinement imposed by the fullerene cage. This results a decrease in the $R_{(B-N)}$ distance and increase in the electrostatic repulsion energy.

For the LABC confined in C_{80}, it is observed that the electronic population of NH_3 remains the same (equal to the isolated complex) whereas electronic population on BH_3 substantially increases as compared to the gas phase value. This indicates that there is significant amount of electron charge transfer from C_{80} to LABC.

Table 3.6: Interaction energy of LABC inside the C_{80} cage (E_{C80})

E_{C80}	IE (kcal.mol^{-1})	
	TPSSH/TZVP	**B3LYP/TZVP**
1	-52.5	-47.4
2	-43.3	-38.3
3	-27.7	-22.5
4	-6.3	-1.2
5	-40.2	-35.6
6	-27.9	-23.4
7	-8.2	-3.6
8	21.8	26.6
9	-33.2	-29.0
10	-17.0	-12.8
11	10.5	14.8
12	42.7	47.3
13	-34.4	-30.5
14	-9.5	-5.5
15	20.7	24.6
16	54.6	58.6

3.3.2.3 Important observations

In the present chapter, we have made an attempt to rationalize the role of fullerene cage towards the stability of ammonia-borane complex and its fluorine derivatives. We have considered two fullerene rings, C60 and C80. It may be inferred from our study that the confinement effect and the interaction of fullerene with the LABC can drastically modify the structure, chemical behavior and charge transfer in the spherical fullerene cage. This also allows to control the effective charge transfer in a precise manner and therefore to finely tune the interaction strength of the complex.

3.4 Summary of the work

In this chapter, the spherical confinement effect due to the fullerene cages on the nature of acid-base complexes has been investigated. In the first part, we have considered the NH_3-HCl pair as a prototype system and studied the effect of confinement and polarizability of fullerene cages on the behaviour of this acid-base pair by systematically varying the fullerene diameter (C_{36} to C_{180}) using density functional methods. In the second part, we have investigated the Lewis acid-base complex (LABC) i.e., the ammonia-borane and its fluorine derivatives in fullerene bulky balls.

In our important findings, it has been demonstrated that the diameter of fullerene is one of the crucial factors in deciding the chemical properties of the acid-base pair. In isolated case (gas phase) of the NH_3-HCl pair, the proton is associated with the acid and quite far away from the nitrogen of ammonia. In larger diameter fullerene such as C_{180}, only a slight increase (~ 5%) in chloride-proton distance ($R_{Cl\text{-}H}$) is observed and the acid is still in the undissociated form. As the diameter of fullerene decreases, the acid starts dissociating and a gradual reduction in the nitrogen-proton distance is observed. In C_{60} and other smaller diameter fullerenes, the proton is completely transferred from the acid to ammonia, and a symmetrical ammonium ion is formed. We have observed that the confinement effect along with the interaction of fullerene with the LABC, significantly modify the structure, interaction energy, chemical reactivity and charge transfer in LABC under the spherical cage of fullerene. The results obtained from our study can be utilized to control the effective charge transfer in the acid-base complex and to finely tune the interaction strength of the complex by using proper confinement medium.

Chapter 4

Solvation of multiply charged anions in finite system

4.1 Introduction

Solvation is the interaction of a solute with the solvent and leads to the stabilization of solute species in a solution. The solvation process is a complex phenomenon as it involves different intermolecular interactions depending on the nature of solute and solvent molecule. Of all properties of ion in condensed phase the most fundamental are the solvation properties. Solvation energy plays a major role in connection with the solubility of salts in solvent, stability of transition states of chemical reactions, ion hydration, transport of ions and drugs across biological membranes. It has been the subject of numerous experimental and theoretical studies [223-236]. However, a precise estimation of the solvation energy not only for systems containing finite number (N) of solvent molecules but also for bulk systems ($N=\infty$) with unknown interaction potential still remains intangible. Despite the apparent simplicity, it has not yet been fully understood. In finite system, the solvation process is modified due to the presence of limited number of solvent molecules. As discussed earlier, these kinds of situations are often encountered in biological and chemical systems where the ions are surrounded by a few solvent molecules due to geometrical constraints. Therefore, the ion solvation process in finite system is of greater scientific interest both from academic curiosity and practical implications. In this chapter, we have studied the solvation of ions in a finite system and extended the results through suitable expressions to the bulk. In particular, a microscopic theory-based bottom-up approach has been implemented to derive an analytical expression for the solvation energy for a finite (N) system, including the bulk. This bottom-up approach provides the information on solvation energies of anionic solutes in finite-size clusters, including the bulk ($N = \infty$), from the knowledge of the detachment energies for the system containing a few numbers of solvent molecules. However, in case of dielectric constant, a microscopic theory-based top-down approach has been

prescribed to derive an analytical expression for the static dielectric constant for the finite system.

4.2 Expression for solvation energy of an ion

Max Born was the first campaigner for theoretical investigation of ionic solvation energy for bulk systems [224]. Solvation energy was calculated based on the model, where a charge (-q) is transferred from a conducting sphere of radius R in vacuum with permittivity, ε_0 to the same sphere in a bulk medium of dielectric constant, $\varepsilon_s(\infty)$. The solvation energy for the bulk, $F^{sol}(q,\infty)$ was derived by Max Born based on continuum theory and the simple formula for the quantity can be written as,

$$F^{sol}(q,\infty) = -\left(\frac{1}{\varepsilon_0} - \frac{1}{\varepsilon_s(\infty)}\right)\frac{(qe)^2}{R} \qquad (4.1)$$

The main limitation of Born theory of solvation is that it was derived based on continuum theory where the microscopic details were not considered. However, if solute-solvent and solvent-solvent motions are strongly correlated, the continuum theory breaks down, and one needs to have a microscopic theory based approach to derive an expression for the solvation energy for finite system as well as the same for the bulk. Another disadvantage of Eq.(4.1) is that the solvation energy cannot be calculated from it for finite system. Although *ab initio* quantum mechanics based theoretical methods can bypass this problem, investigations based on this approach are limited only to the small size solvated clusters due to enormous computational cost. Recently, with the advent of sophisticated molecular beam techniques, the solvation process in finite size solvated anionic clusters has been open to the experimental observations [236-242], and a renewed interest has grown in connecting finite size cluster properties to those of the

macroscopic system (bulk) in the theoretical arena also [232]. Much of today's nanoscale research has been designed to reach a better understanding of how matter behaves and chemical reactions such as electron transfer reactions do take place on this scale. Therefore deriving an analytical expression for solvation energy and dielectric constant for finite system including the bulk will be of immense useful to understand the solvation and diffusion dynamics and chemical reactions at nanoscale. To the best of our knowledge no attempt has been made in this direction.

4.3 The microscopic theory based approach

The expression for bulk solvation energy (Eq. 4.1) derived by Max Born was based on continuum theory wherein detailed correlated molecular motions are not considered. However, it is known that the continuum theory breaks down for strongly correlated systems, so a microscopic theory based approach is essential in order to understand the solvation energy not only for the system containing finite number of solvent molecules but also for the bulk. In order to include the molecules effect on solvation energy (SE) into the expression for the SE proposed by Born (Eq. 4.1), we first write the generalized expression for SE as

$$F(q,N) = -C\left(\frac{1}{\varepsilon_0} - \frac{1}{\varepsilon_s(N)}\right)\frac{(qe)^2}{R} \qquad (4.2)$$

where $\varepsilon_s(N)$ corresponds to dielectric constant for finite system and the constant C is an unknown parameter. The molecular effect on SE will be included through $\varepsilon_s(N)$ and C. One can get back the expression of SE defined in Eq. 4.1 from Eq. 4.2 by substituting C =1 and $\varepsilon_s(N) = \varepsilon_s(\infty)$ in the same. We now consider the formation of the daughter anionic hydrated cluster, $A^{-(q-1)}.NS$ (S=solvent) from its parent form, $A^{-q}.NS$. It may be described in three steps as shown in Fig. 4.1. The first step is the desolvation of the parent anionic species having charge -q, the next

step is the electron detachment of A^{-q} anion in gas phase and the final step is the solvation of the daughter anion $A^{-(q-1)}$. The sum of the energies involved in each step of the process viz. desolvation energy corresponding to the anionic cluster, $A^{-q}.NS$, gas phase electron detachment energy of A^{-q} anion, and solvation energy of the $A^{-(q-1)}$ anion is equal to the detachment energy.

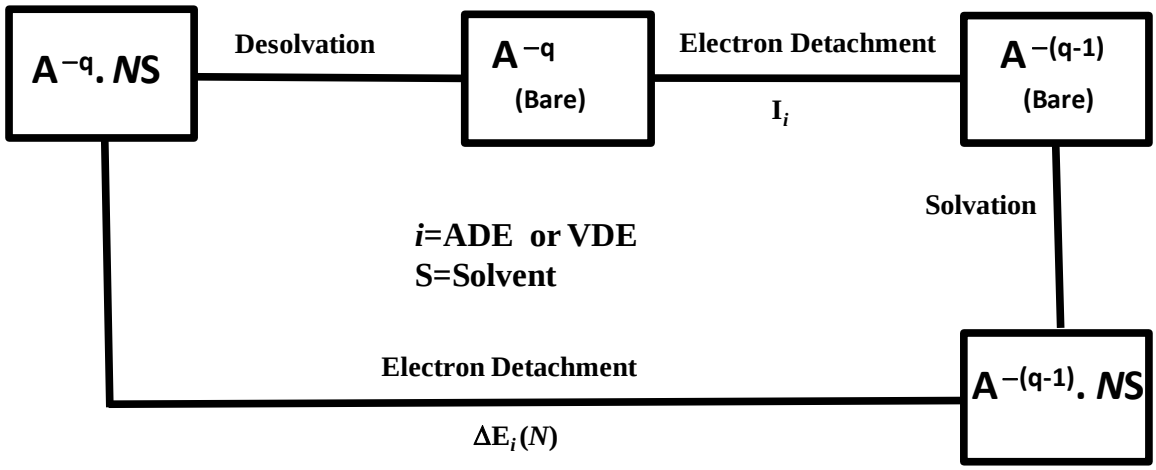

Figure 4.1: Schematic representation of various steps involved in electron detachment process of $A^{-q}.NS$ cluster.

Now, the detachment energy, $\Delta E_i(q,N)$ can be written in terms of these energy components as

$$\Delta E_i(q,N) = I_i + F^{sol}(q-1,N) - F^{sol}(q,N) \qquad (4.3)$$

where, $i = ADE \ or \ VDE$

ADE and VDE respectively represent the adiabatic and vertical detachment energies of the anion A^{-q} in solvent environment containing finite number of solvent molecules. Here I_{VDE} and I_{ADE} denote respectively the vertical (VDE) and adiabatic (ADE) ionization of the isolated anion A^{-q} in vacuum. Now substituting the Eq. 4.2 into Eq. 4.3 we obtain

$$\Delta E_i(q,N) = C_i\left(\frac{1}{\varepsilon_0} - \frac{1}{\varepsilon_s(N)}\right)\frac{(2q-1)e^2}{R} + I_i \qquad (4.4)$$

Here the radius of the A^{-q} and $A^{-(q-1)}$ anions are assumed to be same. Here, both C_i and $\varepsilon_s(N)$ are unknown. In order to obtain an analytical expression for C_i and $\varepsilon_s(N)$, what is needed an explicit expression for detachment energy derived based on microscopic theory. Before, deriving an expression for detachment energy, we first write the solvent number dependent ion-solvent interaction energy for the ground state of the anion in solvent medium is written as

$$F_g^{sol}(q,N) = \int U_{i-s}^{g}(\boldsymbol{X^{N+1}}, q)\exp[-\beta V(\boldsymbol{X}^{N+1}, q)]\, d\boldsymbol{X}^{N+1} \qquad (4.5)$$

where, g represents the ground state of the single anion in solvent medium. Here $U_{i-s}^{g}(\boldsymbol{X^{N+1}}, q)$ represents the anion-solvent interaction energy for the ground state corresponding to the system containing single anion A^{-q} in the ground state and finite number (N) of solvent molecules. Here the configuration of a rigid non spherical system is specified by a 6(N+1) dimensional vector **X** [21] corresponding to the location **R** and orientation **Ω** of the system and β is 1/kT, where k is Boltzmann constant and T is absolute temperature and $V(\boldsymbol{X}^{N+1}, q)$ is the total interaction potential including all solvent molecules and solute. Eq. 4.5 can also be written in terms of two particle distribution function, $\rho^2(\mathbf{X_S}, \boldsymbol{X}, q, N)$ as

$$F_g^{sol}(q,N) = \iint d\boldsymbol{X_S} d\mathbf{X}\, U_{i-s}^{g}(\boldsymbol{X_S}, \mathbf{X}, q)\rho^2 \times (\mathbf{X_S}, \mathbf{X}, q, N) \qquad (4.6)$$

The quantity $\rho^2(\mathbf{X_S}, \boldsymbol{X}, q, N)$ here represents the static equilibrium two particle distribution function for the system contains the single anion with charge –q and finite number (N) of solvent molecules. Here $\mathbf{X_S}$ and $\boldsymbol{X}$ represent, respectively, the configurations of a single anion and solvent molecule in a six dimensional space. We now define two types (1 & 2) of solvation energies for the excited states (ex) viz.

$$F_{ex1}^{sol}(q-1,N) = \iint d\boldsymbol{X_S}\boldsymbol{d}\mathbf{X}_{\boldsymbol{sol}}\, U_{i-s}^{ex} \times (\boldsymbol{X_S}, \mathbf{X}, q-1)\rho^2(\mathbf{X}_{\boldsymbol{S}}, \mathbf{X}, q, N) \quad (4.7)$$

$$F_{ex2}^{sol}(q-1,N) = \iint d\boldsymbol{X_S}\boldsymbol{d}\mathbf{X}_{\boldsymbol{sol}}\, U_{i-s}^{ex}(\boldsymbol{X_S}, \mathbf{X}, q-1)\rho^2 \times (\mathbf{X}_{\boldsymbol{S}}, \mathbf{X}, q-1, N) \quad (4.8)$$

The quantity $\rho^2(\mathbf{X}_{\boldsymbol{S}}, \boldsymbol{X}, q-1, N)$ represents the static equilibrium two particle distribution function for the system containing the single anion with charge –(q–1) in the excited state and finite number of solvent molecules. The vertical (VDE) and adiabatic detachment energies (ADE) can now be written, respectively, in terms of $F_g^{sol}(q,N)$, $F_{ex1}^{sol}(q-1,N)$ and $F_{ex2}^{sol}(q-1,N)$ as

$$\Delta E_{VDE}(q,N) = I_{VDE} + F_{ex1}^{sol}(q-1,N) - F_g^{sol}(q,N) \quad (4.9)$$

$$\Delta E_{ADE}(q,N) = I_{ADE} + F_{ex2}^{sol}(q-1,N) - F_g^{sol}(q,N) \quad (4.10)$$

For both the processes, VDE and ADE, one of the electrons of the solvated anion is removed instantaneously by photo-absorption. However, in the case of VDE, the detachment energy corresponds to the energy difference between the final non-equilibrium configuration (after ejection of one electron) and initial equilibrium configuration and having the same solvent configuration for both the states; whereas ADE refers to the energy difference between the final (after ejection of one electron) and initial equilibrium configuration and having different solvent configuration for both the states.

In order to have an explicit expression for the solvation energy of the system containing finite number of solvent particles, what is needed is a relation between the two particle distribution function $\rho^2(\mathbf{X}_{\boldsymbol{S}}, \mathbf{X}, q, \mu)$ (μ is chemical potential of the solvent molecules) of the thermodynamic system and its finite system counterpart viz. $\rho^2(\mathbf{X}_{\boldsymbol{S}}, \mathbf{X}, q, N)$. A relation can be derived through a Taylor-series expansion in powers of inverse of solvent numbers $(1/N)$ by

following the theoretical method developed by Salacuse et al. [244] for a simple non polar, one component and homogeneous system. The methodology can be extended to the case of polar inhomogeneous system containing one solute anion and a finite number of solvent molecules with arbitrary interaction potential. Here, we consider a semi-grand canonical ensemble (in contrast to the grand canonical ensemble considered by Salacuse), where only the number (N) of solvent molecules is allowed to fluctuate but the single negatively charged ion is kept fixed in each member of the ensemble [245]. The two particle distribution function, $\rho^2(\mathbf{X_S}, \boldsymbol{X}, q, \mu)$ for the thermodynamic system for a given volume V and temperature T may be expressed in terms of its finite system counterpart, $\rho^2(\mathbf{X_S}, \boldsymbol{X}, q, N)$ as

$$\rho^2(\mathbf{X_S}, \boldsymbol{X}, q, \mu) = \sum_{N=0}^{\infty} P(N)\, \rho^2(\mathbf{X_S}, \boldsymbol{X}, q, N) \tag{4.11}$$

Here, $P(N)$ represents the probability of finding the member containing N particles. We first define the average value $\overline{(N)}$ of the number of solvent particles,

$$\bar{N} = \sum_{N=0}^{\infty} P(N) N\,, \tag{4.12}$$

and then expanding $\rho^2(\mathbf{X_S}, \boldsymbol{X}, q, N)$ around the average value $\overline{(N)}$ of the number of solvent particles, one can write

$$\rho^2(\mathbf{X_S}, \boldsymbol{X}, q, N) = \sum_{N=0}^{\infty} P(N)\, [\rho^2(\mathbf{X_S}, \boldsymbol{X}, q, \bar{N})$$

$$+ \frac{1}{2}(N - \bar{N})^2 \frac{\partial^2}{\partial \bar{N}^2} \rho^2(\mathbf{X_S}, \boldsymbol{X}, q, \bar{N})$$

$$+ \tfrac{1}{6}(N - \bar{N})^3 \tfrac{\partial^3}{\partial \bar{N}^3} \rho^2(\mathrm{X}_S, X, q, \bar{N}) + \cdots] \tag{4.13}$$

where the identity $\overline{(N-\bar{N})}$=0 has been used. Using the relation between the average density ρ of the solvent molecules and average number of solvent particles $\bar{N}$ $viz.$ $\bar{N}/V=\rho$, total probability condition, $\sum_{N=0}^{\infty}P(N)=1$ and after some algebra we obtain the simple expressions for detachment energy

$$\Delta E_i(q,N)=\Delta E_i^{sol}(q,\infty)+I_i+\frac{\mathrm{M_i^1}}{(N+\sigma)}+\frac{\mathrm{M_i^2}}{(N+\sigma)^2}, \tag{4.14}$$

where, $i=ADE,VDE$ and σ is defined as the product of the solute to solvent size ratio and numerical value of the charge of the solute anion. The coefficients $\mathrm{M_i^1}$ and $\mathrm{M_i^2}$ are appeared in terms of gradient of density and are expressed as,

$$\mathrm{M_i^1}=-\left[f_{\bar{N}}^1\times\frac{\rho^2}{2}\times\frac{\partial^2}{\partial\rho^2}\Delta E_i(q,\infty)\right] \tag{4.15}$$

and

$$\mathrm{M_i^2}=\left[f_{\bar{N}}^1\times\frac{\rho^2}{2}\times\frac{\partial^2}{\partial\rho^2}\left\{f_{\bar{N}}^1\times\frac{\rho^2}{2}\times\frac{\partial^2}{\partial\rho^2}\Delta E_i(q,\infty)\right\}-f_{\bar{N}}^2\times\frac{\rho^3}{6}\frac{\partial^3}{\partial\rho^3}\Delta E_i(q,\infty)\right] \tag{4.16}$$

The quantity $\Delta E_i^{sol}(q,\infty)$ can be expressed in terms of the difference of two energy components as.

$$\Delta E_{ADE}^{sol}(q,\infty)=\ F_{ex2}^{sol}(q-1,\infty)-F_g^{sol}(q,\infty) \tag{4.17}$$

and

$$\Delta E_{VDE}^{sol}(q,\infty)=\ F_{ex1}^{sol}(q-1,\infty)-F_g^{sol}(q,\infty). \tag{4.18}$$

The fluctuating quantities ($f_{\bar{N}}^{1}$ & $f_{\bar{N}}^{2}$) appearing in the above equations can be expressed in terms of the two particle distribution function $\rho^2(\mathbf{X_1}, \boldsymbol{X_2}, \mu)$ for the solvent molecules (1 & 2) of a thermodynamic system containing single anion and very large number of solvent molecules as

$$\frac{\overline{(N-\bar{N})^2}}{\bar{N}} = f_{\bar{N}}^{1}$$

$$= 1 + \frac{1}{\rho V} \iint d\boldsymbol{X}_1\, d\boldsymbol{X}_2\, [\rho^2(\mathbf{X_1}, \boldsymbol{X_2}, \mu) - \rho(\boldsymbol{X_1})\rho(\boldsymbol{X_2})] \qquad (4.19)$$

$$\frac{\overline{(\bar{N}-\bar{N})^3}}{\bar{N}} = f_{\bar{N}}^{2} - \left[f_{\bar{N}}^{1}\right]^2 + \frac{\partial f_{\bar{N}}^{1}}{\partial(\beta\mu)} \qquad (4.20)$$

where V, $\boldsymbol{X_1}$ and $\boldsymbol{X_2}$ represent the volume of the system, and position vectors of any two solvent molecules. Here, $\rho(\boldsymbol{X_1})$ and $\rho(\boldsymbol{X_2})$ correspond to the solvent density at the position vector $\boldsymbol{X_1}$ and $\boldsymbol{X_2}$, respectively. Now equating the Eq. 4.4 and Eq. 4.14 and then taking the thermodynamic limit, we obtain

$$C_i = \left(\frac{1}{\varepsilon_0} - \frac{1}{\varepsilon_s(\infty)}\right)^{-1} \left(\frac{R}{(2q-1)e^2}\right) \Delta E_i^{sol}(q, \infty). \qquad (4.21)$$

Again substituting the Eq. 4.21 into Eq. 4.2 and Eq. 4.4 and after simplification we obtain

$$F^{sol}(q, N) = -\left(\frac{1}{\varepsilon_0} - \frac{1}{\varepsilon_s(\infty)}\right)^{-1} \left(\frac{1}{\varepsilon_0} - \frac{1}{\varepsilon_s(N)}\right) \times \frac{q^2}{(2q-1)} \Delta E_i^{sol}(q, \infty) \qquad (4.22)$$

and

$$\Delta E_i(q, N) = \left(\frac{1}{\varepsilon_0} - \frac{1}{\varepsilon_s(\infty)}\right)^{-1} \left(\frac{1}{\varepsilon_0} - \frac{1}{\varepsilon_s(N)}\right) \times \Delta E_i^{sol}(q, \infty) + I_i. \qquad (4.23)$$

Solubility of drug in water and organic solvent plays an important role and affects many pharmaceutical processes including absorption and distribution of the same in body fluids. One

of the important properties of solvent that decides the extent of solubility is the dielectric constant. The magnitude of dielectric constant of the medium have a dominant effect on the solubility of the ionizable solute in which higher dielectric constant can cause more ionization of the solute and results in more solubilization. Again magnitude of dielectric constant for a given solvent depends the number of solvent molecules present in the medium. Therefore, it will be useful to have an analytical equation wherefrom the dielectric constant can be calculated for the system containing finite number (N) of solvent molecules. In order to have an analytical expression for dielectric constant for finite system, we equate the Eq. 4.23 and Eq. 4.14 and obtain the result

$$\left(\frac{1}{\varepsilon_0}-\frac{1}{\varepsilon_s(N)}\right)=\left(\frac{1}{\varepsilon_0}-\frac{1}{\varepsilon_s(\infty)}\right)\left[1+\frac{1}{\Delta \mathrm{E}_{\mathrm{i}}^{\mathrm{sol}}(q,\infty)}\times\left[\frac{\mathrm{M}_{\mathrm{i}}^{1}}{N+\sigma}+\frac{\mathrm{M}_{\mathrm{i}}^{2}}{(N+\sigma)^2}\right]\right]. \tag{4.24}$$

This is a new relation where dielectric constant for finite system, $\varepsilon_s(N)$ is related to bulk property, $\varepsilon_s(\infty)$. Now substituting the Eq. 4.24 into the Eq. 4.22, we obtain solvation energy for finite system defined as

$$F^{sol}(q,N)=-\frac{q^2}{(2q-1)}\Delta \mathrm{E}_{\mathrm{i}}^{\mathrm{sol}}(q,\infty)\left[1+\frac{1}{\Delta \mathrm{E}_{\mathrm{i}}^{\mathrm{sol}}(q,\infty)}\times\left[\frac{\mathrm{M}_{\mathrm{i}}^{1}}{N+\sigma}+\frac{\mathrm{M}_{\mathrm{i}}^{2}}{(N+\sigma)^2}\right]\right] \tag{4.25}$$

This is another new analytical expression (Eq. 4.25) for solvation energy for finite system. Now taking the thermodynamic limit ($N\rightarrow\infty$) in Eq. 4.25, we obtain bulk solvation energy as

$$F^{sol}(q,\infty)=-\frac{q^2}{(2q-1)}\Delta \mathrm{E}_{\mathrm{i}}^{\mathrm{sol}}(q,\infty) \tag{4.26}$$

This is to the best of our knowledge, a new relation where the bulk solvation energy (Eq. 4.26) is related to the difference of solvation energy components to the bulk detachment energy (Eq.

4.14, 4.17 & 4.18). In the following section, we discuss the evaluation of dielectric constant (Eq. 4.24) for finite system and solvation energy (Eq. 4.25) for the same as well for the bulk (Eq. 4.26).

4.4 Results and Discussion

4.4.1 Solvation Energy

We will now present the results of numerical calculations carried out using the present formalism. The bulk detachment energy $\Delta E_i(q,\infty)$ is to be evaluated by extrapolation, appearing in the two coefficients, namely, M_i^1 (Eq. 4.15) and M_i^2 (Eq. 4.16) in terms of the gradient of density. In many cases, the exact form of the interaction potential is not known for the complex hetero clusters. Therefore, the calculation of M_i^1 and M_i^2 as a function of density becomes challenging, which forces us to treat the coefficients, namely, M_i^1 and M_i^2 as unknown parameters.[10] The procedure adopted here is to find out the optimum values of M_i^1 and M_i^2 using experimental values of $\Delta E_i(q,N)$ and the Eq. 4.14, so that the calculated results are very close to the experimental one. Using these values of M_i^1 and M_i^2, the $\Delta E_i(q,N)$ values are calculated for a wide ranges of N. Upon extrapolation of $\Delta E_i(q,N)$ to infinite size clusters ($N=\infty$), the bulk detachment energy, namely, $\Delta E_i(q,\infty)$, is obtained. As illustrative examples, we consider doubly negatively charged ionic hydrated clusters, namely, $SO_4^{-2}.NH_2O$ and $C_2O_4^{-2}.NH_2O$. The size of the hydrated clusters for these systems for which experimental values of $\Delta E_{ADE}(q,N)$ are available cover the range from N = 4 to 40 [24]. The variation of $\Delta E_{ADE}(q,N)$ with $(N+\sigma)^{-1}$ is shown in Fig. 4.2 for $SO_4^{-2}.NH_2O$ and $C_2O_4^{-2}.NH_2O$ systems. The best fitted expressions here for the $SO_4^{-2}.NH_2O$ and $C_2O_4^{-2}.NH_2O$ systems are obtained, respectively, as

$$\Delta E_{ADE}(q,N) = 8.07 - \frac{108.4}{(N+8)} + \frac{295.2}{(N+8)^2} \quad (4.27)$$

and

$$\Delta E_{ADE}(q,N) = 6.83 - \frac{102.0}{(N+8)} + \frac{316.4}{(N+8)^2} \quad (4.28)$$

The calculated values of $\Delta E_{ADE}(q,N)$ obtained here based on Eq. 4.27 and Eq. 4.28 for the system $SO_4^{-2}.NH_2O$ and $C_2O_4^{-2}.NH_2O$ are shown along with the available experimental results in Fig. 4.2. The correlation coefficient (R) for all of the plots ($SO_4^{-2}.NH_2O$ and $C_2O_4^{-2}.NH_2O$) is greater than 0.99, which indicates the power of predictability of the analytical expressions defined in Eq. 4.27 and Eq. 4.28.

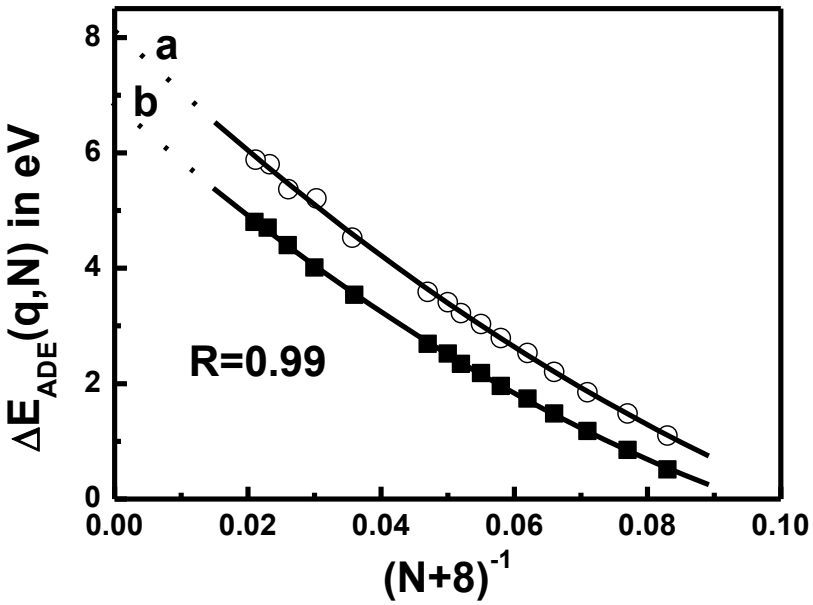

Figure 4.2: Plot of $\Delta E_{ADE}(q, N)$ vs. $(N+\sigma)^{-1}$ (σ=8) for (a) $SO_4^{2-}.NH_2O$ and (b) $C_2O_4^{2-}.NH_2O$ systems (N=4-40). The results based on new relation (Eq. (4.14)) are shown by solid lines in both cases, and the open circle (○) and solid squares (■) represent the experimental values, respectively for sulfate and oxalate systems and are taken from ref. [24].

The values of $\Delta E_{ADE}(q,\infty)$ are also calculated for the $SO_4^{-2}.NH_2O$ and $C_2O_4^{-2}.NH_2O$ systems based on Eq. 4.27 and Eq. 4.28 by taking the limit ($N \to \infty$) in the same and the results of the same quantities are shown in Table 4.1 along with the coefficients M_{ADE}^1 and M_{ADE}^2. The experimental bulk values $\Delta E_{ADE}(q,\infty)$ are also reported in Table 4.1. It is interesting to note that there is an very good agreement (within 7%) for the $\Delta E_{ADE}(q,\infty)$ between experiment [247] and theory. I_{ADE} for sulfate $SO_4^{-2}$and oxalate $C_2O_4^{-2}$ anions are also calculated by taking the limit $N \to 0$ in Eqs. (4.27) and (4.28). In this limit, $\Delta E_{ADE}(q,0) = I_{ADE}$. The calculated values of I_{ADE} are found to be -0.87 eV and -0.98 eV, respectively, for sulfate and oxalate anions and these values are also provided in Table 4.1. The negative values of I_{ADE} for isolated $SO_4^{-2}$and $C_2O_4^{-2}$ indicate that these anions are unstable against spontaneous electron loss in absence of water molecules. This instability arises due to coulomb repulsion. Now substituting the extrapolated results for $\Delta E_{ADE}^{sol}(q,\infty)$ ($\Delta E_{ADE}(q,\infty) - I_{ADE}$), M_{ADE}^1 and M_{ADE}^2 in Eq. 4.25, the expression for the solvation energy are obtained for the systems $SO_4^{-2}.NH_2O$ and $C_2O_4^{-2}.NH_2O$, respectively, as

$$F^{sol}(q,N) = -11.92\left[1 - \frac{12.12}{(N+8)} + \frac{33.02}{(N+8)^2}\right] \quad (4.29)$$

and

$$F^{sol}(q,N) = -11.41\left[1 - \frac{13.06}{(N+8)} + \frac{40.51}{(N+8)^2}\right]. \quad (4.30)$$

The calculated values of $F^{sol}(q,N)$ obtained here based on Eq. 4.29 and Eq. 4.30 for the systems $SO_4^{-2}.NH_2O$ and $C_2O_4^{-2}.NH_2O$ are plotted against $(N+\sigma)^{-1}$ and is shown in Fig.4.3. Now the bulk solvation energies, $F^{sol}(q,\infty)$ are obtained by taking the thermodynamic limit ($N \to \infty$) in Eq. 4.29 & Eq. 4.30 for $SO_4^{-2}.NH_2O$ and $C_2O_4^{-2}.NH_2O$ systems, respectively. The $F^{sol}(q,\infty)$ values are also provided in Table 4.1 along with the experimental results.

Table 4.1: Bulk adiabatic detachment energy $\Delta E_{ADE}(q,\infty)$, coefficients M^1_{ADE} , M^2_{ADE} , ionization potential I_{ADE} and bulk solvation energy, $F^{sol}(q,\infty)$ in eV for $A^{-q}.NH_2O$ systems ($A^{-q} = SO_4^{2-}$ and $C_2O_4^{2-}$).

Systems	Calculated $\Delta E_{ADE}(q,\infty)$ in eV[a]	Exptl. $\Delta E_{ADE}(q,\infty)$ in eV[b]	M_{ADE}^1 in eV	M_{ADE}^2 in eV	I_{ADE} of A^{q-} ion in eV	Calculated $F^{sol}(q,\infty)$ in eV based on microscopic theory [a]	Calculated $F^{sol}(q,\infty)$ in eV based on Born model [a]	Experimental $F^{sol}(q,\infty)$ in eV[c]
$SO_4^{2-}.NH_2O$	8.07 (**7**)	8.65	-108.4	295.2	-0.87	-11.92 (**5**)	-14.95 (**32**)	-11.27 (260)
$C_2O_4^{2-}.NH_2O$	6.83 (**7**)	7.32	-102.0	316.4	-0.98	-10.41	-14.95	-

[a]Bold values in the parentheses refer to % of error with respect to the experimental values. [b]Taken from ref. [257], [c]Taken from refs. [225, 248].

The calculated F^{sol}(q,∞) values for $SO_4^{-2}.NH_2O$ system is found to be -11.92 eV and is very close (within 5%) to the experimental result -11.27 eV [225, 248]. Again a very good agreement between theory and experiment is observed. On the other hand the calculated F^{sol}(q,∞) values (-11.41 eV) for the $C_2O_4^{-2}.NH_2O$ system cannot be validated due the lack of experimental data. The solvation energy is also calculated based on the Born model (Eq. 4.1) for sulfate and oxalate systems. The hydrated radius for the sulfate is taken as 3.8 Å [249]. Due to unavailability of experimental data for the oxalate system forces us to take the radius as 3.8 Å. The dielectric constant for water is taken as 78. Based on these values, the bulk solvation energy is calculated and is found to be -14.95 eV for both the systems. It is interesting to mention that the present calculated value based on the Born model overestimates the experimental one by 32 % for the sulfate system (see Table 4.1).

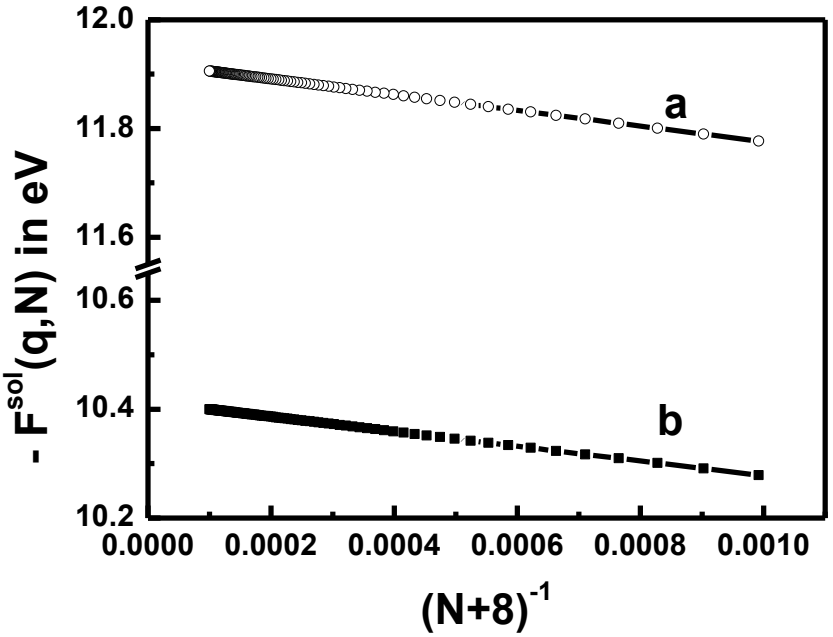

Figure 4.3: Plot of solvation energy, $-F^{sol}(q,N)$ in eV vs. $(N+\sigma)^{-1}$ (σ = 8) for (a) $SO_4^{2-}.NH_2O$ and (b) $C_2O_4^{2-}.NH_2O$ systems. The results based on new relation (Eq. 4.25) are represented by the open circle (○) and solid squares (■), respectively, for sulfate and oxalate systems.

4.4.2 Dielectric Constant

Again by substituting the extrapolated results for $\Delta E_{ADE}^{sol}(q,\infty)$, M_i^1 and M_i^2 corresponding to the hydrated di-anion viz. $SO_4^{-2}.NH_2O$ and $C_2O_4^{-2}.NH_2O$ in Eq. 4.24 we obtain the ratio of dielectric constant for the finite size cluster to that of the bulk, $\left[\frac{\left(\frac{1}{\varepsilon_0}-\frac{1}{\varepsilon_S(N)}\right)}{\left(\frac{1}{\varepsilon_0}-\frac{1}{\varepsilon_S(\infty)}\right)}\right]$, respectively, as

$$\frac{\left(\frac{1}{\varepsilon_0}-\frac{1}{\varepsilon_S(N)}\right)}{\left(\frac{1}{\varepsilon_0}-\frac{1}{\varepsilon_S(\infty)}\right)} = \left[1-\frac{12.12}{(N+8)}+\frac{33.02}{(N+8)^2}\right] \quad (4.31)$$

and

$$\frac{\left(\frac{1}{\varepsilon_0}-\frac{1}{\varepsilon_S(N)}\right)}{\left(\frac{1}{\varepsilon_0}-\frac{1}{\varepsilon_S(\infty)}\right)} = \left[1-\frac{13.06}{(N+8)}+\frac{40.51}{(N+8)^2}\right] \quad (4.32)$$

According to linear theory, dielectric constant is independent of external electric field. In present case, the dielectric constant should be independent of the nature of anions in the hydrated

cluster. So if the linear response theory is valid for these two systems ($SO_4^{-2}.NH_2O$ and $C_2O_4^{-2}.NH_2O$) then the dielectric constant calculated based on Eq. 4.31 and Eq. 4.32 should be nearly same. To test the validity of the linear theory of dielectric constant, we have plotted in Fig. 4.4 the results of the ratio, $\left[\frac{\left(\frac{1}{\varepsilon_0}-\frac{1}{\varepsilon_S(N)}\right)}{\left(\frac{1}{\varepsilon_0}-\frac{1}{\varepsilon_S(\infty)}\right)}\right]$ calculated here based on Eqs. 4.31 and Eq. 4.32 against $(N+\sigma)^{-1}$. It is clear from the Fig. 4.4 that the dielectric constant calculated for water is found to be very close over a wide number of solvent molecules indicating the validity of linear theory. It is also interesting to mention that the ratio is approaching to unity in large N limit. This clearly suggests that the dielectric constant for the finite size cluster, $\varepsilon_s(N)$, can be easily obtained from the knowledge of the same for the bulk solvent, $\varepsilon_s(\infty)$.

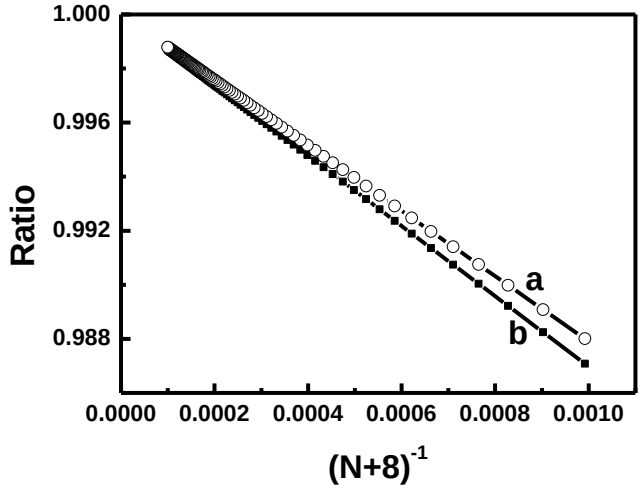

Fig. 4.4: Plot of $\left[\frac{\left(\frac{1}{\varepsilon_0}-\frac{1}{\varepsilon_S(N)}\right)}{\left(\frac{1}{\varepsilon_0}-\frac{1}{\varepsilon_S(\infty)}\right)}\right]$ ratio vs. $(N+\sigma)^{-1}$ (σ = 8) for (a) for $SO_4^{2-}.NH_2O$ and (b) for $C_2O_4^{2-}.NH_2O$ systems. The results based on new relation (Eq. 4.24) are represented by the open circle (○) and solid squares (■), respectively, for sulfate and oxalate systems.

4.5 Summary of the work

The new and important findings of the present study may be highlighted as follows. At present, a microscopic theory based bottom-up approach has been prescribed for the first time to derive an analytical expression for the solvation energy for finite system including the bulk. The newly derived bottom-up approach which is distinct from the earlier theory, provides the information of solvation energies for anionic solutes in finite size clusters including the bulk from the knowledge of the detachment energies for the finite system containing few numbers of solvent molecules. In the case of dielectric constant, we however, propose a microscopic theory based top-down approach to derive an analytical expression for static dielectric constant for finite system. In this approach, the knowledge of dielectric constant for the bulk provides a route to obtain the same quantity for wide number of solvent molecules. The microscopic details are included in the expressions of solvation energy (Eq. 4.25) and dielectric constant (Eq. 4.24) through the system dependent parameters, M_i^1 and M_i^2. The present expressions (Eq. 4.14, Eq. 4.24 & Eq. 4.25) bridge the microscopic (finite size) and macroscopic regions (bulk) and are valid for any inhomogeneous systems and non spherical molecules. In the present study we have considered hydrated doubly charged anions viz. $SO_4^{-2}.NH_2O$ and $C_2O_4^{-2}.NH_2O$ for thorough investigations. The calculated adiabatic detachment energies for $SO_4^{-2}.NH_2O$ and $C_2O_4^{-2}.NH_2O$ systems are found to be very in good agreement with experimental results not only for finite systems (Fig.4.2) but also for the bulk (Table 4.1). The very good agreement between theory and experiment indicates the usefulness of the Eq. 4.14. The calculated bulk solvation energy (-11.92 eV) using the Eq. 4.29 for $SO_4^{-2}.NH_2O$ is found to be very close (within 5%) to the experimental result (-11.27 eV). Again an very good agreement between theory and experiment

indicating the efficacy of the Eq. 4.25. The bulk solvation energy is also calculated (-14.95 eV) for sulphate anion based on the Born model (Eq.4.1), and is found to be largely overestimated (32%) the experimental one. The possible break down of born theory is due to the fact that it has been derived based on continuum theory wherein microscopic details are not included. However, if solute-solvent and solvent-solvent motions are strongly correlated, the continuum theory breaks down. Whereas the success of our theory is due to the fact that the microscopic details are included through the system dependent parameters, M_i^1 and M_i^2. Near identical results of dielectric constant for water calculated based on analytical expressions (Eq. 4.31 and Eq. 4.32) also support (Fig. 4.4) the linear theory of dielectric constant.

Chapter 5

Proton transfer energetics in nanoconfinement

5.1 Introduction

Water molecules confined within the pores of nanoscale dimension facilitate mass and ion transport in biological and geological processes [250]. This type of water framework, commonly known as nanoconfined water plays a vital role in many technologically important applications such as nano-fluidic devices, fuel cells *etc* [251-253]. Water molecules in these confined nanopores portray entirely different behavior compared to the bulk water [253]. The geometric constraint offered by the confinement medium along with the diverse nature of water-medium interaction can have significant effect on various physical and chemical phenomena such as phase transition, diffusion properties and proton transfer (PT) [254-256]. Accordingly, there have been several studies on water confined in various types of nanopores to understand the effect of the confinement medium on the static and dynamical properties water. Among the various nanoporous materials structures [254], primarily the carbon nanotubes (CNTs) have been investigated [145, 162, 252, 257-265] because CNTs are one of the most promising candidates for technologically important applications in different areas [266], such as desalination [267], isotope separation [258], energy storage devices and flow sensors [268]. The hydrophobic interior of a sub-nanometer diameter CNTs provides an ideal nano-channel that allows the water to attain structures those are similar to water present in biological systems [133, 260, 269]. Investigation on water in CNTs indicate that the water molecules undergo molecular ordering to form 1D linear chain configuration or 2D ladder like structures in narrow nanotube (diameter less than ~10 Å) depending on the diameter of the nanotube [145, 165], In wider nanotubes, stacked-ring structures are formed with a linear chain of water molecule present at the center of the nanotube [146, 150, 165].

In general, a reduction in the number of hydrogen bonds of confined water molecule is observed [145, 146, 152] and the restricted coordination of water molecule inhibits the solvation of proton and cause the proton transfer (PT) mechanism inside CNTs to be different from bulk water. In case of such narrow nanotubes, PT is in general, facilitated by a favorable pre-alignment of water molecules whereas in bulk liquid, water solvent reorganization is required prior to PT [265]. It has been reported that the proton mobility can be remarkably enhanced by a factor 40 in CNT as compared to the bulk water [270, 271]. Cao and co-workers have shown that the PT in water confined CNTs takes place through Zundel-Zundel mechanism [272] instead of Eigen-Zundel-Eigen mechanism that is being followed in a normal Grotthus mechanism in bulk water [273, 274]. The Eigen cation ($O_4H_9^+$) is a hydronium ion (H_3O^+) symmetrically being co-ordinated by three water molecules whereas, the Zundel cation ($O_2H_5^+$) is the symmetric protonated water dimer. In addition, the study of PT in smooth hydrophobic cylindrical channels indicate that the dimension of the nanochannel also play a crucial role in the PT process and other static and dynamic properties of the confined water molecules [275, 276].

Although there have been a few studies on the proton transfer dynamics in water, a clear understanding on the role of CNT-water interaction and the diameter of CNT is lacking. In addition, the PT process has not been thoroughly explored for other nanotubes. Further, first principle based report dealing with the effect of different degrees of confinement on the structure of protonated water in a generalized way is also very scarce in the literature. It is worthwhile to mention that boron nitride nanotubes (BNNTs), which are structural analogues of CNTs (alternative carbon atoms of CNT are substituted by boron and nitrogen atom), possess wider band gap, greater thermal stability, more resistant to oxidation and enhanced hydrogen storage capability in comparison to the carbon structure counterpart [277-279]. There are also reports

which show the selective ion transport characteristics of BNNTs [280-282]. These exciting properties and their unique morphology have motivated researchers to explore the possibility of using BNNTs in nano medicine [283, 284], water purification [280, 285] and as gas sensors [286]. Studies on water confined in BNNT [143, 287, 288] also show superior water permeation properties of BNNTs as compared to CNTs [143, 287]. More interestingly, it has been observed that the inclusion of partial charges (obtained through a DFT calculation) in the molecular dynamics (MD) simulations can significantly enhance the wetting behavior and reduce the diffusion coefficient of confined water molecules in BNNT(5,5) [143]. It has also been reported that the surface polarity of the nano-channel modulates the water-channel interaction and plays a key role in altering the properties of the confined water molecules [289]. Therefore, further study at *ab initio* level on the nature of structure and energetics of protonated water systems is required for the molecular level understanding of nanotube based nanofluidic systems. Accordingly, in the present work, we have performed DFT based calculations to investigate the structure, vibrational spectra and proton transfer energetics (energy barrier) in Zundel cation (ZC), i.e. protonated water-dimer, under the confinement of single walled CNTs and BNNTs by varying the degree of confinement in a systematic manner. We have also considered a dissimilar system (ammonia and water) and investigated proton transfer energetics of this system under confinement. In what follows, we will systematically elucidate the confinement induced change in structure and proton transfer energetics in these prototypical systems.

5.2 Model and method

It is already discussed in the previous section that the PT process in many important physical, chemical and biological processes occurs in a nanoconfined environment. In the present work, carbon and boron nitride nanotubes have been used as model nanoconfinement media to

develop molecular understanding of this complex phenomenon. ZC is the most prevalent ion in the linear chain of protonated water cluster [290] and also observed in the structure of large protonated water clusters ($H^+(H_2O)_n$) [290, 291]. This ion has been extensively used as a model system to study the proton transfer process in water in several theoretical studies [292-294]. Based on these studies, we have selected this prototypical ion to investigate the structure and the energetics of PT process under the confinement of nanotubes. The equilibrium structure for the ZC is initially obtained in gas phase. Then the complexes comprising of ZC and nanotubes have been optimized to get the minimum energy structure of the Nanotube-ZC complexes. The structure of the nanotube framework is in general observed to be least affected during the course of optimization. The potential energy surface (PES) for the PT processes in ZC, both in the case of gas phase and under the confinement of nanotubes is constructed by scanning the proton at the center of the O-O axis of the two water molecules. The terminal atoms of the nanotubes are saturated with dangling hydrogen atoms to minimize the end effects. The variation in confinement length (or the degree of confinement) has been achieved by selecting nanotubes of different diameters and herein, we have considered the armchair CNTs and BNNTs ranging from the chirality (4,4) to (8,8) with the corresponding diameter of 5.7 to 11.2 Å.

All the calculations have been performed by employing density functional theory with B3LYP exchange-correlation hybrid functional as implemented in TURBOMOLE program [166]. The reliability of DFT calculations in describing the ZC and other hydrogen-bonded systems has been already tested with respect to other schemes such as MP2 and CCSD, through several studies [167, 295]. The correlation-consistent triple-zeta basis set augmented with diffuse basis functions (augCC-pvTZ) is used for ZC, whereas for the nanotube framework, simple contracted Gaussian basis sets (SVP or split valence with polarization) are used. Since in these

types of systems, dispersion interaction plays an important role, dispersion correction has been incorporated in all the calculations [168]. Since the size of the systems is considerably larger (with more than 200 atoms in some cases), the infra-red vibrational modes of the confined ZC have been calculated by freezing the coordinates of the nanotube framework (after geometry optimization) and following the NumForce module of the TURBOMOLE program.

5.3 Results & discussion

This chapter is organised in four sections. In the first section, we have discussed the structure and energetics of Zundel cation in gas phase. Then in the second and third section, the effect of CNT and BNNT on the PT process is discussed. In the last section, the PT energetics of ammonia-water system in CNT is discussed. In the end, the outcome of these studies has been summarized in a generalized way.

5.3.1 Structure and energetics of Zundel cation in gas phase

Before we discuss the effect of confinement due to nanotube on ZC, we first discuss the structure and energetics of proton transfer in isolated ZC. The optimization of the ZC in the gas phase leads to a centro-symmetric structure as shown in Figure 5.1(a), and it can be seen that the shared proton is located exactly at the center of the oxygen atoms of both water molecules at a distance of 1.2 Å from each oxygen atom. The O_1-H_p-O_2 angle is observed to be 174.4 degree, where O_1 and O_2 are the two oxygen atoms and H_p denotes the hydrogen atom at the center of the ZC. This nonlinear configuration reduces the overall symmetry of the cluster to C_2 point group. The important geometrical parameters of the optimized structure (Figure 5.1(a)) obtained in the present study along with other theoretical results are summarized in Table 5.1. It can be inferred from Table 5.1 that the results obtained with hybrid density functional, B3LYP with

dispersion correction in combination with a good basis set are in excellent agreement with high level methods like MP2 or CCSD [167, 295, 296]. The computed interaction energy of H_3O^+ with H_2O is -36.3 kcal/mol is close to the reported MP2 result of -34.2 kcal/mol [167] and indicates the presence of a strong hydrogen bonding between the proton with two water molecules in ZC.

The potential energy surface (PES) for the isolated ZC has been generated by calculating the energy of various structures obtained by displacing the proton in ZC from the center of the equilibrium geometry with an increment of 0.1Å along the O-O axis (as shown in Figure 5.1(a)). Herein, we define the barrier of PT process as the energy difference between the minimum and maximum point in the PES plot. The PES for the equilibrium O···O distance, 2.41Å is found to have a single minimum which indicates a barrier-free proton translocation at the equilibrium O-O distance [292]. However, this observation is only an idealized static picture and for the case of protonated water confined in nanotube, the O···O separation distance varies in the range of 2.52 -2.72 Å [297]. Thus, we have altered the O···O separation distance (R_{O-O}) to 2.7Å from its equilibrium distance of 2.41Å without changing any other parameters and generated the PES for the O···O separation distance of 2.7Å in an analogous manner to the equilibrium geometry case. The PES generated by varying the inter-oxygen distance is represented in Figure 5.1(b), and from this figure it is evident that the PES is strongly dependent on the inter-oxygen distance. For R_{O-O} = 2.7Å, the PES resembles a symmetrical double well with a calculated barrier height of 2.61 kcal/mol. It is quite evident that the PES is strongly dependent on the inter-oxygen distance and herein, we have mainly focused to illuminate the PT process occurring at an O-O distance of 2.7Å under confinement. It is worthwhile to mention that the PT process occurring at these non-equilibrium O-O distances is having great significance in biology as it is believed that the

enzyme controls the PT between two residues at a particular stage of its catalytic mechanism via small conformational changes leading to the change in inter-residue hetero-atomic distances containing oxygen/nitrogen along with proton [298].

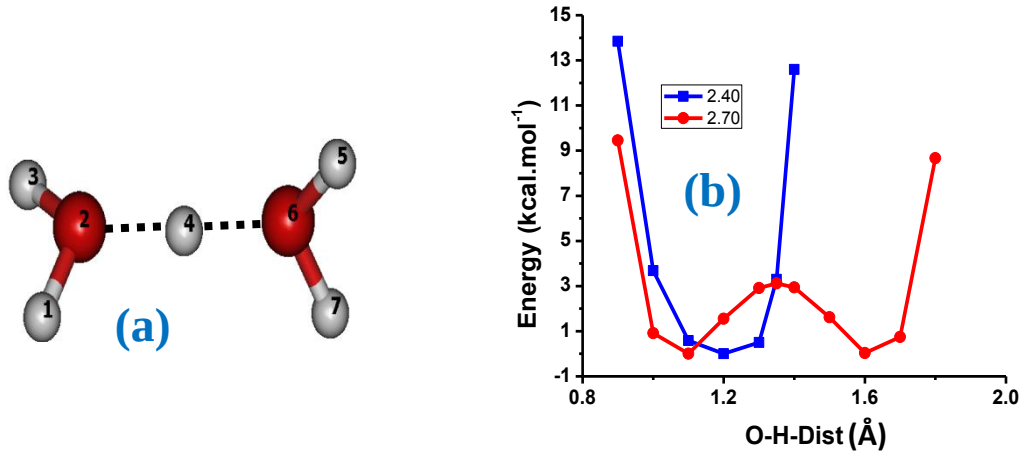

Figure 5.1: (a) The optimized structure of the isolated ZC and **(b)** PES of ZC at different inter-oxygen distance of ZC. The atoms shown in red colour are the oxygen atoms. The remaining atoms are the hydrogen atoms.

Table 5.1: Important structural parameters of the Zundel cation in gas phase. The numbers in the first row corresponds to the atoms as shown in Figure 5.1(a). Bond distances (R) are in Angstrom and bond angles (θ) are in degree.

Source	$\theta_{(1-2-3)}$	$R_{(1-2)}$	$\theta_{(2-4-6)}$	$R_{(2-4)}$	$R_{(2-6)}$	ΔE (kcal/mol)
Present study	109.96	0.970	174.41	1.204	2.406	-36.3
CCSD/DZP[a]	108.90	0.973	174.10			-36.3
MP2(FC)/QTZ[b]	109.06	0.968	173.70	1.197		

[a]Ref.[295] ; [b]Ref. [296]

5.3.2 Zundel cation in CNT

In the following sections, the effect of CNT on the structure and properties of ZC are separately discussed.

5.3.2.1 Structure and electronic properties of Zundel cation in CNT

The gas phase optimized structure of ZC has been kept inside CNT and the geometry of the entire CNT-ZC complex has been optimized by using DFT/B3LYP level of theory with dispersion correction. The degree of confinement is varied systematically by considering CNTs with diameter from 5.7Å to 11.2Å. The structures of the optimized CNT-ZC complexes are presented in Figure 5.2. The optimization of the geometry of ZC inside the narrow carbon nanotube, CNT(4,4) (diameter = 5.7Å) leads to an asymmetric structure with the central H^+ preferentially bonded to one of the water molecules. The O_1-H_p-O_2 angle is strikingly observed to be 178.04^0 with a minor increase in O-O distance as compared to the corresponding to the isolated ZC structure. The important structural and electronic properties such as O_1-H_p-O_2 angle, O-H bond distance and natural atomic charges on oxygen and hydrogen atoms of the optimized ZC under the confinement of CNTs are presented in Table 5.2 and 5.3. A very close look at the structural parameters of the individual water molecules confined under CNT(4,4), it can be observed that the O-H bond length of one water molecule is slightly elongated as compared to the other water molecule. This can be ascribed to the intermolecular hydrogen bonding interaction with the π-cloud of CNT [163, 177, 178]. In order to get more insights, we have also analyzed the radial distance distribution profile of individual atoms of ZC from the inner surface of carbon nanotube and the closest distance values are presented in Table 5.4. As expected, the hydrogen atoms of the elongated O-H bonds are relatively closer to the wall of the CNT. Interestingly, the water molecule involved in pronounced H-π interaction has greater affinity for

the central proton in comparison to the other. It is worthwhile to mention that such type of H-π interaction between water and aromatic hydrocarbons exists even at high temperatures and pressure [299].

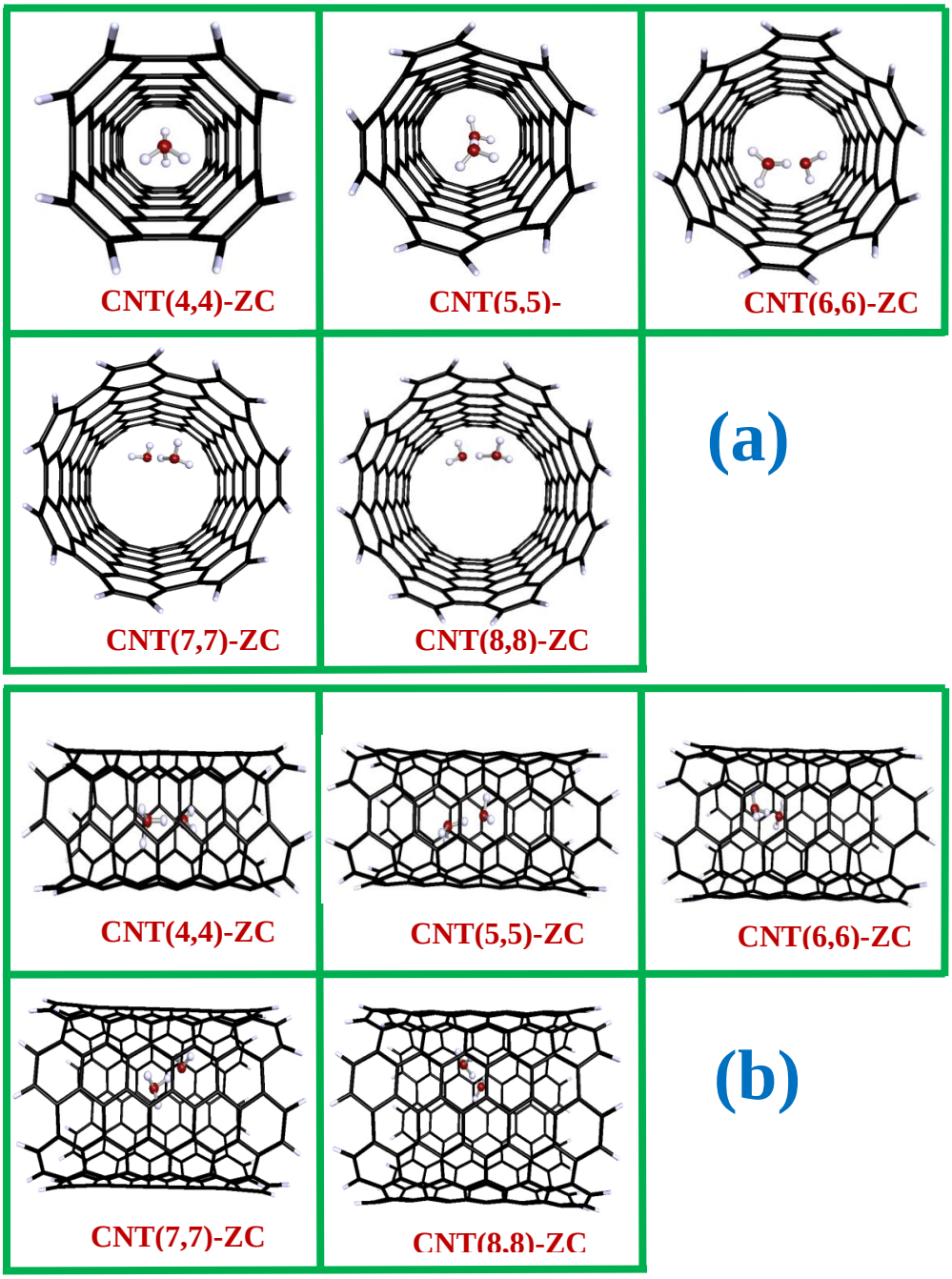

Figure 5.2: (**a**) The radial view and (**b**) the axial view of the optimized structures of CNT(X,X)-Zundel cation complex, where X varies from 4 to 8.

Table 5.2: Important geometrical parameters of the optimized Zundel cation in CNT. Bond distances (R) are in Angstrom and bond angles (θ) are in degree. Refer Figure 5.1(a) for the numbers used in the specification of the parameters.

Conf. medium	$\theta_{(1-2-3)}$	$R_{(1-2)}$	$R_{(2-3)}$	$\theta_{(2-4-6)}$ ($O-H_p-O$)	$R_{(2-4)}$ ($O-H_p$)	$R_{(4-6)}$ (H_p-O)	$R_{(2-6)}$ (O-O)	$\theta_{(5-6-7)}$	$R_{(5-6)}$	$R_{(6-7)}$
CNT(4,4)	105.79	0.981	0.983	178.04	1.082	1.346	2.428	110.56	0.963	0.963
CNT(5,5)	106.56	0.983	0.984	179.93	1.122	1.308	2.430	107.08	0.972	0.974
CNT(6,6)	106.49	0.977	0.987	179.47	1.132	1.300	2.432	105.73	0.973	0.977
CNT(7,7)	105.51	0.975	0.985	179.07	1.146	1.290	2.435	105.39	0.972	0.976
CNT(8,8)	105.03	0.974	0.987	178.97	1.152	1.271	2.423	106.16	0.968	0.983

Table 5.3: Natural atomic charges on oxygen and hydrogen atoms of the Zundel cation in gas phase and under confinement of CNT. In the last column, the net charge transfer from CNT surface to Zundel cation is listed.

System	**Natural Atomic Charge (a.u)**							
	H_1	O_2	H_3	H_4	H_5	O_6	H_7	Net Charge Transfer
Isolated ZC	0.54	-0.85	0.54	0.52	0.54	-0.85	0.54	--
ZC@CNT(4,4)	0.56	-1.09	0.56	0.65	0.58	-1.23	0.59	0.40
ZC@CNT(5,5)	0.54	-0.87	0.54	0.50	0.52	-0.91	0.52	0.15
ZC@CNT(6,6)	0.54	-0.83	0.54	0.51	0.52	-0.87	0.52	0.07
ZC@CNT(7,7)	0.54	-0.82	0.54	0.51	0.52	-0.86	0.52	0.05
ZC@CNT(8,8)	0.53	-0.82	0.54	0.51	0.52	-0.87	0.53	0.06

The preferential attachment of the central proton to one of the water molecules introduces asymmetry in its structure. As expected, the hydrogen atoms of the elongated O-H bonds are relatively closer to the wall of the CNT. Interestingly, the water molecule involved in pronounced H-π interaction has greater affinity for the central proton in comparison to the other.

The preferential attachment of the central proton to one of the water molecules introduces asymmetry in its structure. It is important to note that the simultaneous formation of H-π bonds with both the water molecules is energetically less feasible in such cases. This will become clearer while discussing the interaction energy in the next section.

Table 5.4: Closest distance between the individual atoms of ZC and carbon atom of CNT.

System	Minimum distance from the nearest carbon atom of CNT (Å)						
	H_1	O_2	H_3	H_4	H_5	O_6	H_7
ZC@CNT(4,4)	1.85	2.81	1.85	2.76	1.99	2.80	2.00
ZC@CNT(5,5)	2.24	3.06	2.19	3.27	2.53	3.18	2.33
ZC@CNT(6,6)	2.45	3.01	2.08	3.49	2.58	3.13	2.24
ZC@CNT(7,7)	2.54	3.03	2.12	3.24	2.67	3.12	2.31
ZC@CNT(8,8)	2.59	3.02	2.13	3.18	2.96	3.06	2.14

Let us now move to the case of CNT(5,5) and other larger diameter nanotubes up to CNT(8,8). The optimization of the ZC inside the CNT(5,5) nanotube led to an asymmetric structure similar to that of CNT(4,4) but the O_1-H_p-O_2 angle in this case is increased further to 179.6^0 and the geometry becomes almost linear. This increase in O_1-H_p-O_2 angle has been observed for ZC inside all other larger diameter CNTs. However, beyond CNT(5,5), the O_1-H_p-O_2 angle starts decreasing marginally and the variation of this angle as a function of the confinement length is represented in Figure 5.3. The horizontal line in Figure 5.3 indicates the O_1-H_p-O_2 angle of the isolated ZC and it is evident that as the degree of confinement is relaxed (*i.e.* the diameter of the tube is increased), the O_1-H_p-O_2 angle gets saturated with the value of 178.97 for CNT(8,8). It may be noted that although the CNT(8,8) diameter (11.2 Å) is

sufficiently larger than the ZC, the O_1-H_p-O_2 angle is substantially different from the original gas phase structure. As it can be seen from Table 5.2, the structural parameters of the optimized ZC confined under larger diameter tubes, from CNT(6,6) to CNT(8,8) are very much similar to that of CNT(5,5). It may also be noted that the inter-oxygen distance of the ZC under the confinement is always observed to be larger (Table 5.2) than its gas phase value. This indicates a reduction in hydrogen bond strength between hydronium ion and neutral water molecule which is due to the result of the interaction of CNT with the ZC.

Another important observation is the stabilization of the ZC near the wall of nanotube irrespective of the diameter of the CNT. As illustrated in Figure 5.2(a), this effect is clearly noticeable for larger diameter CNTs. This can be considered as the consequence of enhanced H-π interaction as discussed earlier. As a result, the hydrogen atoms of the ZC preferentially orient towards the π-cloud of the CNT wall, and a suitable rearrangement of the rest of the cluster occurs to minimize the total energy of the system. In a very narrow CNT, the ZC feels the effect of the CNT surface relatively to a similar extent in all directions. On the other hand, in a larger diameter nanotube, the H-π interaction drives the whole ZC from the center of the CNT towards the inner surface of the CNT and hence the ZC is located close to the inner surface of CNT and not at the center of the nanotube.

These findings evidently agree with the first principles based molecular dynamics study of Cicero *et al*. performed on water confined in the CNT and graphene sheets [138]. According to their study, the microscopic structure and thickness of the thin layer of water formed at the interface are independent of the diameter of the nanotubes as the perturbation induced by the confining media is extremely localized at the interface. These observations, namely the ZC being stabilized near the wall and a significant modification in the structure of the ZC can have a great

impact in devising structures related to nano-fluidic applications using CNT as the transport medium.

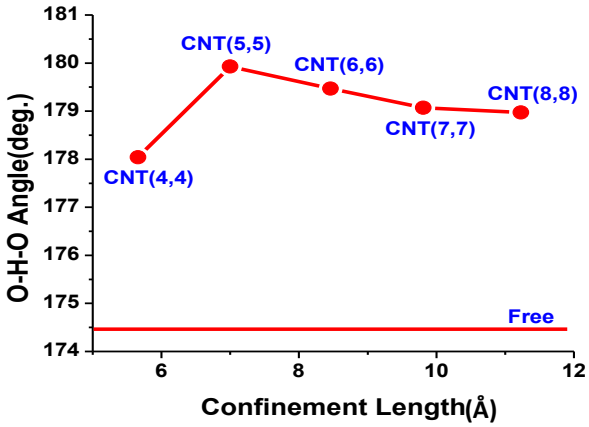

Figure 5.3: The variation of O_1-Hp-O_2 angle in Zundel cation as a function of confinement length (or the diameter of CNT).

5.3.2.2 Infra-red vibrational frequency spectrum of Zundel cation in CNTs

The infrared absorption spectral signatures of hydrated protons in water clusters of size ranging from 2 to 11, have recently been studied by experimental [291, 300-306] and theoretical groups [256, 303, 307-312]. These studies have primarily shown that four fundamental frequencies are important, *viz.*, O-H symmetric and asymmetric stretching, bending as well as the central proton oscillation frequencies (POF). The frequency corresponds to POF in the range of 1000 cm^{-1} and the O-H stretching frequencies are observed to be near 3700 cm^{-1}. Regarding the applicability of B3LYP level of theory in obtaining the infra-red spectrum of protonated water dimer in the gas phase, Fridgen *et. al.* [303] have shown that the DFT results are found to have a fairly good agreement with the experimental results. For the case of free ZC, the POF occurs at two well defined absorption regions i.e. near 900 and 1400 cm^{-1} which have been shown to arise from the coupling of low frequency motions of the two water molecules to the central proton motion along (in-plane) and out-of-plane or perpendicular to the O-O axis respectively [311].

Our frequency analysis reveals that the POF in-plane frequencies are observed to be increased under confinement, particularly for the case of CNT(4,4) which is significantly blue shifted to 1990 cm^{-1} from the vacuum value which is close to 900 cm^{-1}. On the other hand, the POF out-of-plane frequency values are found to initially decrease from 1390 to 1310 cm^{-1} with confinement length and thereafter it saturates at 1460 cm^{-1}. Since the decrease in POF is not very obvious with the degree of confinement, we have analyzed the first order gradient of POF with respect to confinement length (R) to find out which of the nanotubes is having least effect on the vibrational properties or the force constants of ZC. The corresponding plot is presented in Figure 5.4. As shown in the Figure 5.4, the minimum value of the gradient of POF is observed for CNT(6,6) and the variation is shown to be strongly linear in nature. It may also be noted that there are two regimes of POF with respect to the degree of confinement. Accordingly, we have proposed the confinement length dependence frequency relations for these regimes as given in equation 5.1 and 5.2.

$$d\gamma/dR = C_1 + k_1 * (R_0 - R) \qquad (5.1)$$

$$d\gamma/dR = C_2 + k_2 * (R - R_0) \qquad (5.2)$$

where, γ and R are the POF and confinement length, respectively.

At $R = R_0$, from Figure 5.4, the value of C_1 and C_2 is found to be -58.7.

The values for k_1 and k_2 can be obtained by following the best fitting method. The calculated values of k1 and k2 are -15.0 and 11.8, respectively and hence, the above two equations can be generalized to evaluate the POF for any values of confinement by integrating the corresponding expression.

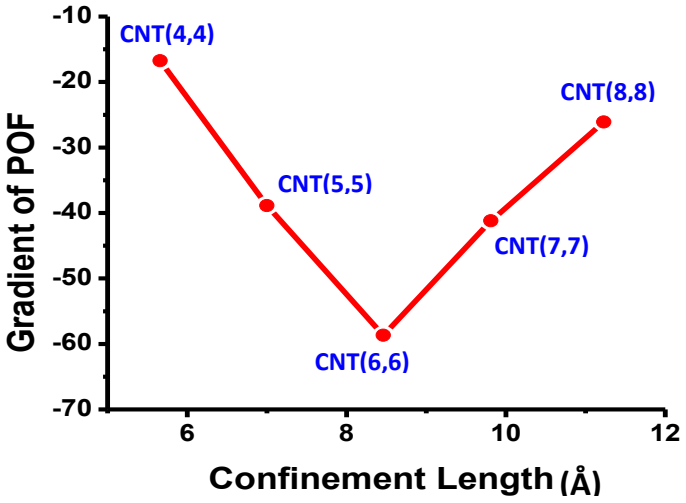

Figure 5.4: Gradient of proton oscillation frequency (POF) of Zundel cation under the confinement of CNT.

5.3.2.3 CNT-ZC interaction & stability of Zundel cation in CNT

Let us now discuss about the interaction energy and stability of the ZC under confinement. The interaction energy (ΔE) of the ZC has been calculated by subtracting the energies of individual entities from the CNT- ZC complex as shown in Equation 5.3.

$$\Delta E_{(ZC)} = E_{(CNT\text{-}ZC)} - [E_{(CNT)} + E_{(ZC)}] \qquad (5.3)$$

where $E_{(CNT\text{-}ZC)}$, $E_{(CNT)}$ and $E_{(ZC)}$ represent the energies of CNT(X,X)-ZC complexes, CNT(X,X) and ZC respectively, with X,X denoting the chiral vector (n,m) of CNT which varies here from 4,4 to 8,8. In addition to this, the interaction energy values for H_3O^+ and H_2O are also calculated independently by optimizing these two entities inside CNTs by following a relation similar to Equation 5.3. These interaction energy values are presented in Table 5.5. The negative value of the interaction energy in all the cases clearly indicates that all the systems including the

ZC can be encapsulated inside these CNTs in a favorable manner. It is imperative to note from Table 5.5 that stabilization of the hydronium ion appears to be the strongest as compared to the two other complexes (water and ZC). The interaction energy of hydronium ion sharply decreases (by 10%) as the diameter of CNT increases from 7 Å to 8.5 Å and thereafter, as the diameter of CNT is increased from 8.5 Å to 11.2 Å, the change is observed to be marginal. Similarly, in the case of neutral water molecule, the interaction energy is observed to be strikingly more pronounced for CNT(5,5) by 50% as compared to CNT(8,8). The overall interaction energy of the hydronium ion and the ZC is higher than that of the water molecule, indicating higher affinity towards filling the CNT than neutral water, which is obviously due to the enhanced charge induced interaction with the CNT wall.

In general, the lowest value of interaction energy for CNT(4,4) suggests that the complexes are least stabilized inside CNTs whose diameter is ≤ 5.7 Å irrespective of the charged or neutral nature of the species due to the strong geometrical constraints by the nanotube inner walls. It has also been observed earlier [313] that if the water molecule is confined in between two hydrophobic model systems separated by a very small distance ~4 Å, the water molecule undergoes severe geometrical distortion and is eventually dissociated into proton and hydroxyl ions. Our results also reveal a wide variation in the interaction energy values for the CNT-ZC complex which is in the range of -39.64 to -65.45 kcal/mol for different nanotubes. For the case of CNT(5,5), the ΔE value increases significantly and it is found to be the strongest interacting system. The ΔE value is found to decrease in a systematic manner as we decrease the degree of confinement beyond CNT(5,5). From the interaction energy trend, it can be concluded that there is an optimum confinement length for which the stabilization of ZC is maximum, and as the degree of confinement is further decreased, the interaction is reduced quite significantly which

finally saturates at a value close to -51.0 kcal/mol. The maximum interaction observed in the case of CNT(5,5) (diameter = 7.0 Å) can be rationalized in terms of the inherent nanoscale curvature in the individual six membered ring. This is well supported by the earlier studies performed on model systems which demonstrated that the interaction energy increases quadratically as a function of curvature of the system [314-316]. It has also been observed that the curvature and confinement effects play an important role and decide the nature of the structure as well as stability of the species confined within it.

Table 5.5: Interaction energy of hydronium ion (PW), water molecule (W), Zundel cation(ZC) with CNT and hydrogen bond energy of Zundel cation ($HB_{(Conf)}$) under the confinement of CNTs. All the values are in kcal/mol.

Confining medium	$\Delta E_{(PW)}$	$\Delta E_{(W)}$	$\Delta E_{(ZC)}$	$HB_{(Conf)}$
None	--	--	--	-36.3
CNT(4,4)	-59.98	-3.31	-39.64	-12.67
CNT(5,5)	-62.21	-16.60	-65.45	-22.96
CNT(6,6)	-57.10	-11.06	-57.80	-25.96
CNT(7,7)	-55.08	-9.00	-52.88	-25.12
CNT(8,8)	-54.43	-8.02	-50.91	-24.78

It may be noted that the value of curvature increases as we increase the degree of confinement of the nanotube and hence, the optimum confinement length and curvature are crucial in attaining the maximum stability of the system. A similar trend in interaction energy values has been observed in an analogous study by Hirunsit and Balbuena [317] who considered the confinement effect by modeling two parallel naphthalene rings. It may be noted these results completely neglect the effect of curvature of the nanotubes which however has recently been

established to be a crucial factor in determining the interaction energies [313, 314, 318, 319]. It may be noted that the value of curvature increases as we increase the degree of confinement of the nanotube and hence, the optimum confinement length and curvature are crucial in attaining the maximum stability of the system.

5.3.2.4 Hydrogen bond energy of Zundel cation in CNT

It is known that there is a strong hydrogen bonding between hydronium ion and water molecule and the value of this hydrogen bond energy is -36.3 kcal/mol in gas phase. As we discussed in the earlier section, the interaction energy of ZC under confinement varies between –39.6 to -65.5 kcal/mol. Thus, the modification in hydrogen bonding between the hydronium ion and the water molecule due to the confinement of CNTs will significantly affect the overall interaction energy of CNT(X,X)- ZC complex. We have used an approximate relation as given in Equation 5.4 to define the extent of hydrogen bonding under the confinement of CNTs ($HB_{(Conf)}$) and the corresponding values are presented in Table 5.5.

$$HB_{(Conf)} = E_{(CNT\text{-}ZC)} - E_{(CNT\text{-}PW)} - E_{(CNT\text{-}W)} + E_{CNT} \qquad (5.4)$$

As shown in Table 5.5, the hydrogen bond energy for the ZC decreases from -36.3 to -12.7 kcal/mol, corresponding to isolated ZC and under confinement in CNT(4,4), respectively. As the degree of confinement decreases, the hydrogen bonding energy is found to increase sharply by ~30%. The decrease in the energy is mainly due to the enhanced stabilization of individual components, hydronium ion in particular, inside the CNT, thereby affecting the effective interaction between the individual ions. However, for the case of CNT(6,6), hydrogen bond stabilization energy is significantly higher than that of the narrowest tube, CNT(4,4) mainly because of the effective interaction of ZC with two opposite surfaces of CNT(6,6). This also

means that the individual components are not severely modified or affected inside CNT(6,6), leading to the formation of a more symmetric ZC in comparison to other CNTs. For other larger nanotubes, the ZC is observed to interact with only one surface, and the HB_{conf} energy difference between CNT(66) and other larger diameter CNTs is found to be of the order of ~1kcal/mol. Hence, it can be inferred that CNT(6,6) may be the suitable stabilizing nanotube for the ZC.

The trend in the hydrogen bond energy primarily indicates that the role played by the local environment of the ZC is very remarkable. In principle, the nanotube being an electron rich center can effectively interact with the ZC through charge transfer and hence, the net charge transfer can describe the effect of the confinement due to nanotubes on the stability of ZC as well as its HB strength. Accordingly, we have rationalized the HB strength through two parameters, *viz.*, (i) the radial distance between the proton or hydronium ion and inner surface of the nanotube wall and (ii) net charge transfer from the nanotube to ZC.

Let us first discuss the radial distance profile for the center proton with respect to the carbon atom of the nanotubes. It may be noted that the shorter distance between any two atoms can directly be correlated with stronger interaction while the weaker interaction can be related with longer distances. The shortest distances between the carbon atom of CNT and center proton are reported in Table 5.4 and these results reveal that the center proton is found to be very close to the carbon atom of CNT(4,4) which may effectively destabilize the ZC by reducing the hydrogen bond strength. However, for the case of CNT(6,6), the distance is found to be the highest among the nanotubes studied here. This radial distance profile correlates very well with the calculated hydrogen bond energies, -12.68 and -25.96 kcal/mol respectively, for the CNT(4,4) and CNT(6,6) cases.

The shortest distance between carbon of CNT and center proton of ZC can also lead to an effective charge transfer from CNT to proton and hence, the effective charge of the ZC complex can significantly be modified. In view of this, we analyzed the net charge transfer from CNT to ZC through the natural population analysis method. As shown in Table 5.3, the charge transfer is observed to be maximum for CNT(4,4) and saturate at CNT(6,6). More interestingly, it can be seen from Figure 5.5, that there is an inverse correlation between the charge transfer and the hydrogen bond energy. Hence, it can be mentioned that any surface modifications by electron donors or acceptor groups can effectively tune the stability of the ZC which can have significant impact on the proton transfer rates. In parallel to our observations, Mann and Halls have reported that the stability of the protonated water clusters confined inside CNT relative to the gas phase is enhanced which was ascribed due to the high polarizability of the carbon nanotube. In addition to the net charge transfer, the change in the structure of the ZC due to the confinement can also compete in modifying the hydrogen bond strength, which can be referred to as structural deformation energy. In order to quantify the deformation energy, the optimized ZC obtained inside CNTs are taken out of the nanotubes and the single point energy calculation is carried out on these clusters. The difference between the energy of the isolated and confined geometries has been considered as the structural deformation energy. It can be noted that the maximum deformation energy is observed to be 2.08 kcal/mol for CNT(4,4) and interestingly, the minimum deformation energy with 40% lesser than CNT(4,4) is observed for the case of CNT(6,6).

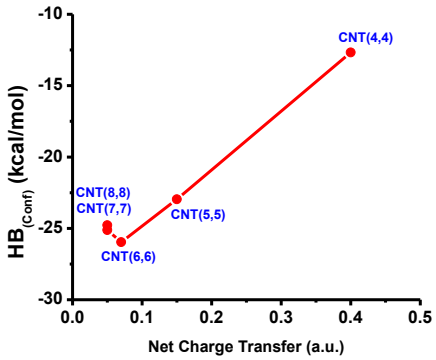

Figure 5.5: Hydrogen bond strength ($HB_{(Conf)}$) in Zundel cation under the confinement of CNTs as a function of net charge transfer from CNT surface.

As we have already discussed, the ZC is in general, stabilized closer to the inner surface of the nanotube than at the center of the nanotube. Hence, even if the nanotube is widened further, there will be certain deformation in the structure of the complex. The minimum deformation energy implies the stronger hydrogen bonding within the ZC under confinement. The present analysis lucidly suggests that the hydrogen bond strength or the interaction between water and hydronium ion is significantly reduced in a very highly confined environment as exhibited by CNT(4,4) or CNT(5,5). In addition, these results also demonstrate that the hydrogen bond energy is maximum for the case of CNT(6,6) which is attributed to the minimum deformation and less charge transfer between the nanotube and ZC.

5.3.2.5 Energy barrier for proton transfer in Zundel cation in CNT

Let us now move to the energetics or energy barriers for the PT process under confinement. The PES for the PT in the ZC under the confinement of CNTs is constructed in a way similar to the case of isolated/gas phase by scanning the central proton along the O-O axis and it is represented in Figure 5.6 as a function of the degree of confinement. As it can be seen

from Figure 5.6, the barrier for PT from H_3O^+ to the other water molecule under highly confined space of CNT(4,4) is quite large (7.71 kcal/mol) and as we move to a next higher diameter nanotube CNT(5,5), the barrier is sharply reduced to 4.79 kcal/mol. It is evident that as the degree of confinement is decreased, the barrier height is reduced and the reduction in the barrier height is found to be very marginal among the higher nanotubes. For instance, the barrier height difference between CNT(7,7) and CNT(8,8) is only 0.15 kcal/mol, which is far less than the thermal energy, and further increase in the diameter appears to have insignificant effect on the energy barrier. It is interesting to note that the barrier height, although reduced upon decreasing the degree of confinement, is always higher than that of gas-phase ZC. This is arising due to the fact that the hydronium ion is attracted to the nanotube walls in a preferential manner at the CNT interface. This scenario is different from the isolated ZC and the difference in energy barrier between the widest nanotube and the isolated case is ~1 kcal/mol, which can primarily be attributed to the interaction between the nanotube wall and the ZC. In one of the recent studies by Hirunsit and Balbuena, the calculated barrier heights for the model systems reveal that the barrier height is reduced upon increase in confinement length up to 14.5 Å, beyond which, the barrier height is increased very marginally. In their study, CNT has been modeled by the aromatic planar molecules, *viz.*, two benzene or naphthalene molecules arranged in a parallel manner and the structure of the ZC is placed at the center of these aromatic molecules. It is also noted that the barrier height obtained from these model systems is little overestimated as compared to the present results. Nevertheless, the trend remains unaltered and our results quantify the important role played by the channel wall in determining the structure of the ZC and hence, the proton transfer.

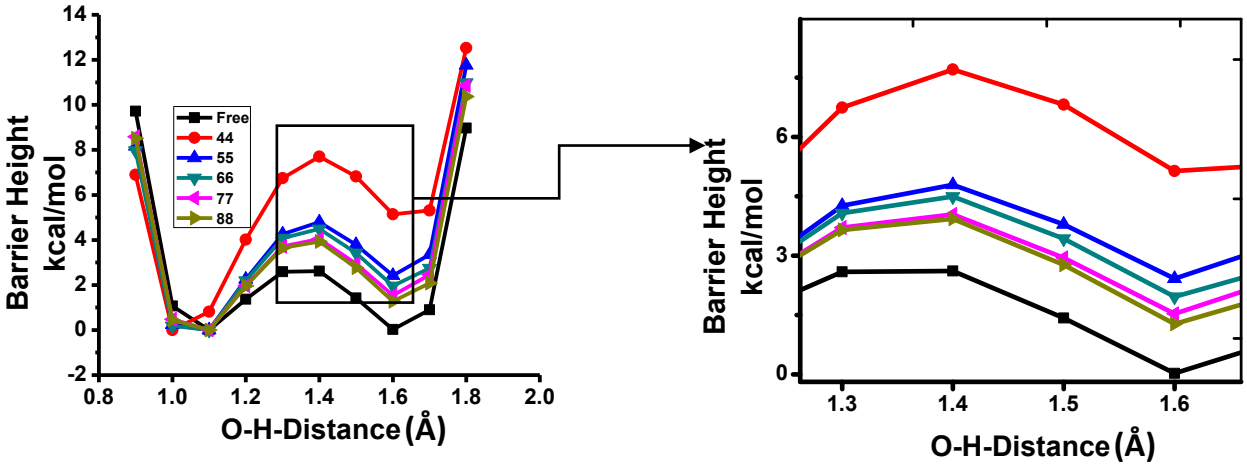

Figure 5.6: PES for PT process in Zundel cation as a function of O-H distance for free and confined cases.

5.3.3 Zundel cation under the confinement of BNNT

Let us now move to BNNT and find out the effect of this highly polarizable confinement medium on the structure and proton transfer energetics of Zundel cation.

5.3.3.1 Structure and stability of ZC under the confinement of BNNTs

The optimized structures of the BNNT-ZC complex by employing DFT/B3LYP method are presented in Figure 5.7. The important structural parameters and charges on oxygen and hydrogen atoms of the optimized ZC under the confinement of BNNTs are presented in Table 5.6 and 5.7. The optimization of the geometry of ZC in BNNT(4,4) leads to a distorted asymmetric ZC similar to CNT(4,4). However, a more symmetric structure of ZC is formed in BNNT(5,5) with values of O_1-H_p, H_p-O_2 and $O_1\cdots O_2$ distance close to the corresponding values of the isolated ZC. Strikingly, the O_1-H_p-O_2 angle increases to 179.7^0 and the geometry of the ZC becomes almost linear. As shown in Figure 5.7, the spatial confinement provided by this nanotube favors such a configuration for the BNNT-ZC complex that allows the two water molecules of ZC to effectively interact with exactly opposite surfaces of BNNT through $H_{water}\cdots N_{BNNT}$ hydrogen bonding.

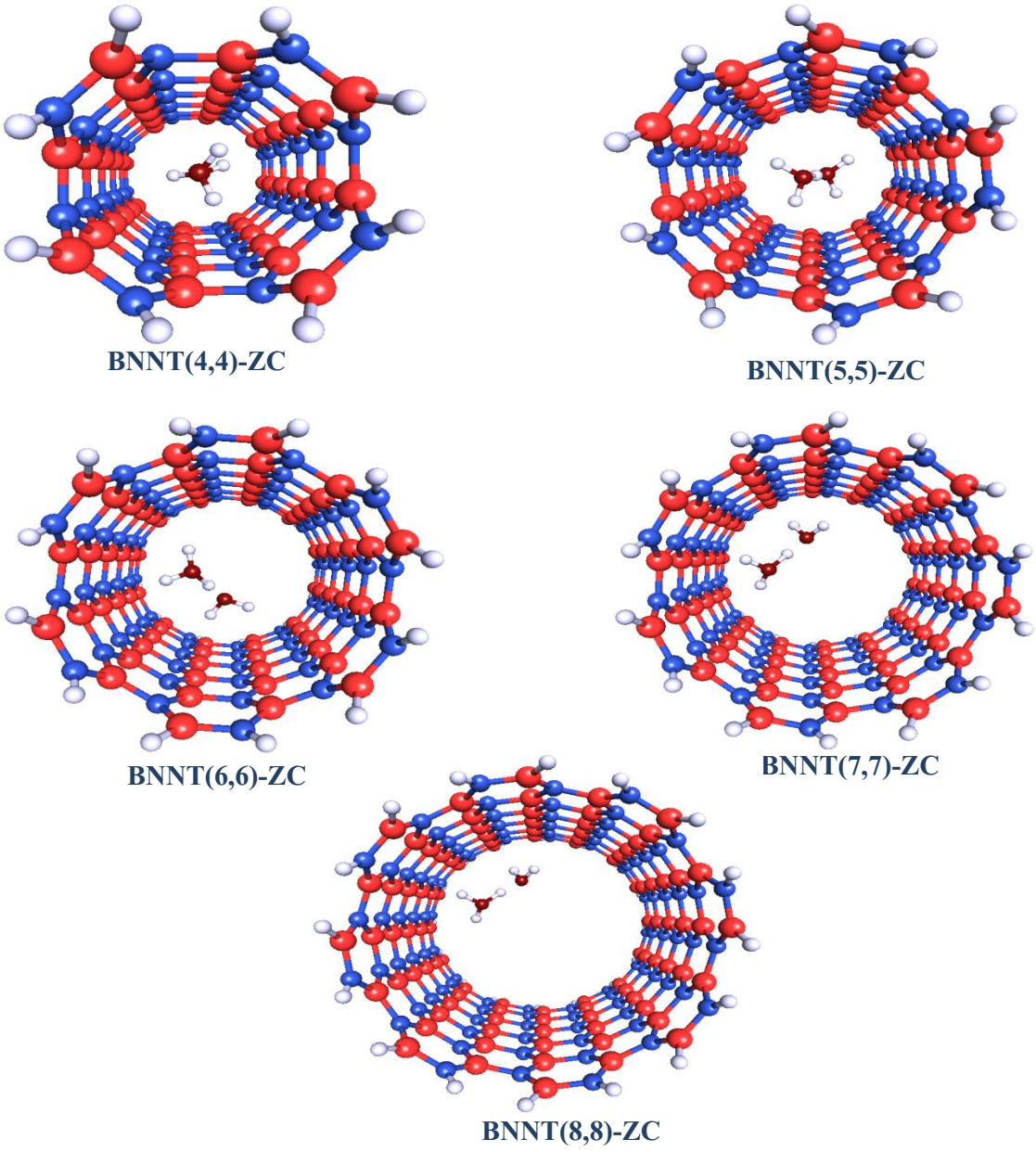

Figure 5.7: Radial view of the optimized structures of BNNT- ZC complexes.

Table 5.6: Important geometrical parameters of the optimized ZC under the confinement of BNNTs. Bond distances (R) are in angstrom and bond angles (θ) are in degree. Refer Figure 5.1(a) for the numbers used in the specification of the parameters.

Confining medium	$R_{(1-2)}$	$\theta_{(1-2-3)}$	$R_{(2-3)}$	$R_{(2-4)}$ ($O-H_p$)	$\theta_{(2-4-6)}$ ($O-H_p-O$)	$R_{(4-6)}$ (H_p-O)	$R_{(2-6)}$ (O-O)	$R_{(5-6)}$	$\theta_{(5-6-7)}$	$R_{(6-7)}$
BNNT(4,4)	0.97	109.7	0.98	1.12	173.3	1.29	2.40	0.97	112.0	0.97
BNNT(5,5)	0.98	106.4	0.98	1.20	179.7	1.21	2.41	0.98	106.5	0.98
BNNT(6,6)	0.98	106.4	0.98	1.18	178.7	1.24	2.42	0.97	106.4	0.98
BNNT(7,7)	0.97	105.1	0.99	1.15	179.4	1.28	2.43	0.97	104.1	0.98
BNNT(8,8)	0.97	106.5	1.00	1.14	177.4	1.29	2.43	0.97	103.9	0.98
Isolated ZC	0.97	109.9	0.97	1.20	174.3	1.20	2.40	0.97	109.9	0.97

As we move to wider nanotubes i.e., from BNNT(6,6) to BNNT(8,8), the diameter of the nanotube becomes substantially larger than the length of ZC and hence, the simultaneous interaction of ZC with exactly opposite surfaces of BNNT is less feasible. It may be noted that both the water molecules in ZC reorients themselves such a way that they form hydrogen bond via $H_{water}\cdots N_{BNNT}$ to the same side of the BNNT surface. As a result, the ZC gets stabilized near the surface of BNNT rather than at the center of the BNNT (Figure 5.7). In these wider BNNTs, the O-H bond length of one water molecule is elongated from its original value of 0.97 Å (e.g., 1.0 Å in BNNT(8,8)) leading to the formation of a distorted ZC.

Table 5.7: Natural charges (in a.u.) on oxygen and hydrogen atoms of isolated ZC and under the confinement of BNNTs. In the last column, net electronic charge transfer from BNNT surface to ZC is listed.

Confining Medium	H_1	O_2	H_3	H_p	H_5	O_6	H_7	Total charge on ZC	Net electronic charge transfer from BNNT
Free	0.54	-0.85	0.54	0.52	0.54	-0.85	0.54	+1.0	0.00
BNNT(4,4)	0.55	-0.89	0.55	0.52	0.54	-0.92	0.54	+0.89	0.11
BNNT(5,5)	0.53	-0.84	0.53	0.50	0.53	-0.84	0.53	+0.95	0.05
BNNT(6,6)	0.54	-0.83	0.54	0.51	0.53	-0.85	0.53	+0.96	0.04
BNNT(7,7)	0.54	-0.82	0.54	0.51	0.53	-0.86	0.53	+0.96	0.04
BNNT(8,8)	0.53	-0.83	0.54	0.51	0.53	-0.86	0.53	+0.96	0.04

From the radial distance distribution profile presented in Table 5.8, it has been observed that the terminal hydrogen atoms of ZC are relatively closer to the nitrogen atom of BNNT as compared to the boron atom due to the formation of $H_{water}\cdots N_{BNNT}$ hydrogen bond. Moreover, the distance between the hydrogen of elongated O-H bonds and the nitrogen atoms of BNNT are relatively smaller to the non-elongated ones. It is interesting to note that the water molecule, which is involved in strong hydrogen bonding interaction has greater affinity for the central proton as compared to the other water molecule. The radial distance distribution profile in case of BNNT(5,5) indicates that the hydrogen atoms of both the water molecules maintain nearly same distance (2.31, 2.36 & 2.21, 2.29 **Å**) from the BNNT surface compared to other BNNTs.

Let us now discuss about the interaction energy (IE) and stability of the ZC under the confinement of BNNTs. The IE of the ZC has been calculated by subtracting the energies of BNNT and ZC from BNNT- ZC complex similar to the CNT case. In addition to this, the IE

values for hydronium ion (H_3O^+) and water are also calculated independently by optimizing these two entities inside BNNTs in a similar way.

Table 5.8: Distance of hydrogen and oxygen atom of ZC from the closest nitrogen and boron atom on BNNT.

Confining Medium	Distance from the nearest nitrogen atom of BNNT (Å)							Distance from the nearest boron atom of BNNT (Å)						
	H_1	O_2	H_3	H_4	H_5	O_6	H_7	H_1	O_2	H_3	H_4	H_5	O_6	H_7
BNNT(4,4)	2.07	2.81	2.02	2.83	2.08	2.84	2.01	2.01	2.71	2.06	2.78	2.01	2.77	2.10
BNNT(5,5)	2.30	3.18	2.28	3.42	2.35	3.18	2.22	2.50	3.05	2.43	3.37	2.52	3.06	2.34
BNNT(6,6)	2.61	3.10	2.15	3.44	2.61	3.17	2.21	2.52	3.00	2.29	3.43	2.59	3.12	2.40
BNNT(7,7)	2.55	2.99	2.02	3.23	2.51	3.04	2.19	2.74	2.92	2.25	3.35	2.71	3.05	2.45
BNNT(8,8)	2.82	2.91	1.92	3.09	2.54	3.03	2.23	2.88	2.95	2.22	3.24	2.66	2.95	2.46

The calculated IE values are presented in Table 5.9. The negative value of interaction energy for all the complexes suggests that water, hydronium ion and ZC can be encapsulated inside these BNNTs in an energetically favorable manner. It can be observed that the interaction energy of hydronium ion as well as ZC is more that than of neutral water molecule due to the enhanced dipole-charge induced interaction with the polar BNNT surface [278].

Table 5.9: Interaction energy (in kcal/mol) of Zundel cation (ZC), hydronium ion (PW) and water molecule (W) with BNNT.

Confining medium	$IE_{(ZC)}$	$IE_{(PW)}$	$IE_{(W)}$
BNNT(4,4)	-21.1	-37.4	-4.8
BNNT(5,5)	-47.9	-42.6	-16.0
BNNT(6,6)	-42.4	-39.1	-12.0
BNNT(7,7)	-39.3	-38.7	-10.2
BNNT(8,8)	-38.0	-38.5	-9.1

It is worth noting that the polar character of BNNT decreases with the increase in the BNNT diameter [320] and the maximum value of IE is expected for narrowest BNNT-ZC complex, i.e. in the present case BNNT(4,4). However, the highest value of IE is achieved with BNNT(5,5) irrespective of the charged or neutral nature of species. The variation of IE as a function of the degree of confinement (or the diameter of BNNT) is presented in Figure 5.8 and it is evident from this figure that regardless of the nature of the species, if the degree of confinement is very high as in the case of BNNT(4,4), the strong geometrical constraints offered by the nanotube inner walls is becoming the dominant factor in determining the structure and energetics of the confined species.

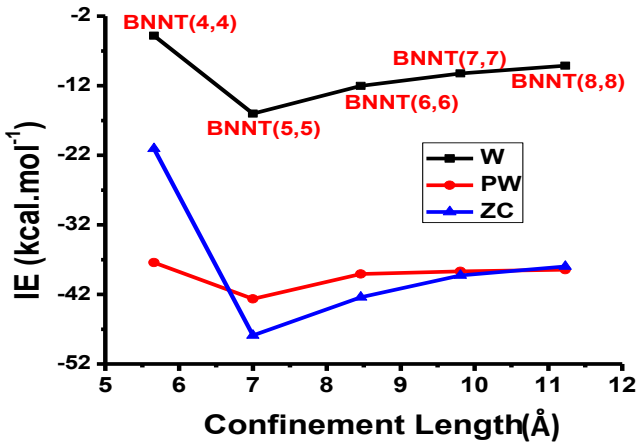

Figure 5.8: The variation of interaction energy of the confined species as a function of confinement length. (or the diameter of BNNT).

For the case of confined ZC, a pronounced increase (~130%) in the value of interaction energy is observed with increase in nanotube diameter from 5.7 to 7.0 Å. Thereafter, the interaction energy value starts decreasing with the increase in the diameter of BNNT. A sharp decrease (~12%) is observed for an increase in the diameter of BNNT from 7.0 to 8.5 Å. Thereafter, only a marginal decrease in interaction energy is observed with further increase in

diameter of BNNT, and it nearly saturates at BNNT(8,8). The highest value of interaction energy observed for BNNT(5,5) indicates that it is the most favorable interacting medium for the ZC.

On analyzing the net charge transfer from BNNT surface to ZC, as shown in Table 5.7, it is found that the charge transfer is substantially higher in case of BNNT(4,4) and as the tube diameter increases, it sharply decreases and saturates at BNNT(6,6). Based on the above discussions, it can be mentioned that the structural modification in ZC is small and the major contributors for the stabilization of ZC in BNNT are due to the effective interaction of ZC with the polarized BNNT through the formation of hydrogen bond and charge transfer. In a very recent theoretical study, Rimola and Sodupe have also observed that adsorption of polar molecule is favored over nonpolar molecules in smaller diameter BNNTs [320].

5.3.3.2 Effect of BNNT on the vibrational modes of ZC

The calculated vibrational absorption spectra for ZC confined in BNNTs and the isolated ZC case are presented in Figure 5.9.

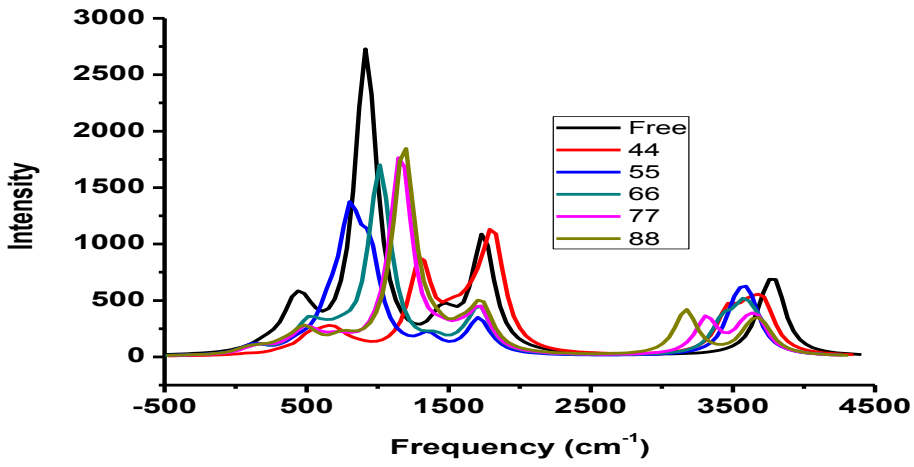

Figure 5.9: Infra-red vibrational absorption spectrum of ZC confined in BNNTs along with the isolated ZC.

The frequency analysis reveals that the in-plane POF depends heavily on the degree of confinement of BNNT and for the case of highly confined system *i.e.* BNNT(4,4), the in-plane POF is significantly blue shifted to 1300 cm^{-1} from its isolated value of 916 cm^{-1}. It can be mentioned that the blue shifting in BNNT(4,4) is less as compared to the CNT(4,4) case. As the degree of confinement is reduced, the in-plane POF decreases dramatically and attains the value of 803 cm^{-1} for the case of BNNT(5,5) and thereafter, the in-plane POF continuously increases up to BNNT(8,8). Since the in-plane POF is having a minimum for BNNT(5,5) (See Figure 5.10), the central proton connected to water can be mentioned to be more flexible in BNNT(5,5) than that of other nanotubes confined structures due to other BNNTs. In other words, it also means that the BNNT(5,5) provides the spatial confinement on ZC which requires lesser energy to break or form a bond between the central proton and water molecules than that of other confined structures due to other BNNTs.

The calculated symmetric and asymmetric stretching frequencies of water molecules in ZC are presented in Table 5.10. For the isolated ZC, the symmetric and asymmetric frequencies are observed close to 3600 and 3670 cm^{-1} respectively. Under the confinement of BNNT, in general, it is observed that the O-H stretching frequency of water molecule is red shifted due to its interaction with BNNT. In particular, the stretching frequency of one of the O-H bond of one water molecule in ZC is substantially reduced as compared to the other (except BNNT(5,5)). For example, in BNNT(4,4), the symmetric and asymmetric frequencies of one water molecule are 3354 and 3483 cm^{-1} whereas for the other, the values are 3540 and 3602 cm^{-1}. This can be attributed to the $H_{water}\cdots N_{BNNT}$ hydrogen bond formation with the magnitude of red shift in frequency proportional to the hydrogen bond strength. For example in BNNT(8,8), the stretching frequency corresponding to the elongated O-H bond (bond length ~ 1.0 Å) is strikingly observed

to be 3070 cm^{-1}. However in BNNT(5,5), the degree of red shifting in the O-H stretching frequency is similar in magnitude for both the water molecules and the observed frequency values are 3447, 3488, 3402 and 3519 cm^{-1}. Therefore it can be mentioned that both the water molecules form $H_{water}\cdots N_{BNNT}$ hydrogen bond to a similar extent in this nanotube. This correlates very well with the observed O-H bond elongation and the symmetric ZC structure in this nanotube.

Table 5.10: Symmetric and asymmetric stretching vibrational frequencies of ZC confined in BNNT.

System	Stretching Frequency of ZC (cm^{-1})	
	Symmetric	Asymmetric
Isolated ZC	3596, 3604	3680, 3670
ZC@BNNT(4,4)	3354, 3540	3483, 3602
ZC@BNNT(5,5)	3447, 3402	3488, 3519
ZC@BNNT(6,6)	3321, 3452	3498, 3580
ZC@BNNT(7,7)	3209, 3468	3553, 3564
ZC@BNNT(8,8)	3070, 3505	3607, 3570

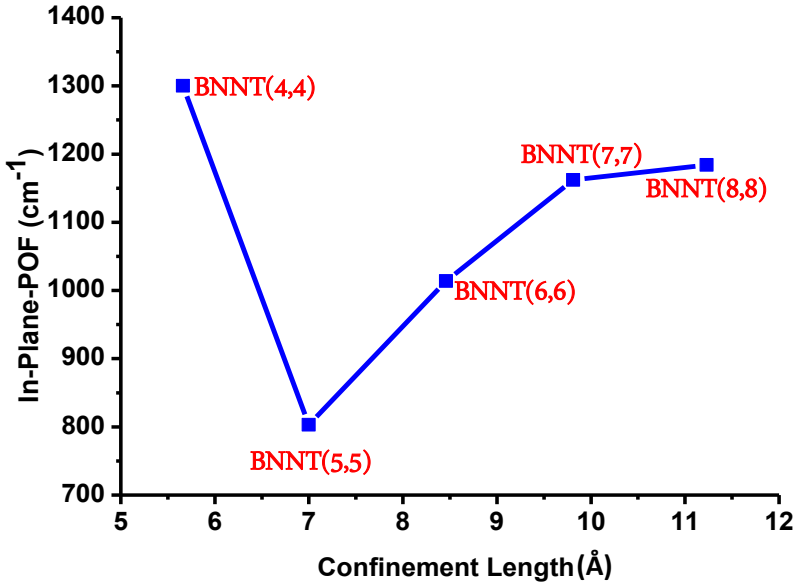

Figure 5.10: Variation of In-plane Proton Oscillation Frequency of ZC under the confinement of BNNTs as a function of confinement length.

5.3.3.3 Energy barrier for proton transfer in ZC in BNNT

The PES for the PT in the ZC under the confinement of BNNTs represented as a function of O-H distance in Figure 5.11(a). The barrier for PT from H_3O^+ to the other water molecule under highly confined cavity of BNNT(4,4) is quite large (5.96 kcal/mol). However for the next wider diameter nanotube *i.e.* BNNT(5,5), a sharp reduction in the barrier occurs with a lowest barrier height of 3.14 kcal/mol. The barrier for the case of BNNT(6,6) is found to be 3.51 kcal/mol which is ~12% higher than the value of BNNT(5,5). A pronounced increase in the barrier is observed for further increase in diameter of the nanotube beyond BNNT(6,6). To get a clear picture, the barrier height of the PT process as a function of the confinement length is pictorially represented in Figure 5.10(b) and it is evident that BNNT(5,5) provides an optimum confined medium for easier transport of proton.

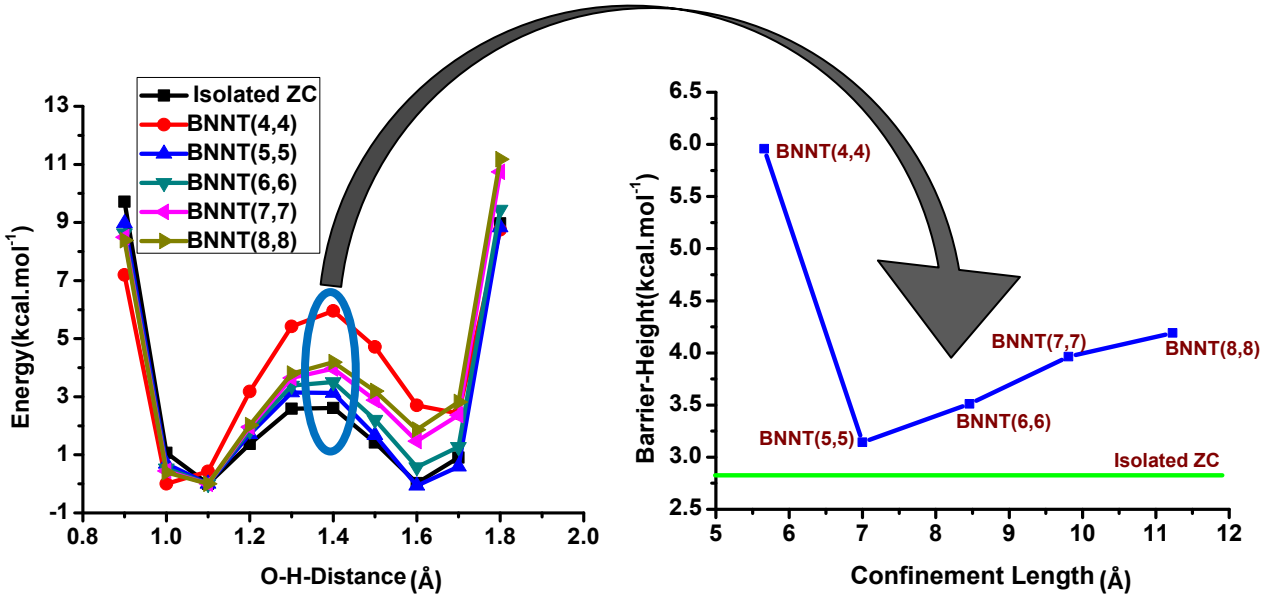

Figure 5.11: (a) PES of isolated and confined ZC at a O···O separation distance of 2.7 Å
(b) Barrier height of PT process under the confinement of BNNTs as function of confinement length (Radius of BNNT).

5.3.4 Comparison and summary

In the present work, we have performed DFT based quantum chemical calculations with dispersion correction to investigate the effect of nanoconfinement on the structure, vibrational spectra and proton transfer energetics (energy barrier) in Zundel cation (ZC), i.e. protonated water-dimer. The effect of the confinement medium has been systematically illustrated by employing a series of carbon nanotubes (CNTs) and boron nitride nanotubes (BNNTs) of varying diameter. We have demonstrated that the structure of ZC is significantly modified under the confinement of nanotube and resulting to the formation of a distorted ZC structure where the central proton of the ZC is preferentially attracted to one of the water molecules. The interaction of ZC with the nanotube largely depends on the diameter of the nanotube and the interaction energy of ZC with CNT is observed to be significantly higher (~40%) than that of BNNT. In larger diameter nanotubes, ZC is stabilized near the inner surface of the nanotube because of the formation of hydrogen bond between the ZC and the nanotube. It has also been shown that the effect of marginal change in degree of confinement on the energy barrier for the PT process is very remarkable and we have explained why the proton transfer may be facilitated in nanotubes with diameter in the range of 7 to 9 Å.

5.3.5 Proton transfer energetics in NH_3-H_2O system

In this part of the work, we have considered a dissimilar system and studied the effect of confinement by CNT on the proton transfer energetics in this system.

5.3.5.1 Structure and energetics

The optimizations of the isolated ammonia-proton-water (APW) and CNT-APW complexes are carried out following similar procedure discussed in the model and method section (Section 5.2). The optimized structures are presented in Figure 5.12.

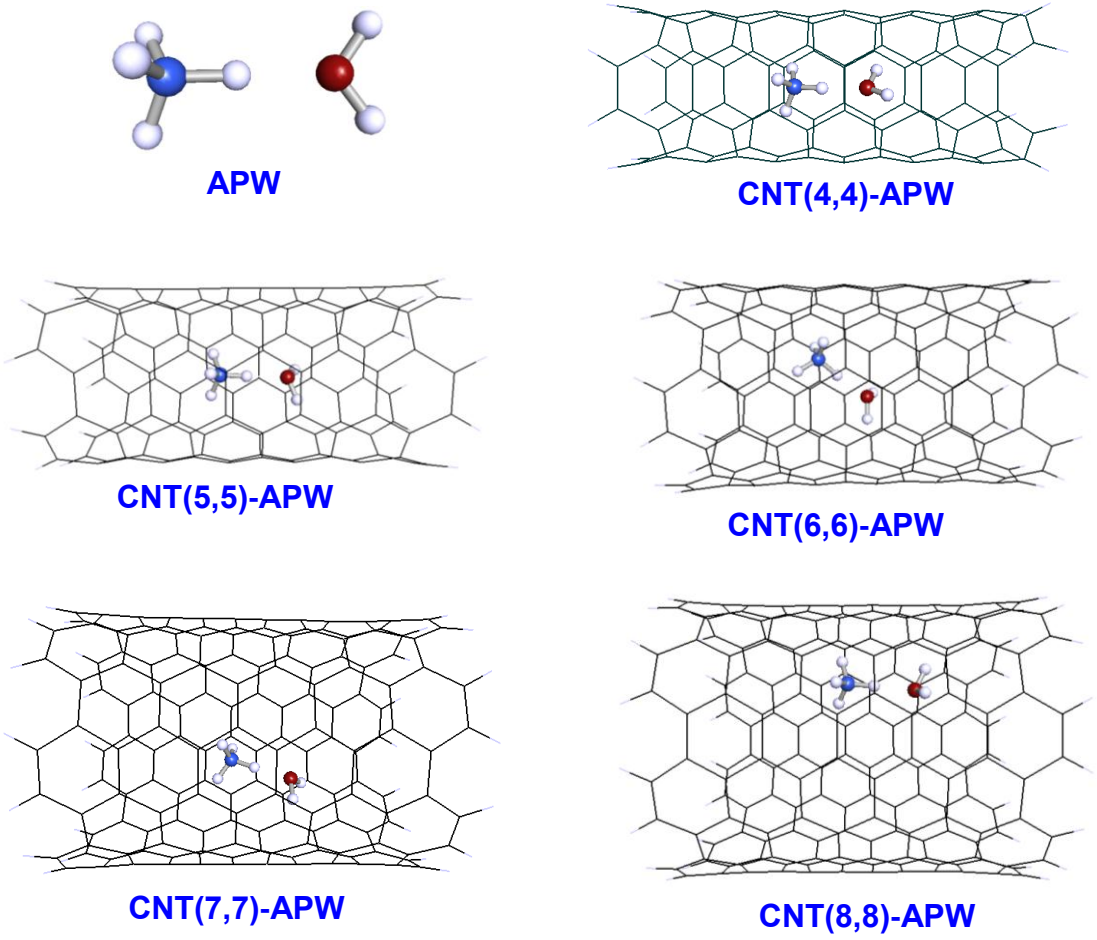

Figure 5.12: Optimized structures of the CNT-APW complexes.

The important structural parameters and energy values of the APW system are presented in Table 5.11. The interaction energies (IE) are calculated by using the following relations

$$SE_{APW} = E_{(CNT\text{-}APW)} - E_{(CNT)} - E_{(APW)} \quad (5.5)$$

$$IE(1) = E_{(CNT\text{-}APW)} - [E_{(CNT\text{-}AP)} + E_{(W)}] \quad (5.6)$$

$$IE(2) = E_{(CNT\text{-}APW)} - [E_{(CNT\text{-}PW)} + E_{(A)}] \quad (5.7)$$

$$HB_{Conf} = E_{(CNT\text{-}APW)} - E_{(CNT\text{-}AP)} - E_{(CNT\text{-}W)} + E_{(CNT)} \quad (5.8)$$

Table 5.11: Important parameters of the optimized NH_3-H^+-H_2O system in the gas phase (Free-APW) and under the confinement of CNTs.

Confining medium	**$\theta_{(N\text{-}H\text{-}O)}$**	**SE_{APW} (kcal/mol)**	**IE(1) (kcal/mol)**	**IE(2) (kcal/mol)**	**HB_{Conf} (kcal/mol)**
Free-APW	179.9	--	0.0	0.0	40.34
CNT(4,4)	161.5	-25.3	17.0	34.7	-1.32
CNT(5,5)	178.5	-68.0	-8.5	-5.8	-13.48
CNT(6,6)	177.1	-55.3	-5.5	1.8	-16.04
CNT(7,7)	178.1	-49.5	-3.0	5.6	-15.62
CNT(8,8)	178.0	-47.6	-2.4	6.8	-15.98

It can be seen from Table 5.11 that the interaction of water towards the proton connected to ammonia molecule is significantly enhanced (as much as ~40%) in the confining media, especially for CNT(5,5) case. For other confining media larger than CNT(5,5), the corresponding interaction energy is also observed to stabilize the protonated water molecule. However, for the case of NH_3, the protonated complex is found to be destabilized in all confining media by ~11 % except for the case of CNT(5,5) for which the calculated interaction energy is -

5.8 kcal/mol as compared to the free (unconfined) case. Thus, our results lucidly demonstrate that the proton affinity of water is certainly more enhanced under hydrophobic nanoconfinement than that of ammonia. It is also interesting to note that the APW complex initially kept at the center of the tube, tends to stabilize near the nanotube wall which can be one of the reasons why there is an enhanced stability of the protonated water in the confined case.

Let us now turn our discussion on the effect of confinement on the energy barrier for the proton transfer from ammonia to water inside CNT. The PES for the translocation of proton under the confinement of CNTs generated in a similar way to the gas phase for N-O distance of 3Å is presented in Figure 5.13. Under highly confined scenario like CNT(4,4), the geometry is observed to be highly distorted (N_A-H_P-O_W angle for free APW and CNT(4,4) are ~180^0 and 162^0, respectively) and there is also a reduction in the N-H_P distance. Hence, there is a significant increase in the barrier for the case of CNT(4,4) primarily due to the geometrical confinement.

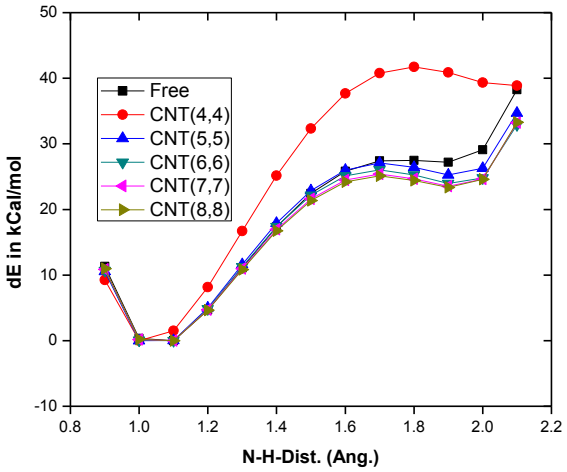

Figure 5.13: Variation of PES as a function of N_A-H distance at different confinement lengths.

On the other hand, for larger diameter tubes, the energy barrier for the proton transfer towards the water molecule is significantly reduced in comparison to the one obtained in gas phase. In addition, we also observe that there is only a marginal reduction in the energy barrier for the case beyond CNT(6,6) and this may be due to the limitation in the interaction of the protonated water in APW complex with CNT, as discussed earlier. These results unambiguously explain that the proton transfer towards the water molecule can become energetically feasible under the confinement.

5.4 Summary of the work

We have investigated the effect of confinement on the structure and proton transfer energetics in small model systems using several nanoconfinement media. Our results reveal that the interaction of confined species with the nanotube leads to the drastic modification in structure and energetics of the confined species. It has been demonstrated through this study that the nanotube diameter plays a crucial role in modifying the proton transfer energetics in the confined system. It has also been shown that the effect of marginal change in diameter of the confinement medium (degree of confinement) on the energy barrier (12-45%) for the PT process is very remarkable. After analysing several factors, it has been concluded that among all the nanotubes considered in the present study, the proton transfer may be facilitated in nanotubes with diameter in the range of 7 to 9 Å. The conclusions drawn from our results can have important implications and motivate further investigation on the systems to understand the fluidics under different confined nanomaterials.

Chapter 6

Catalytic properties of hydrogen doped gold nanoclusters: The hydrogen island effect

6.1 Introduction

In this chapter, we have investigated the catalytic properties of small pristine gold clusters and hydrogen doped gold clusters. To assess their catalytic properties we have considered the CO oxidation process which is considered as a favorite prototypical reaction to test the performance of heterogeneous catalysts [321]. The other aspect of CO oxidation process is associated with the health hazard of CO. Due to its high affinity with hemoglobin, carbon monoxide is a very toxic gas for human. Long term exposure to higher concentration of CO can cause detrimental effects. Therefore, CO cannot be released from any industry as a byproduct. This has prompted immense research interest to devise suitable methods to convert the CO to CO_2 efficiently and economically. In addition, it is well known that CO can act like a poisoning agent specifically for the metal catalysts such as Pt and Pd [322] in fuel cells. Hence, removal of CO is an extremely important requisite parameter for the effective function of these industrial catalysts [323].

6.2 Gold nanoclusters for CO oxidation

Gold in its bulk form is well known for its noble character and has been regarded as a poor catalyst [324]. However, this is not the case for gold nanoclusters and it has been shown that gold clusters catalyze several chemical reactions such as carbon monoxide oxidation, selective oxidation of hydrocarbons and alkene epoxidation [325-330]. The extraordinary catalytic activity has prompted many researchers to investigate the structure and reactivity of the gold clusters. These studies have established that the reactivity of gold clusters is influenced by quantum size effect and relativistic effect [327]. Among the above-mentioned reactions, the CO-oxidation reaction has been studied extensively because of its importance as mentioned

above [321, 328, 331, 332]. The initial studies by Masatake Haruta and his co-workers [325] reported that very small (< 5nm) gold particles supported on suitable oxides are active towards carbon monoxide oxidation reaction even below room temperature which triggered the interest in gold in nano regime as a catalyst. Since then, a number of experimental and theoretical studies have focused their attention on the catalytic activity of gold clusters. In general, gold is more catalytically active than the noble metals of Groups 8-10. The latter easily dissociate the oxygen molecule and chemisorb oxygen atoms, and bind carbon monoxide very strongly leading to low catalytic activity while gold does not adsorb them very strongly and it is therefore nearer the top of the volcano curve for this reaction, where it exhibits much greater activity. Subsequent studies have shown the unusual size dependence of the low-temperature catalytic oxidation of carbon monoxide using gold clusters [329]. The size dependence catalytic activity of gold clusters has been studied by many groups and it has been shown that the structure and reactivity of gold nanoclusters are highly influenced by the strong relativistic and quantum mechanical effects [333].

6.3 Effect of support material in CO oxidation by gold cluster

Regarding the CO oxidation reaction, it is now known that the reactivity of gold clusters depends on factors such as size and shape of the cluster [334], charge state of the cluster [335,336], ligand adsorption[337], and nature of the supporting material [338, 339]. In relation, the role of various metal oxide supports such as MgO, TiO_2, Al_2O_3, Fe_2O_3, Co_3O_4 , and NiO have been tested for CO oxidation reaction on gold clusters. Some of the support materials have shown to promote very high catalytic activity in gold clusters [340]**.** The basis of the difference in the catalytic activity of these supported gold clusters can be attributed to the dispersed nature and charge state of gold clusters that is regulated by the support material [341]. In one of the

most recent studies, the high catalytic activity for CO oxidation is correlated with the presence of bilayer clusters which contain nearly ten gold atoms [342]. The size and structure sensitivity of this reaction is related to the quantum size effect with respect to the thickness of the gold islands with two layers of gold which are effective for catalyzing the oxidation of carbon monoxide.

6.4 Effect of dopant in CO oxidation by gold cluster

Apart from the support material, another important aspect of tuning the structural and electronic properties of gold clusters is the use of dopant. In the initial years, gold clusters were doped with transition metal atoms and the chemical properties were studied by theoretical and experimental methods. For example, the $W@Au_{12}$ structure, investigated by density functional theory [343] and photoelectron spectroscopy [344] indicated a closed-shell icosahedral structure (I_h) with HOMO-LUMO gap close to 3 eV. Similarly, photoelectron spectroscopy studies carried out for V, Nb and Ta doped in Au_{12} also revealed I_h symmetry [345]. There are also studies comprising other transition metals such as Cu, Si, Ge, Ti and Sn in the gold clusters [346-348]**.** In these studies, the main focus was to elucidate the effect of dopant atom on the structure, physical and chemical properties of gold clusters [343-345, 349].

However, in recent years, there is growing interest in studying the effect of light atom on the properties of gold cluster [350]. Alkali metal, hydrogen atom and gold have similarity in electronic configuration by having one electron in the valence shell, S-orbital. In addition, the electronegativity of hydrogen and gold is very close to each other. Kiran *et al*. [351] have demonstrated the resemblances of gold with hydrogen in a specifically chosen system. In the similar line, several recent theoretical studies have also explored this in different Au-alloy clusters and observed similar analogy in these systems [352]**.** It has also been demonstrated that doping gold clusters with alkali metal and hydrogen atoms can drastically modify the electronic

structure and properties of pristine gold clusters [350]. More importanntly, some recent theoretical studies have shown that the catalytic activity of the gold cluster towards CO oxidation can be significanntly improved by doping it with hydrogen or Si atom [353-355]. These studies indicate that not only does hydrogen doping result in preferential activation of an oxygen molecule but also leads to reduction in the activation barrier for the CO oxidation reaction. However, a systematic study of the effect of hydrogen doping on the gold nanoclusters is scarce in the literature. Therefore, in the present study, we have systematically doped hydrogen atoms in gold clusters (Au_n, n=1 to 6 and studied the structure and stability of each hydrogen doped clusters. For each gold cluster, we have considered various possible conformations and did the sequential hydrogen doping to the maximum extent possible. The important properties such as IP, EA and HOMO-LUMO gap have been thoroughly analysed for each of these clusters. The objective for the present work is to investigate the change in structure, electronic properties and the energetics of CO interaction due to hydrogen doping. Taking the clue from this enhanced CO interaction, we have investigated the activation barrier for the CO oxidation leading to CO_2 process using some of the selected hydrogen doped gold clusters.

6.5 Computational details

All the calculations in the present work have been performed using density functional theory as implemented in the Turbomole program. The geometry optimization has been done without any symmetry constraint at the DFT/TPSSH level of theory. The triple-zeta basis set (def2-TZVP) has been used for all the atoms. For sixty inner electrons of Au, ecp-60-mwb has been used.

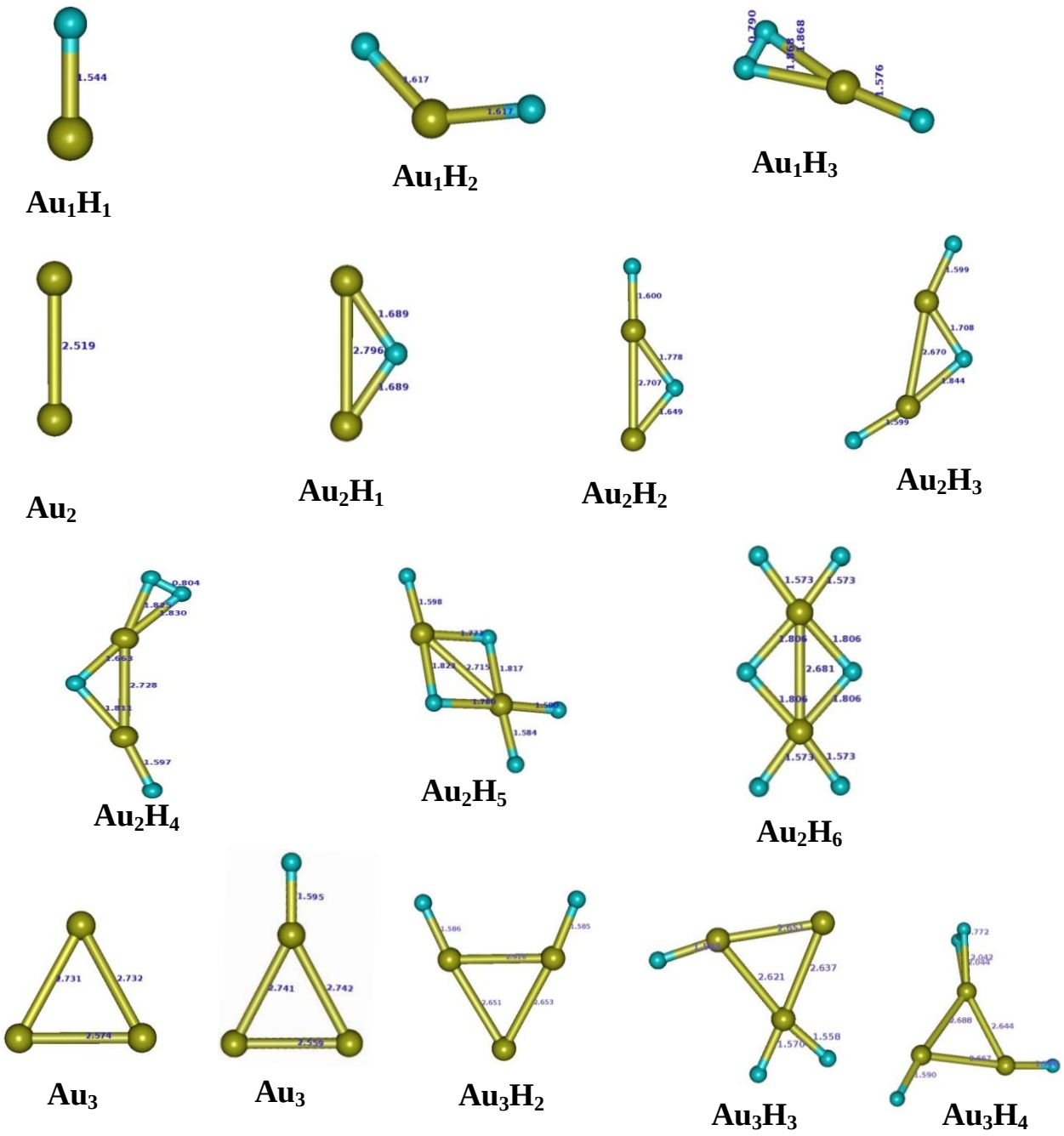

Figure 6.1: Optimized geometries of pristine and hydrogen doped gold clusters for Au_1 to Au_3 obtained by TPSSH based DFT method. The atom in yellow color is gold and rest are hydrogen.

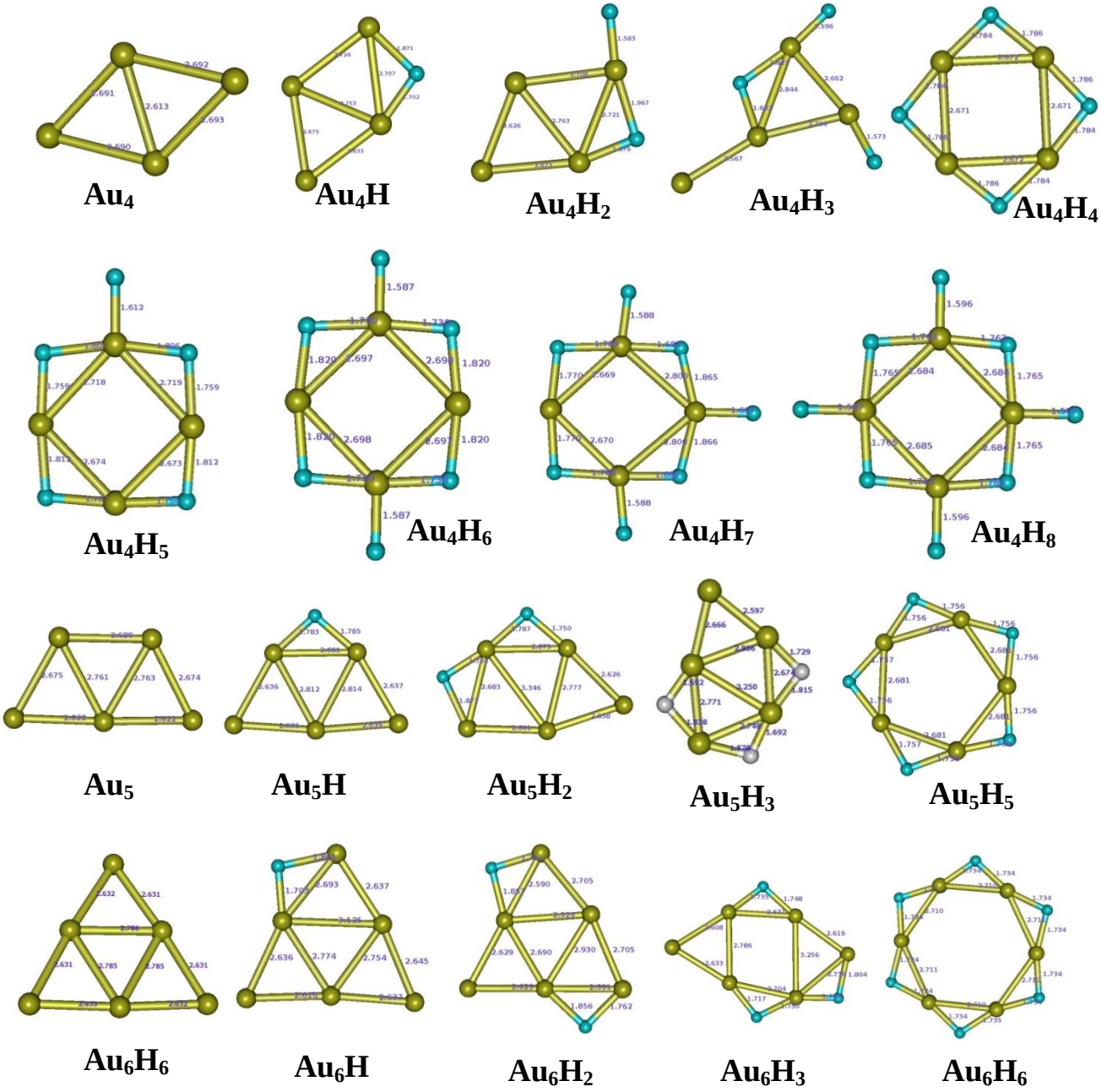

Figure 6.2: Optimized geometries of pristine and hydrogen doped gold clusters for Au_4, Au_5 and Au_6 obtained by TPSSH based DFT method.

6.6 Structure, electronic properties and the nature of CO interaction of hydrogen doped gold clusters

Earlier theoretical studies have established that small neutral gold clusters tend to favour planar geometry up to the cluster size of Au_8 and a thereafter a crossover from planarity to nonplanarity occurs (2-to-3 dimensions) [356]. The tendency to form planar structures for gold clusters is much more prevalent than copper and silver, which is strongly favored by relativistic effects [357]. The geometries obtained in the present work by employing the TPSSH Exchange Correlation functional for pristine gold clusters for sizes *n*=2-6 are given in Figure 6.1 and 6.2.

We have considered several possible configurations for both pristine and hydrogen doped clusters and the hydrogen doping has been done for the lowest energy structures of the pristine gold clusters. We have compared the lowest energy structures of the pristine and single hydrogen doped gold clusters with the already existing reports and it is found that the structures are similar to those already predicted earlier [350, 357]. Thus, we continued the doping of hydrogen and optimized the possible structures using the same method. For example, in the case of Au_2, the Au-Au distance obtained in the present study is 2.56 Å which is quite close to the value of 2.57 Å obtained in the earlier study. For Au_3, we observed a triangular geometry which has been reported to be the lowest energy structure in comparison to the bent (V-shaped) structure [358, 359]. The Au-Au bond lengths calculated in this case are 2.73 Å and 2.57 Å, and closely agree with the earlier reported values 2.78 Å and 2.57 Å [350]. Similarly, in the case of Au_4 and Au_5, we observed good agreement in the strucural parameters obtained in the present study with the earlier repoted results.

Let us now discuss the effect of hydrogen doping on the structure of these gold clusters. It should be mentioned that we have considered several possible positions for hydrogen doping and the energetically lowest isomer obtained after the geometry optimization has been reported here. In many cases, for a particular cluster, optimization of hydrogen doped structures at different sites lead to same optimized geometry. Initially the pristine clusters were doped with a single hydrogen atom and optimized. The second hydrogen was doped with the optimized structure obtained in the first step. The doping process was continued until we get favourable interaction of hydrogen with the cluster. The geometries of hydrogen doped clusters are presented in Figure 6.1 and 6.2.

The Au-H bond length in Au_1H_1 is 1.54 Å which is significantly shorter than the Au-Au bond length of 2.52 Å. The Au-H bond length slowly increases with the increase in number of doped hydrogen atom. In case of Au_1H_3, two hydrogen atoms converged very close to molecular hydrogen with one short Au-H distance and two long Au-H distance. Beyond three hydrogen atoms, we did not observe any interaction between the hydrogen atom and the cluster. Moreover, a hydrogen molecule is formed which goes far away from the cluster and does not interact with the cluster. The distance between the hydrogen molecule and the cluster is significantly high. In case of Au_2, the first doped hydrogen atom prefers to occupy the bridge bonding position between two Au atoms. This observation is consistent with the earlier reported structure by several groups [355, 360, 361]. When second hydrogen atom is doped in to Au_2 cluster, it is observed that one hydrogen atom remains at the bridging mode whereas, the other prefers the normal bonding mode with one of the Au atom. This leads to slightly different Au-H bond lengths for the bridged hydrogen atom. For the hydrogen doped clusters of Au_2, it is always observed that there is at least one bridging hydrogen is present in the structure. Following the

sequential hydrogen doping procedure, we observed that maxium six number of hydrogen atoms can be doped to the Au_2 cluster. Similarly, for all other larger clusters (Au_3 to Au_6) we predicted maximum number of hydrogen atoms that can be doped in these clusters following the same sequential hydrogen doping procedure. From the interaction energy and the structure of the cluster, it is established that maximum eight hydrogen atoms can be doped with Au_4 clusters.

Let us now discuss the electronic properties of the pristine and hydrogen doped gold clusters. We have perfomed the charge analysis on the clusters by natural bond orbital (NBO) method. The charge on the Au atoms of the cluster are presented in Table 6.1. In general, it is observed that hydrogen atom withdraw electrons and makes the Au atom as positive centers. Similar qualitative results has been obtained by Jena *et al.* recently [353].

Table 6.1: Charge on Au atoms of hydrogen doped gold clusters.

	Charge on Au atoms (a.u.)					
No. of "H" atom doped	Au_1	Au_2	Au_3	Au_4	Au_5	Au_6
0	0.0	0.0, 0.0	0.11, -0.21, 0.11	-0.27, 0.27, -0.27, 0.27	0.02, -0.08, 0.11, -0.08, 0.02	-0.08, 0.08, 0.08 -0.08, -0.08, 0.08
1	0.05	0.07, 0.07	0.11, -0.01, 0.11	0.14, 0.23, 0.02, -0.12	-0.12, 0.24, 0.24, -0.12, 0.09	-0.06, 0.09, 0.20 -0.09, 0.16, -0.01
2	0.26	0.17, 0.15	0.31, -0.28, 0.31	0.23, 0.17, 0.22, -0.13	-0.13, 0.26, 0.27, 0.06, -0.02	-0.02, 0.22, 0.22 0.32, 0.32, -0.40
3	0.11	0.39, 0.09	0.10, 0.41, -0.25	0.11, 0.15, 0.31, -0.06	0.29, -0.13, 0.46, 0.24, 0.19	-0.10, 0.18, 0.17 0.12, 0.29, 0.14
4		0.30, 0.08	0.22, 0.04, 0.03	0.34, 0.34, 0.34, 0.34	-0.15, 0.23, 0.29, 0.08, -0.04	
5		0.49, 0.48		0.35, 0.26, 0.26, 0.45	0.30, 0.30, 0.30, 0.30, 0.30	
6		0.51, 0.51		0.46, 0.15, 0.15, 0.46		0.21, 0.25, 0.25 0.21, 0.21, 0.25
7				0.40, 0.24, 0.21, 0.40		
8				0.33, 0.32, 0.32, 0.33		

We have further analyzed the ionization potential (IP) and the HOMO-LUMO gap of these hydrogen doped clusters. These results are presented in Table 6.2. In general, It can be seen from this table that the IP of the pristine gold cluster shows an odd-even oscillatory behavior with the number of Au atom in the cluster. Similar trend has has been reported earlier in a theoretical study [350]**.** But the variation in IP with number of doped hydrogen atom has not reported previously. It is interesting to note that for a particular hydrogen doped gold cluster, the IP value depends on the number of gold and hydrogen atoms present in the cluster. In geneal, it is observed the IP value of a cluster is high if the total number of gold and hydrogen atom adds up to an even number.

Table 6.2: The ionization potential (IP) and HOMO-LUMO gap of pristine and hydrogen doped gold clusters. The first row in each column indicate the IP value and the second row represent the HOMO-LUMO gap of the cluster.

	IP & HOMO-LUMO gap (eV)					
No. of hydrogen atoms doped	Au_1	Au_2	Au_3	Au_4	Au_5	Au_6
0	6.22 1.63	6.66 2.94	4.78 0.63	5.72 1.59	5.47 0.93	6.25 2.93
1	6.81 4.09	5.23 1.26	6.14 1.86	5.46 1.07	6.19 2.85	5.21 1.02
2	6.54 2.13	6.58 2.96	6.72 1.28	6.48 2.53	5.83 1.02	5.49 1.58
3	6.86 5.74	6.91 1.61	6.75 3.46	6.30 1.13	6.36 2.76	5.54 1.14
4		6.18 4.13	5.79 1.15	6.97 3.59	5.76 1.82	---
5		6.54 1.60		5.95 1.19	7.29 4.98	---
6		8.02 4.92		6.55 2.99		6.67 2.57
7				5.98 1.26		
8				6.63 2.62		

Let us consider the Au_4 case. It contains even number of gold atom and doping it with one hydrogen make it a odd system. The corresoponding IP value chages from 5.72 eV to 5.46 eV. As the number of dopant hydrogen increases to two, the system becomes even and the IP value increases to 6.48 eV. It is clear from the IP trend that the even-numbered and closed shell clusters have higher IP values than their neighboring clusters. The observed trend for higher stability of these clusters can be attributed to the presence of even number of delocalized electrons.

Another parameter which describes the relative stability of these clusters is the HOMO-LUMO gap. It can be mentioned that higher the value of HL gap, more stable is the cluster than the neighboring clusters and vice-versa. From Table 6.2, the odd-even behaviour of HOMO-LUMO gap is clearly seen. More importantly, a large difference in the value of HOMO-LUMO gap (> 1eV) between the odd and the even cluster is observed. This clearly indicates that the hydrogen doped cluster is relatively more stable if the total number of atom in the cluster is an even number. For instance, the even numbered clusters, Au_2, Au_2H_2, Au_2H_4 and Au_2H_6, the calculated HOMO-LUMO gap is found to be in the increasing order (See Table 6.2).

6.7 CO adsorption on the pristine and hydrogen doped gold clusters

The CO adsorption process with pristine gold cluster has been investigated by a number of workers [362]. It has been reported that CO can interact with transition metals through electron donation as well as acceptance (back donation). Among various possible CO adsorption sites, the on-top (one-fold coordinated) is found to be the most favorable one, irrespective of the charge state of the cluster. It has also been reported that the adsorption energies of CO on the cationic clusters are generally greater than those on the neutral and anionic complexes [362].

In the present study, we have considered CO interaction at various possible sites of the pristine and hydrogen doped gold cluster and the energy values corresponding to the most suitable configurations are presented in Table 6.3. The optimized geometries comprising the cluster and the CO molecule are presented in Figure 6.3 and 6.4.

Table 6.3: CO interaction energy values for pristine and hydrogen doped gold clusters.

	CO Interaction Energy (kcal/mol)					
No. of H atoms	**Au**	**Au_2**	**Au_3**	**Au_4**	**Au_5**	**Au_6**
0	-30.1	-34.4	-39.4	-36.5	-24.6	-20.0
1	-32.6	-28.0	-38.1	-43.5	-17.2	-20.2
2	-19.5	-36.8	-14.3	-29.7	-24.8	--
3	-2.4	-25.8	-33.4	-30.0	-29.3	-5.8
4	--	-15.8	--	-13.1	-22.3	--
5	--	-13.5	--	-12.1	-8.1	--

From the results presented in Table 6.3, it is clear that CO can bind to the pristine as well as hydrogen doped clusters in an energetically favourable manner. It is observed that the preferred mode of interaction for all the pristine and hydrogen doped gold clusters is through the carbon atom of CO.

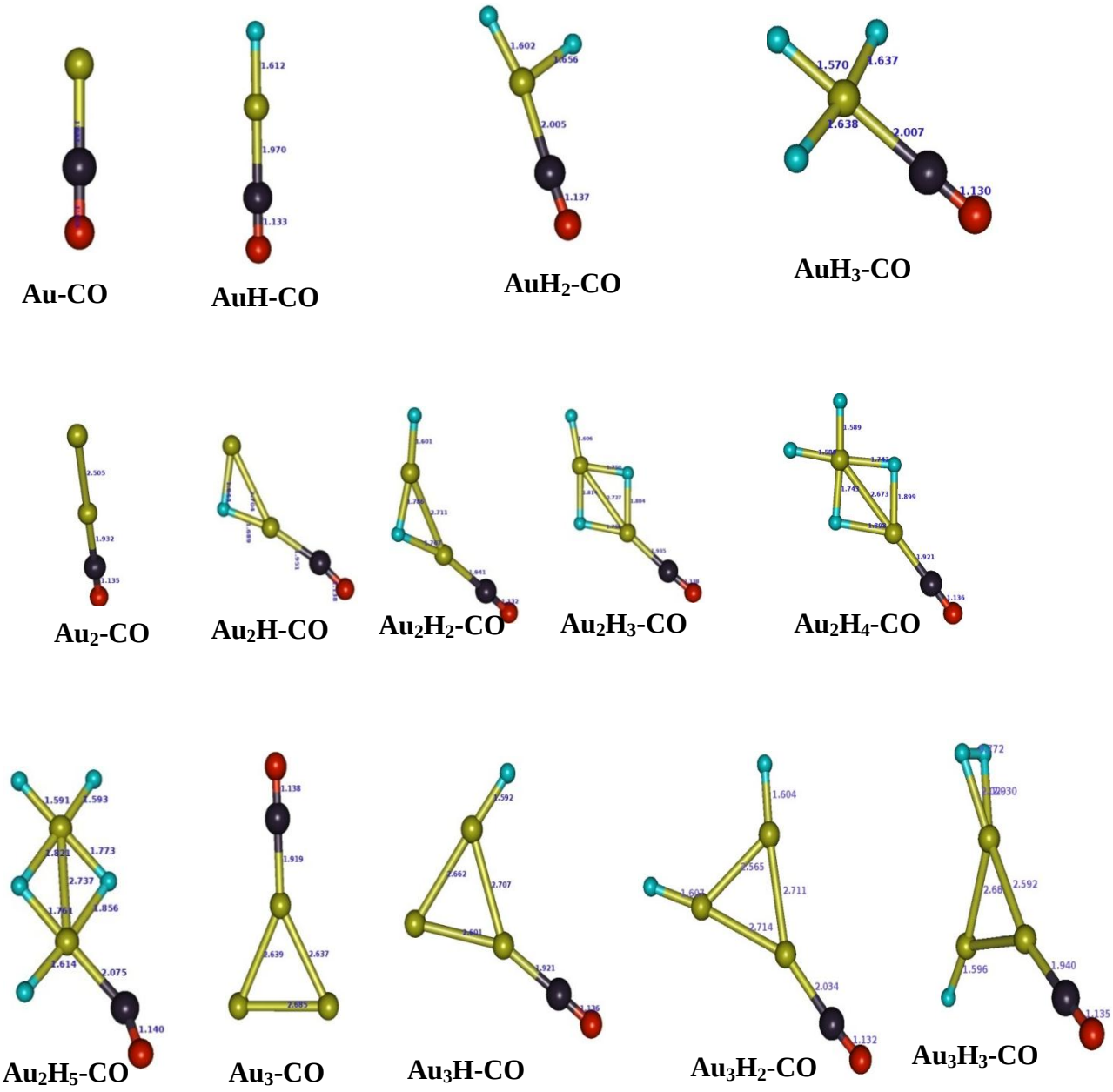

Figure 6.3: Optimized geometries of pristine and hydrogen doped gold clusters (Au_1 to Au_3) interacting with CO molecule.

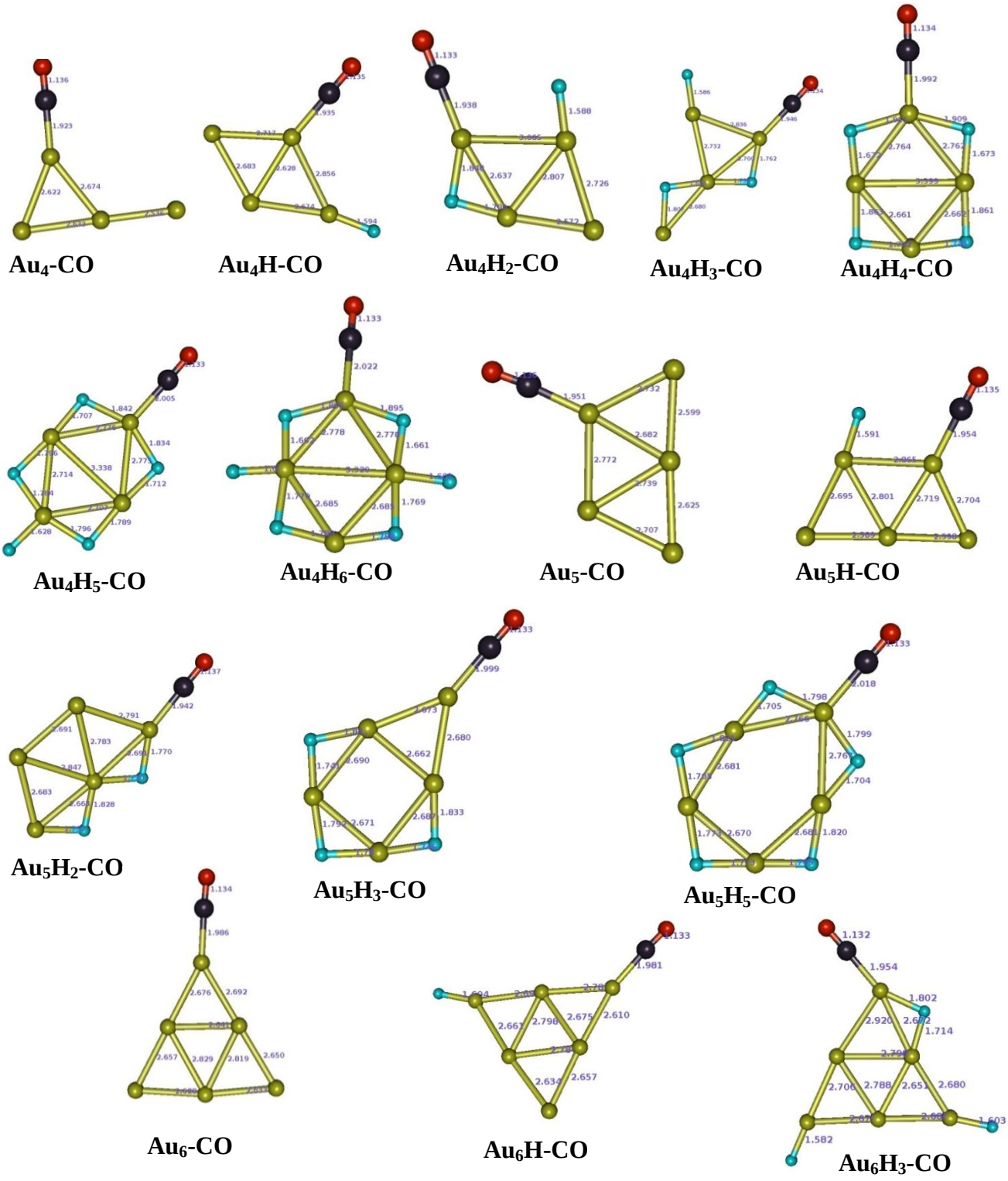

Figure 6.4: Optimized geometries of pristine and hydrogen doped gold clusters (Au_4 to Au_6) interacting with CO molecule.

In general, it has been observed that for hydrogen doped gold clusters, CO binds strongly to the gold atom adjacent to H atom. This can be attributed to the positively charged gold center created by the doped hydrogen atom as discussed in the previous section. It is noteworthy that the positive gold atom can strongly interact with CO in comparison to the neutral counterpart [362]. The CO interaction values are presented in Table 6.3. From the trend in the CO interaction energy, it can be presumed that the interaction energy depend on the structure of the cluster and the number of hydrogen atoms doped in the cluster. In general, the highest CO interaction energy is observed for a optimum number of hydrogen atoms doped in the cluster. More interestingly, this value in some caes is more than 20% in comparision to the pristine cluster. At the same time, it has also been observed that the hydrogen doping need not necessarily always enhance the binding energy of CO and for different Au-H ratios, the BE of CO is decresed. In general, when the number of H-atoms is equal to more than the number of gold atoms (Au_mH_n, $n \geq m$), the BE is observed to be much lesser than the pristine cluster. These results unambiguishly suggests the optimal dopants concentration is the key to achieve best CO interaction.

6.8 Oxidation of CO to CO_2 with hydrogen doped gold clusters

In general, the CO oxidation reaction on nanocatalysis proceeds through two mechanisms [363, 364], Langmuir-Hinshelwood (L-H) and Eley-Rideal (E-R). In the L-H mechanism, both the reactants (CO and O_2) are pre-adsorbed on the gold cluster in the IS. On the contrary, the E-R mechanism proceeds with the adsorption of only one of the reactant species in the IS. These two schemes are pictorially represented in Figure 6.5. In the present study, we have selected Au_5 and Au_5H_3 clusters and investigated the CO oxidation process. The scientific basis for selecting this particular pair of cluster lies with the large difference in their CO interaction energy as discussed in the previous section.

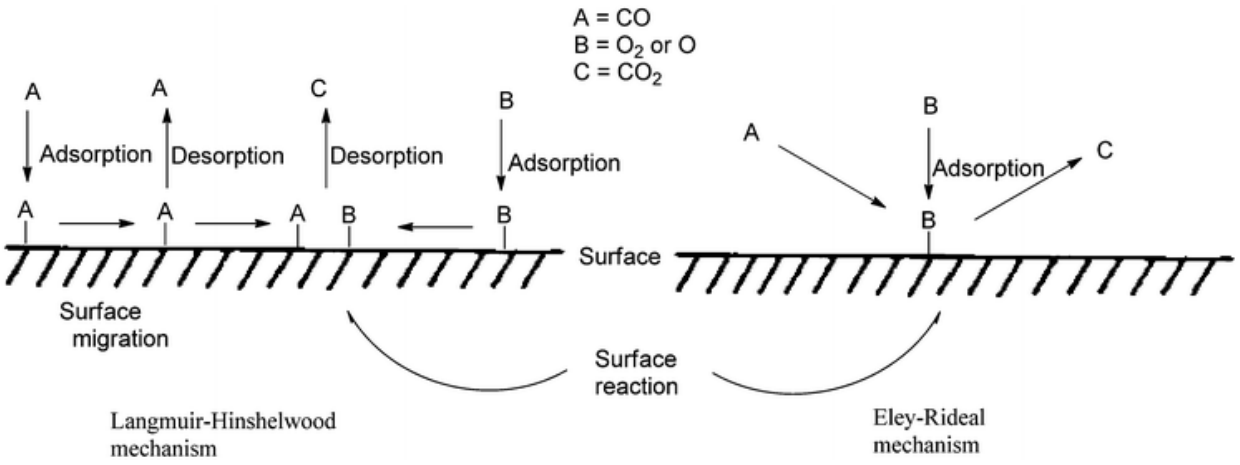

Figure 6.5: Schematic representation of the Langmuir-Hinshelwood (L-H) and Eley-Rideal (E-R) mechanism. (Ref: [364])

In our study, we have considered the L-H mechanism and in the starting point (IS) of the reaction, both O_2 and CO molecules are simultaneously adsorbed on the cluster. The complete reaction profile for the CO oxidation process is presented in Figure 6.6 (a) and (b). From this figure, it can be easily noted that the geometry of the pristine cluster does not change appreciably in IS, TS or the final state of the reaction. In contrast, for the doped cluster case, the geometry of the TS differs significantly from that of the IS. This fluxionality in the structure of the doped cluster can be attributed to the effect of hydrogen doping which has been reported in an earlier study [350]. The adsortion of CO and O_2 molecules on both pristine and hydrogen doped gold cluster are favourable with a net interaction energy value of ~ 65 kcal/mol. But in the case of Au_5H_3, the O_2 molecule preferred a bridging mode of bonding. The CO oxidation reaction is observed to be exothermic in both the cases.

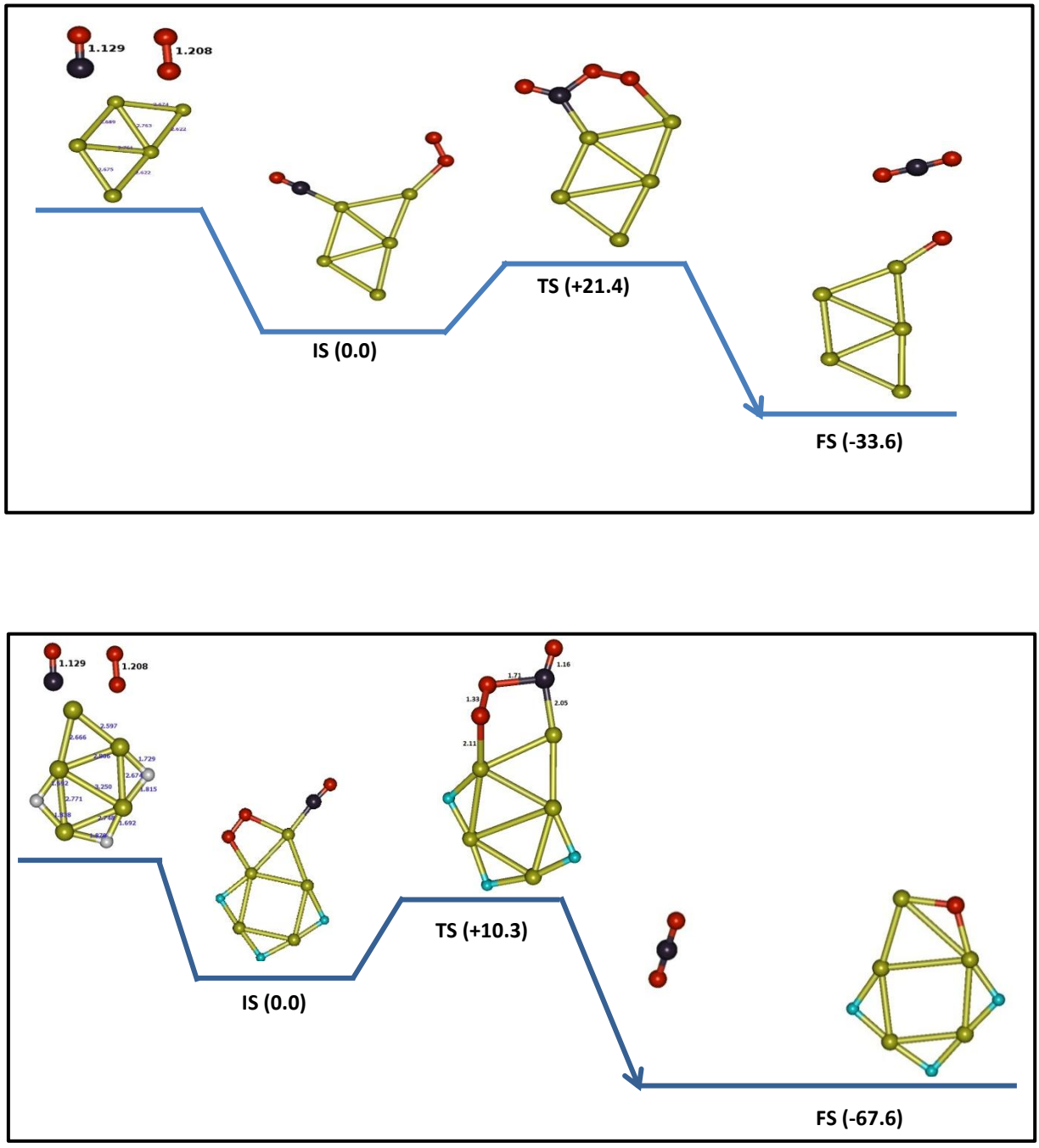

Figure 6.6: Reaction profile for CO oxidation process on (a) pristine gold cluster (Au_5) and on (b) hydrogen doped cluster (Au_5H_3). All the values are in kcal/mol.

The barrier height for the CO oxidation reaction, estimated in the present work for Au_5 and Au_5H_3 is 21.4 and 10.3 kcal/mol respectively. In an earlier study comprising Au_8 cluster, the estimated barrier height for the CO oxidaton reaction was 30 kcal/mol [353]**.** The difference in barrier height for Au_8 and Au_5 can be attibuted to the cluster size effect. This is also reflected in the CO binding energy which sharply increses with reduction in cluster size. Further reduction in barrier height in the case of Au_5H_3 can be attibuted to the bridging mode of O_2 bonding which activate the O_2 molecule significantly (Elongation in O—O bond lengthh after bonding). Therefore, the hydrogen doped gold clusters (Au_5H_3 in particular) can be very efficient catalyst for CO oxidation.

6.9 Summary of the Work

Doping with hydrogen atom can play a pivotal role in modifying the electronic properties gold clusters and enhance their catalytic activity. Irrespective of the number of dopant atoms or the cluster size, for all the hydrogen doped clusters, it is observed that hydrogen atom withdraws electrons from the gold cluster and hence the gold atoms acquire high positive charge. A substantial increase in the CO interaction energy (more than 20% in some cases) is observed when the numbers of hydrogen atom reach to an optimum value in the gold clusters. One of the reasons for this remarkable enhancement in interaction energy is attributed to the charging of the gold cluster. We also demonstrated that the CO oxidation can occur with these hydrogen doped gold clusters with a significantly lower barrier (100 %) in comparison to their pristine counterparts. Thus hydrogen doped gold clusters can be considered as a potential catalyst for CO oxidation from economic point of view.

We hope that the outcome of this particular work would stimulate further research in this area, particularly in designing materials involving the doped gold clusters by exploiting the nature of similarity in their electronic structure, as investigated here. Thus, a molecular-level understanding of the present study is expected to provide a better understanding of the structure-reactivity relations in the nanosurface-catalyzed reactions.

Chapter 7

Water dissociation on metal atom decorated boron nitride nanotube

4.6 Introduction

Research on nonpolluting and green energy has gathered momentum in recent years due to the higher energy demands of burgeoning world population, depletion of fossil fuel sources and CO_2 induced climate change. In such scenario, much attention is centered for a search of a suitable alternative fuel. In recent years, hydrogen has emerged as a potential energy carrier due to its fuel value and clean burning process. Hence, the generation and storage of hydrogen has become important areas of research. Although direct thermal splitting of water to generate hydrogen and oxygen seems as a clean route for hydrogen production as it is not associated with the release of CO_2, the higher kinetic barrier and temperature requirements are inherent drawbacks of this process [365, 366]. Furthermore, generation of hydrogen by electro-catalysis of water is highly energy intensive associated with very low yield and requiring expensive catalysts [366]. Hence, the search for inexpensive and robust catalysts for water splitting is of considerable interest to the scientific community.

Interaction of water with metals plays an important role in several processes involving catalysis, corrosion, electrochemistry etc. In many catalytic processes with industrial importance such as steam reforming or water gas shift reaction, formation and dissociation of water holds a central position. In view of this, it is of larger fundamental importance to investigate the interaction of water at the interface of metals. Specifically, such knowledge will provide us improved understanding of the catalytic phenomena as well as help to improve their catalytic performances.

Nanostructures based on transition metals have been thoroughly explored, both theoretically and experimentally in recent times for water dissociation catalysts and media for

high-capacity hydrogen storage [366-371]. Adsorption and dissociation of a water monomer on (111) surfaces of a series of transition metal atoms viz., Cu, Au, Pt, Pd, and Ni have been investigated by Pathak et al. [368]. In another related first principle calculations by Pozzo et al. [370], they have discussed the dissociation of water on (111) surfaces of Rh and Ni. In their study, the calculated barrier heights for water dissociation on Rh(111) and Ni(111) surfaces are found to be 0.92 and 0.89 eV respectively.

The hydrogen storage capacity of carbon based nanostructures has generated immense interest in recent years and a flurry of related literature is available [372-377]. Lei et al. [369] have discussed the initial stages of interaction of water molecules on Ti-doped CNTs. They have calculated the barrier for dissociation of a single water molecule which is ~ 0.4 eV and the subsequent barrier for splitting of the second water molecule which in turn releases H_2 is as low as 0.1 eV [369]. Similarly, Liu et al. [371] have proposed Ti-decorated C_{60} as a prototypical nanostructure for water dissociation. Hence, it follows from our preceding discussions that metal-based catalysts along with carbon based nanostructures (CNTs, C_{60} fullerenes etc.) are ideal nano-systems to investigate two important aspects associated with hydrogen energy; (1) splitting of water to generate hydrogen and (2) storage of molecular hydrogen for portable application.

In analogy to the CNTs, boron nitride nanotubes (BNNT) can be considered as the cylindrical structures resulted from wrapping a single honeycomb hexagonal sheet of BN (*h*-BN) which has already discussed in the introduction chapter [378]. BNNTs are emerging as technologically important materials following their successful synthesis in last two decades [379-380]. One of the most fascinating aspect of BNNTs are these belong to a class of semiconductors and the band gap is independent of the tube chirality, unlike the CNTs where chirality decisively

determines the band gaps of the CNTs [381-383]. In the early 1970s, the seminal work of Fujishima and Honda has opened up a new avenue for employing semiconducting TiO_2 as a photocatalyst for water splitting [384]. The possibility of coating CNT with Ti has been demonstrated both theoretically and experimentally [385, 386]. Very recently, Tang et al. have demonstrated improved photocatalytic reduction properties of TiO_2 when nanocomposites of this material are functionalized on the surface of BNNTs [387].

With this initial motivation, in the present study, we have considered the dissociation of water by the transition metal decorated on BNNT. Ti and V atom have been considered as a representative transition metal atoms. From our calculations, we have demonstrated that the dissociation of water to H and OH fragments is extremely facile in both the cases. Further, we have also shown that a second water molecule also interact with the product from the splitting of the first water molecule. Interestingly, the splitting of the second water molecule proceeds with extremely small barrier leading to the evolution of one H_2 molecule.

4.7 Computational Details

All the theoretical calculations have been carried out by the computational chemistry software TURBOMOLE and by employing the exchange-correlation energy density functional the Perdew–Burke–Ernzerhof (PBE) in conjunction with def2-SV(P) basis set for all the atoms. The BNNT has been modeled by considering a small segment of BNNT(4,4) to BNNT(6,6) where the terminal B and N atoms have been saturated with H atoms. One of the O-H bonds of the water molecule is chosen as the reaction coordinate and the potential energy surface for water dissociation has been generated from several single point calculations. The highest point on the potential energy surface is taken as the initial guess geometry for TS optimization.

4.8 Results and Discussions

Let us begin our discussion from the adsorption of single Ti and V atom on the top of BNNT. It is worthwhile to mention that we have considered several spin states for both the systems and the lowest lying states are presented here. In the lowest energy state, Ti atom prefer to adsorb above the center of BN hexagon as compared to other binding possibilities like on top of B atom, N atom or a bridged site between B-N bond. On the other hand, V atoms adsorb on the bridged site between B-N bond. This observation is consistent with the earlier result from a DFT study of transition metal atoms adsorbed on BNNT(8,0) [388]. The shortest distance of Ti atom (adsorbed on BNNT) from the nitrogen and boron atom of the BNNT are 2.22 and 2.18 Å whereas, the corresponding values for V atom are 2.18 and 2.43 Å respectively. These distance values are quite close to the earlier reported results. We have considered BNNT with smaller diameter having chirality (4, 4) to minimize the computational cost arising out of considering wider tubes with more number of atoms. It has already been mentioned in the previous section that the band gap energy of BNNT is independent of the selection of chirality (n, m). On the contrary, the selection of chiral vectors (semiconducting (n, 0); metallic (n, n)) can influence the electronic properties for CNTs.

The binding energy of Ti atom on (4, 4) BNNT is found to be -1.03 eV whereas for V the binding energy value is -1.26 eV. It can be mentioned that the energy value is very highly dependent on the site of adsorption [388]. Upon the interaction of these adatoms with BNNT, the later acquires significant partial positive charge (> 0.4 e), computed by the Mulliken population analysis. In order to understand the effect of surface curvature of BNNT on the binding energy of these two atoms, we have also considered two more variants of BNNT viz. (5, 5) and (6, 6). The diameter of the three BNNTs (4, 4), (5, 5) and (6, 6) follow an increasing trend viz. 5.6, 7.0

and 8.5 Å (including atomic radii) and the surface curvature follow an inverse trend. We have calculated the binding energy of Ti atom for these BNNTs and the values are -0.79 eV and -0.65 eV for BNNT(5, 5) and BNNT(6, 6) respectively. We, therefore, infer that the adsorption of the transition metal atoms are more favorable for highly curved (smaller diameter) nanotubes. It is worthwhile to mention that in a very recent study it has been demonstrated that the adsorption strength of molecules on BNNT increases from physisorption to chemisorption as the diameter of the BNNT decreases [320].

The optimized geometry (IS) of water adsorbed on Ti decorated BNNT (4, 4) has been presented in Figure 7.1 (a). The binding energy of a single water molecule is calculated to be -1.78 eV. This high binding energy suggests that water adsorption is favorable process on a Ti-BNNT system. We have also presented the dissociation of this water molecule bound to Ti-BNNT system in Figure 7.1 (a). The barrier for the splitting of the water molecule atop Ti adatom is computed to be 0.12 eV. Lei et al. have estimated the barrier for water dissociation to be ~0.4 eV on a Ti-CNT system [369]. Our observation of extremely lower barrier can be pertinent for the design of nanostructures for splitting of water. In the FS, we find that one of the dissociated product (OH fragment) is adsorbed on Ti adatom whereas the other (H) is held by a bridged bond between Ti adatom and one of the B atom on the BNNT surface. The overall heat of formation of the product is calculated to be -2.89 eV. This suggests that spitting of water molecule on a Ti-BNNT system is extremely exothermic. With this initial observation that the dissociation of first water molecule on a Ti adatom on BNNT surface is highly facile, we have attempted to investigate the subsequent dissociation of the second water molecule. The dissociation process of the second water molecule is pictorially presented in part (b) of Figure 7.1. The binding energy of the second water molecule on the Ti (shown in IS of Figure 7.1 (b)) adatom is found to be -3.94 eV which is higher than that of the first water molecule (-1.78 eV).

This indicates that, even after the splitting of the first water molecule, Ti adatom can still act as a catalytic active center for subsequent interaction of water molecule.

The higher binding energy of the second water molecule can be attributed to the formation of a hydrogen bond (O-H⋯N) between one of the H atoms of the second water molecule and one of the surface N atom of BNNT. The corresponding O-H bond is considered as the reaction coordinate for the generation of the potential energy surface. Further, we have estimated the barrier height for the splitting of the second water molecule to be 0.01 eV. This observation emphatically demonstrates that the splitting of the second water molecule is almost barrier-less. This extremely low barrier for splitting of the second water molecule can, in principle, be ascribed to the stabilization of the TS structure (Figure 7.1 (b)) by hydrogen bonding. The O-H bond distance (reaction coordinate) is increased from its initial value of 1.002 Å in the IS geometry to 1.230 Å in the TS. Like the case of the IS structure, the hydrogen bonding involving O-H⋯N is still intact in the TS structure and this stabilization is the possible reason for barrier-less nature of the second step. Lei et al. for the barrier height for the dissociation of the second water molecule for a Ti-CNT system to be 0.12 eV [369]. BNNT and CNT manifest quite different behavior as substrates and in terms of their interaction with water. While the surface of CNT is essentially hydrophobic, the BNNT surface can act as hydrophilic and the N-atoms on the latter's surface may facilitate hydrogen bonding with water molecules. Our observations based on this rationale make Ti-BNNT system a promising candidate for water splitting. Another worth mentioning point is that, in the product state two OH fragments are bonded to Ti adatom with the liberation of one H_2 molecule. Moreover, the heat of formation of the product is estimated to be -0.97 eV which indicates the exothermicity of this step. The preceding discussions, therefore, lead us to conclude that water dissociation on a Ti-BNNT nanostructure is an extremely favorable process.

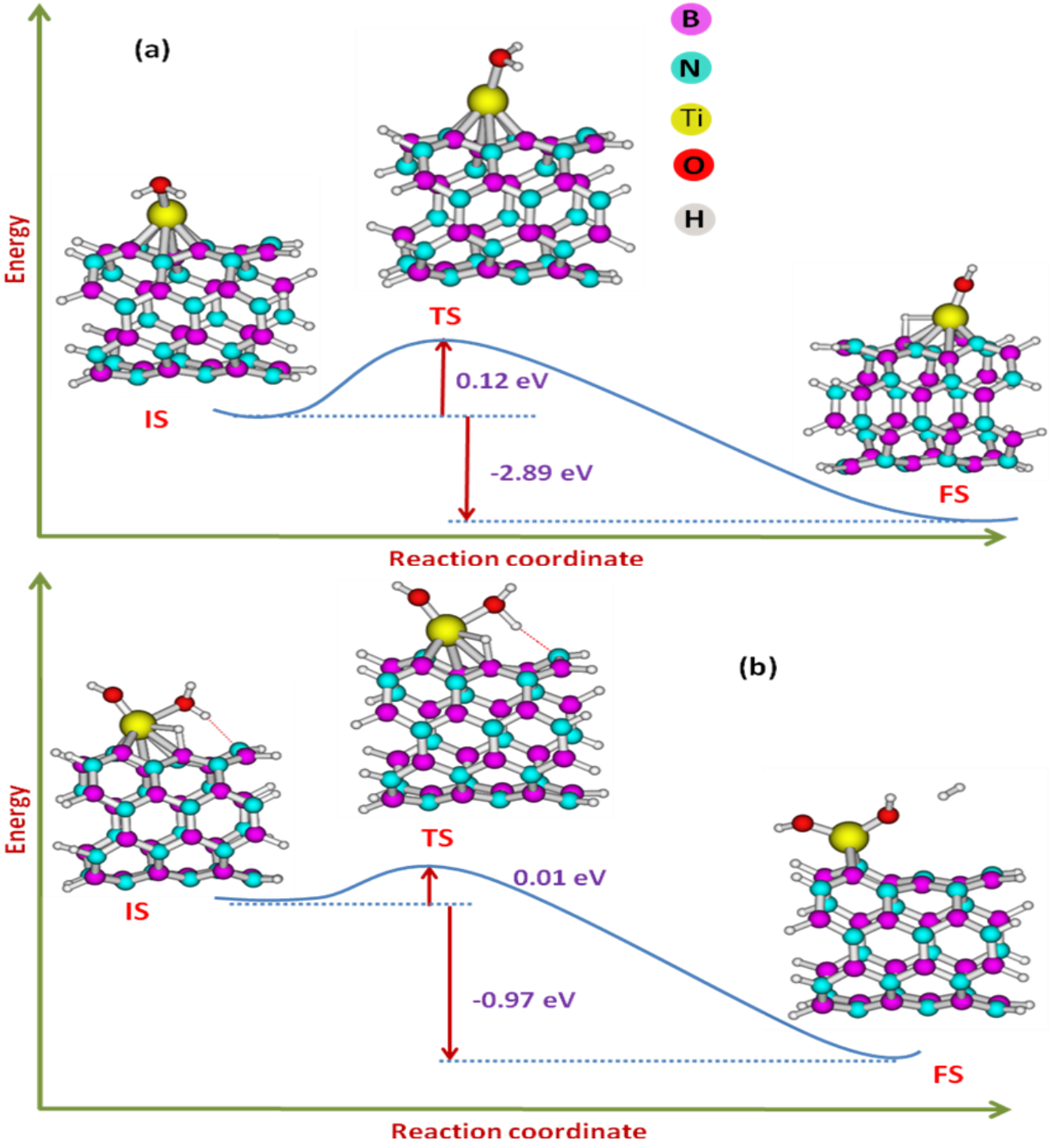

Figure 7.1: The schematic potential energy surface for splitting of first water molecule (a) and second water molecule (b) on a Ti-decorated BNNT.

From the above results it is clear that the dissociation of first molecule of water is a process with minimal barrier and subsequent dissociation of the second water molecule which in turn leads to the formation of hydrogen molecule is almost barrier-less. Some of the interesting innate properties of BNNT like their semiconducting nature irrespective of their chirality, the hydrophilic nature of the surface, can make Ti-BNNT system an effective nanostructure for water splitting and generation of hydrogen.

To elucidate the role of BNNT on the water dissociation reaction, we have also studied the water dissociation process on V atom adsorbed on BNNT. The whole process is presented in Figure 7.2(a) and 7.2(b). In this case, we observed that the water dissociation process leading to the generation of hydrogen atom is also exothermic in nature. The first water molecule binds to the V adatom quite strongly with an binding energy value -1.11 eV. The barrier height for the dissociation of this water molecule is only 0.27 eV. This value is found to be much lower than that of the water dissociation process on isolated metal catalysts but slightly higher for the barrier we have estimated for the Ti-BNNT case. We also studied the interaction and dissociation of second water molecule similar to the Ti case. Although we observed that the V adatom can still bind strongly to the second water molecule with a binding energy value of -1.22 eV, the barrier for the splitting of this second water molecule increased to a value close to 1 eV. The difference in barrier height in these two cases largely related to the stabilization of the transition state geometry. The stabilization of the TS geometry depends on the several factors such as electronic state of the adatom, hydrogen bonding and the interaction of the partially dissociated species with the metal atom and the substrate. However, from the above results, it can be concluded that BNNT plays a key role in the catalytic dissociation of water molecule by the metal atoms adsorbed on its surface.

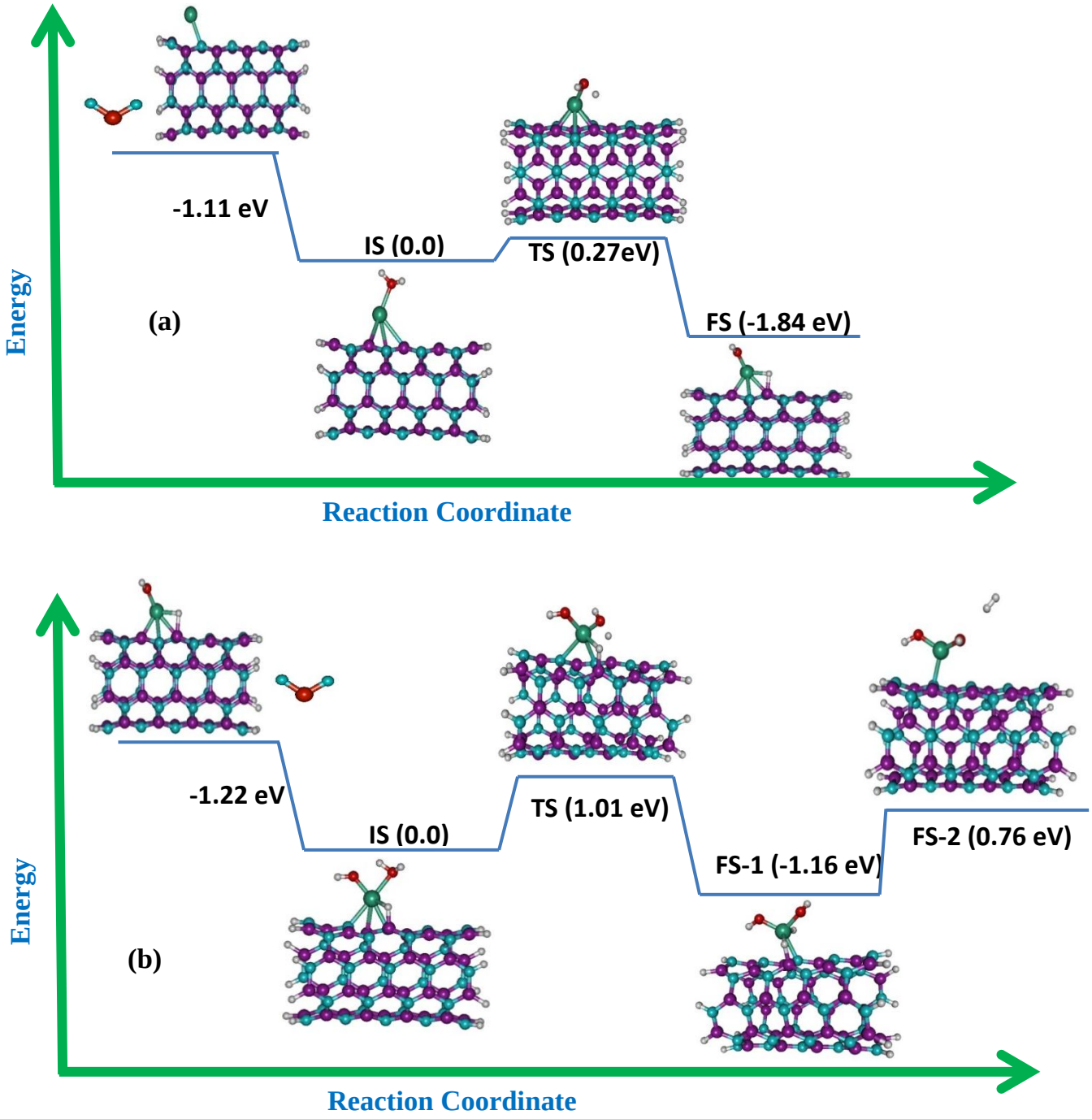

Figure 7.2: The schematic potential energy surface for splitting of first water molecule (a) and second water molecule (b) on a V-decorated BNNT.

4.9 Summary of the work

In this study, we have considered Ti and V decorated BNNT as model nanostructures for the dissociation of water. Our results demonstrate that the adsorption of Ti or V atom on a BNNT surface depends on the surface curvature of the latter and among all the BNNTs considered in the study, highest adsorption energy (~ 1eV) is obtained in the case of BNNT(4,4). Then the interaction of water with the adsorbed Ti and V atom has been studied and the binding is found to be favourable in both cases with the corresponding binding energy value of -1.78 and -1.11 eV for Ti and V. The large binding energy values are attributed to the significant partial positive charge acquired by these adatoms. Further, we have investigated the water dissociation reaction with these BNNT decorated with Ti and V atom. From our calculations, we have demonstrated that the dissociation of water to H and OH fragments is extremely facile with barrier height of 0.12 and 0.27 eV for Ti and V adsorbed structure respectively. We further studied the adsorption and dissociation of another water molecule on the final state (product) of the first water splitting reaction. It is observed that the second water molecule also interact strongly (binding energy > 1eV) with the product and the water dissociation proceed with very low energy barrier (particularly in Ti-BNNT) with the production of H_2 molecule. The barrier height for the water dissociation reaction estimated in the present study is lower than that of pure metal cluster and other supported nanostructured materials. Stabilization of the transition state structure by hydrogen bond involving O-H⋯N is the possible reason for the low barrier of this process. It is lucidly demonstrated through our study that the Ti-decorated BNNT system can be a potentially promising nanostructure for dissociation of water and generation of hydrogen.

Chapter 8

Outlook and future explorations

In this final concluding chapter, we present brief conclusions to all the works elaborated throughout the thesis and also discuss the possible future extensions of these studies. From chapters 2-7, we have mainly concentrated on two important problems viz. the effect of nanoconfinement on chemical processes and the catalytic activity of nanoclusters. Our main objective was to study the behavior of the system in a length scale of nanometer. In addition to the quantum size effect in this length scale, the situation becomes more interesting when the physical confinement effect is imposed on the system. The results obtained from the present work will be helpful in designing new materials for nanofluidic and catalytic applications.

As water present in nanoconfined regimes is crucial to many biological processes, in chapter 2 we have explored the effect of confinement on the structure and properties of water clusters employing carbon nanotube as a model confinement medium. We have used CNTs as confined medium because of its tremendous potential in technologically important applications. It has been demonstrated that the unusual properties of water molecules in carbon nanotubes arise from the interplay between the strong hydrogen bond between water molecules and the confinement effect. The present results is helpful for achieving a comprehensive understanding on the behavior of water clusters in the nonpolar cavities and is of great interests to better characterizing water in a biologically relevant environment. To further understand water clusters confined in hydrophobic protein cavities, interaction between the (hydrophobic or hydrophilic) chemical groups inside the cavities and the confined water clusters have to be taken into account. Therefore, the present work can be extended in that direction to investigate the properties of water in various other mediums in particular the chemically functionalized nanotubes to address these issues.

In chapter 3, the spherical confinement effect due to the fullerene cages on the nature of acid-base complexes is presented. It has been demonstrated that the diameter of fullerene is one of the crucial factor in deciding the chemical properties of the acid-base pair. In particular, we have observed that the confinement effect along with the interaction of acid-base with the fullerene, significantly modify the structure, interaction energy, chemical reactivity and charge transfer in acid-base pair under the spherical cage of fullerene. The results obtained from our study nicely illustrate that the acid base strength can be finely tuned by choosing a proper confinement length. These studies can be further extended to other spherical polar cavities to get more generalized idea on the behaviour of acid and base in confined environment. Furthermore, this work may encourage theorists and experimentalists to explore the molecular cage reaction tank, endohedral chemical reaction, and particular molecular structures inside the cage. In addition, these reactions can also provide deeper insights for several chemical reactions carried out under high pressure conditions.

In chapter 4, we have investigated the solvation of multiply charged anions in finite system. In finite system, the solvation process is modified due to the presence of limited number of solvent molecules. The solvation energy values of an ion are estimated in these environments (N & ∞). A microscopic theory-based bottom-up approach has been used to derive an analytical expression for the solvation energy for a finite (N) system, including the bulk. As an illustrative example, the hydrated doubly charged anions, $SO_4^{-2}.NH_2O$ and $C_2O_4^{-2}.NH_2O$, have been considered, and the calculated bulk solvation energy for the $SO_4{-}2.NH_2O$ system is found to be in very good agreement (within 5%) with the available experimental result. The theory therefore can be useful in deriving the solvation energy and dielectric constant of ions a precise and

accurate manner. These studies can be further extended to incorporate the effect of the medium to get exact solvation behaviour in confined environment.

In chapter 5, we have investigated proton transfer energetics in water and ammonia under nanoconfinement. In many important physical, chemical and biological processes, PT occurs in a nanoconfined environment. To understand the molecular origin of the enhancement in proton transfer, we have studied the proton transfer energetics in CNT and BNNT using the protonated water dimer (Zundel cation) as a model system and employing dispersion corrected DFT method. The effect of water-nanotube interaction and the diameter of nanotube (different degrees of confinement) on the structure and proton transfer energetics of Zundel cation (ZC) has been thoroughly investigated. Among all the nanotubes considered in the present study, it has been concluded that the proton transfer may be facilitated in nanotubes with diameter in the range of 7 to 9 Å. The present study has direct correlation with biological systems. Therefore, the study can be further extended to illustrate the mechanism of proton transfer process in protein environment.

In chapter 6, we have investigated the effect of hydrogen doping in gold clusters for CO oxidation process. It is well known that CO can act like a poisoning agent specifically for the metal catalysts such as Pt and Pd. Hence, the elimination of CO from the reaction mixture is very essential through a suitable catalyst. Herein, we have systematically investigated the effect of hydrogen atoms on the structure, stability and catalytic activity of gold clusters $\{(Au)_n$, n=1 to 6$\}$. In case of hydrogen doped clusters, it is observed that hydrogen atom withdraws electrons from the gold cluster and hence the gold atoms acquire high positive charge. Irrespective of the cluster size or number of hydrogen dopants, the phenomenon of charge transfer from gold cluster to hydrogen dopants is observed. A substantial increase in the CO interaction energy (more than 20% in some cases) is observed when many hydrogen atoms are doped with the gold clusters.

We have also demonstrated that the CO oxidation can occur with these hydrogen doped gold clusters with a significantly lower barrier (100 %) in comparison to their pristine counterparts. The results of the present work can be summarized as; the properties of nanoclusters can be tuned by chemical doping method. The present work will encourage further investigation in the area of doped nanoclusters particularly for environmentally important chemical reactions.

In chapter 7, we have made an attempt to investigate the effect of boron nitride nanotube on the catalytic activity of different metal atoms especially, titanium and vanadium for water dissociation reaction leading to the generation of hydrogen molecules. It has been demonstrated that the dissociation of water to H and OH fragments is extremely facile with barrier height of 0.12 and 0.27 eV for Ti and V adsorbed structure respectively. It is lucidly demonstrated through our study that the Ti-decorated BNNT system can be a potentially promising nanostructure for dissociation of water and generation of hydrogen. This particular work has important applications in the area of hydrogen energy. Therefore, the study can be extended to other nanoclusters such as nickel and hematite and suitable substrates.

In future, we have planned to develop and apply cutting-edge multiscale theoretical and simulation methods at different length and time scales to solve the challenging problems in the area of energy-related materials. In particular, we aim to understand (i) the electronic structure and complex behavior of molecular and nanomaterials, (ii) the thermodynamic processes associated with their catalytic properties, etc. towards designing molecular and nanomaterials as efficient photocatalysts and for hydrogen generation and storage. These objectives will be addressed by a fundamental understanding of the structure-function relationships of the molecular and nanostructured materials through the multiscale modeling and simulation approaches.

References:

[1] The Chemistry of Nanostructured Materials, Edited by P. Yang University of California, Berkeley, USA World Scientific Publishing, (2003).

[2] C.N.R. Rao, G.U. Kulkarni, and P.J. Thomas, Metal nanoparticles and their assemblies, Chem. Soc. Rev., 29 (2000) 27.

[3] Nanotechnology For Dummies, by Richard Booker and Earl Boysen Published by Wiley Publishing, Inc. (2005).

[4] G. Schmid, Ed., Nanoparticles: from Fundamentals to Applications, VCH, Weinheim, (2004).

[5] A. Aviram,; M. Ratner, Molecular Electronics: Science and Technology (Annals of the New York Academy of Sciences), Vol. 852, NYAS, New York, (1998).

[6] M.G. Bawendi, M.L. Steigerwald and L.E. Brus, Annu. Rev. Phys. Chem. 41(1990) 477.

[7] Surface and Nanomolecular Catalysis edited by Ryan Richards, CRC Press Taylor & Francis Group, (2006).

[8] B. Zhou, S. Hermans, and G.A. Somarjai, Eds., Nanotechnology in Catalysis, Vols. 1 and 2, Kluwer Academic/Plenum Publishers, New York, (2004).

[9] Bönnemann H. and Nagabhushana K.S., Chemical synthesis of nanoparticles, in Encyclopedia of Nanoscience and Nanotechnology, Vol. 1, Nalwa, H.S., Ed., American Scientific Publishers, Stevenson Ranch, CA, USA, (2004) 777.

[10] H. Bönnemann and K.S. Nagabhushana, Colloidal nanometals as fuel cell catalyst precursors, in Encyclopedia of Nanoscience and Nanotechnology, Vol. 1, J.A., Schwarz, C.I. Contescu,, and K. Putyera, Eds., Marcel Dekker, New York, (2004) 739.

[11] J.-M. Lehn Supramolecular chemistry: concepts and perspectives, VCH Publishers, New York, (1995).

[12] N. Freestone, M. S. Meeks, C. Higgitt, Gold Bulletin, 4 (2007) 270.

[13] M.C. Daniel, D. Astruc, Chemical Reviews 104 (2004) 293.

[14] G. Schmid, Ed., Clusters and Colloids, VCH, Weinheim, Germany, (1994).

[15] M. Faraday, Philos. Trans. R. Soc., London, 147 (1857) 145.

[16] R. Zsigmondy, Z. Phys. Chem., 56 (1906) 65.

[17] C.J. Jones, S. Aizawa, Adv Microb Physiol., 32 (1991)109.

[18] Handbook of Nanotechnology - Edited by B. Bhushan Springer - Verlag, Heidelberg (2010).

[19] Metal Nanoparticles: Synthesis, Characterization, and Applications, Edited by D. L. Fedlheim and C. A. Foss. CRC Press (2001).

[20] R.P. Feynman, Eng. Sci. 23 (1960) 22

[21] Introduction to Nanoscience and Nanotechnology, Chris Binns, John Wiley & Sons (2010)

[22] C.M. Niemeyer, Angew. Chem. Int. Ed. Engl., 40 (2001) 4128.

[23] C.S.S.R. Kumar, J. Hormes, and C. Leuschner, Eds., Nanofabrication Towards Biomedical Applications, Wiley, Weinheim, (2005).

[24] (a) R. W. Cahn, P. Haasen, E. J. Kramer, "Material Science and Engineering: Characterization of Materials", VCH Publisher Inc., New York. (1991), (b) W. Zhou, Z. L. Wang, "Scanning microscopy for nanotechnology: Techniques and applications", Springer science and business media, New York (2006). (c) M. D. Graef, "Introduction to Conventional Transmission Electron Microscopy", Cambridge University Press, Cambridge, UK (2000). (d) B.

Fultz, J. M. Howe, "Transmission Electron Microscopy and Diffractometry of Materials", Springer Berlin Heidelberg, New York (2008).

[25] Multiscale simulation methods for nanomaterials edited by Richard B. Ross and Sanat Mohanty by John Wiley & Sons, Inc. (2008)

[26] B.F.G. Johnson, Coord. Chem. Rev., 190–192 (1999) 1269.

[27] C. Cui, and C.M. Lieber, Science, 291 (2001) 851.

[28] G. R. Desiraju Crystal engineering: the design of organic solids. Elsevier, New York, (1989).

[29] S. Chen, Adv. Mater., 12 (2000) 186.

[30] A.P. Alivisatos, Science, 271 (1996) 933.

[31] O. M. Yaghi, H. Li, C. Davis, D. Richardson and T. L. Groy, Acc. Chem. Res. 31 (1998) 474.

[32] M. J. Sailor, J. L. Heinrich, and J. M. Lauerhaas, Semiconductor Nanoclusters, Edited . by P. V. Karmat and D. Meisel, Elsevier, Amsterdam, (1996) pp. 209.

[33] Metal Nanoclusters in Catalysis and Materials Science: The Issue of Size Control, Edited by Benedetto Corain, Guenter Schmid, N Toshima, Elsevier Publications (2007).

[34] Y. Tan, Y. Li, D. Zhu, Noble Metal Nanoparticles in Encyclopedia of Nanoscience and Nanotechnology Edited by H. S. Nalwa Volume 8 (2004) 9.

[35] W. Vielstich, A. Lamm, and H. A. Gateiger, Handbook of Fuel Cells, Fundamentals, Technology and Applications, Vols. 1–4, Wiley, West Sussex, (2003).

[36] M. Haruta, T. Kobayashi, H. Sano; N. Yamada, Chem. Lett. 16 (1987) 405.

[37] (a) M. Haruta, Catal. Today 36 (1997) 153–166. (b) M. Haruta, Appl. Catal. A 222 (2001) 427.

[38] M. Haruta, Gold Bull. 37 (2004) 27.

[39] M. Haruta, N. Yamada, T. Kobayashi, S. Iijima, J. Catal. 115 (1989) 301–309. (b) T. Hayashi, K. Tanaka, M. Haruta, J. Catal. 178 (1998) 566.

[40] (a) H. Hakkinen, U. Landman, Phys. Rev. B 62 (2000) R2287. (b) K. H. Allers, H. Pfnur, P. Feulner, J. Chem. Phys. 100 (1994), 3985. (c) A. Eichler, J. Hafner, J. Phys. Rev. B 59 (1999), 5960.

[41] M. Valden, X. Lai, D. W. Goodman, Science 281 (1998) 1647.

[42] F. Boccuzzi, A. Chiorino, M. Manzoli, D. Andreeva, T. Tabakova, J. Catal. 188 (1999) 176.

[43] R. Meyer, C. Lemire, S. K. Shaikhutdinov, H. Freund, H.-J. Gold Bull. 37 (2004) 72.

[44] (a) D. T. Thompson, Top. Catal. 38 (2006) 231 (b) S. Lee, L. M. Molina, M. J. Lopez, J. A. Alonso, B. Hammer, B. Lee, S. Seifert, S. W. E. Winans, J. W. Elam, M. J. Pellin,; S. Vajda, Angew. Chem., Int. Ed. 48 (2009)1467.

[45] (a) P. Pyykko, Angew. Chem. 116 (2004) 4512. (b) Angew. Chem., Int. Ed. 2004, 43, 4412. (c) P. Pyykko, N. Runeberg, Angew. Chem., Int. Ed. 41 (2002) 2174.

[46] (a) A. Stephen, K. Hashmi, G. J. Hutchings, Angew. Chem. 118 (2008) 8064 ;(b) Angew. Chem., Int. Ed. 45 (2006), 7896.

[47] (a) X. Li, B. Kiran, J. Li, H. J. Zhai, L. S. Wang, Angew. Chem.,Int. Ed. 41 (2002) 4786; (b) B. Kiran, X. Li, H. J. Zhai, L.-F. Cui, L.-S. Wang, Angew. Chem., Int. Ed. 43 (2004) 2125.

[48] H. J. Zhai, J. Li, L. S. Wang, J. Chem. Phys. 121 (2004) 8369.

[49] (a) H.-J. Zhai, B. Kiran, L.-S. Wang, J. Chem. Phys. 121 (2004,) 8231. (b) H.-J. Zhai, L.-S. Wang, D. Y. Zubarev, A. I. Boldyrev, J. Phys. Chem. A 110 (2006) 1689. (c) X. Li, B. Kiran, L.-S. Wang, J. Phys. Chem. A109 (2005) 4366.

[50] (a) Y. Gao; S. Bulusu, X. C. Zeng, ChemPhysChem 7 (2006) 2275; (b) L. M. Wang, S. Bulusu, H. J. Zhai, X. C. Zeng, L. S Wang, Angew. Chem., Int. Ed. 46 (2007) 2915; (b) L. M. Wang, S. Bulusu, W. Huang, R. Pal, L. S. Wang, X. C. Zeng, J. Am. Chem. Soc. 129 (2007) 15136; (C) Y. Gao, S. Bulusu, X. C. Zeng, J. Am. Chem. Soc. 127, (2005)15680.

[51] M.-X. Chen, X. H. Yan, J. Chem. Phys. 128 (2008) 174305.

[52] T. K. Ghanty, J. Chem. Phys. 123 (2005) 241101.

[53] T. Baruah, S. A. Blundell, R. R. Zope, Phys. Rev. A 64 (2001) 043202.

[54] D. Fischer, W. Andreoni, A. Curioni, H. Gronbeck, S. Burkart, G. Gantefor, Chem. Phys. Lett. 361 (2002) 389.

[55] R. Coquet, K. L. Howard, D. J. Willock, Chem. Soc. Rev. 37 (2008) 2046.

[56] B. Kiran, X. Li, H.-J. Zhai, L. S. Wang, J. Chem. Phys. 125 (2006) 133204.

[57] L. Gagliardi, P. Pyykko, Phys. Chem. Chem. Phys. 6 (2004) 2904.

[58] (a) H. W. Kroto, J. R. Heath, S. C. O'Brien, R. F. Curl, R. E. Smalley, Nature 318 (1985) 162; (b) W., Krätschmer, et al., Nature, 347 (1990) 354.

[59] Fullerenes: Principles and Applications Edited By Fernando Langa, Jean-Francois Nierengarten Published by RSC publications. (2007)

[60] (a) J. Cioslowski, Electronic structure calculations on fullerenes and their derivatives; Oxford University Press: New York, (1995). (b) M. S. Dresselhaus, G. Dresselhaus, P. C. Eklund, Science of Fullerenes and Carbon Nanotubes; Academic Press: New York, 1996. (c) J. Cioslowski,: J. Am. Chem. Soc. 113 (1991) 4139 (d) Y. H. Hu, E. Ruckenstein. J. Am. Chem. Soc. 127 (2005) 11277, (e) A. A. Popov, S. Yang and L. Dunsch Chemical Reviews, 113 (2013) 5989.

[61] (a) M. N. Chaur, F. Melin, A. L. Ortiz, L. Echegoyen, Angew. Chem. Int. Ed. 48 (2009) 7514. (b) M. Khatua, S. Pan, P. K. Chattaraj, Chem. Phys. Lett. 616–617 (2014) 49.

[62] (a) S. Iijima, Nature 354 (1991) 56. (b) S. Iijima, T. Ichihashi Nature 363 (1993) 603.

[63] (a) R. Tenne, L. Margulis, M. Genut, G. Hodes, Nature 360 (1992) 444 (b) R. Tenne, Nature Nanotechnology 1 (2006) 103. (c) R. Tenne, C. N. R. Rao, Phil. Trans. R. Soc. Lond. A 362 (2004) 2099 & (d) Y. Feldman, E. Wasserman, D. J. Srolovitz, R. Tenne, Science 267 (1995) 222.

[64] M. F. L. De Volder, S. H. Tawfick, R. H. Baughman, A. H. Hart, Science 339 (2013) 535

[65] Carbon nanomaterials edited by Yury Gogotsi , by Taylor and Francis Group (2006).

[66] S. Reich, C. Thomsen, J. Maultzsch, Carbon Nanotubes: Basic Concepts and Physical Properties; Wiley-VCH: Weinheim, Germany, (2004) 215.

[67] Nanotubes and Nanowires by C. N. R. Rao and A. Govindaraj RSC Publications, (2011).

[68] R. H. Baughman, A. A. Zakhidov and W. A. De Heer, Science 297 (2002) 787.

[69] (a) E.G. Rakov, Russ. Chem. Rev. 69 (2000) 35. (b) E.G. Rakov, Russ. Chem. Rev. 70 (2001) 827.

[70] P. Avouris, Chem. Phys. 281 (2002) 429.

[71] T.W. Odom, J.-L. Huang, and C.M. Lieber, Ann. N.Y. Acad. Sci. 960 (2002) 203.

[72] M. Daenen, R.D. de Fouw, B. Hamers, P.G.A. Janssen, K. Schouteden, and M.A.J. Veld, The Wondrous World of Carbon Nanotubes. A Review of Current Carbon Nanotube Technologies. Eindhoven University of Technology, (2003) 93.

[73] R.H. Baughman, A.A. Zakhidov, and W.A. de Heer, Science 297 (2002) 787. (b) Carbon Nanotubes: Present and Future Commercial Applications Science-339 (2013) 535; (c) P. Ajayan-Chem. Rev., 99 (1999) 1787.

[74] (a) Karnik et. al., Nature Communication, 4 (2013) 2220. (b) R. Das et al. Desalination 336 (2014) 97.

[75] Z. Liu et al. ACS Nano 1 (2007) 50.

[76] D. Golberg et.al., Advanced Materials 19 (2007) 2413

[77] C Zhi et.al.,Materials Science and Engineering: R: Reports 70 (2010)92.

[78] C. Y. Won et.al JACS, 129 (2007) 2748

[79] X. Chen, G. X. Cao, A. J. Han, V. K. Punyamurtula, L. Liu, P. J. Culligan, T. Kim, Y . Qiao, Nano Lett 8 (2008) 2988.

[80] (a) S. H. Han,; M. Y. Choi,; P. Kumar,; H. E. Stanley, Nature Physics 6 (2010) 685. (b) V. V. Chaban,; O. V. Prezhdo, ACS Nano 5 (2011) 5647.

[81] (a) M. Alcoutlabi, G. B. McKenna, J. Phys.: Condens. Matter 17 (2005) R461; (b) S. Granick, Science 253 (1991) 1374.

[82] Appl. Surf. Science 253 (2003) 5570.

[83] V. N. Popov, Mater. Science Eng R.: Reports (2004) 43.

[84] Hummer et. al, Nature 414 (2001) 188.

[85] Kplen, J. Am. Chem. Soc. 137 (2015) 477.

[86] Chem. Commun. 47 (2008) 627

[87] Acc. Chem. Res. 44 (2011) 553

[88] (a) W. Chen et.al, J. Am. Chem. Soc. 129 (2007) 7421. (b) W. Chen et al., J. Am. Chem. Soc. 128 (2006) 3136

[89] W. Chen et.al, J. Am. Chem. Soc. 130 (2008) 9414

[90] X. Pan et al., Nat. Mater.6 (2007) 507

[91] J. Xiao et al., J. Am. Chem. Soc. 137 (2015) 477

[92] W. Chen et al., J. Am. Chem. Soc. 133 (2011) 14896

[93] F. Zhang et al., ACS Catal. 5 (2015) 1381

[94] R. G. Amorim, A. Fazzio, A. J. R. da Silva and A. R. Rochaa, Nanoscale 5 (2013) 2798.

[95] L. Pauling, The Nature of Chemical Bond and Structure of Molecule and Crystals; Oxford and IBH: New Delhi, (1967).

[96] (a) R. B. Woodward, R. Hoffman, J. Am. Chem. Soc. 87 (1965) 2511; (b) ibid. Acc. Chem. Res.; 1 (1968) 17; (c) ibid. The Conservation of Orbital Symmetry, New York, Academic Press, (1989). (d) G. Klopman, J. Am. Chem. Soc. 86 (1964) 1463; (e) Theoretical Models of Chemical Bonding: The Concept of the Chemical Bond; Maksic, Z. B. Ed.; Springer-Verlag: Berlin, (1990).

[97] K. Szalewicz, B. Jeziorski, Molecular Interactions: from van der Waal`s to strongly Bond Complexes: Ed. by Scheiner, S. p.3, John-Wiley&Sons New York, (1997). (b) A. J. Stone, Theory of Intermolecular Forces. Oxford University Press, new York (1996).

[98] (a) C. E. Dykstra, J. Mol. Struct. THEOCHEM, 573 (2001) 63; (b) C. E. Dykstra, J. M. Lisy, J. Mol. Struct. THEOCHEM, 500 (2000) 375

[99] (a) A. D. Buckingham; P. W. Fowler,; A. J. Stone Int. Rev. Phys. Chem. 5 (1986) 107. (b) A. D. Buckingham; P. Fowler; J. M. Huston Chem. Rev. 88 (1988) 963. (d) A. D.; Buckingham Adv. Chem. Phys. 12 (1967) 107.

[100] (a) G. Chalasinki,; M. Gutowski,; Chem. Rev. 88 (1988) 943 (b) B. Jeziorski,; R. Moszynski; K. Szalewicz Chem. Rev. 94 (1994) 1887. (c) B. Jeziorski,; K. Szalewicz Intermolecular Interactions by Perturbation Theory, In Encyclopadia of Computational Chemistry, Ed. by P.v.R. Schleyer; N. L. Allinger,; T. Clark, J. Gasteiger,; P. A. Kollman,; H. F. Schaefer,; P. R. Schreiner, Wiley, UK, , 2 (1998), p.1376

[101] Supramolecular Chemistry J. W. Steed, J. L. Atwood. – 2nd ed. John Wiley & Sons, Ltd (2009)

[102] G. A. Jeffrey, An Introduction to Hydrogen Bonding, Oxford University Press: Oxford, (1997).

[103] E. Schrödinger, Quantisierung als Eigenwertproblem. Ann. Phys., 385 (1926) 437.

[104] Quantum Chemistry, by Ira N. Levine Fifth Edition, by Prentice-Hall, Inc. (2000)

[105] R. Mc Weeny, Coulson`s Valence, Oxford University Press , Oxford, (1979).

[106] X. Simons and X Nichols, Quantum Mechanics in Chemistry, Oxford University Press, (1997).

[107] A. Szabo, and N. S. Ostlund, Modern Quantum Chemistry, rev. ed., McGraw-Hill, (1996).

[108] (a) J. C. Slater, Quantum Theory of Atomic Structure, vols. I and II, McGraw-Hill, (1960); (b) J. C. Slater, Quantum Theory of Molecules and Solids, vol. I, Electronic Structure of Molecules, McGraw-Hill, (1963).

[109] P. W.Atkins, and R. S. Friedman, Molecular Quantum Mechanics, 3rd ed., Oxford University Press, (1997).

[110] K. Fukui, Theory of Orientation and Stereo Selection, Springer-Verlag, Berlin (1975).

[111] A. Stretwieser, Jr., Molecular Orbital Theory for Organic Chemists; John-Wiley & Sons, New York, (1961).

[112] M.J.S. Dewar, The Molecular Orbital Theory of Organic Chemistry; McGraw-Hill, New York (1969).

[113] (a) M.J.S. Dewar, Trans. Faraday Soc., 42 (1946) 764; (b) C. A. Coulson, Discussions Faraday Soc; 2 (1947) 9; (c) ibid J. Chem. Phys., 45 (1948) 243; (d) C. A. Coulson, H. Longuet-

Higgins, C; Proc. Roy. Soc. A (London), 191 (1947) 39; (e) G. W. Wheland, J. Am. Chem. Soc. 64 (1942) 900.

[114] (a) K. Fukui, ; T. Yonezawa,; H. Shingu, J. Chem. Phys., 20 (1952) 722; (b) K. Fukui, T. Yonezawa,. C. Nagata, H. Shingu, J. Chem. Phys. 22 (1954) 1433; (c) S. Nagakura,; J. Tanaka, J. Chem. Soc. Japan, 75 (1954) 993. (d) K. Fukui, Molecular Orbitals in Chemistry, physics and biology, Ed. by P. O. Lowdin and B. Pullman, Academic Press, New York. 1964, p.513. (e) Fukui, K. Science, 218 (1982) 747.

[115] R.S. Mulliken, J. Am. Chem. Soc. 74 (1952) 811.

[116] M. Born and J. R. Oppenheimer (1927). "Zur Quantentheorie der Molekeln" [On the Quantum Theory of Molecules]. Annalen der Physik (in German) 389 (1927) 457.

[117] (a) D. R. Hartree, Proc. Cambridge Phil Soc. 24 (1928) 89. (b) V. Z. Fock, Phisyk, 61 (1930) 126.

[118] C. C. J. Roothaan, Rev. Mod. Phys. 23 (1951) 69; (b) Roothaan, C. C. J. Rev. Mod. Phys. 32 (1960) 179.

[119] (a) P. Fulde, Electron Correlations in Molecules and Solids, Third Edition Springer, Berlin (1995). (b) E. R. Davidson, Encycl. Comput. Chem. 3 (1998) 1811. (c) C. Moller and M. S. Plesset Phys. Rev. 46, (1934) 618. (d) I. Shavitt, Mol. Phys. 94 (1998) 3. (e) R. J. Bartlett, Ann. Rev. Phys. Chem., 32 (1981) 359. (f) Modern Electronic Structure Theory, Yarkony, D. R., Ed., World Scientific: New York, Part 2 (1995) Chapter 6. (f) M. R. A. Blomberg, and P. E. M. Siegbahn, In: Computational Chemistry, ACS Symposium (1998). (g) E. R. Davidson, Adv. Quantum Chem. 6 (1972) 235. (h) F. Bernardi, A. Bottini, J. J. W. McDougall, M. A. Robb, H. B. Schlegel, Far. Symp. Chem. Soc. 19 (1984) 137. (i) R. McWeeny, “The Nature of Electron Correlation in Molecules”, Int. J. Quant. Chem., 1S (1967) 351.

[120] (a) R. G. Parr, W. Yang Density-Functional Theory of Atoms and Molecules Oxford, Oxford (1989). (b) Density Functional Theory E. K. U. Gross, R. M. Dreizler, Eds., Plenum, New York (1995). (c) W. Koch, M. C. Holthausen, A Chemist's Guide to Density Functional Theory Wiley-VCH, Weinheim (2000). (d) E. S. Kryachko, E. V. Ludeña, Energy Density Functional Theory of Many-Electron Systems, Kluwer Academic Press, (1990). (f) (j) T. Ziegler, Chem. Rev., 91 (1991) 651.

[121] L. H. Thomas, Proc. Camb. Phil. Soc., 23 (1927) 542. (b) E. Fermi, Rend. Accad.Lincei, 6 (1927) 602. (c) N. H. March, , Electron Density Theory of Atoms and Molecules, Academic Press, London (1992) .

[122] P. A. M. Dirac, Proc. Camb. Phil. Soc., 26 (1930) 376

[123] (a) P. Hohenberg, and W. Kohn, Phys. Rev., 136 (1964) B864. (b) W. Kohn, and L. J. Sham, Phys. Rev., 140, (1965)A1133.; (c) W. Kohn, A. D. Becke,, R. G. Parr, J. Phys. Chem., 100 (1996) 12974. (d) Computational Chemistry and Molecular Modeling, Principles and Applications, by K. I. Ramachandran, G. Deepa, K. Namboori, Springer-Verlag Berlin, Heidelberg (2008).

[124] (a) Becke, A. D. J. Chem. Phys., 84 (1986) 4524; (b) Becke, A. D. J. Chem. Phys., 88 (1988) 1053. (c) Becke, A. D. Phys. Rev. A, 38 (1988) 3098.

[125] (a) C. Lee, W. Yang, R. G. Parr, Phys. Rev. B, 37 (1988) 785. (b) J. P. Perdew, K. Burke, and M. Ernzerhof, Phys. Rev. Lett. 77, 3865 (1996). (c) J. P. Perdew, K. Burke, and M. Ernzerhof, Phys. Rev. Lett. 77 (1996) 3865. (d) J. Tao, J. P. Perdew, V. N. Staroverov, and G. E. Scuseria, Phys. Rev. Lett. 91 (2003) 146401. (e) S. H. Vosko, L. Wilk, and M. Nusair, Can. J. Phys. 58 (1980) 1200.(f) A. D. Boese and N. C. Handy, J. Chem. Phys. 116 (2002) 9559. (f) J. Heyd, G. E. Scuseria and M. Ernzerhof J. Chem. Phys. 118 (2003) 8207. (g) Y. Zhao and D. G.

Truhlar Theo. Chem. Acc. 120 (2008) 215. (h) Y. Zhao and D. G. Truhlar J. Phys. Chem. A, 110 (2006)13126.

[126] S. K. Pal, J. Peon, A. H. Zewail, Proc. Natl. Acad. Sci. U. S. A. 99 (2002) 1763.

[127] J. A. Ernst, R. T. Clubb, H. X. Zhou, A. M. Gronenborn, G. M. Clore, Science 267 (1995) 1813.

[128] J. J. Dwyer, A. G. Gittis, D. A. Karp, E. E. Lattman, D. S. Spencer, W. E. Stites, B. G-M. E, Biophys. J. 79 (2000) 1610.

[129] B. Yu, M. Blaber, M. Gronenborn, M. Clore, L. D. Caspar, Proc. Natl. Acad. Sci. U S A., 96 (1999) 103.

[130] A. M. Buckle, P. Cramer, A. R. Fersht, Biochemistry 35 (1996) 4298.

[131] R. Wolfenden, A. Radzicka, Science 265 (1994) 936.

[132] V. N. Popov, Mater. Sci. Eng. R: Reports 43 (2004) 61.

[133] G. Zuo, R. Shen, S. Ma, W. Guo, ACS Nano 4 (2010) 205.

[134] Y. Zhao, L. Song, K. Deng, Adv. Mater. 20 (2008) 1772.

[135] Q. Yuan, Y-P. Zhao, J. Am. Chem. Soc. 131 (2009) 6374.

[136] B. Corry, J. Phys. Chem. B 112 (2008) 1427.

[137] A. Bianco1, K. Kostarelos, M. Prato, Current Opinion in Chemical Biology 9 (2005) 674.

[138] G. Cicero, J.C. Grossman, E. Schwegler, F. Gygi, G. Galli, J. Am. Chem. Soc. 130 (2008) 1871.

[139] R. Zangi, A. E. Mark, Phys. Rev. Lett. 91 (2003) 025502.

[140] R. Zangi, A. E. Mark, J. Chem. Phys. 119 (2003) 1694.

[141] J. Marti, G. Nagy, M. C. Gordillo, E. Guàrdia, J. Chem. Phys. 124 (2006) 094703.

[142] T. Nanok, N. Artrith, P. Pantu, P. A. Bopp, J. Limtrakul, J. Phys. Chem. A, 113 (2009) 2103.

[143] C.Y. Won, N.R. Aluru, J. Phys. Chem. C, 112 (2008) 1812.

[144] F-X. Coudert, R. Vuilleumier, A. Boutin, ChemPhysChem 7 (2006) 2464.

[145] G. Hummer, J.C. Rasaiah, J.P. Noworyta, Nature 414 (2001) 188.

[146] A.I. Kolesnikov, J-M. Zanotti, C.-K. Loong, P. Thiyagarajan, A.P. Moravsky, R.O. Loutfy, C.J. Burnham, Phys. Rev. Lett. 93 (2004) 035503.

[147] S. Ghosh, K. V. Ramanathan, A. K. Sood, Europhys. Lett. 65 (2004) 678.

[148] Y. Maniwa, H. Kataura, M. Abe, S. Suzuki, Y. Achiba, J. Phys. Soc. Jpn. 71 (2002) 2863.

[149] Y. Maniwaa, H. Kataurab, M. Abea, A. Udakaa, S. Suzukic, Y. Achibac, H. Kiraa, K. Matsudaa, Chem. Phys. Lett. 401 (2005) 534.

[150] O. Byl, J-C. Liu, Y. Wang, W-L. Yim, J. K. Johnson, J. T. Yates, J. Am. Chem. Soc. 128 (2006) 12090.

[151] A. Alexiadis, S. Kassinos, Chem. Rev. 108 (2008) 5014.

[152] M.C. Gordillo, J. Martí, Chem. Phys. Lett. 329 (2000) 341

[153] S. Joseph, N. R. Aluru, Nano Lett. 8 (2008) 452.

[154] A. Striolo, Nano Lett. 6 (2006) 633.

[155] D. J. Mann, M. D. Halls, Phys. Rev. Lett. 90 (2003) 195503.

[156] T. Ohba, K. Kaneko, M. Endo, K. Hata, H. Kanoh, Langmuir 29 (2013) 1077.

[157] J. K. Holt, Adv. Mater. 21 (2009) 3542.

[158] J. K. Holt, H. G. Park, Y. Wang, Science 312 (2006) 1034.

[159] M. Majumder, N. Chopra, R. Andrews, B. J. Hinds, Nature 438 (2005) 44.

[160] R. J. Mashl, S, Joseph , N. R. Aluru , E. Jakobsson, Nano Lett. 3 (2003) 589.

[161] K. Koga, G. T. Gao, H. Tanaka, X. C. Zeng, Nature 412 (2001) 802.

[162] Y. Liu, Q. Wang, T. Wu, L. Zhang, J. Chem. Phys. 123 (2005) 234701.

[163] L. Wang, J. Zhao, F. Li, H. Fang, J.P. Lu, J. Phys. Chem. C 113 (2009) 5368.

[164] X. Li, Y. Shi, J. Chem. Phys. 136 (2012) 175101.

[165] J. Hernández-Rojas, F. Calvo, J. Bretón, J.M. Gomez Llorente, J. Phys. Chem. C 116 (2012) 17019.

[166] R. Ahlrichs, M. Bär, M. Häser, H. Horn, C. Kölmel, Chem. Phys. Lett. 162 (1989) 165.

[167] V.S. Bryantsev, M.S. Diallo, A.C.T. van Duin, W.A. Goddard, J. Chem. Theory Comput. 5 (2009) 1016.

[168] S. Grimme, J. Comput. Chem. 27 (2006) 1787.

[169] J. P. Merrick, D. Moran, J. Phys. Chem. A 111 (2007) 11683.

[170] S. S. Xantheas, C. J. Burnham, R. J. Harrison, J. Chem. Phys. 116 (2002) 1493.

[171] S.S. Xantheas, T. H. Dunning Jr., J. Chem. Phys. 99 (1993) 8774.

[172] C.J. Gruenloh, Science 276 (1997) 1678.

[173] R. N. Pribble, T. S. Zwier, Science 265 (1994) 75.

[174] J. P. Devlin, V. Buch, J. Phys. Chem. 1995, 99, 16534.

[175] P. Andersson, C. Steinbach, U. Buck, Eur. Phys. J. D 24 (2003) 53.

[176] M. E. Dunn, T. M. Evans, J. Phys. Chem. A 110 (2006) 303.

[177] S. Suzuki, P.G. Green, R.E. Bumgarner, S. Dasgupta, W.A. Goddard, G.A. Blake, Science 257 (1992) 942.

[178] I. Rozas, I. Alkorta, J. Elguero, J. Phys. Chem. A 101 (1997) 9457.

[179] M. Sharma, D. Donadio, E. Schwegler, Nano Lett. 8 (2008) 2959.

[180] J. Cioslowski, J. Am. Chem. Soc. 113 (1991) 4139.

[181] W. Jaskólski, Phys. Rep. 271 (1996) 1.

[182] M. Khatua, S. Pan, P.K. Chattaraj, J. Chem. Phys. 140 (2014) 164306.

[183] P. Lipkowski, J. Kozlowska, A. Roztoczynska, W. Bartkowiak, Phys. Chem. Chem. Phys. 16 (2014) 1430.

[184] D. Chakraborty, P.K. Chattaraj, Chem. Phys. Lett. 621 (2015) 29

[185] P.K. Chattaraj, U. Sarkar, J. Phys. Chem. A 107 (2003) 4877

[186] W. Bartkowiak, K. Strasburger, J. Mol. Struct. THEOCHEM 960 (2010) 93

[187] B. Chatelet, H. Gornitzka, V. Dufaud, E. Jeanneau, J.-P. Dutasta, A. Martinez, J. Am. Chem. Soc. 135 (2013) 18659

[188] A. Borgoo, D.J. Tozer, P. Geerlings, F. De Proft, Phys. Chem. Chem. Phys. 11 (2009) 2862

[189] A.L. Buchachenko, J. Phys. Chem. B 105 (2001) 5839

[190] Y.H. Hu, E. Ruckenstein, J. Am. Chem. Soc. 127 (2005) 11277

[191] A.A. Popov, S. Yang, L. Dunsch, Chem. Rev. 113 (2013) 5989

[192] J.F. Stoddart, Angew. Chem. Int. Ed. in English 30 (1991) 70.

[193] M.N. Chaur, F. Melin, A.L. Ortiz, L. Echegoyen, Angew. Chem. Int. Ed. in English 48 (2009) 7514

[194] M. Khatua, S. Pan, P.K. Chattaraj, Chem. Phys. Lett. 616–617 (2014) 49

[195] C.N. Ramachandran, N. Sathyamurthy, Chem. Phys. Lett. 410 (2005) 348

[196] A. Equbal, S. Srinivasan, C.N. Ramachandran, N. Sathyamurthy, Chem. Phys. Lett. 610–611 (2014) 251

[197] T.B. Lee, M.L. McKee, J. Am. Chem. Soc. 130 (2008) 17610

[198] M. Bühl, W. Thiel, Chem. Phys. Lett. 233 (1995) 585

[199] G.A. Dolgonos, G.H. Peslherbe, Phys. Chem. Chem. Phys. 16 (2014) 26294

[200] A. Krapp, G. Frenking, Chemistry – A European Journal, 13 (2007) 8256

[201] A.A. Popov, S.M. Avdoshenko, A.M. Pendas, L. Dunsch, Chem. Commun. 48 (2012) 8031

[202] F. Ma, Z.-R. Li, H.-L. Xu, Z.-J. Li, D. Wu, Z.-S. Li, F.L. Gu, ChemPhysChem 10 (2009) 1112

[203] B.G. Janesko, J. Chem. Theory Comput. 6 (2010) 1825

[204] A. Haaland, Angew. Chem. Int. Ed. in English 28 (1989) 992

[205] Y. Mo, L. Song, W. Wu, Q. Zhang, J. Am. Chem. Soc. 126 (2004) 3974

[206] J.A. Plumley, J.D. Evanseck, J. Phys. Chem. A 111 (2007) 13472

[207] Y. Mo, J. Gao, J. Phys. Chem. A 105 (2001) 6530

[208] K.R.S. Chandrakumar, S. Pal, J. Phys. Chem. A 106 (2002) 11775

[209] C.W. Hamilton, R.T. Baker, A. Staubitz, I. Manners, Chem. Soc. Rev. 38 (2009) 279

[210] A. Staubitz, A.P.M. Robertson, I. Manners, Chem. Rev. 110 (2010) 4079

[211] T.B. Marder, Angew. Chem. Int. Ed. in English 46 (2007) 8116

[212] F.H. Stephens, V. Pons, R. Tom Baker, Dalton Transactions, (2007) 2613

[213] J. Demaison, J. Liévin, A.G. Császár, C. Gutle, J. Phys. Chem. A 112 (2008) 4477.

[214] M.P. Mitoraj, J. Phys. Chem. A 115 (2011) 14708.

[215] T.M. Gilbert, J. Phys. Chem. A 108 (2004) 2550.

[216] V. Horváth, A. Kovács, I. Hargittai, J. Phys. Chem. A 107 (2003) 1197.

[217] A. Skancke, P.N. Skancke, J. Phys. Chem. 100 (1996) 15079.

[218] L.R. Thorne, R.D. Suenram, F.J. Lovas, J. Chem. Phys. 78 (1983) 167.

[219] K.R.S. Chandrakumar, S. Pal, J. Phys. Chem. A, 106 (2002) 5737.

[220] M.D. Ganji, M. Mohseni, O. Goli, J. Mol. Struct. THEOCHEM 913 (2009) 54.

[221] K. Kobayashi, Y. Sano, S. Nagase, J. Comput. Chem. 22 (2001) 1353.

[222] T. Korona, H. Dodziuk, J. Chem. Theory Comput. 7 (2011) 1476.

[223] H. Ohtaki, T. Radani, Chem. Rev. 93 (1993) 1157.

[224] M. Born, Z. Phys. 1 (1920) 45.

[225] Y. Marcus, Ion Solvation; Wiley: New York, 1985.

[226] Y. Marcus, Chem. Rev. 88 (1988) 1475.

[227] R. A. Robinson, R.H. Stokes, Butterworths: London, U. K., 1955.

[228] P. J. Rossky, Annu. Rev. Phys. Chem. 36 (1985) 321.

[229] P. G. Wolynes, Annu. Rev. Phys. Chem. 31 (1980) 345.

[230] M. F. Kropman, H. J. Bakker, Science 291 (2001) 2118.

[231] D. Eisenberg, A. D. Mclachlan, Nature 319 (1986) 199.

[232] A. K. Pathak, A. K. Samanta, D. K. Maity, T. Mukherjee, S. K. Ghosh, Phys. Rev. E 83 (2011) 21112 and references there in.

[233] A. K. Samanta, S. M. Ali, S. K. Ghosh, Phys. Rev. Lett. 87 (2001) 245901.

[234] R. Neubert, Pharm. Res. 6 (1989) 743.

[235] P. Slavicek, B. Winter, M. Faubel, S. E. Bradforth, P. Jungwirth, J. Am. Chem. Soc. 131 (2009) 6460.

[236] W. H. Robertson, M. A. Johnson, Annu. Rev. Phys. Chem. 54 (2003) 173.

[237] X. B. Wang, L. S. Wang, Annu. Rev. Phys. Chem. 60 (2009) 105.

[238] A. E. Bragg, J. R. R. Verlet, A. Kammrath, O. Cheshnovsky, D. M. Neumark, Science 306 (2004) 669.

[239] M. F. Bush, R. J. Saykally, E. R. Williams, J. Am. Chem. Soc. 129 (2007) 2220.

[240] M. Miyazaki, A. Fujii, T. Ebata, N. Mikami, Science 304 (2004) 1134.

[241] D. J. Miller, J. M. Lisy, J. Am. Chem. Soc. 130 (2008) 15381.

[242] J. L. Alonso, E. J. Cocinero, A. Lesarri, M. E. Sanz, J. C. López, Angew. Chem. Int. Ed. in English 45 (2006) 3471.

[243] A. Ben-Naim, Molecular Theory of Solutions, Oxford University Press, 2006.

[244] J. J.Salacuse, A. R. Denton, P. A. Egelstaff, Physical Review E, 53 (1996) 2382.

[245] G. C. Lynch, B. M. Pettitt, Chem. Phys. 258 (2000) 405.

[246] X. B. Wang, X. Yang, J. B. Nicholas, L. S. Wang, Science 294 (2001) 1322.

[247] P. Delahay, Acc. Chem. Res, 15 (1982) 40.

[248] W. R. Cannon, B. M. Pettitt, J. A. McCammon, J. Chem. Phys. 98 (1994) 6225.

[249] E. R. Nightingale, J. Chem. Phys. 63 (1959) 1381.

[250] J.H. Wang, Science 161 (1968) 328.

[251] K.-D. Kreuer, S.J. Paddison, E. Spohr, M. Schuster, Chem. Rev. 104 (2004) 4637.

[252] J.C. Rasaiah, S. Garde, G. Hummer, Annu. Rev. Phys. Chem. 59 (2008) 713.

[253] P. Balbuena, J. Seminario, Nanomaterials: Design and Simulation, Theoretical and Computational Chemistry, Elsevier, 2006.

[254] R. Mancinelli, J. Phys.: Condens. Matter. 22 (2010) 404213.

[255] S. Granick, Science 253 (1991) 1374.

[256] W.H. Thompson, Annu. Rev. Phys. Chem. 62 (2011) 599.

[257] A. Noy, H.G. Park, F. Fornasiero, J.K. Holt, C.P. Grigoropoulos, O. Bakajin, Nano Today 2 (2007) 22.

[258] Y. Jiao, A. Du, M. Hankel, S.C. Smith, Phys. Chem. Chem. Phys. 15 (2013) 4832.

[259] A. Alexiadis, S. Kassinos, Chem. Rev. 108 (2008) 5014.

[260] J. Kofinger, G. Hummer, C. Dellago, Phys. Chem. Chem. Phys. 13 (2011) 15403.

[261] B. Mukherjee, P.K. Maiti, C. Dasgupta, A.K. Sood, J. Chem. Phys. 126 (2007) 124704.

[262] B. Mukherjee, P.K. Maiti, C. Dasgupta, A.K. Sood, J. Nanosci. Nanotechnol. 7 (2007) 1796.

[263] A. Das, S. Jayanthi, H.S.M.V. Deepak, K.V. Ramanathan, A. Kumar, C. Dasgupta, A.K. Sood, ACS Nano 4 (2010) 1687.

[264] V.V. Chaban, V.V. Prezhdo, O.V. Prezhdo, ACS Nano 6 (2012) 2766.

[265] J. Chen, X.-Z. Li, Q. Zhang, A. Michaelides, E. Wang, Phys. Chem. Chem. Phys. 15 (2013) 6344.

[266] R.H. Baughman, A.A. Zakhidov, W.A. de Heer, Science 297 (2002) 787.

[267] B. Corry, J. Phys. Chem. B 112 (2008) 1427.

[268] S. Ghosh, A.K. Sood, N. Kumar, Science 299 (2003) 1042.

[269] H.-J. Wang, X.-K. Xi, A. Kleinhammes, Y. Wu, Science 322 (2008) 80.

[270] C. Dellago, M.M. Naor, G. Hummer, Phys. Rev. Lett. 90 (2003) 105902.

[271] A. Bankura, A. Chandra, J. Phys. Chem. B 116 (2012) 9744.

[272] Z. Cao, Y. Peng, T. Yan, S. Li, A. Li, G.A. Voth, J. Am. Chem. Soc., 132 (2010) 11395.

[273] N. Agmon, Chem. Phys. Lett., 244 (1995) 456.

[274] O. Markovitch, H. Chen, S. Izvekov, F. Paesani, G.A. Voth, N. Agmon, J. Phys. Chem. B, 112 (2008) 9456.

[275] M.L. Brewer, U.W. Schmitt, G.A. Voth, Biophysical Journal, 80 (2001) 1691.

[276] J. Su, H. Guo, J. Phys. Chem. B, 116 (2012) 5925.

[277] D. Golberg, Y. Bando, C.C. Tang, C.Y. Zhi, Advanced Materials, 19 (2007) 2413.

[278] C. Zhi, Y. Bando, C. Tang, D. Golberg, Materials Science and Engineering: R: Reports, 70 (2010) 92.

[279] J. Wang, C.H. Lee, Y.K. Yap, Nanoscale, 2 (2010) 2028.

[280] T.A. Hilder, D. Gordon, S.-H. Chung, Small, 5 (2009) 2183.

[281] C.Y. Won, N.R. Aluru, Chem. Phys. Lett., 478 (2009) 185.

[282] J.J. Sardroodi, J. Azamat, A. Rastkar, N.R. Yousefnia, Chemical Physics, 403 (2012) 105.

[283] G. Ciofani, V. Raffa, A. Menciassi, A. Cuschieri, Nano Today, 4 (2009) 8.

[284] L. Calucci, G. Ciofani, D. De Marchi, C. Forte, A. Menciassi, L. Menichetti, V. Positano, J. Phys. Chem. Letters, 1 (2010) 2561.

[285] W. Lei, D. Portehault, D. Liu, S. Qin, Y. Chen, Nat Commun, 4 (2013) 1777.

[286] H. Mousavi, J. Kurdestany, M. Bagheri, Appl. Phys. A, 108 (2012) 283.

[287] C.Y. Won, N.R. Aluru, J. Am. Chem. Soc., 129 (2007) 2748.

[288] C.Y. Won, N.R. Aluru, J. Am. Chem. Soc., 130 (2008) 13649.

[289] S. Liu, D. Guo, G. Xie, Journal of Applied Physics, 108 (2010) 084315.

[290] W. Kulig, N. Agmon, J. Phys. Chem. B, 118 (2013) 278.

[291] J.M. Headrick, E.G. Diken, R.S. Walters, N.I. Hammer, R.A. Christie, J. Cui, E.M. Myshakin, M.A. Duncan, M.A. Johnson, K.D. Jordan, Science, 308 (2005) 1765.

[292] S. Scheiner, J. Am. Chem. Soc., 103 (1981) 315.

[293] C. Lao-ngam, P. Asawakun, S. Wannarat, K. Sagarik, Phys. Chem. Chem. Phys., 13 (2011) 4562.

[294] C. Lao-ngam, M. Phonyiem, S. Chaiwongwattana, Y. Kawazoe, K. Sagarik, Chemical Physics, 420 (2013) 50.

[295] Y. Xie, R.B. Remington, H.F. Schaefer Iii, J. Chem. Phys., 101 (1994) 4878.

[296] A.A. Auer, T. Helgaker, W. Klopper, Phys. Chem. Chem. Phys., 2 (2000) 2235.

[297] E.S. Stoyanov, I.V. Stoyanova, F.S. Tham, C.A. Reed, J. Am. Chem. Soc., 131 (2009) 17540.

[298] H. Luecke, B. Schobert, H.-T. Richter, J.-P. Cartailler, J.K. Lanyi, Science, 286 (1999) 255.

[299] S. Furutaka, S.-i. Ikawa, J. Chem. Phys., 117 (2002) 751.

[300] L.I. Yeh, M. Okumura, J.D. Myers, J.M. Price, Y.T. Lee, J. Chem. Phys., 91 (1989) 7319.

[301] L.I. Yeh, Y.T. Lee, J.T. Hougen, Journal of Molecular Spectroscopy, 164 (1994) 473.

[302] K.R. Asmis, N.L. Pivonka, G. Santambrogio, M. Brümmer, C. Kaposta, D.M. Neumark, L. Wöste, Science, 299 (2003) 1375.

[303] T.D. Fridgen, T.B. McMahon, L. MacAleese, J. Lemaire, P. Maitre, J. Phys. Chem. A, 108 (2004) 9008.

[304] J.M. Headrick, J.C. Bopp, M.A. Johnson, J. Chem. Phys., 121 (2004) 11523.

[305] N.I. Hammer, E.G. Diken, J.R. Roscioli, M.A. Johnson, E.M. Myshakin, K.D. Jordan, A.B. McCoy, X. Huang, J.M. Bowman, S. Carter, J. Chem. Phys., 122 (2005) 244301.

[306] G.E. Douberly, R.S. Walters, J. Cui, K.D. Jordan, M.A. Duncan, J. Phys. Chem. A, 114 (2010) 4570.

[307] E.F. Valeev, H.F. Schaefer Iii, J. Chem. Phys., 108 (1998) 7197.

[308] M. Park, I. Shin, N.J. Singh, K.S. Kim, J. Phys. Chem. A, 111 (2007) 10692.

[309] A.L. Sobolewski, W. Domcke, J. Phys. Chem. A, 106 (2002) 4158.

[310] F. Agostini, R. Vuilleumier, G. Ciccotti, J. Chem. Phys., 134 (2011) 084303.

[311] O. Vendrell, F. Gatti, H.-D. Meyer, Angew. Chem. Int. Ed. in English, 46 (2007) 6918.

[312] J. Sauer, J. Döbler, ChemPhysChem, 6 (2005) 1706.

[313] N. Jena, M. Tripathy, A. Samanta, K.R.S. Chandrakumar, S. Ghosh, Theor Chem Acc, 131 (2012) 1205.

[314] K.R.S. Chandrakumar, K. Srinivasu, S.K. Ghosh, J. Phys. Chem. C, 112 (2008) 15670.

[315] Z. Wang, S. Irle, G. Zheng, K. Morokuma, J. Phys. Chem. C, 112 (2008) 12697.

[316] G. Zheng, Z. Wang, S. Irle, K. Morokuma, J. Am. Chem. Soc., 128 (2006) 15117.

[317] P. Hirunsit, P.B. Balbuena, J. Phys. Chem. A, 111 (2007) 10722.

[318] R.M. Kumar, M. Elango, V. Subramanian, J. Phys. Chem. A, 114 (2010) 4313.

[319] D. Umadevi, G.N. Sastry, Chem. Phys. Lett., 549 (2012) 39.

[320] A. Rimola, M. Sodupe, Phys. Chem. Chem. Phys., 15 (2013) 13190.

[321] H.-J. Freund, G. Meijer, M. Scheffler, R. Schlögl, M. Wolf, Angew. Chem. Int. Ed. in English, 50 (2011) 10064.

[322] X. Cheng, Z. Shi, N. Glass, L. Zhang, J. Zhang, D. Song, Z.-S. Liu, H. Wang, J. Shen, Journal of Power Sources, 165 (2007) 739.

[323] E. Christoffersen, P. Liu, A. Ruban, H.L. Skriver, J.K. Nørskov, Journal of Catalysis, 199 (2001) 123.

[324] B. Hammer, J.K. Norskov, Nature, 376 (1995) 238.

[325] M. Haruta, T. Kobayashi, H. Sano, N. Yamada, Chemistry Letters, 16 (1987) 405.

[326] A.S. Hashmi, Gold Bull, 36 (2003) 3.

[327] M.D. Hughes, Y.-J. Xu, P. Jenkins, P. McMorn, P. Landon, D.I. Enache, A.F. Carley, G.A. Attard, G.J. Hutchings, F. King, E.H. Stitt, P. Johnston, K. Griffin, C.J. Kiely, Nature, 437 (2005) 1132.

[328] G.J. Hutchings, M. Brust, H. Schmidbaur, Chem. Soc. Rev., 37 (2008) 1759.

[329] M. Valden, X. Lai, D.W. Goodman, Science, 281 (1998) 1647.

[330] M. Haruta, Catalysis Today, 36 (1997) 153.

[331] B.K. Min, C.M. Friend, Chem. Rev., 107 (2007) 2709.

[332] P. Pyykkö, Angew. Chem. Int. Ed. in English, 43 (2004) 4412.

[333] O. Lopez-Acevedo, K.A. Kacprzak, J. Akola, H. Häkkinen, Nat Chem, 2 (2010) 329.

[334] B. Yoon, H. Häkkinen, U. Landman, J. Phys. Chem. A, 107 (2003) 4066.

[335] L.D. Socaciu, J. Hagen, T.M. Bernhardt, L. Wöste, U. Heiz, H. Häkkinen, U. Landman, J. Am. Chem. Soc., 125 (2003) 10437.

[336] D. Tang, C. Hu, J. Phys. Chem. Letters, 2 (2011) 2972.

[337] C. Liu, Y. Tan, S. Lin, H. Li, X. Wu, L. Li, Y. Pei, X.C. Zeng, J. Am. Chem. Soc. 135 (2013) 2583.

[338] C. Zhang, B. Yoon, U. Landman, J. Am. Chem. Soc., 129 (2007) 2228.

[339] C. Harding, V. Habibpour, S. Kunz, A.N.-S. Farnbacher, U. Heiz, B. Yoon, U. Landman, J. Am. Chem. Soc., 131 (2009) 538.

[340] M. Haruta, The Chemical Record, 3 (2003) 75.

[341] A. Sanchez, S. Abbet, U. Heiz, W.D. Schneider, H. Häkkinen, R.N. Barnett, U. Landman, J. Phys. Chem. A, 103 (1999) 9573.

[342] A.A. Herzing, C.J. Kiely, A.F. Carley, P. Landon, G.J. Hutchings, Science, 321 (2008) 1331.

[343] P. Pyykkö, N. Runeberg, Angew. Chem. Int. Ed. in English, 41 (2002) 2174.

[344] X. Li, B. Kiran, J. Li, H.-J. Zhai, L.-S. Wang, Angew. Chem. Int. Ed. in English, 41 (2002) 4786.

[345] H.-J. Zhai, J. Li, L.-S. Wang, J. Chem. Phys., 121 (2004) 8369.

[346] Y. Gao, S. Bulusu, X.C. Zeng, ChemPhysChem, 7 (2006) 2275.

[347] L.-M. Wang, S. Bulusu, H.-J. Zhai, X.-C. Zeng, L.-S. Wang, Angew. Chem. Int. Ed. in English, 46 (2007) 2915.

[348] L.-M. Wang, S. Bulusu, W. Huang, R. Pal, L.-S. Wang, X.C. Zeng, J. Am. Chem. Soc., 129 (2007) 15136.

[349] Y. Gao, S. Bulusu, X.C. Zeng, J. Am. Chem. Soc., 127 (2005) 15680.

[350] N.K. Jena, K.R.S. Chandrakumar, S.K. Ghosh, J. Phys. Chem. C, 113 (2009) 17885.

[351] B. Kiran, X. Li, H.-J. Zhai, L.-S. Wang, J. Chem. Phys., 125 (2006) 133204.

[352] L. Gagliardi, P. Pyykko, Phys. Chem. Chem. Phys., 6 (2004) 2904.

[353] N.K. Jena, K.R.S. Chandrakumar, S.K. Ghosh, J. Phys. Chem. Letters, 2 (2011) 1476.

[354] D. Manzoor, S. Krishnamurty, S. Pal, J. Phys. Chem. C, 118 (2014) 7501.

[355] D. Manzoor, S. Pal, J. Phys. Chem. C, 118 (2014) 30057.

[356] R.M. Olson, S. Varganov, M.S. Gordon, H. Metiu, S. Chretien, P. Piecuch, K. Kowalski, S.A. Kucharski, M. Musial, J. Am. Chem. Soc., 127 (2005) 1049.

[357] E.M. Fernández, J.M. Soler, I.L. Garzón, L.C. Balbás, Physical Review B, 70 (2004) 165403.

[358] K. Balasubramanian, M.Z. Liao, J. Chem. Phys., 86 (1987) 5587.

[359] L. Xiao, B. Tollberg, X. Hu, L. Wang, J. Chem. Phys., 124 (2006) 114309.

[360] S. Zhao, Y. Ren, Y. Ren, J. Wang, W. Yin, J. Phys. Chem. A, 114 (2010) 4917.

[361] N.S. Phala, G. Klatt, E.v. Steen, Chem. Phys. Lett., 395 (2004) 33.

[362] X. Wu, L. Senapati, S.K. Nayak, A. Selloni, M. Hajaligol, J. Chem. Phys., 117 (2002) 4010.

[363] M. Arenz, U. Landman, U. Heiz, ChemPhysChem, 7 (2006) 1871.

[364] L. Ma, M. Melander, K. Laasonen, J. Akola, Phys. Chem. Chem. Phys., 17 (2015) 7067.

[365] J. A. Turner, Science, 305 (2004) 972.

[366] M. A. Henderson, Surface Science Reports, 46 (2002) 1.

[367] P. A. Thiel, T. E. Madey, Surface Science Reports, 7 (1987) 211.

[368] A. A. Phatak, W. N. Delgass, F. H. Ribeiro, W. F. Schneider, J. Phys. Chem. C, 113 (2009) 7269.

[369] Y. Lei, Z. X. Guo, W. Zhu, S. Meng, Z. Zhang, Applied Physics Letters, 91 (2007) 161906.

[370] M. Pozzo, G. Carlini, R. Rosei, D. J. Alfe, Chemical Physics, 126 (2007) 164706.

[371] Y. Liu, L. Huang, K. E. Gubbins, M. B. Nardelli, J. Chem. Phys., 133 (2010) 084510.

[372] L. Schlapbach, A. Züttel, Nature, 414 (2001) 353.

[373] A. C. Dillon, K. M. Jones, , T. A. Bekkedahl, C. H. Kiang, D. S. Bethune, M. J. Heben, Nature, 386 (1997) 377.

[374] T. Yildirim, Jorge Íñiguez, and S. Ciraci, Physical Review B, 72 (2005) 153403.

[375] E. Durgun, S. Ciraci, T. Yildirim, Physical Review B, 77 (2008) 085405.

[376] Y. Zhao, Y.-H. Kim, A. C. Dillon, M. J. Heben, S. B. Zhang, Phys. Rev. Lett., 94 (2005) 155504.

[377] S.-P. Chan, G. Chen, X. G. Gong, Z.-F. Liu, Phys. Rev. Lett., 87 (2001) 205502.

[378] J.-C. Charlier, S. Blase, S. Roche, Reviews of Modern Physics, 79 (2007) 677.

[379] N. G. Chopra, R. J. Luyken, K. Cherrey, V. H. Crespi, M. L. Cohen, S. G. Louie, A. Zettl, Science, 269 (1995) 966.

[380] A. Loiseau, F. Willaime, N. Demoncy, G. Hug, H. Pascard, Phys. Rev. Lett., 76 (1996) 4737.

[381] R. Arenal, O. Stephan, M. Kociak, D. Taverna, A. Loiseau, C. Colliex, Phys. Rev. Lett., 95 (2005) 127601.

[382] L. Wirtz, A. Marini, A. Rubio, Phys. Rev. Lett., 96 (2006) 126104.

[383] C. H. Park, C. D. Sparatu, S. G. Louie, Phys. Rev. Lett., 96 (2006) 126105.

[384] A. Fujishima, K. Honda, Nature, 238 (1972) 37.

[385] S. Dag, E. Durgun, S. Ciraci, Physical Review B, 69 (2004) 121407(R).

[386] Y. Zhang, N. W. Franklin, R. J. Chen, H. Dai, Chemical Physics Letters, 331 (2000) 35.

[387] C. Tang, J. Li, B. Y., C. Zhi, D. Golberg, Chemistry – An Asian Journal, 5 (2010) 1220.

[388] X. Wu, X. C. Zeng, J. Chem. Phys. 125 (2006) 04471.